Technische Universität München
TUM School of Engineering and Design

TUM

# Transient flow of thixotropic cementitious pastes

Mareike Thiedeitz, M. Eng.

Vollständiger Abdruck der von der TUM School of Engineering and Design der Technischen Universität München zur Erlangung einer Doktorin der Ingenieurwissenschaften (Dr.-Ing.) genehmigten Dissertation.

Vorsitz:            Prof. Dr.-Ing. Dirk Lowke

Prüfende der Dissertation:

1.    Prof. Dr.-Ing. Christoph Gehlen
2.    Prof. Dr.ir. Eduardus Koenders
3.    Prof. Dr.-Ing. Michael Haist

Die Dissertation wurde am 19.02.2024 bei der Technischen Universität München eingereicht und durch die TUM School of Engineering and Design am 18.07.2024 angenommen.

# Abstract

Understanding the deformation and flow of cement and concrete is crucial for predicting, adapting and optimizing the processing and placement of concrete. The rheology of concrete has been researched for more than a hundred years. Concrete mixtures and processing methods are constantly being developed. While the flow behavior of concrete is simplified described as linear viscoplastic, various mixtures exhibit increasingly complex rheological flow behavior, which includes high viscosities, nonlinear flow behavior, elastic components and thixotropy. Numerous established experimental methods and mathematical models neglect these properties and do not adequately represent the transient flow behavior.

This thesis provides a methodology to comprehensively classify the transient flow behavior of thixotropic cementitious suspensions. Mixtures varying in their binder composition, solid volume fraction, and flowability, were rheologically investigated using phenomenological modeling, experimental investigations and numerical simulations by means of Computational Fluid Dynamics (CFD). Cementitious pastes were examined for their linear and nonlinear viscoelasticity and viscoplasticity. An elasto-visco-plastic mapping with the most descriptive model parameters was presented. Based on existing experimental methods, thixotropy and structural build-up was experimentally investigated. Subsequently, thixotropy was modeled using a time- and shear rate-dependent structural parameter. Rheometric investigations for the experimental determination of rheological parameters were supplemented by mini-slump flow tests and mini-L-Box flow tests. The applicability of analytical correlation equations between the results of the flow tests and rheological parameters decreased once time- and shear rate- dependent phenomena affected the flow. While the slump flow result is almost time-independent, the L-box flow is significantly affected by the thixotropy of the tested material. However, this correlation is nonlinear. Numerical flow modeling assists in the understanding of flow rather than an explicit correlation equation based on viscoplastic material models. Therefore, the flow tests were numerically simulated using CFD with the Volume-of-Fluid (VoF) method, and analyzed on their transient properties during flow. CFD modeling requires a reliable numerical model and numerical calculation parameters, as well as a rheological model that realistically captures the time- and shear rate-dependent flow properties. Consequently, a numerical framework for reliable free-surface flow modeling was evaluated, and the experimentally and phenomenologically analyzed flow behavior was depicted in the CFD transport model. While the slump flow test could be represented with a small error even with highly viscous flow using viscoplastic modeling, accurate L-box flow required a rheological model that includes time-dependent phenomena such as thixotropy.

The results will be used for the time- and shear rate-dependent analysis in cement and concrete rheology. Experimental results, model proposals and numerical simulations support the analysis, optimization and further development of innovative but complex fine-grain adhesives and concretes.

# Kurzfassung

Das Verständnis der Verformung und des Fließens von Beton ist notwendig für die Vorhersage, Anpassung und Optimierung der Verarbeitung und des Einbaus von Beton. Betonrheologie wird seit mehr als hundert Jahren erforscht. Betonmischungen und Verarbeitungsverfahren werden stets weiterentwickelt. Während das Fließverhalten vieler Betone meist vereinfacht als linear viskoplastisch beschrieben wird, weisen zahlreiche moderne Betonmischungen ein zunehmend komplexeres rheologisches Fließverhalten mit hohen Viskositäten, nichtlinearem Fließverhalten, elastischen Komponenten und Thixotropie auf. Etablierte experimentelle Methoden und rheologische Modelle vernachlässigen diese Eigenschaften und bilden das instationäre Fließverhalten unzureichend ab.

Die vorliegende Arbeit präsentiert eine Methodik zur rheologischen Klassifizierung des instationären Fließverhaltens thixotroper Zementleimsuspensionen. Mischungen, die sich in ihrer Bindemittelzusammensetzung, ihrem Feststoffvolumenanteil und ihrer Fließfähigkeit unterschieden, wurden mithilfe phänomenologischer Modellierung, experimentellen Untersuchungen und numerischen Simulationen analysiert. Die nichtlineare Viskoelastizität und Viskoplastizität der Zementleime wurde klassifiziert, und ein elasto-visko-plastisches Modelldiagramm mit den aussagekräftigsten Modellparametern wurde entwickelt. Zur Modellierung der Thixotropie wurde das Modell eines zeit- und scherratenabhängigen Strukturparameters mit experimentellen Methoden zur Analyse des Strukturaufbaus und Strukturabbaus kombiniert. Zusätzlich wurde das Fließverhalten durch die makroskopischen Fließtests Mini-Setzfließmaß und Mini-L-Box-Test ermittelt. Die Anwendbarkeit analytischer Korrelationsgleichungen zwischen den Ergebnissen der Fließtests und rheologischen Parametern nahm ab, sobald zeit- und scherratenabhängige Phänomene das Fließen beeinflussten. Da das thixotropieabhängige Fließen in der L-Box nichtlinear ist, kann es nicht durch herkömmliche explizite Korrelationsgleichungen berechnet werden. Numerische Simulationen können bei der Abbildung des transienten Fließverhaltens unterstützen. Allerdings erfordern sie ein korrektes numerisches Modell und numerische Berechnungsparameter sowie ein rheologisches Modell, das die zeit- und scherratenabhängigen Fließeigenschaften realitätsnah erfasst. Daher wurde zuerst ein zuverlässiges numerisches Modell für die Fließsimulation mit Computational Fluid Dynamics (CFD) mit der Volume-of-Fluid (VoF)-Methode ermittelt. Anschließend wurden die experimentell ermittelten rheologischen Parameter in das CFD-Modell implementiert. Während der Setzfließmaß-Test selbst bei hochviskosem Fließen mit einer viskoplastischen Modellierung mit einem geringem Fehler dargestellt werden konnte, erforderte die Abbildung des L-Box-Tests ein rheologisches Modell, das zeitabhängige Phänomene wie die Thixotropie einbezieht.

Die Ergebnisse finden Anwendung in der zeit- und scherratenabhängigen Analyse in der Zement- und Betonrheologie. Experimentelle Ergebnisse, Modellvorschläge und numerische Simulationen unterstützen die zukünftige gezielte Weiterentwicklung von innovativen, aber komplexen Feinkornleimen und Betonen.

# Preface

Die vorliegende Arbeit ist in den Jahren 2018-2024 am Centrum für Baustoffe und Materialprüfung an der Technischen Universität München entstanden. Eine Doktorarbeit zu schreiben ist vor allem gegen Ende eine sehr einsame Angelegenheit. Daher möchte ich mich zuerst bei meinen Liebsten bedanken, dass sie mir meine Abwesenheit in den letzten Wochen und Monaten verziehen und mir so viel Kraft und Liebe geschenkt haben.

Ein herzlicher Dank geht an Prof. Christoph Gehlen für die Betreuung und Prüfung meiner Arbeit, sowie Prof. Eddie Koenders und Prof. Michael Haist für die Korrektur.

Lieber Thomas, vielen Dank für alles. Danke für die fachliche und menschliche Unterstützung, die vielen Diskussionen und dass du einfach immer ein offenes Ohr hast, die tolle Atmosphäre bei uns in der Arbeitsgruppe und vor allem danke, dass ich die letzten Jahre so viele Freiheiten genießen durfte. Mit der Rheologie als einzigem Forschungsschwerpunkt wäre ich wohl über kurz oder lang verrückt geworden.

Lieber Maik und Janusch: Danke, dass ihr es so lang am Rheometer ausgehalten habt, und dass ich mich immer auf euch verlassen konnte. Ich habe darauf verzichtet, eine Statistik über durchgeführte Rheometerversuche, verworfene Rheometerversuche und leider nicht auswertbare Rheometerversuche aufzustellen. Ohne euch wäre diese Arbeit vielleicht nie fertig geworden. Ebenso gilt mein Dank Rundi, Deniz und Leonie für die Unterstützung in den letzten Jahren.

Liebe AG2, ich werde euch vermissen. Nico, du hast mich bei uns im Büro aufgenommen und mir die erste Zeit in Süddeutschland sehr erleichtert. Viktor, die letzten zwei Jahre waren einfach toll. Entschuldige bitte mein Rheologie-Tourette, aber noch viel mehr, dass ich nicht mehr mit nach Garching komme. Eva und Juan, ich werde nicht nur das Kaffeebüro, sondern euch als Freunde vermissen.

In den vergangenen Jahren haben viele Studentinnen und Studenten ihre Abschlussarbeiten bei mir geschrieben und so einen Teil zu dieser Arbeit beigetragen. Danke euch allen für das Interesse an dem Thema.

Thank you Robin, that we met in simulation universe, for all our scientific exchanges and discussions and that you could help me with so many questions.

Danke Wolfram für die beste und wertvollste Vermittlung meines Lebens, danke für die letzten Jahre Forschung und ich freue mich auf alles, was noch kommt.

Zuletzt ein abstraktes Dankeschön an Hans Zimmer und Mark Eliyahu, die mich mit ihrer Musik seit Jahren beim Schreiben begleiten und aus jedem emotionalen Loch herausholen.

# Content

## I   Synopsis: Aim of this thesis, state of the art reviews and methodology

## II   Summary of publications related to preliminary investigations

## III   Summary of publications related to transient flow modeling and simulation

# IV   Wrap-up

# Appendix

# List of Tables

# List of Figures

# List of Variables

## Greek characters

| Variable | Definition | Unit |
|---|---|---|
| $\alpha$ | deflocculation parameter | $[-]$ |
| $\beta$ | viscosity parameter | $[\text{s}^{-1}]$ |
| $\delta$ | phase shift angle | $[°]$ |
| $\epsilon$ | normal deformation | $[-]$ |
| $\dot{\epsilon}$ | normal strain rate | $[\text{s}^{-1}]$ |
| $\gamma$ | shear deformation | $[-]$ |
| $\gamma_0$ | strain amplitude | $[-]$ |
| $\gamma_l$ | yield strain | $[-]$ |
| $\gamma_F$ | yield strain at $\tau_F$ | $[-]$ |
| $\dot{\gamma}$ | shear rate | $[\text{s}^{-1}]$ |
| $\dot{\gamma}_{crit}$ | critical shear rate | $[\text{s}^{-1}]$ |
| $\eta$ | dynamic viscosity | $[\text{Pas}]$ |
| $\eta_0$ | zero viscosity | $[\text{Pas}]$ |
| $\eta_0$ | dynamic viscosity of the fluid phase | $[\text{Pas}]$ |
| $\eta_L$ | large strain secant viscosity | $[\text{Pas}]$ |
| $\eta_M$ | minimum strain tangent viscosity | $[\text{Pas}]$ |
| $[\eta]$ | intrinsic viscosity | $[\text{Pas}]$ |
| $\eta_\infty$ | infinity viscosity | $[\text{Pas}]$ |
| $\eta^*$ | complex viscosity | $[\text{Pas}]$ |
| $\zeta$ | zeta potential | $[\text{V}]$ |
| $\lambda$ | characteristic time scale | $[-]$ |
| $\lambda$ | structural parameter | $[-]$ |

| Variable | Definition | Unit |
|---|---|---|
| $\lambda_0$ | boundary structural parameter at t=0 | $[-]$ |
| $\lambda_{equi}$ | equilibrium structural parameter | $[-]$ |
| $\mu$ | plastic viscosity | $[Pas]$ |
| $\mu_1$ | linear viscosity | $[Pas]$ |
| $\mu_2$ | exponential viscosity contribution | $[Pas]$ |
| $\mu_{eff}$ | dynamic viscosity of the suspension | $[Pas]$ |
| $\mu_0$ | dynamic viscosity of the fluid phase | $[Pas]$ |
| $\nu$ | kinematic viscosity | $[m^2/s^2]$ |
| $\phi$ | quantity | $[-]$ |
| $\Phi_{ads}$ | molar adsorption potential | $[J/mol]$ |
| $\Phi_{crit}$ | critical solid volume fraction | $[-]$ |
| $\Phi_{max}$ | maximum solid volume fraction | $[-]$ |
| $\Phi_{perc}$ | percolation threshold | $[-]$ |
| $\Phi_{wd}$ | packing density at water demand content | $[-]$ |
| $\Phi_s$ | solid volume fraction | $[-]$ |
| $\Psi_0$ | Stern potential | $[V]$ |
| $\rho$ | density | $[g/cm^3]$ |
| $\rho_p$ | paste density | $[g/cm^3]$ |
| $\rho_s$ | density of the solid | $[g/cm^3]$ |
| $\rho_w$ | water density | $[g/cm^3]$ |
| $\sigma$ | stress tensor | $[Pa]$ |
| $\tau$ | shear stress | $[Pa]$ |
| $\tau_i$ | inner shear stress (Vane test) | $[Pa]$ |
| $\tau_o$ | outer shear stress (Vane test) | $[Pa]$ |
| $\tau_0$ | yield stress | $[Pa]$ |
| $\tau_{0,d}$ | dynamic yield stress | $[Pa]$ |
| $\tau_{0,B}$ | BINGHAM yield stress | $[Pa]$ |
| $\tau_{0,H-B}$ | HERSCHEL-BULKLEY yield stress | $[Pa]$ |
| $\tau_{0,C}$ | CASSON yield stress | $[Pa]$ |
| $\tau_F$ | yield stress at fracture (oscillatory measurement) | $[Pa]$ |
| $\tau_{0,modB}$ | MODIFIED BINGHAM yield stress | $[Pa]$ |

| Variable | Definition | Unit |
|---|---|---|
| $\tau_{0,s}$ | static yield stress | [Pa] |
| $\tau_{0,T}$ | TOUSSAINT yield stress | [Pa] |
| $\tau_y$ | yield stress (oscillatory measurement) | [Pa] |
| $\Theta$ | flocculation time | [s] |
| $\omega$ | rotational speed | [rad/s] |

## Roman characters

| Variable | Definition | Unit |
|---|---|---|
| $a^*$ | particle curvature radius | [m] |
| $A_0$ | Hamaker constant | [J] |
| $A$ | area | [m$^2$] |
| $A_{thix}$ | thixotropy rate | [Pa/s] |
| $A_{thix,early}$ | early thixotropy rate | [Pa/s] |
| $A_{thix,late}$ | late thixotropy rate | [Pa/s] |
| $B_3$ | friction coefficient | [−] |
| $c$ | flocculation rate | [Pa] |
| $Co$ | Courant number | [−] |
| $D$ | slump flow diameter | [m] |
| $\mathbf{D}$ | Strain rate tensor | [s$^{-1}$] |
| $e_n$ | elastic strain-softening index | [Pa] |
| $E$ | elasticity modulus | [Pa] |
| $E$ | total energy | [J] |
| $F$ | force | [N] |
| $F_d$ | drag force | [N] |
| $F_{VdW}$ | sum of London Van-der-Waals forces | [N] |
| $F_{Es}$ | sum of electrostatic forces | [N] |
| $F_{Ste}$ | sum of steric hindrances | [N] |
| $F_s$ | sum of surface forces | [N] |

| Variable | Definition | Unit |
|---|---|---|
| $F_{k,l}$ | interparticle forces | [N] |
| $g$ | gravitational acceleration | [m/s$^2$] |
| $G$ | shear modulus | [Pa] |
| $G^*$ | complex shear modulus | [Pa] |
| $G'$ | storage modulus | [Pa] |
| $G'_L$ | large strain secant modulus | [Pa] |
| $G'_M$ | minimum strain tangent modulus | [Pa] |
| $G''$ | loss modulus | [Pa] |
| $G_{max}$ | sum of particle interactions | [Pa] |
| $G_{rig}$ | rigidification rate | [Pa/s] |
| $h$ | height | [m] |
| $h_o$ | height of paste in the front of the L-Box | [m] |
| $H$ | geometric factor | [m] |
| $i$ | counter for discretization | [m] |
| $j$ | counter for discretization | [m] |
| $J$ | number of junctions in a particle network | [−] |
| $J_t$ | coagulation rate | [−] |
| $k$ | consistency index | [Pa(s$^n$)] |
| $k_1$ | deflocculation parameter | [−] |
| $k_2$ | flocculation parameter | [−] |
| $k_B$ | Boltzmann constant | [J/K] |
| $L$ | L-Box flow length | [m] |
| $l_0$ | width of the L-Box | [m] |
| $m$ | mass | [kg] |
| $m$ | blending parameter Papanastasiou regularization | [−] |
| $M$ | molar mass | [mol] |
| $m_1$ | pre-factor YODEL model | [−] |
| $\mathbf{n}$ | normal vector | [−] |
| $n$ | non-Newtonian index | [−] |
| $n$ | number of particles | [−] |
| $n$ | rotational speed | [rpm] |

| Variable | Definition | Unit |
|---|---|---|
| $N_1$ | number of molar adsorption places | $[-]$ |
| $N_A$ | Avogadro constant | $[\text{mol}^{-1}]$ |
| $N_{k,l}$ | Number of contact points | $[-]$ |
| $p$ | pressure | $[\text{Pa}]$ |
| $q$ | charge density | $[\text{mol}]$ |
| $r$ | radius | $[\text{m}]$ |
| $R$ | outer radius | $[\text{m}]$ |
| $Re$ | Reynolds number | $[-]$ |
| $R_0$ | hydrodynamic radius | $[\text{m}]$ |
| $R_1$ | inner radius (Reiner-Riwlin equation) | $[\text{m}]$ |
| $R_2$ | outer radius (Reiner-Riwlin equation) | $[\text{m}]$ |
| $S$ | elastic strain stiffening index | $[-]$ |
| $S$ | structural parameter in OpenFOAM | $[-]$ |
| $t$ | time | $[\text{s}]$ |
| $T$ | torque | $[\text{Nm}]$ |
| $T$ | temperature | $[\text{K}]$ |
| $T$ | viscous shear thickening index | $[-]$ |
| $T$ | flocculation time | $[\text{s}]$ |
| $T_n(x)$ | Chebyshev polynomial in x-direction | $[-]$ |
| $T_n(y)$ | Chebyshev polynomial in y-direction | $[-]$ |
| $\mathbf{T}$ | shear stress tensor | $[\text{Pa}]$ |
| $\mathbf{u}$ | velocity vector | $[\text{m/s}]$ |
| $v_n$ | viscous shear-thinning index | $[\text{Pa}]$ |
| $V$ | volume | $[\text{cm}^3]$ |
| $V_S$ | volume of the solid fraction | $[\text{cm}^3]$ |
| $V_W$ | volume of the liquid fraction | $[\text{cm}^3]$ |
| $V_t$ | total Volume | $[\text{cm}^3]$ |
| $w/b$ | water-to-binder ratio | $[-]$ |
| $w/c$ | water-to-cement ratio | $[-]$ |
| $u$ | velocity in x-direction | $[\text{m/s}]$ |
| $u_{k,k}$ | curvature parameter | $[-]$ |

| Variable | Definition | Unit |
|---|---|---|
| $v$ | velocity in y-direction | [m/s] |
| $w$ | velocity in z-direction | [m/s] |
| $x$ | x-direction | [m] |
| $y$ | y-direction | [m] |
| $z$ | z-direction | [m] |
| $z$ | particle distance | [m] |
| $\Delta x$ | spatial discretization in x-direction | [m] |
| $\Delta y$ | spatial discretization in y-direction | [m] |
| $\Delta z$ | spatial discretization in z-direction | [m] |

# Acronyms

| Variable | Definition |
|---|---|
| AM | Additive Manufacturing |
| BET | Brunauer-Emmett-Teller analysis |
| bwoc | by weight of cement |
| CC | Calcined clay |
| CEMI | CEM I A 42.5 R |
| CEMII | CEM II A LL 42.5 N |
| CFD | Computational Fluid Dynamics |
| DEM | Discrete Element Method |
| DPDM | Dissipative Particle Dynamics Method |
| EVP | Elasto-Visco-Plastic |
| FDM | Finite Differences Method |
| FEM | Finite Element Method |
| FVM | Finite Volume Method |
| GNF | Generalized Newtonian Fluid |
| LAOS | Large Amplitude Oscillatory Shear |
| LBM | Lattice Boltzmann Method |

| Variable | Definition |
|---|---|
| LC3 | Limesone Calcined Clay Cement |
| LVE | Linear Viscoelastic Regime |
| OPC | Ordinary Portland Cement |
| PCE | Polycarboxylatether |
| PDE | Partial Differential Equation |
| PEG | Polyethylenglycol |
| PIMPLE | Combination of PISO and SIMPLE |
| PISO | Pressure-Implicit Split-Operator |
| PP | Parallel Plates test |
| PSD | Particle Size Distribution |
| RR | Reiner-Riwlin regression |
| SAOS | Small Amplitude Oscillatory Shweep |
| SCC | Self-Compacting Concrete |
| SF | Slump flow |
| SIMPLE | Semi-Implicit Method for Pressure-Linked Equations |
| SPH | Smoothed Particle Hydrodynamics |
| SSA | Specific surface area |
| SYS | Static yield stress test |
| TEVP | Thixo-Elasto-Visco-Plastic |
| UHPC | Ultra-High Performance Concrete |
| ViC | Vane in Cup |
| VOF | Volume-of-Fluid method |

# Part I

# Synopsis: Aim of this thesis, state of the art reviews and methodology

Figure 1: Quay wall in Friedrichshafen, Germany

# 1. Introduction

*Each flow prediction is only as good as the model that is behind. But which model is the best choice and when should I use which model?*

## 1.1   Concrete and rheology

Concrete is a human-made composite material made of aggregates, cement, fines, and water. Archaeologists have traced the origins of concrete-like materials back thousands of years [Sparavigna (2014); Jahren and Sui (2018)]. *Opus Caementitium* is known as predecessor of the contemporary concrete. It was invented by the Romans who burnt limestone and mixed it with reactive ashes (subsequently known as pozzolanic ashes) to construct the Roman Colosseum, the Pantheon (see Figure 1.1, left), and aqueducts [Artioli and Oberti (2019)]. Their strength and durability properties let them endure until today [Lamprecht (1985)].

After the *Portland cement* was produced as a hydraulic building material in the 19$^{\text{th}}$ century, high-rise buildings with high load-bearing structures, such as the Ingalls building in Cincinnati, Ohio (see Figure 1.1, middle), could be constructed. With the contemporary use of further mineral additives and chemical admixtures, concrete has become a versatile building material that determines, to the greatest extent, our built environment. [Elsen et al. (2022)]



Figure 1.1: Concrete as high performance material: The Pantheon in Rome,125-128, the Ingalls Building in Cincinnati, 1903 [Wikimedia Commons (2023)] and the Raftsund Bridge in Nordland, Norway, 1998 [Dittmar (2023)]

While its targeted properties are the final strength and durability, concrete workability determines the successful processing from manufacturing to its final placement. Depending on its mixture composition, concrete consistency can range from earth-moist to self-consolidating concrete. The workability must be tailored to the formwork and reinforce-

ment geometric boundary conditions, the processing, and the consolidation method. Concrete can be poured (e.g., from concrete trucks or buckets), pumped, sprayed, injected, or printed. After placement, consolidation methods remove air voids and ensure a homogeneous distribution. Figure 1.2 exemplary illustrates different tailored concrete consistencies and placement methods: In Figure 1.2 (a), printed concrete must be flowable during pumping but dimensionally stable after spreading concrete. Figure 1.2 (b) shows the pouring of concrete with a plastic consistency. On the contrary, Figure 1.2 (c) illustrates a pumpable concrete with a lower consistency. In, Figure 1.2 (d) Self-Compacting Concrete (SCC), which must flow and de-air under gravity without external consolidation, is tested for its flowable, self-leveling consistency.

| | |
|:---:|:---:|
| (a) Layers of printed concrete | (b) Pouring of plastic concrete |
| (c) Pumping of concrete | (d) Flow test of SCC |

Figure 1.2: Tailored concrete consistencies for different processing methods

Consistency classes describe the workability properties of concrete for on-site construction applications. They display subjective descriptions rather than scientifically proven laws. The scientific discipline of concrete flow is the field of *Rheology*, a term derived from the ancient Greek words *rhei*, meaning "flow," and *logos*, representing "doctrine." Rheology describes material properties between viscous, elastic and plastic deformation and flow. Rheological properties provide a scientific basis for evaluating concrete flowability. Well-established properties are the *yield stress*, which is the stress that needs to be surpassed for the start-up of flow, *viscosity*, which is the material resistance against shear, and *thixotropy* and *structural buildup*, respectively, which are the time-dependent reversible and irreversible increase of structural strength. A systematic assessment of the relationship be-

tween macroscopic flow characteristics and the chemical and physical composition of the concrete mixture allows the scientific understanding of concrete rheology. It consequently facilitates the precise targeting and optimization of concrete mixture designs based on the intended processing requirements.

Numerous rheological models have been proposed to describe concrete flow. Often, however, the rheological modeling is simplified, and concrete is idealized as a homogeneous fluid governed by a linear viscosity $\mu$ and a yield stress $\tau_0$, signifying its characterization as a linear viscoplastic fluid or *Bingham fluid*. The flow behavior of many concrete mixtures is sufficiently described by these two rheological parameters.

The discipline of *Computational Fluid Dynamics* (CFD) has enabled researchers to compute concrete flow numerically and, thus, to calculate and visualize the concrete placement, see, for example, Figure 1.3, [Vasilic et al. (2019)].
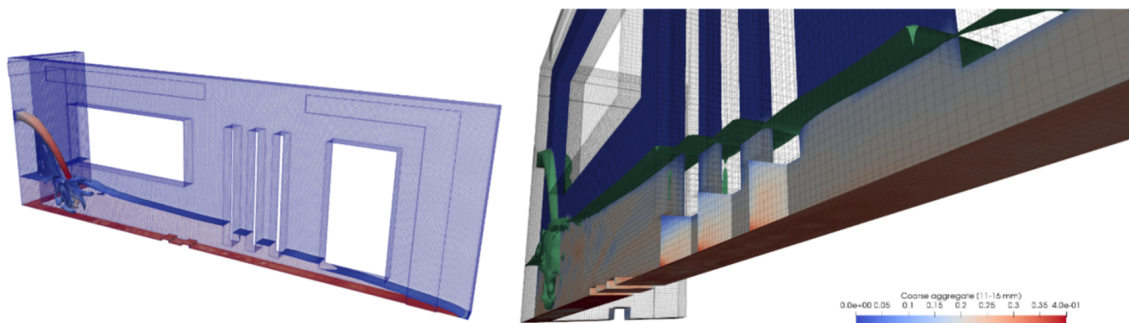


Figure 1.3: CFD modeling of concrete processing, reproduced from [Vasilic et al. (2019)]

CFD pledges a scientific approach to estimate large-scale processing properties, reduce experimental tests, and optimize concrete mixtures and their processing [Vasilic et al. (2019)]. Also in CFD frameworks, concrete is frequently modeled as a linear viscoplastic material [Roussel et al. (2016); Vasilić (2016)]. However, with the constantly developing field of concrete technology, various concrete types are being designed which incorporate mechanisms that lead to deviations from linear viscoplasticity. For instance, *Ultra High Performance Concrete* (UHPC) or *ecological concretes* possess multi-blended mixture compositions with an increased use of additives and chemical admixtures, which can lead to complex rheological behavior. In *Additive Manufacturing* (AM) processing, the concrete mixture requires a process-related, time dependent rheology. The different concretes and their rheological characteristics are shortly introduced:

**UHPC**, introduced in 1994, was designed to exceed concrete compressive strength values of more than 150 MPa. The compressive strength significantly depends on a dense cementitious paste matrix. Water-to-binder (w/b) ratios of around 0.3 or less, and a high amount of fine particles, such as silica fume, are required, leading to high shear rate dependent viscosities and strong thixotropic structural buildup properties. Research findings have enhanced the material properties over the past three decades [Azmee and Shafiq (2018)]. Comprehensive studies are published in [Fehling and Schmidt (2005); Schmidt et al. (2014); Shi et al. (2015)] and [Wang et al. (2015)]. Despite extensive UHPC research, a standardized

procedure for the rheological assessment of UHPC and its optimization is yet to be established. Future perspectives emphasize two potential approaches. Firstly, particle packing optimization shall reduce viscosities while maintaining the desired strength and durability properties. Additionally, Computational Fluid Dynamics (CFD) is proposed to enhance the understanding of the rheological flow of UHPC [Khayat et al. (2019)].

**Ecological concretes** utilize significantly reduced amounts of clinker. Cement clinker, formed through the decarbonization of calcium carbonate ($CaCO_3$) to calcium oxide (CaO), involves the chemical sequestration of carbon dioxide ($CO_2$) and occurs at high temperatures (approximately $1450\,°C$). This process contributes to 8-10 % of global greenhouse gas emissions [Andrew (2019)]. Clinker-efficient binders partially supplement cement clinker with alternative binders [Scrivener et al. (2018)]. However, clinker content reductions may compromise the concrete performance [Ram et al. (2023)]. Increased particle packing, reduced water-to-binder ratios and the use of chemical admixtures shall counteract decreased concrete performance while ensuring good workability. The overall rheology of these multi-blended mixtures, however, can diverge from linear viscoplasticity.

**Concrete for Additive Manufacturing:** AM, also referred to as 3D printing, has been conceptualized in the 1990s, with first printed walls in 2004 through the approach of *Contour Crafting* [Hwang and Khoshnevis (2004)]. For concrete extrusion, rheological properties need to change rapidly between pumping and extruding. Low viscosities are required for the pumping process. After extruding, fast structural buildup for high elasticity and plasticity properties are required to be able to cast the concrete in layers. The precise calculation of rheological properties determines the targeted processing to prevent the failure of the construction [Rehman and Kim (2021)]. The rheological analysis of concretes for 3D printing is a field of ongoing research. However, contemporary AM research considers, most often, concrete as Bingham fluid that has a linear viscosity during pumping and builds up its structure fast and at rest after extruding [Roussel (2018); Jeong et al. (2019); Matthäus (2022); Arunothayan et al. (2023); Ivanova et al. (2022); Ivanova (2023); Pott and Stephan (2021)].

Although the complex rheology of these and similar concretes is known, most research computes and models the concrete flow as linear viscoplastic material, investigates solely the steady-state flow or the structural buildup at rest. This approach neglects shear rate and time-dependent flow phenomena resulting in over- or underestimated processing properties. Consequently, the correct flow computation not only of well-established, but also of more complex mixtures requires an enhanced transient flow description.

Starting from the straightforward linear viscoplastic, time-independent flow description, the rheological classification must extend to a shear rate and time-dependent rheology map, considering viscous, plastic and elastic contributions and structural buildup.

The aim of this thesis, therefore, is to investigate, analyze and classify the transient flow properties of cementitious building materials with increasingly non-Newtonian flow properties. The findings shall provide an applicable methodology to classify transient cementitious paste flow in the interplay of rheological phenomenological modeling, experimental

assessment and numerical CFD modeling:
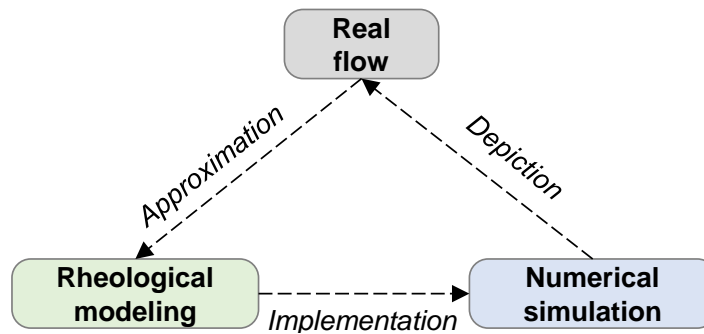


Figure 1.4: Rheology as interplay between real flow, mathematical description and numerical simulation

Various existing rheological models provide a stable basis for the investigation of transient cementitious paste flow features. This includes theories for viscous, plastic, and elastic material characterization as well structural parameter theories. In the field of phenomenological rheological flow description, the main challenge is to find the most appropriate rheological model depending on the mixture composition, the research task or the targeted processing.

Challenges arise when combining theoretical modeling with both experimental measurements and numerical flow modeling. Although numerous experimental procedures have been effectively tested and applied to linear viscous or viscoplastic materials, see e.g., [Chhabra and Richardson (2008)], the parameter assessment for more complex paste flow becomes challenging. The research task is to test the applicability of well-established rheometric frameworks for a broad experimental program, and identify the mixture protocols, experimental boundary conditions and flow test methods to examine reliable, repeatable and comparable rheological investigations.

The most descriptive phenomenological models must be implemented into CFD modeling. However, while the depiction of transient flow properties is a huge benefit of computational models, they are prone to error [Moukalled et al. (2016)]. The applicability of the chosen rheological models and the effect of numerical and physical boundary conditions on the numerical result must be carefully assessed.

## 1.2 Structure of this thesis

This thesis, cumulative in its nature, compiles summaries of published or submitted research. Investigations were conducted in the field of experimental rheology, phenomenological rheological modeling and numerical simulations using Computational Fluid Dynamics. While various researchers are advanced in at least one of these disciplines, the understanding of all rheological disciplines becomes crucial to further develop the field of transient ce-

mentitious paste rheology. Therefore, fundamentals and a comprehensive literature review for each rheological discipline precede the summaries of the publications. The structure of this thesis is illustrated in Figure 1.5.
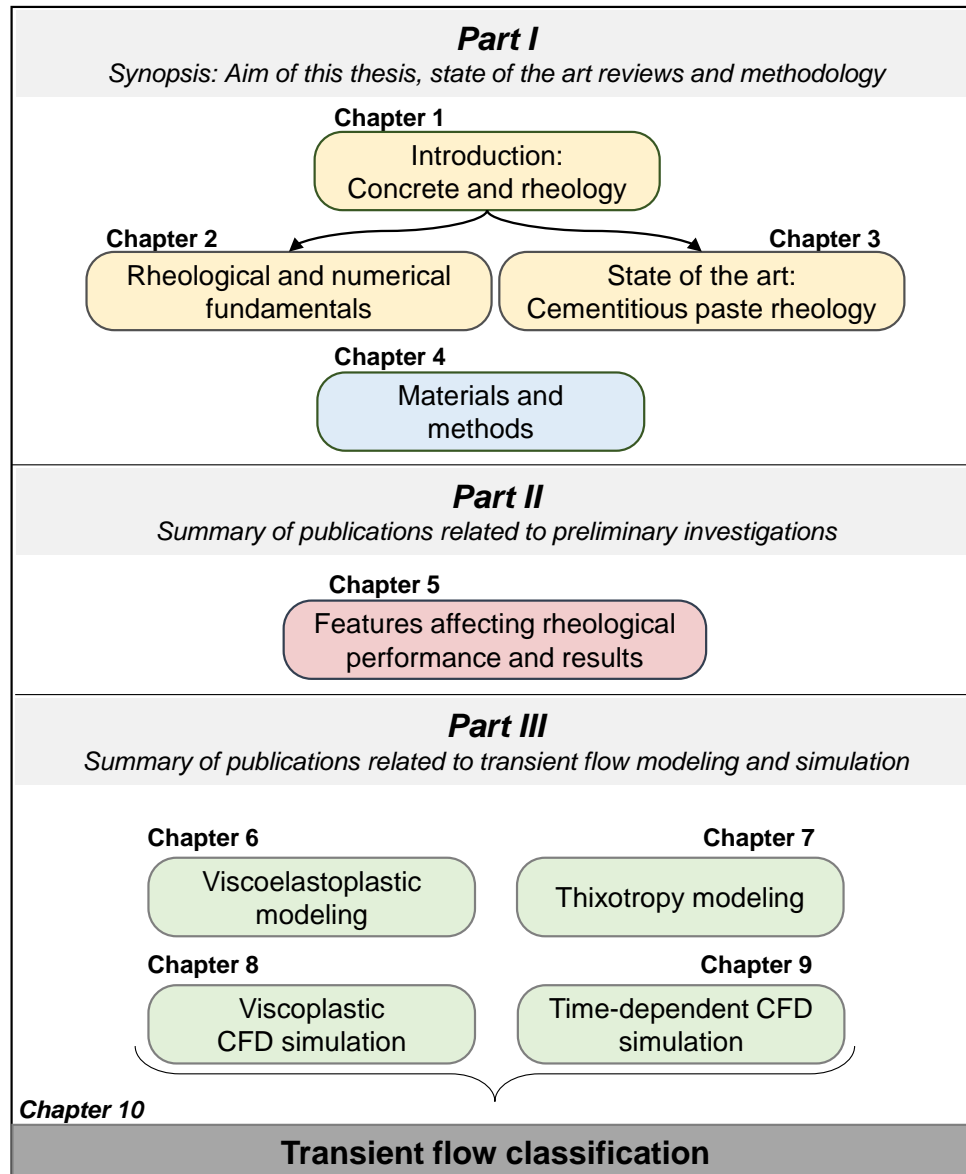


Figure 1.5: Structure of this thesis

**Part I** is the synopsis of this thesis, providing required fundamental knowledge and state of the art reports.

- **Chapter 1** outlines the research significance and structure of this thesis.

- **Chapter 2** provides fundamentals in the field of rheology and Computational Fluid Dynamics. A state of the art review about rheology summarizes rheological modeling between viscosity, elasticity and plasticity. Phenomenological and microstructural

modeling methods are presented, followed by an introduction into the field of experimental rheology using rheometry. Finally, fundamentals of Computational Fluid Dynamics are introduced.

- **Chapter 3** provides a state of the art and literature review for cementitious paste rheology. Well-established phenomenological and microstructural rheological models, flow tests for the estimation of workability, and numerical methods that can be used to compute cementitious paste or concrete flow are summarized.

- **Chapter 4** describes all materials and methods applied in this thesis.

**Part II** summarizes published research related to preliminary investigations. Bibliographic information and *doi* numbers are provided. All publications have been published open source.

- **Chapter 5** incorporates findings from comparative small and large gap rheometric investigations, the effect of pre-shear on rheological properties, thixotropy measurement at low shear rates and the effect of thixotropy on flow tests. Finally, initial CFD modeling of the flow tests with increasingly viscous pastes is presented. Findings were crucial to be able to conduct further robust and error-conscious investigations.

**Part III** is the core of this thesis, comprising **Chapter 6** to **Chapter 9**. Following the preliminary findings, experimental investigations were conducted to analyze the transient properties of cementitious pastes. Again, summaries of open source publications are provided, with the bibliographic information attached.

- **Chapter 6** deals with the characterization of complex cement paste rheology that deviates from common viscoplastic flow. Experimental and mathematical methods were applied to investigate increasingly non-Newtonian cementitious pastes as viscoelastoplastic material. Finally, a rheology map incorporating the most significant rheological parameters for the elasto-visco-plastic classification is proposed.

- **Chapter 7** summarizes findings of steady and transient phenomenological thixotropy modeling. Moreover, different rheometric techniques to analyze thixotropy and structural buildup are compared regarding their ability to grasp rheological properties that fit a time- and shear rate dependent mathematical model.

- **Chapter 8** provides a robust slump flow test setup in CFD, comprising a numerical convergence study, the analysis of the regularization method and regularization parameters, and computation of transient properties

- **Chapter 9** presents the transient thixotropy modeling in CFD to compare the time-dependent and time-independent flow progress of increasingly non-Newtonian cementitious pastes.

**Chapter 10** concludes the findings, critically analyzes possibilities and limitations of the provided rheological classification, and provides ideas for prospective research. Prospectively, research findings shall be adoptable for a wide range of increasingly non-Newtonian concrete mixtures, and provide a guideline on how to classify the rheological behavior mathematically, experimentally and numerically.

## 1.3   Limitations

The focus of this thesis is to establish an adoptable guideline. The experimental framework comprises of cementitious pastes with different binders and mixture compositions, but not of various, multi-blended systems, mortars or concrete.

Fundamentals of microstructural modeling are introduced in the literature review, and several correlations between the conducted experimental investigations and the paste microstructure are discussed. However, no scientific correlation between chemical compositions, microstructural analysis and phenomenological modeling is applied.

Finally, the field of cement paste and concrete rheology is broad. All experimental frameworks, modeling approaches and numerical computations display the justified choices of the author of this thesis.

# 2. Rheological and numerical basics

## 2.1  From continuum mechanics to fluid flow

The flow of matter has been investigated since ancient times. The first scientific research findings were published by Sir Isaac Newton in the $17^{th}$ century [Newton (1687)]. The basis of rheology is the field of *continuum mechanics*, which describes the deformation of solids and fluids in an idealized continuum. *Rheology* was invented as a separate discipline for flow analysis by Eugene Bingham, who published his first article "An investigation of the laws of plastic flow" in 1916 [Bingham (1916)]. He defined the term *Rheology* in 1920 and was the co-founder of *The Society of Rheology* in 1929. Nowadays, the discipline combines the theories of elasticity, plasticity, and viscosity with the laws of fluid dynamics and thus is a fundamental part of understanding physical, chemical, and biological flow processes. [Giesekus (1994)] distinguishes the fields of rheology into the disciplines *structural* and *phenomenological rheology*, *rheometry*, and *applied rheology*. *Structural rheology* combines microstructural properties of matter with the deformation and flow behavior. *Phenomenological rheology* describes the visible flow behavior of a continuum through mathematical formulations without regard to inner structural characteristics. *Applied rheology*, including *rheometry* and *flow tests*, investigates material flow experimentally. The combination with the fundamental laws of *fluid dynamics* allows the material-dependent calculation of the flow of matter, see illustration in Figure 2.1 Altenbach (2018)].
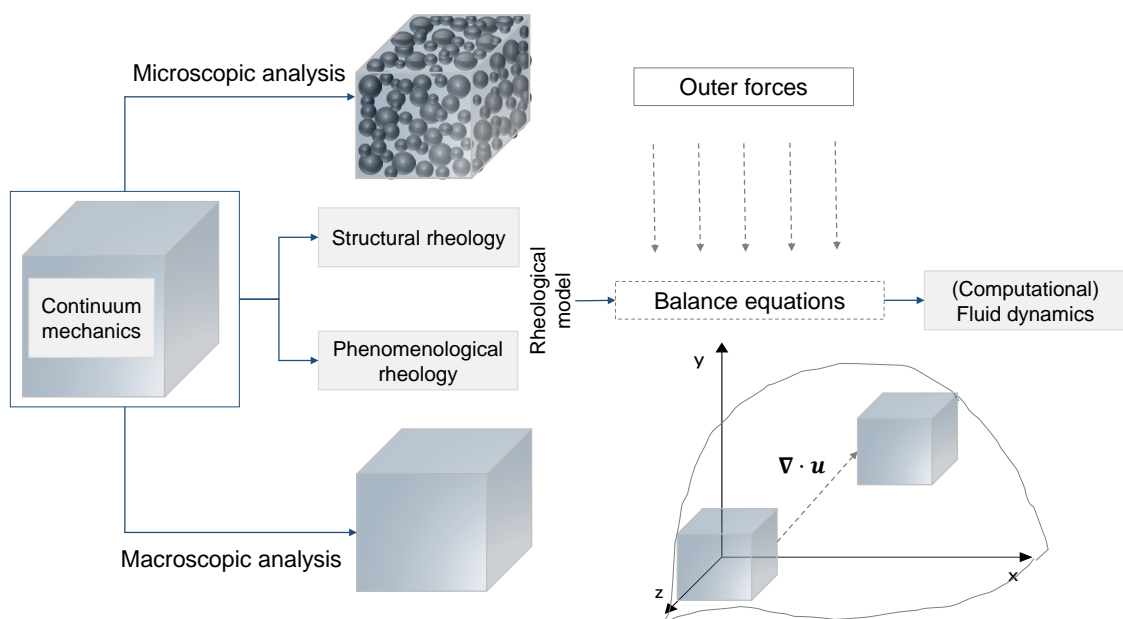


Figure 2.1: From continuum mechanics to the material-dependent calculation of flow

## 2.2   Fundamentals of suspension rheology

Suspension rheology is the scientific discipline to describe the deformation and flow of colloidal suspensions. A colloid (greek from $\kappa o \lambda \lambda \alpha$, which is the word for "paste") comprises of a two-phase system with a cluster- or network-forming phase in a suspending medium. Both phases can be either solid, fluid, or gas. [Everett (1992)]

The definition of colloidal particles varies across scientific disciplines, often characterized by particle diameters below 1 $\mu m$. Depending on the phase properties, emulsions, dispersions, and suspensions are distinguished. Two-phase media with high particle packing densities are categorized as suspensions or pastes. [Lauth and Kowalczyk (2016)]

The macroscopic rheological properties of suspensions are governed by particle packing. The solid volume fraction $\phi_s$ is the most critical parameter to classify the suspension rheology:

$$\phi_s = \frac{V_S}{V_t} \qquad\qquad [-] \quad (2.1)$$

where $V_S$ is the volume of the solid fraction, which is calculated by the mass divided by its density $\frac{m_s}{\rho_s}$, and $V_t$ is the total volume (which is the sum of solid and liquid, $\frac{m_s}{\rho_s} + \frac{m_w}{\rho_w}$). In dilute systems, the liquid content significantly surpasses the solid content, leading to minimal or no interactions between particles. Beyond a percolation threshold, particle distances decrease, and interparticle interactions become significant, schematically illustrated in Figure 2.2. [Liu (2000); Firth and Hunter (1976)].

$$\phi_s < \phi_{perc} \qquad\qquad \phi_s > \phi_{perc}$$
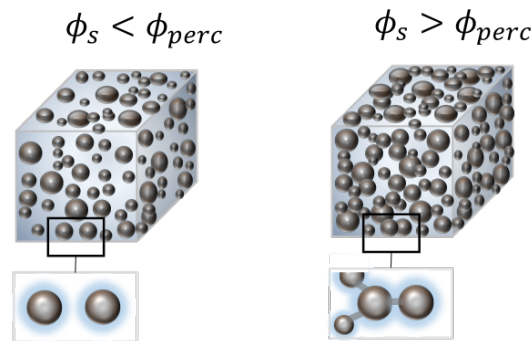


Figure 2.2: Schematic particle interaction in a dilute and a densely packed system

The sum of attractive and repulsive surface forces and particle interactions determines the network strength, which forms the colloidal particle network. The magnitude of interparticle forces depends on the particle surface area, particle distances and the chemical composition of the carrier liquid and particle surfaces. [Genovese (2012)]

The particle network finally determines the resistance of the material against deformation and flow. Rheological properties can be investigated through phenomenological flow formulations or with particle-related models. Both approaches are presented in the following.

## 2.2.1 Phenomenological modeling

"*The stress at the location of a material particle is determined exclusively by the history of motion in an infinitesimal environment of this particle*". [Giesekus (1994), p.114].

Depending on the field of rheology and the matter to be investigated, common phenomenological models vary. Comprehensive work beyond this literature review is found, e.g., in Oldroyd (1950); Barnes et al. (1993); Giesekus (1994); Mezger (2016).

**Fundamental models**

In the simplest description of continuum mechanics, stress and deformation are exemplified on a geometrically defined continuum. By combining infinitesimal small continua, one can describe mechanical quantities of a volume [Rütten (2019)]. Augustin-Louis Cauchy introduced the stress tensor $\boldsymbol{\sigma}$ for an infinitesimal continuum, which is now the *Cauchy stress tensor*:

$$\boldsymbol{\sigma} = \begin{pmatrix} \sigma_{xx} & \tau_{xy} & \tau_{xz} \\ \tau_{yx} & \sigma_{yy} & \tau_{yz} \\ \tau_{zx} & \tau_{zy} & \sigma_{zz} \end{pmatrix} \tag{2.2}$$

with the normal stress components $\sigma_{xx}$, $\sigma_{yy}$ and $\sigma_{zz}$ and all shear stress components $\tau_{ij}$, subsequently illustrated in Figure 2.3 (a) with corresponding deformations $\epsilon$ and $\gamma$ in Figure 2.3 (b) when the continuum is distorted.
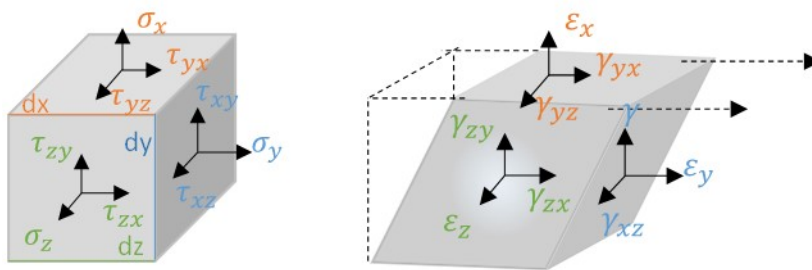


Figure 2.3: Left: continuum with stress declarations $\sigma$ and $\tau$, right: deformation $\epsilon$ and $\gamma$

The simple shear flow analogy reduces the three-dimensional stress calculation within a continuum. The idealized shear deformation and flow of a material between two parallel plates are illustrated in Figure 2.4.

If the upper plate with an area $A$ is sheared with a force $F$, see Figure 2.4(a), a shear stress $\tau$ in [N/mm$^2$] or [Pa] occurs on infinitesimal layers moving towards the upper plate. The shear stress $\tau_{xy}$ is calculated as

(a) $\tau$            (b) $\gamma$            (c) $\dot{\gamma}$
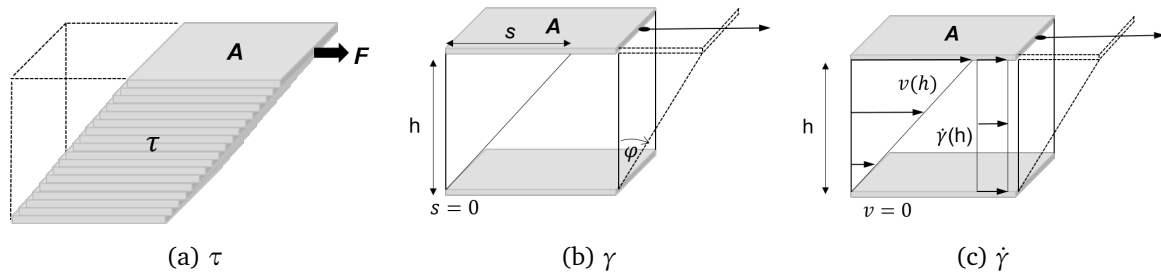
Figure 2.4: Simple shear analogy of the parallel plates

$$\tau_{xy} = \frac{F}{A} \qquad\qquad \left[\text{N/mm}^2\right] \quad (2.3)$$

The corresponding deformation $\gamma$ is calculated as

$$\gamma = \tanh\varphi = \frac{s}{h} \qquad\qquad [-] \quad (2.4)$$

with $s$ as displacement of the element over the height $h$, see Figure 2.4(b). The shear rate $\dot{\gamma}$ is the derivation of the shear velocity $v$ in $[\text{m/s}]$ over the height $h$, also known as the temporal derivative of the shear deformation, see Figure 2.4(c):

$$\dot{\gamma} = \frac{dv}{dh} = \frac{d\gamma}{dt} \qquad\qquad \left[\text{s}^{-1}\right] \quad (2.5)$$

Basic rheological models to describe the relation between stress and deformation or flow are the ideal elements of the elastic Hookean spring, viscous Newtonian dashpot, and plastic St. Venant block. Figure 2.5 depicts the idealized mechanical models.
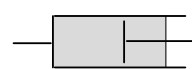
| Elasticity | Viscosity | Plasticity |
|:---:|:---:|:---:|
| Hooke element: spring | Newton element: dashpot | St. Venant element: block |
|  |  |  |

Figure 2.5: Idealized elements of rheological behavior

**Hooke's elasticity law** describes ideal elastic behavior of a body with its fully reversible, time-dependent deformation. For normal forces, the deformation $\epsilon$ is proportional to the normal stress $\sigma$ with the elasticity modulus $E$ as proportionality constant in $[\text{Pa}]$. The constitutive equation is given in Eq. 2.6

$$\sigma = E\epsilon \qquad\qquad \text{[Pa]} \quad (2.6)$$

In case of shear forces, the proportionality factor between the shear deformation $\gamma$ and the shear stress $\tau$ is the shear modulus $G$ in [Pa]:

$$\tau = G\gamma \qquad\qquad \text{[Pa]} \quad (2.7)$$

**Newton's viscosity law**   describes the resistance against shear forces when the material flows. According to DIN 1342-1:2003-11, viscosity is defined as "the property of a flowable substance to flow and be irreversibly deformed under the action of a stress" [DIN1324]. Irreversible deformation of the material occurs due to viscous dissipation. The deformation occurs retarded. [Freundlich (1939)]

The dashpot depicted in Figure 2.6 describes Newton's law. The proportionality constant between the deformation velocity or shear rate $\dot{\gamma}$ in [s$^{-1}$] and the shear stress $\tau$ in [Pa] is the material viscosity $\eta$ in [Pas]:

$$\tau = \eta\dot{\gamma} \qquad\qquad \text{[Pa]} \quad (2.8)$$

Newtonian fluids are ideal viscous fluids that possess a linear velocity gradient. The kinematic viscosity $\nu$ displays a density independent material constant, Eq. 2.9:

$$\nu = \frac{\eta}{\rho} \qquad\qquad \left[\text{m}^2/\text{s}\right] \quad (2.9)$$

**Plasticity**   describes the material's ability to resist applied stress without deformation, described by the St. Venant block in Figure 2.5. Once surpassing a critical stress, it undergoes irreversible deformation, referred to as "yielding". The stress at the plasticity limit is termed the yield stress. Various stress theories exist to explain the plasticity criterion and characterize the failure of a material. [Freundlich (1939); Feda (1992)]

**Combined rheological models and non-Newtonian flow**

Deformation and flow of matter is generally a combination of elastic, viscous and plastic contributions. Three simple linear model combinations for viscoelasticity and viscoplasticity are illustrated in Figure 2.6.

| Viscoelastic deformation | Viscoelastic flow | Viscoplastic flow |
|---|---|---|
| Kelvin-Voigt element | Maxwell element | Bingham model |
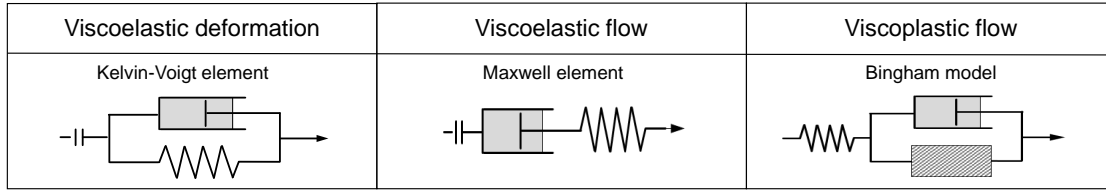
Figure 2.6: Kelvin-Voigt element, Maxwell element, and Bingham element

**Viscoelastic deformation and flow** are described by combining the elastic spring and viscous damper element. The Kelvin-Voigt model connects the Hooke spring and Newtonian damper in parallel. Once stress is applied, the spring and damper deform simultaneously, with the damper slowing down the spring to the deformation speed and delaying the deformation. After removing the stress, the material completely deforms reversely but time-delayed. The model is mainly used for the description of elastic deformation. Eq. 2.10 displays the governing equation:

$$\sigma = E\epsilon + \eta\dot{\epsilon} \qquad [\text{Pa}] \qquad (2.10)$$

The Maxwell model describes viscoelastic flow and is used for materials like polymers or gels. The elastic spring deforms immediately, while the damper experiences no initial change. Once the system is unloaded, the spring returns to its initial state and the damper stops at the last deformation reached, which results in a partially irreversibly deformed state, which can yield fluidity of the viscoelastic material even after removing the load [Khokhlov (2023)]. Eq. 2.11 displays the governing equation for a Maxwell element:

$$\frac{1}{E}\dot{\sigma} + \frac{\sigma}{\eta} = \dot{\epsilon} \qquad [-] \qquad (2.11)$$

A further insight into viscoelastic material models can be found, e.g., in [John et al. (1986); Phan-Thien and Mai-Duy (2017)].

**Viscoplastic materials** only deform once a particular shear stress, commonly referred to as the yield stress $\tau_0$, is surpassed. If the applied stress is smaller than the internal structural strength, the material behaves solid-like, purely plastic (without deformation), or elastic (with deformation). The Bingham model displays the simplified linear viscoplastic flow. After surpassing the plasticity limit $\tau_{0,B}$, the material flows with a linear viscosity. The constitutive equation is presented in Eq. 2.12:

$$\tau = \tau_{0,B} + \mu\dot{\gamma} \qquad [\text{Pa}] \qquad (2.12)$$

However, many fluids undergo microstructural changes during shear, also referred to as *structural viscosity*. They possess a shear rate dependent, nonlinear viscosity, which can be either decreasing (shear-thinning material behavior) or increasing (shear-thickening behavior). Figure 2.7 displays non-Newtonian flow of a Bingham material, shear-thinning and shear-thickening flow. Figure 2.7 shows the $\tau - \dot{\gamma}$ - diagram, with the corresponding viscosity in Figure 2.7(b).
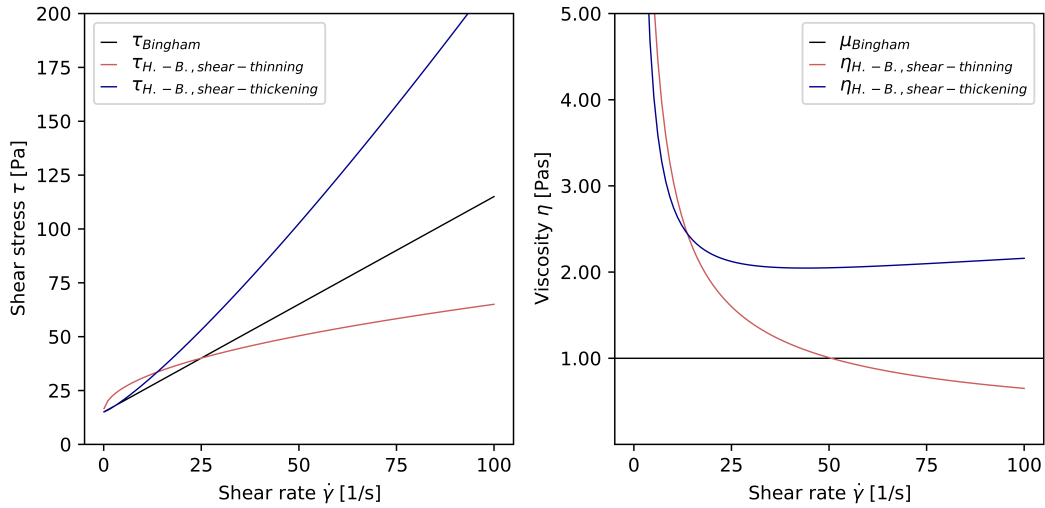


Figure 2.7: Bingham flow, shear-thinning and shear-thickening flow

## Thixotropy

Contrary to structural viscosity, which is the instantaneous shear rate dependent viscosity change, thixotropy describes the time-dependent, fully reversible viscosity change. The word thixotropy originates from the Greek word "*thixis*" ("*act of touching, shaking, stirring*), and "*trepo*" ("*turning, changing*")and was first used by the Hungarian biologist Tibor Péterfi in 1927 [Peterfi (1928)].

[Freundlich (1935)] defined thixotropy as "isothermal reversible sol-gel transformation". [Cheng (1987)] associated thixotropy with the microstructural flocculation and agglomeration potential resulting from interparticle forces, which could be attractive (e.g. Van-der-Waals forces) or repulsive (e.g. electrical or steric repulsion). At a constant shear rate $\dot{\gamma}$, shear stress $\tau$ decreases over time. At $\dot{\gamma}_{rest}$, the material restructures time-dependently. On the contrary, if the shear stress increases with time and recovers after shear stoppage, the phenomenon is called rheopexy. Figure 2.8 illustrates both thixotropy and rheopexy.

The simplified constitutive equation for thixotropy-dependent shear stress is provided in Eq. 2.13 and Eq. 2.14, proposed by [Cheng and Evans (1965)]:

$$\tau = \tau(\dot{\gamma}; \lambda) \tag{2.13}$$
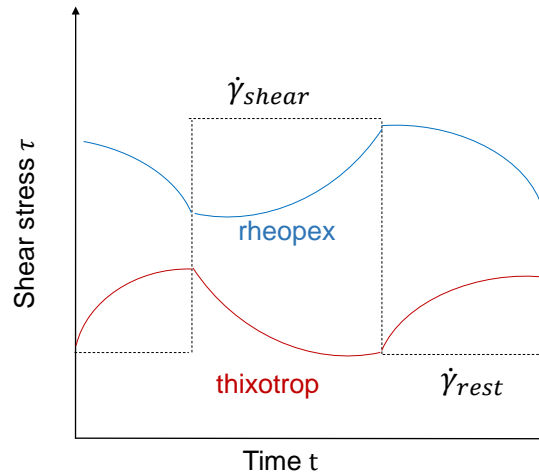
Figure 2.8: Illustration of thixotropy and rheopexy

In Eq. 2.13, $\lambda$ is the time- and shear rate dependent structural build-up and breakdown rate:

$$\frac{d\lambda}{dt} = g(\dot{\gamma}; \lambda) \qquad (2.14)$$

Various models have been proposed for the function $g$ to model thixotropy, which is part of Chapter 3 and Chapter 7.

### 2.2.2   Structural rheology

Structural rheology combines constitutive rheological models with chemical and physical properties of the investigated material. On the nano-scale, random particle motion, colloidal surface forces and interparticle forces define interactions between molecules, colloids and particles. In combination with granulometric properties on the micro-scale (particle packing, particle size distribution and particle shapes), structural interactions define a system's ability to flow, schematically illustrated in Figure 2.9.
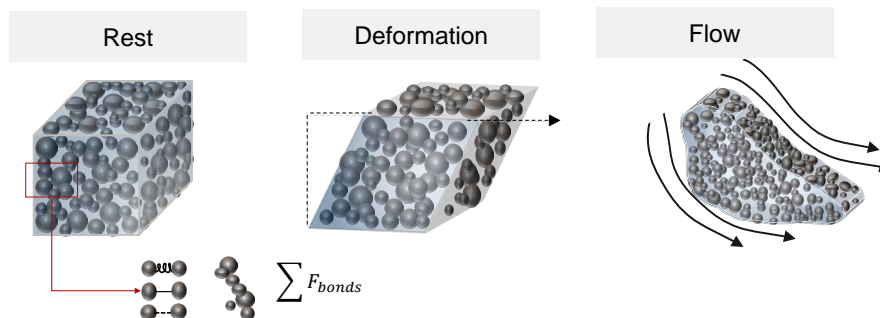


Figure 2.9: Schematic illustration of structural rheology

### Particle interactions on nano-scale

Attractive particle surface forces, such as electrostatic attraction or Van-der-Waals forces, result in particle agglomeration. Colloidal dispersion forces are physically and thermally driven by Brownian motion, hydrodynamic interactions, and contact collision interactions, as well as chemically driven by electrostatic repulsion or steric hindrances. The particle distance determines the particle interaction forces [Lauth and Kowalczyk (2016)]).

**Brownian motion** is the thermally initiated random particle motion of molecules within a viscous fluid occurs in each system, observed by [Brown (1828)]. The fluid viscosity, the particles entropy and the particles hydrodynamic radius affect the the intensity of the motion [Philipse (2018)]:

$$x^2 = \frac{k_B T}{3 R_0 \pi \eta} t \qquad \left[\mathrm{m}^2\right] \quad (2.15)$$

with $x^2$ characterizing the mean square displacement of particles due to Brownian motion, $k_B$ as Boltzmann constant[1], $T$ as absolute temperature in $[K]$, $R_0$ as hydrodynamic radius in $[m]$, and $\eta$ as fluid viscosity in $[Pas]$. A simplified energy calculation $E$ in $[J]$ is Eq. 2.16

$$E = k_B T \qquad [J] \quad (2.16)$$

Brownian motion drives fluid rheology primarily in dilute systems at very low shear rates [Coussot and Ancey (1999)].

**Electrostatic interactions** are the sum of attractive or repulsive forces between molecules or particles due to their charge density $q$, which is calculated with Eq. 2.17

$$q = \frac{N_1 v_e}{1 + \frac{N_A}{M * n} \exp\left\{\frac{v_e \psi_\delta + \phi_{ads}}{kT}\right\}} - \int_0^\infty \phi_{el} \, dz \qquad [\mathrm{mV}] \quad (2.17)$$

where $N_1$ is the number of molar adsorption places, $N_A$ is the Avogadro constant[2], $M$ the molar mass of the solvent in $[\mathrm{g/mol}]$, $\phi_{ads}$ the molar adsorption potential in $[\mathrm{J/mol}]$, $n$ the number of particles and $z$ the particle distance in $[\mathrm{m}]$. According to Stern, for diluted suspensions, particles do not directly interact with each other, but form an electrostatic double layer that determines the interaction forces [Helmholtz (1879)]. The electrostatic double

---

[1]The Boltzmann constant is a conversion factor to change absolute temperature into energy. It is $1.38 \cdot 10^{-23}$ J/K

[2]The Avogadro constant is $6.022 \cdot 10^{23}$ particles / mol

layer has a clear ionic charge density and, thus, electric potential (called the Stern potential $\psi_0$ in [V]) and a diffusive double layer $\frac{d\psi}{dz}$, which decreases with increasing distance from the particle surface. The thickness of the Stern layer depends on the ion size and charge density and is called Debye-length. A direct surface charge measurement of $\psi_0$ is not possible. An experimental approach to measure the initial surface charge at the Stern layer $\psi_0$ is the Zeta-Potential $\zeta$. [Daimon and Roy (1979); Hunter (2013)]

**Attractive London-Van-der-Waals forces**    The London Van-der-Waals forces are attractive dipole-dipole interactions that apply to non-charged particles due to short-term asymmetric charge distribution [Hamaker (1937)]. A simple formulation of the energy $\psi_0$ caused by London Van-der-Waals forces is

$$\psi_0 = \frac{A_0 a^*}{12H} \qquad [\text{J}] \qquad (2.18)$$

with $A_0$ as Hamaker constant in [J], $a^*$ as particle curvature radius in [m], and $H$ as a geometric factor, i.e., the particle distance in [m]. $A_0$ depends on the number density of molecules, the polarizability, the Boltzmann constant, and the absolute temperature. The formulation is only valid for spherical particles [Hamaker (1937); Flatt (2004b)]. The force $F_{VdW}$ between two spherical particles is calculated by derivation of Eq. 2.18 by the particles distance:

$$F_{VdW} = \frac{A_0 a^*}{12H^2} \qquad [\text{N}] \qquad (2.19)$$

London-Van-der-Waals forces are weaker than dipole-dipole attraction or ionic attraction. Thus, they only become relevant if no ionic attraction or constant dipoles exist. Van-der-Waals forces decrease significantly with increasing particle distance. [Hamaker (1937)]

**Particle interactions on micro-scale**

Particle models correlate granulometric properties, such as the particle shape and the solid volume fraction $\Phi_s$, to rheological properties. In most cases, empirical formulations correlate granulometry to the suspension viscosity. Einstein formulated Eq. 2.20 for dilute systems:

$$\mu_{eff} = \mu_0(1 + \frac{5}{2}\phi_s) \qquad [Pas] \qquad (2.20)$$

with $\mu_{eff}$ as dynamic viscosity of the suspension in [$Pas$] and $\mu_0$ as dynamic viscosity of the fluid phase in [$Pas$].

Once $\Phi_s$ increases and particles interact, Einstein's law is not valid anymore. The viscosity then depends on the amount of particles, the particle size distribution (PSD), particle

sizes and shapes. Once $\Phi_s$ approaches the maximum possible solid volume fraction $\Phi_m$, the viscosity increases to infinity. Several models describe the viscosity of densely packed suspensions. [Krieger and Dougherty (1959)] formulated Eq. 2.21:

$$\frac{\eta}{\eta_0} = \left(1 - \frac{\phi_s}{\phi_m}\right)^{-[\eta]\phi_m} \qquad [\text{Pas}] \qquad (2.21)$$

with $\eta$ as dynamic viscosity of the suspension in [Pas], $\eta_0$ as dynamic viscosity of the fluid phase in [Pas], $\Phi_s$ as current solid volume fraction [-], $\Phi_m$ as maximum solid volume fraction [−] and [$\eta$] as the intrinsic viscosity, which is a dimensionless quantity. $\Phi_m$ can be calculated due to particle size distribution and particles shapes, or experimentally investigated [Santhanam and Kumar (2003)].

Eq. 2.21 has proven valid for dilute and densely packed suspensions without the consideration of colloidal interparticle forces [Coussot and Ancey (1999)]. Figure 2.10 (a) illustrates the effect of different intrinsic viscosity values, i.e. [$\eta$] = 2.5 , 4.0 and 6.0, while Figure 2.10 (b) maps Eq. 2.21 for different $\Phi_m$. Further effects on viscosity, e.g. the effect of particle shapes, were analyzed by [Genovese (2012)].
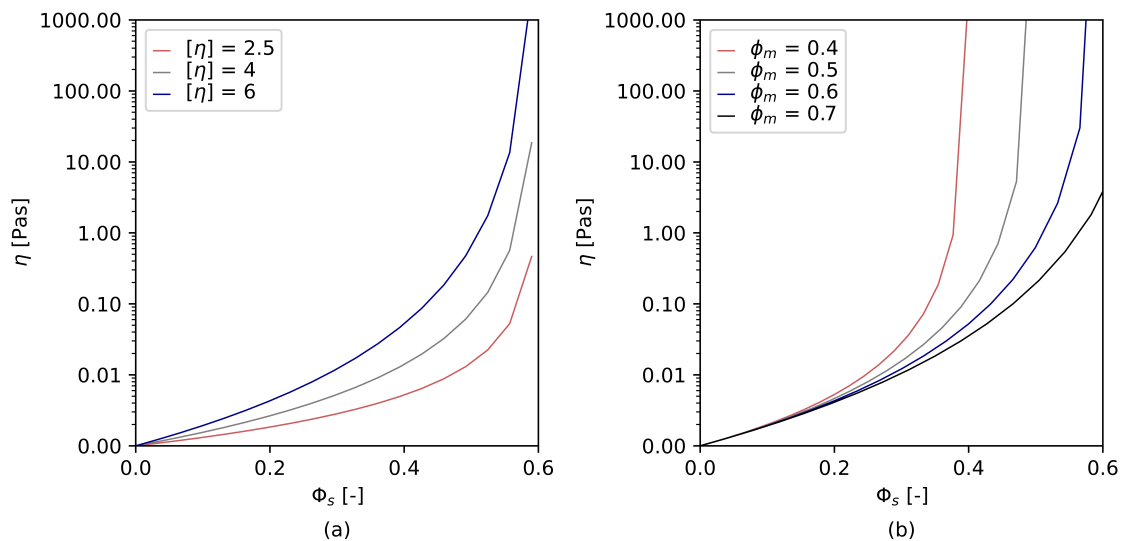


Figure 2.10: $\eta$ according to Eq. 2.21

## 2.3   Rheometry

Measurements with rheometers or viscosimeters facilitate the experimental investigation of rheological properties by measuring a sample's resistance against an applied shear load. Figure 2.11 illustrates a simplified overview of rheometric procedures with regard to this thesis:
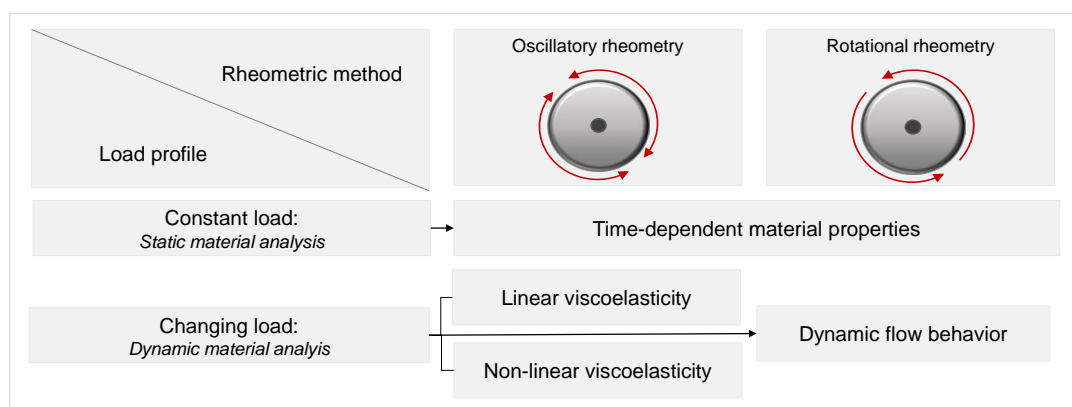


Figure 2.11: Rotational and oscillatory material analysis with static or dynamic measurement techniques

Rheometers apply a stress $\tau$ or strain $\gamma$ to a sample and measure the material response. Consequently, rheological properties can be calculated from $\dot{\gamma} - \tau$ - flow curves or $\gamma - \tau$ - deformation curves. The load can be applied by rotational or oscillatory deflection. Static analysis methods investigate material changes over time.

The calculation of $\tau$, $\gamma$ and $\dot{\gamma}$ outgoing from the device raw data, which are the torque $T$ and the angular velocity $\omega$, depends on the measurement geometry and can affect the final rheological result. Absolute measuring systems, according to DIN 53019-1 standards, offer precise solutions for the velocity field and, consequently, the shear rate $\dot{\gamma}$, see [DIN53019]. They include measuring systems with concentric cylinders, cone and plate and parallel plates. [Mezger (2016)]

In relative measuring systems, the velocity field is unknown, which is the case e.g., in large gap geometries. Large gap devices are used when samples contain large particles or exhibit low viscosities with a tendency for strong wall slip. An extensive overview of different geometries is provided in [Mezger (2016); Macosko (1994); Chhabra and Richardson (2008)]. This thesis utilizes the parallel-plate geometry (subsequently PP) as an absolute measurement device and a Vane-in-Cup geometry (subsequently ViC) as a relative measurement device.

### 2.3.1 Rotational rheometry

Rotational rheometry facilitates the analysis of viscous and viscoplastic (Newtonian and non-Newtonian) fluids. $\dot{\gamma} - \tau$ - flow curves are obtained and rheological parameters like the yield stress $\tau_0$ and plastic or apparent viscosity $\mu$ and $\eta$ can be calculated.

**Absolute measurements with parallel plates (PP)** are illustrated in Figure 2.12. The geometry resembles the simple shear flow analogy: PP systems possess a lower and an upper plate with the radius $r$. The plates are arranged at a distance $h$ with $h << r$.
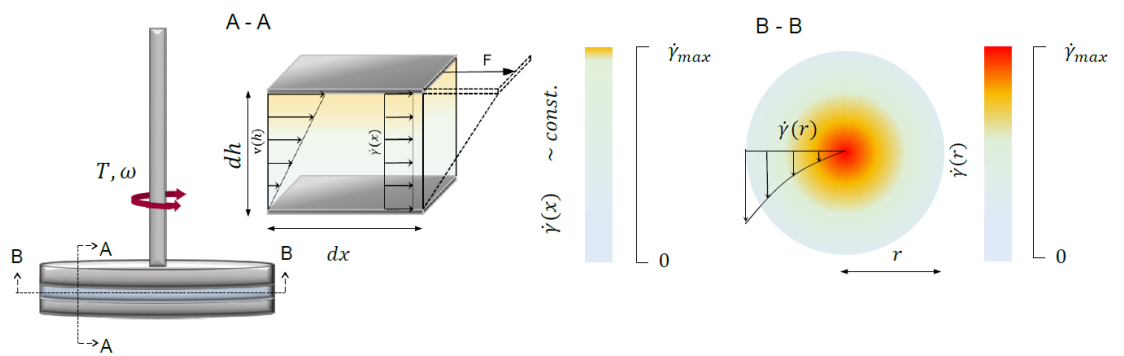


Figure 2.12: PP rheometry with radial and tangential illustration of the shear rate distribution

The shear rate $\dot{\gamma}(r)$ in $[1/s]$ is calculated from the angular velocity $\omega$ in $[rad/s]$ depending on the gap height $h$ in $[mm]$ and the radius $r$ in $[mm]$:

$$\dot{\gamma}(r) = \frac{\omega r}{h} \qquad [1/s] \qquad (2.22)$$

The shear stress $\tau(r)$ is calculated from torque data $T$:

$$\tau(r) = \frac{2T}{\pi r^3} \qquad [Pa] \qquad (2.23)$$

Figure 2.12 in section B-B highlights that the shear rate distribution is heterogeneous. The shear rate $\dot{\gamma}$ achieves its maximum at the upper plate, and, in radial direction, at the outer radius $r = R$. Various methods are available for determining radius-independent rheological parameters $\dot{\gamma}$ and $\tau$. In cone-plate systems, a defined angular of the cone (instead of an upper plate) adjusts the radius-dependent gap height, resulting in a similar shear rate $\dot{\gamma}$ over the gap height. PP geometries with a small gap minimize deviations and assume a nearly constant shear rate $\dot{\gamma}$ over the gap height. In radial direction, one approach is the specification of $\dot{\gamma}$ at the outer radius ($r = R$). The Weissenberg-Rabinowitch approach uses correction factors, see e.g. [Hornig and Kielmann (2014); Haist et al. (2020)]. [Mezger (2016)] proposes volume-weighted averaged $\tau$ and $\dot{\gamma}$ at $r = \frac{2}{3}R$. Ovarlez proposed the calculation of $\tau$ and $\dot{\gamma}$ at $r = \frac{3}{4}R$ for non-Newtonian materials, see [Roussel et al. (2012), pp. 23-62].

**Relative measurements with the Vane-in-cup geometry (ViC)** are illustrated in Figure2.13.
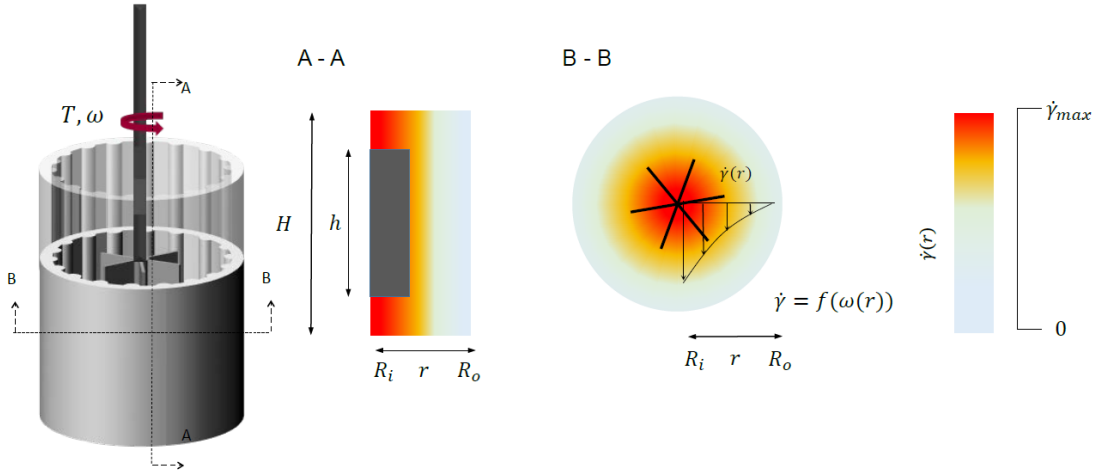


Figure 2.13: ViC rheometry with the illustration of the shear rate distribution $\dot{\gamma}(r)$

The shear stress $\tau$ is calculated from the torque $T$. Thus, the inner shear stress $\tau_i$ at $r = R_i$ and the outer shear stress $\tau_o$ at $r = R_o$ possess different values, calculated according Eq. 2.24 and Eq. 2.25:

$$\tau_i = \frac{T}{2\pi h R_i^2} \qquad\qquad [\text{Pa}] \quad (2.24)$$

$$\tau_o = \frac{T}{2\pi h R_o^2} \qquad\qquad [\text{Pa}] \quad (2.25)$$

For Newtonian fluids with $\tau = \mu\dot{\gamma}$, a correlation equation between the rotational velocity $\omega$ and the material viscosity $\mu$ was proposed by [Nguyen and Boger (1985)]:

$$\omega = \frac{T}{4\pi h \mu}\left[\frac{1}{R_i^2} - \frac{1}{R_o^2}\right] \qquad\qquad [\text{rad/s}] \quad (2.26)$$

From Eq. 2.26, $\dot{\gamma}$ can be calculated according Eq. 2.27:

$$\dot{\gamma} = \frac{T}{2\pi h \mu R^2} \qquad\qquad [\text{1/s}] \quad (2.27)$$

For Bingham fluids, the shear rate distribution depends on the yield stress $\tau_0$. The Reiner-Riwlin equation, published by [Reiner and Eyring (1950)], correlates the rotational velocity $\omega$ with the parameters $\tau_0$ and $\mu$. If the large gap is not fully sheared, plug flow occurs, and the outer radius $R_o = R_{plug}$ [Estelle et al. (2008)]:

$$\omega = \frac{T}{3\pi h\mu}\Big(\frac{1}{R_i^2} - \frac{1}{R_o^2}\Big) - \frac{\tau_0}{\mu}\ln\frac{R_o}{R_i} \qquad [\text{rad/s}] \qquad (2.28)$$

A solution for the conversion from $\omega$ to $\dot{\gamma}$ was proposed by [Krieger (1968)]:

$$\dot{\gamma} = \frac{\big(\frac{2\omega}{n}\big)}{1 - \frac{Ro}{Ri}^{\frac{-2}{n}}} \qquad [1/\text{s}] \qquad (2.29)$$

$$n = \frac{d\ln\tau_i}{d\ln\omega} \qquad [-] \qquad (2.30)$$

Further correlation formulations exist. The *affine-translation approach* uses conversion factors to scale $T$ and $\omega$ to the rheological data $\tau_0$ and $\dot{\gamma}$, see e.g.,[Haist (2009)]. Numerical methods approximate the velocity field in large-gap rheometry through numerical simulation and, thus, estimate the shear rate distribution numerically (see [Hamedi et al. (2014); Pirharati et al. (2019)]). For materials with or close to Bingham-like rheological behavior, the different approaches provide similar results compared to absolute measurement methods [Haist et al. (2020); Estelle et al. (2008)].

## 2.3.2   Oscillatory rheometry

Oscillatory rheometry facilitates the determination of viscoelastic material behavior. It is frequently used for the characterization of molecules and complex polymers [Ewoldt (2009)], in the field of food processing rheology [Norton et al. (2011); Joyner (2019)], or medical rheology [Stoltz et al. (1980); Nader et al. (2019)].

In a strain-controlled oscillatory measurement, a sinusoidal strain $\gamma(t)$ with the amplitude $\gamma_0$ is applied:

$$\gamma(t) = \gamma_0 \sin\omega t \qquad [-] \qquad (2.31)$$

The stress response as a function of time $\tau(t)$ is measured, which can be time-delayed with a phase shift of $\delta$:

$$\tau(t) = \tau_0 \sin\omega t + \delta \qquad [-] \qquad (2.32)$$

The phase shift angle $\delta[°; rad]$ describes the time-delayed phase shift of the system answer after an applied sinusoidal stress or strain, and, thus, depicts a measure for the viscous, elastic or viscoelastic material state:

- $\delta = 0°$: Ideal-elastic material behavior, no time delay

- $\delta = 90°$: Ideal-viscous material behavior, complete phase shift

- $0° \leq \delta \leq 90°$: visco-elastic material behavior

In purely elastic materials, the system response occurs instantaneously and Hooke's law can be applied:

$$\tau = G^* \gamma \qquad \text{[Pa]} \qquad (2.33)$$

With $G^*$ as complex shear modulus in [Pa]. In purely viscous materials, the system response is shifted by 90°. The Newtonian law can be applied:

$$\tau = \eta^* \gamma \qquad \text{[Pas]} \qquad (2.34)$$

With $\eta^*$ as complex viscosity in [Pas]. The system response is harmonic as long as no material changes occur during one oscillatory cycle. If the applied strain $\gamma$ changes the material structure, the stress response shifts from a harmonic sinusoidal signal to an increasingly non-harmonic stress response, illustrated in Figure 2.14 (a). While the first stress response $\tau$ is harmonic, two increasingly nonlinear $\tau$ curves are illustrated. The $\gamma - \tau$ - relation is often illustrated in time-resolved graphs. Figure 2.14 (b) displays the normalized relation between stress and strain, which is the so-called Lissajous-Bowditch curve (LB curve).
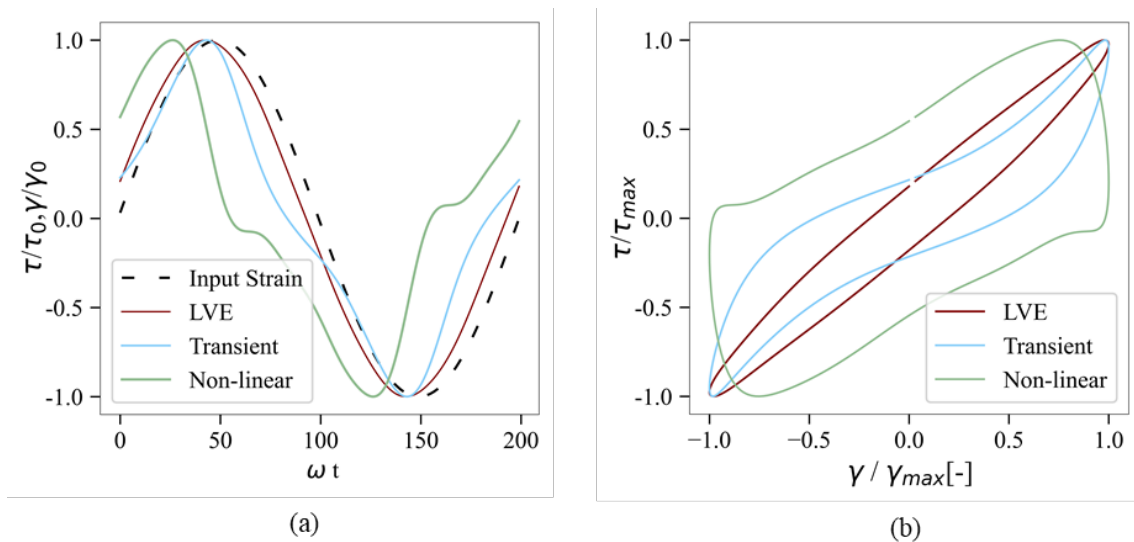


Figure 2.14:   (a) Increasingly nonlinear material response (b) with corresponding Lissajous-Bowditch curves

The enclosed area of an LB curve represents the dissipated energy within the material [Ewoldt (2009)]. In the ideal-elastic case, the ellipse reduces to a line, while in the ideal

viscous case, it forms a circle. For viscoelastic material, the phase shift angle $\delta$ is the tilt angle of the ideal circle to an ellipse.

**Inter- and intra-cyclic oscillatory analysis**

The output of an oscillatory test can be analyzed using two approaches: *inter-cyclic* or *intra-cyclic*. Inter-cyclic calculation methods focus solely on the maximum value $\tau_A$ of an applied strain amplitude $\gamma_0$. Intra-cyclic material analysis uses the entire sinusoidal deflection $\gamma(t)$; $\tau(t)$ of one oscillatory cycle.

**Inter-cyclic material analysis**   facilitates the viscoelastic analysis of a $\gamma - \tau$ curve with data points of each strain amplitude $\gamma_0$. Alternatively, the complex shear modulus $G^*$ is analyzed. $G^*$ can be divided into two parts following Pythagoras rules with $\delta$ as a dividing angle, see Figure 2.15.



$$G' = \frac{\tau_A}{\gamma_A} * \cos(\delta) \quad G'' = \frac{\tau_A}{\gamma_A} * \sin(\delta)$$

$$G^* = \sqrt{(G')^2 + (G'')^2} \quad \tan(\delta) = \frac{G''}{G'}$$

$$\tau(t) = \gamma_0 \cdot (G' \cdot \sin(\omega t) + G'' \cdot \cos(\omega t))$$
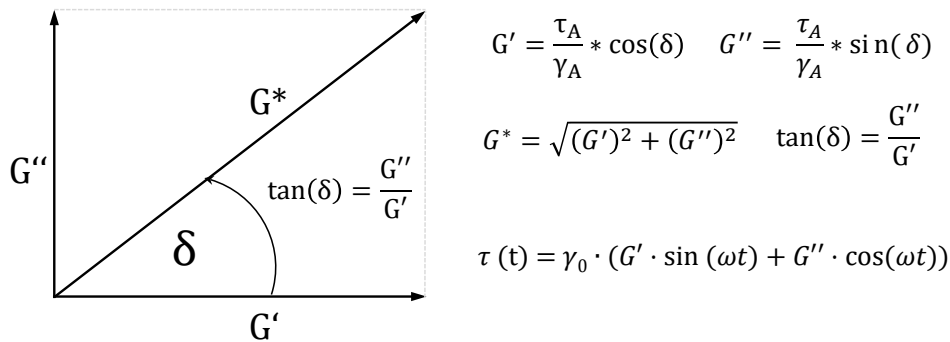
Figure 2.15: Combination of $G'$ as (real) elastic part and $G''$ as viscous part of $G^*$

For the rheological characterization, $G'$ is defined as storage modulus that is in phase with the deflection, and, thus, corresponds to the elastic material part. $G''$ corresponds to the modulus out of phase, is notated loss modulus, and deflects the viscous material response. $G'$ and $G''$, together with the phase shift angle $\delta$, can be illustrated in a $\gamma - G'/G''$ flow curve, illustrated in Figure 2.16. The Linear-Viscoelastic regime (LVE) is the zone where $G'$ and $G''$ possess almost constant values. If $G' > G''$ , the elastic component predominates and the material is solid or gel-like. Conversely, if $G'' > G'$ , the material is liquid. Once the material starts to change, it reaches its yielding limit $\tau_y$ at a yield strain $\gamma_l$. The yield stress $\tau_F$ at the flow deformation $\gamma_F$ is the shear stress at the intersection of $G''$ and $G'$. A direct calculation of $\tau_F$, corresponding to the yield stress $\tau_0$ is not possible in a strain-controlled oscillatory amplitude test because the output signal $\tau(t)$ contains a non-harmonic, non-sinusoidal system response, and Hooke's law is not applicable. The region between $\tau_\gamma$ and $\tau_F$ is the yielding zone. The ratio of $\tau_F$ and $\tau_\gamma$ is the yield index. The closer the ratio is to 1, the more brittle material fails. Surpassing the yielding limit implies increasing material destruction and, thus, a progressively nonlinear viscoelastic material response.
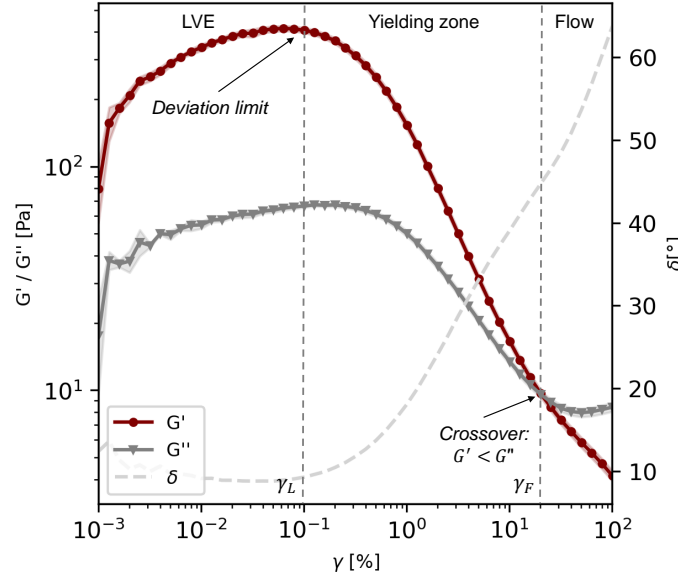
Figure 2.16: $\gamma$ - $G'/G''$ - curve from an oscillatory experiment with increasing $\gamma_0$

**Intra-cyclic characterization**   analyzes the sinusoidal and non-sinusoidal system response. Mathematical techniques such as *Fourier-Transform analysis* or *stress decomposition with Chebyshev polynomials*[3] facilitate the mathematical description of each stress-strain cycle at a given strain amplitude $\gamma_0$, resulting in mathematical parameters that describe viscoelasticity. Fourier-Transformation (FT-rheology) decomposes the non-sinusoidal periodic signal $\tau(t)$ into a row of harmonic, sinusoidal oscillations containing viscous and elastic parts:

$$\tau(t) = \gamma_0 \sum_{n,odd} G''_n \cos n\omega t + G'_n \sin n\omega t \tag{2.35}$$

The intensity of $G'$ and $G''$, depending on the order of $n$, provides information on the viscous and elastic material properties [Wilhelm et al. (1998); Hyun and Wilhelm (2009)]. Eq. 2.35 is widely applied in the field of polymer rheology.

The Chebyshev polynomials $T_n(x)$ and $T_n(y)$ are orthogonal polynomials, which are defined in an interval $[-1, 1]$. While, generally, Chebyshev polynomials are used to decompose spectral data, they were employed, e.g. by [Ewoldt (2009)], to decompose $\tau(t)$ from an oscillatory rheological measurement of biological soft matter into an elastic and a viscous stress contribution:

$$\begin{aligned} \tau(t) &= \tau_{elastic}(\gamma(t)) + \tau_{viscous}(\dot{\gamma})_t \\ &= \gamma_0 \sum_{n=1}^{N} e_n T_n(x) + \gamma_0 \omega \sum_{n=1}^{N} v_n T_n(y) \end{aligned} \tag{2.36}$$

---

[3]Chebyshev polynomials are orthogonal polynomials with respect to a weighting function. They are named after the Russian mathematician Pafnuty Chebyshev. Further mathematical introduction is beyond the scope of this thesis, fundamentals can be found, e.g., in [Morel et al. (2006)]

Similarly to FT-rheology, the coefficients $e_n$ and $v_n$ characterize the elastic and viscous behavior of the $n^{th}$ harmonic order [Ewoldt et al. (2008); Ewoldt (2009)]. $T_n(x)$ and $T_n(y)$ display the Chebyshev polynomials in x- and y-direction. By extracting the third harmonic $n = 3$, the third-order coefficients $e_3$ and $v_3$ classify viscoelasticity:

$$e_3 \begin{cases} \leq 0 & , \quad \text{intra-cycle elastic strain-softening} \\ \geq 0 & , \quad \text{intra-cycle elastic strain-stiffening} \end{cases}$$

$$v_3 \begin{cases} \leq 0 & , \quad \text{intra-cycle viscous shear-thinning} \\ \geq 0 & , \quad \text{intra-cycle viscous shear-thickening} \end{cases}$$

Alternatively, [Ewoldt et al. (2008)] mathematically described LB curves by a tangent module $G'_M$ (with $M$ as minimum strain) at $\gamma = 0$ and a secant module $G'_L$ (with $L$ as large strain) at $\gamma = \gamma_0$, see Figure 2.17 (b).
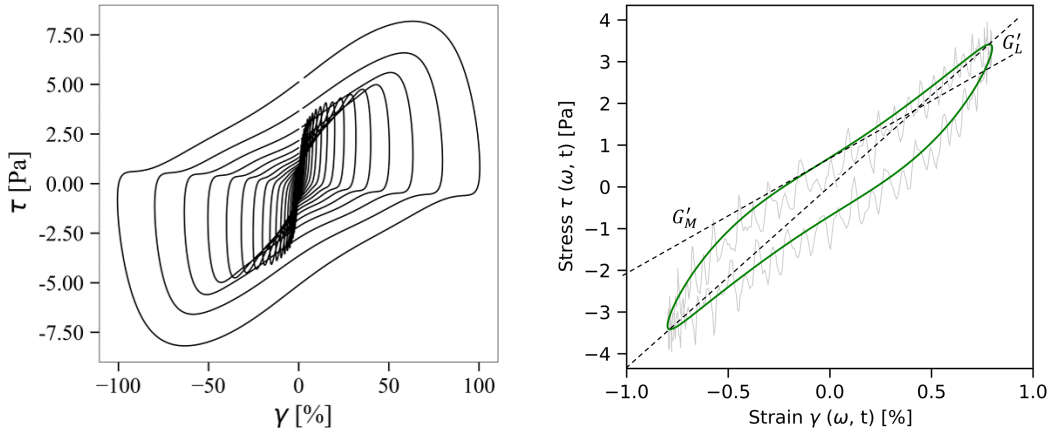




(a) nonlinear time-resolved LB curves     (b) Visualization of $G'_L$ and $G'_M$ in an LB curve

Figure 2.17: nonlinear material material characterization in an oscillatory sweep test

By relating $G'_L$ and $G'_M$, [Ewoldt et al. (2008)] introduced the dimensionless elastic strain stiffening index $S$ and, accordingly, the viscous shear thickening index $T$ :

$$S = \frac{G'_L - G'_M}{G'_L} \tag{2.37}$$

$$T = \frac{\eta'_L - \eta'_M}{\eta'_L} \tag{2.38}$$

With:

$$S \begin{cases} \leq 0 & , \quad \text{intra-cycle strain-softening} \\ \geq 0 & , \quad \text{intra-cycle strain-stiffening} \end{cases}$$

$$T \begin{cases} \leq 0 & , \quad \text{intra-cycle shear-thinning} \\ \geq 0 & , \quad \text{intra-cycle shear-thickening} \end{cases}$$

### 2.3.3 Rheometric uncertainties

Rheological analysis using rheometry depends on various factors that can yield variations in calculating rheological parameters. Material preparations, the rheometric procedure and the final data handling affect the rheological result. The choice of rheometric device and software affects experimental results, as analyzed in [Chhabra and Richardson (2008); Dinkgreve et al. (2016); Feys et al. (2017)]. The material treatment (shear and rest history, shear intensity) and the material handling during measurement affect the rheological parameters [Ewoldt et al. (2015); Kim and Mason (2017)]. Also the analysis of experimental raw data affects the calculation result of rheological parameters [Wallevik et al. (2015)].

In summary, Figure 2.18 illustrates various factors that likely introduce parameter variability."
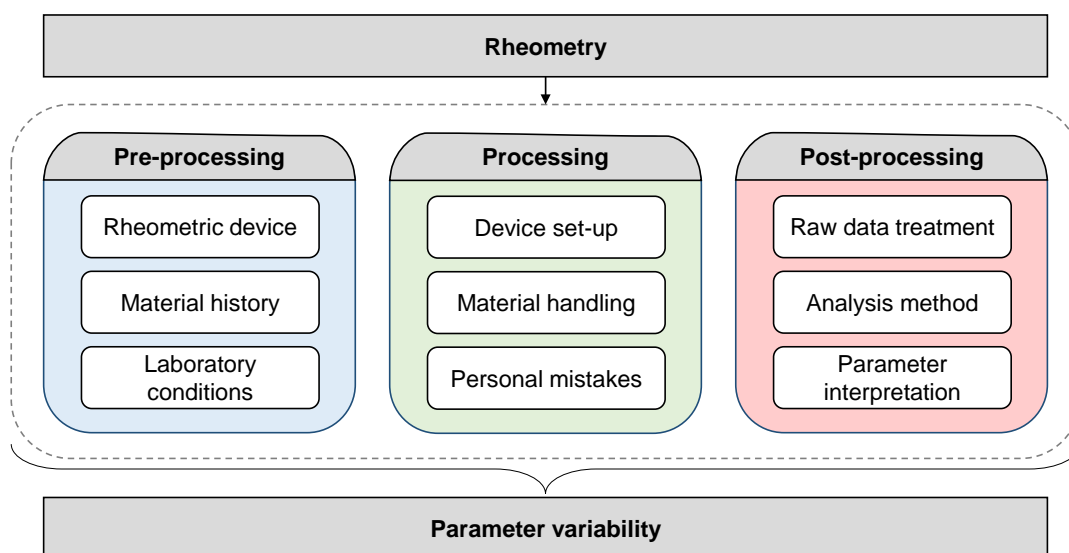


Figure 2.18: Simplified overview of rheometric challenges before, during and after a rheometric measurement

## 2.4   (Computational) fluid dynamics

### 2.4.1   The transport equations of flow

*Fluid dynamics* considers a fluid a continuous medium governed by the universal conservation laws of mass, momentum, angular momentum, energy, and entropy. Various models calculate material flow by connecting stress, body force, velocity, and density to these laws. The Navier-Stokes equations, named after Claude-Louis Navier and George Gabriel Stokes, describe viscous fluid flow. Based on the laws for the conservation of mass and momentum, they determine the velocity of each continuum element over time based on external forces, pressure, and internal viscosity, yielding a system of partial differential equations (PDEs).

**Mass conservation** assumes that the time derivative $\partial t$ of a mass $m$ is zero. The mass density stays constant over its time derivative $\frac{D\rho}{Dt}$ during flow. The mass of a fluid that enters a defined volume, mathematically described as $\int_V \rho \, dV$, equals the flux through a defined closed surface $dS$, see Eq. 2.39:

$$\frac{D}{Dt} \int_V \rho \, dV = -\int_S (\mathbf{n} * \rho \mathbf{u}) dS \quad \rightarrow \quad \frac{D}{Dt} \int_V \rho(\mathbf{x}, t) dV = 0 \quad \rightarrow \quad \frac{Dm}{Dt} = 0 \quad (2.39)$$

with $m$ in $[\text{kg}]$ and $\rho$ in $[\text{kg/m}^3]$. Satisfying the Reynolds transport theorem, which relates the rate of change of a property with its variation in position and time, and the Gauss divergence theorem, which relates the divergence of a vector field to the flux of a closed surface, Eq. 2.39 yields:

$$\frac{\partial \rho}{\partial t} + \nabla \cdot (\rho \mathbf{u}) = 0 \tag{2.40}$$

Eq.2.40 is also known as continuity equation. For constant density, Eq.2.40, simplifies to

$$\nabla \cdot \mathbf{u} = 0 \tag{2.41}$$

In the presence of external forces $\mathbf{f}$, the momentum of a fluid element changes. However, Newton's second law expresses **Momentum conservation**: The alteration in the impulse or momentum, which is the product of mass $m$ and velocity $\mathbf{u}$) of a fluid element, is equivalent to the sum of forces $\Sigma \mathbf{f}$, see. Eq. 2.42; or Eq. 2.43 according to the Reynolds transport theorem:

$$\frac{D(m\mathbf{u})}{Dt} = \Sigma \mathbf{f} \tag{2.42}$$

$$\frac{\partial \rho \mathbf{u}}{\partial t} + \nabla \cdot (\rho \mathbf{u}\mathbf{u}) = \Sigma \mathbf{f} \tag{2.43}$$

In Eq. 2.43, $\Sigma\mathbf{f}$ is the sum of point or surface forces. The latter is the surface integral of the traction $\mathbf{T}$, also written as Eq. 2.44:

$$F_s = \int_S \mathbf{T} \cdot \mathbf{n}\, ds \tag{2.44}$$

The traction vector $\mathbf{T}$ is related to the Cauchy stress tensor $\boldsymbol{\sigma}$ by

$$\mathbf{T} = \boldsymbol{\sigma} \cdot \mathbf{n} \tag{2.45}$$

where $\mathbf{n}$ is the outward unity normal vector. If a material-dependent law is connected to $\mathbf{T}$ and inserted into Eq. 2.43, material-dependent flow is calculated. The tensorial notation of the law for a Newtonian fluid is depicted in Eq. 2.46:

$$\mathbf{T} = 2\mu\mathbf{D} \tag{2.46}$$

$\mu$ represents a constant scalar viscosity value. The strain rate tensor $\mathbf{D}$ is calculated from the velocity vector as

$$\mathbf{D} = \frac{1}{2}(\nabla\mathbf{u} + (\nabla\mathbf{u})^T) \tag{2.47}$$

To calculate the shear stress dependent flow, only the deviatoric part of $\mathbf{T}$ is calculated, denoted by the deviatoric stress tensor $\tau$. Several rheological models can be implemented for $\tau$ for the calculation of the viscosity-dependent flow, as previously introduced in Section 2.2.1. By assuming the incompressibility of the fluid, the momentum equation in Eq. 2.43 yields:

$$\frac{\partial \rho\mathbf{u}}{\partial t} + \nabla \cdot (\rho\mathbf{u}\mathbf{u}) = -\nabla p + \nabla \cdot \tau + \rho g \tag{2.48}$$

In Eq. 2.48, $\nabla p$ is the pressure gradient, $\tau$ is the deviatoric stress tensor and $g$ is the gravitational acceleration ($9.81 \text{ m/s}^2$). Together with the conservation of mass in 2.41, Eq. 2.48 forms the Navier-Stokes equations for incompressible fluid flow. Further derivations, including compressible flow, can be found, e.g., in [Hieber et al. (2020)]. Owing to the convective term $\nabla \cdot (\rho\mathbf{u}\mathbf{u})$, the Navier-Stokes equations are highly nonlinear.

The solution of Eq. 2.41 and Eq. 2.48 involves spatial discretization of $\Delta x$, $\Delta y$ and $\Delta z$, and temporal discretization $\Delta t$, and leads to a set of Partial Differential Equations (PDEs). Numerical integration schemes are used to solve the discretized PDEs, which requires a high computational effort. Obtaining an exact analytical solution for the Navier-Stokes equations is generally impractical for most real-life geometries and unsteady, time-dependent flow. Numerical analysis methods facilitate the solution of the discretized transport equations by the application of approximation schemes. With high computational power, solutions for

the time-dependent flow can be examined. The numerical solution using computers is the field of *Computational Fluid Dynamics*.

## 2.4.2   Computational fluid dynamics (CFD)

Numerical computations have facilitated various scientific branches to solve complex fluid flow phenomena, such as aerospace, meteorology, biomedical engineering, and building physics. Numerical methods can be divided into mesh-free or mesh-based approaches. Mesh-free methods calculate quantities depending on geometrical definitions, e.g., for particles, without the definition of a mesh with fixed coordinates. The quantities $p$ and $\mathbf{u}$ are tracked directly, following the *Lagrangian formulation*. Common mesh-free methods are the Discrete Element Method (DEM), the Dissipative Particle Dynamics Method (DPDM), Smoothed Particle Hydrodynamics (SPH) and the Lattice Boltzmann Method (LBM).

Mesh-based simulations define a numerical mesh with spatial discretizations $\Delta x$ , $\Delta y$ and $\Delta z$. The progress of the quantities $p$ and $\mathbf{u}$ is tracked over cells with fixed Cartesian coordinates at defined time steps, following the *Eulerian formulation*. CFD is generally categorized as mesh-based method (as critically discussed in [de Schryver, Robin (2022)], p.180, the term CFD is more ambiguous). The most common mesh-based numerical methods are the Finite Differences Method (FDM), Finite Element Method (FEM), or Finite Volume Method (FVM). FDM is the oldest discretization method, probably invented by Euler in the $18^{th}$ century [Ferziger et al. (2020)]. In FDM, the geometry is divided into a structured grid. For each node, an algebraic equation is formulated, and the set of equations is solved through the application of Taylor polynomials. In FEM, a two-dimensional structured or unstructured mesh with the quantity at the vertices is defined. The solution requires interpolation schemes. FVM uses control volumes that specify surfaces, edges, nodes, boundaries and the cell centroids. Numerical integration schemes are required to calculate a quantity from a cell centroid to its nodes or edges. With regard to the scope of this thesis, solely the FVM method is explained more detailed.

## 2.4.3   The FVM method for numerical discretization

**Spatial discretization and integration**

The volume shapes in FVM can be triangular or hexahedral cells, pyramids, triangular prisms and sometimes polyhedral cells, illustrated in Figure 2.19:

Figure 2.19 (a) shows the definition of different cell shapes. In (b), a three-dimensional mesh is discretized with cube-shaped cells. For one cube cell (c), surface notations are defined as illustrated in (d). At each cell centroid $P$, a scalar conservation quantity $\phi$ (which is, in terms of the Navier-Stokes equations, the pressure $p$ and the velocity $u_x, u_v, u_w$) needs to be calculated through solution of the PDEs. The Gaussian divergence theorem is applied, which transforms the divergence of a volume integral into surface integrals:

(a) Cell shapes          (b) Mesh with cubes          (c) Cube with centroid          (d) Surface notation
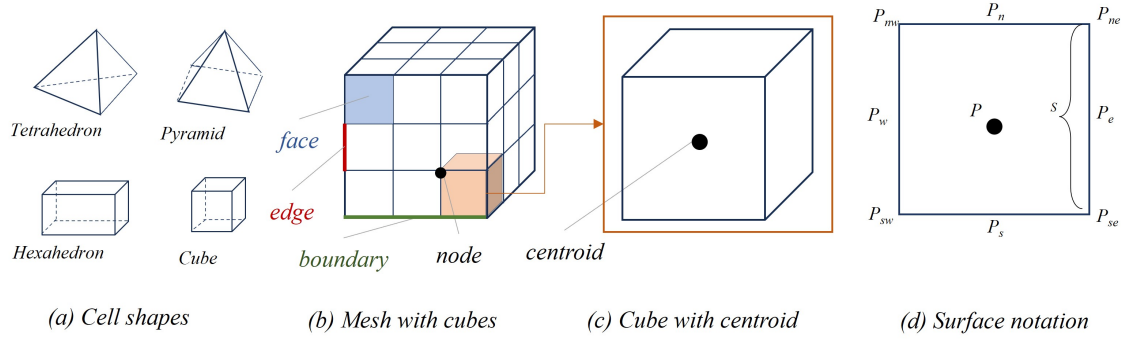
Figure 2.19: Schematic illustration of FVM cells

$$\int_V (\nabla\phi)dV = \int_S (\mathbf{n}\phi)dS \tag{2.49}$$

Eq. 2.49 states that the surface integral is a sum of all integral calculations on all faces of a cell:

$$\int_S f\,dS = \sum_k \int_{S_k} f\,dS \tag{2.50}$$

with $f$ being the part of the quantity $\phi$ normal to the cell surface. Approximation methods solve the surface integral from the centroid at $P$ to its surface. Straightforward methods are quadrature rules, e.g,. the midpoint rule, the trapezoidal rule, or the Simpson rule, summarized in table 2.1:

Table 2.1: Surface integration [Ferziger et al. (2020)]

| Integration rule | Equation | Order |
|---|---|---|
| Midpoint rule | $\int_S f\,dS \approx \bar{f}S$ | 2 |
| Trapezoidal rule | $\int_S f\,dS \approx \frac{f_n e + f_s e}{2}S$ | 2 |
| Simpson rule | $\int_S f\,dS \approx \frac{f_n e + 4f_e + f_s e}{6}S$ | 4 |

Quadrature rules can be applied for the solution of steady-state phenomena and uniform grids. The solution is unstable for time-dependent flow phenomena. For transient flow phenomena and convection-dominated processes, the quantity $\phi$ at the cell centroid $P$ is calculated considering the values $\phi$ of the neighboring cells $P_w$ and $P_e$, illustrated in Figure 2.20.

The PDEs are converted to algebraic equations through Taylor expansion. This numerical approximation is depicted for $\frac{\partial}{\partial x}$ in Eq. 2.51:
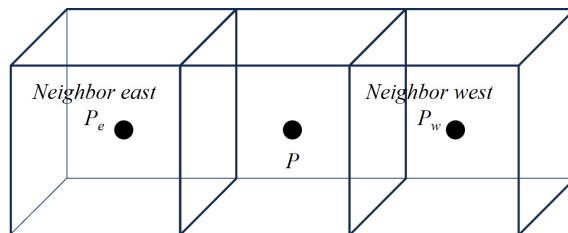
Figure 2.20: Neighboring cells in FVM

$$f(x_0 - \Delta x) = f(x_0) - f'(x_0)(x - \Delta x) + \frac{f''(x_0)}{2!}(x - \Delta x)^2$$

$$+ \frac{f'''(x_0)}{3!}(x - \Delta x)^3 + \cdots + R_n(x_0 - \Delta x) \tag{2.51}$$

where $f'(x_0)$, $f''(x_0)$, and $f'''(x_0)$ represent the first, second, and third derivatives of the function, and $R_n$ is the rest, also defined as error or truncation error of the chosen approximation. The discretization step $\Delta x$ is specified by the defined mesh and, thus, cell size. To solve the derivatives $f'(x_0)$, $f''(x_0)$, and $f'''(x_0)$, different interpolation methods can be applied, see Tab. 2.2:

Table 2.2: Spatial integration schemes [Ferziger et al. (2020)]

| Integration scheme | Equation | Order |
|---|---|---|
| Upwind scheme | $\frac{\partial \phi_{i,j}}{\partial x_{i,j}} = \frac{\phi_{i,j} - \phi_{i-1,j}}{\Delta x}$ | $O(\Delta x)$ |
| Downwind scheme | $\frac{\partial \phi_{i,j}}{\partial x_{i,j}} = \frac{\phi_{i+1,j} - \phi_{i,j}}{\Delta x}$ | $O(\Delta x)$ |
| Central differences scheme | $\frac{\partial \phi_{i,j}}{\partial x_{i,j}} = \frac{\phi_{i+1,j} - \phi_{i-1,j}}{2\Delta x}$ | $O(\Delta x^2)$ |

The *upwind scheme* and *downwind scheme* calculate the quantity $\Phi$ one-directional, whereas the *central difference method* considers both neighboring cells. The central difference method exhibits second-order accuracy, leading to a quadratic reduction in error with mesh refinement. However, while it provides higher numerical accuracy, one-directional numerical schemes can be more stable. Therefore, the decision regarding which spatial integration scheme to employ involves a trade-off between accuracy and stability. [Ferziger et al. (2020)]

**Temporal integration**

Temporal integration schemes specify how the quantity $\phi$ is temporally integrated by $\frac{D}{Dt}$:

$$\int_{t_n}^{t_{n+1}} \frac{\partial \phi}{\partial t} = \phi^{n+1} - \phi^n = \int_{t_n}^{t_{n+1}} f(t, \phi(t)) \tag{2.52}$$

A selection of integration rules for the temporal derivatives is presented in Tab. 2.3.

Table 2.3: Time integration schemes [Ferziger et al. (2020)]

| Integration scheme | Equation | Order |
|---|---|---|
| Explicit Euler | $\phi^{n+1} = \phi^n + \Delta t f^n$ | $O(\Delta t)$ |
| Implicit Euler | $\frac{\partial \phi}{\partial t} = \frac{\phi^{n+1} - \phi^n}{\Delta t}$ | $O(\Delta t)$ |
| Crank Nicholson | $\frac{\partial \phi}{\partial t} = \frac{\phi^{n+1} - \phi^n}{2\Delta t}$ | $O(\Delta t^2)$ |

**Initial and Boundary conditions**

Every CFD simulation requires the definition of initial conditions for the transport quantities $\phi$ (here, $p$ and $\mathbf{u}$), and boundary conditions at the walls or free surfaces. They are specified in two classes, i.e. *Dirichlet* and *Neumann* condition:

- **The Dirichlet condition** specifies a value of $\phi$. The condition can be set to *no slip*, which means that the quantity $\phi$, in this case the velocity $\mathbf{u} = 0$

- **The Neumann condition** defines a gradient $\frac{\partial \phi}{\partial t}$. A special Neumann condition is the *zero gradient* boundary condition, where $\frac{\partial \phi}{\partial t} = 0$. This condition is especially implemented as wall boundary or at outlets.

**Numerical solution algorithm: Coupling of pressure and velocity**

The discretized transport equations provide solutions for $p$ and $\mathbf{u}$. However, while a solution is found for the momentum equation, the continuity equation also needs to be satisfied. A coupled solution for $p$ and $\mathbf{u}$ to satisfy both Eq. 2.41 and Eq. 2.48 needs to be found iteratively. [Wendt (1992)]

Several algorithms were designed to solve the pressure-velocity coupling with different iteration rules. In general, the momentum equations are solved with a guessed pressure field called the *momentum predictor stage*. The solution, however, needs to satisfy the continuity equation. Thus, the velocity field is substituted in the continuity equation. Once this pressure field is solved, the velocity field satisfies the continuity equation called the *correction stage*. However, the corrected velocity field does not satisfy the initial velocity field. The process is then iteratively repeated until the solution converges. Different computational algorithms have been implemented in computer programs. Commonly used algorithms are the SIMPLE algorithm (Semi-Implicit Method for Pressure-Linked Equations), which solves steady-state flow problems, and the PISO algorithm ( Pressure-Implicit Split-Operator), which solves transient flow procedures. For more information, technical literature is available, e.g., [Wendt (1992); Ferziger et al. (2020)].

## 2.4.4   Assessment of the discretized numerical solution

Numerical computation approximates the exact solution of the transport equations. The accuracy of the solution depends on the applied mathematical methods, discretization schemes and numerical rules, and the chosen boundary conditions. While all mathematical solution schemes must be converged, consistent and stable, a compromise must be defined between the final accuracy and the computation time, also referred to as computational cost. [Moukalled et al. (2016)]

**Convergence**   of the numerical setup means that within the iterative solution algorithm, the error reduces and the numerical solution converges towards one value. The perfectly converged numerical solution would not reduce its error with increasing iterative steps. However, as each iterative step requires computational costs, a *convergence criterion* defines the allowed error or numerical residual.

**Consistency**   means that a numerical solution is consistent if it approaches the algebraic solution of the transport equations when the discretization steps $\Delta t$, $\Delta x$, $\Delta y$, and $\Delta$ approach zero.

**Stability**   of the numerical solution algorithm means that it can be solved dependent on initial and boundary conditions and the numerical schemes. Especially for transient test cases, stability must be ensured by the choice of explicit or implicit solution algorithms. While explicit solution algorithms are generally stable (but have less accuracy, as the error of the numerical approximation is higher), implicit solution algorithms can become unstable, which means that a set of discretized equations yields a non-physical result. In most cases, a stable simulation requires the quantity **u** not to pass a single cell within one time step.

The Courant number (Co, [−], or Courant-Friedrichs-Lewy number, CFL condition) is a dimensionless number that relates the distance that a fluid passes during one time step to the cell size, and, thus, helps to estimate the stability of a numerical solution. It is defined as:

$$Co = \frac{u\Delta t}{\Delta x} \tag{2.53}$$

A Courant number $Co < 1$ means that **u** does not pass the cell $\Delta x$ within $\Delta t$. For transient test cases and turbulent flow, $Co$ might be even reduced. [Jiri Blazek (2015)]

**Accuracy**   is defined, e.g., as "A computational model relates well to the theory if the computational model describes the mathematical model well and the mathematical model relates to the theory well" [Babuska and Oden (2004)]. The accuracy analysis, including verification and validation procedures for the numerical solution compared to the real-life

case, can be conducted in different ways, and various theories and procedures have been published, e.g. [Oberkampf and Trucano (2002); Thacker et al. (2004); Babuska and Oden (2004); Liu et al. (2016); John W. Slater (Wednesday, 10-Feb-2021 09:38:59 EST)].

Summarized, CFD requires a reliable numerical framework, which is illustrated in Figure 2.21. **Pre-processing** involves all steps for the specification of the geometrical domain, the discretization method, the definition of initial and boundary conditions, numerical differentiation, and solution schemes. Further, pre-processing requires the specification of all physical parameters, such as the rheological properties of the fluid. The **processing** step is the solution of the PDEs with the chosen algorithm solver with defined iteration steps and approximation rules, such as the limitation of the permitted residuals. Finally, **post-processing** involves the flow visualization and the calculation of further relevant parameters.
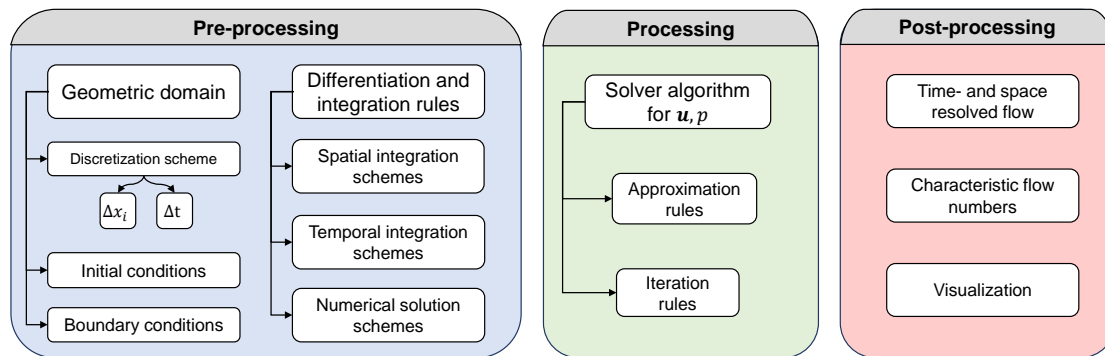


Figure 2.21: Steps in CFD

# 3. Cementitious paste rheology

## 3.1 Cement composition

*Opus caementitium* was the first hydraulic hardening building material invented by the ancient Romans in the 3rd century BC. They mixed burnt lime as a binder with natural and artificial pozzolans like pumice, tuff, ashes, and brick dust to produce hydraulic hardening material. Contemporary cement (still derived from the word *caementium* = building stone) was invented in 1824 by Joseph Aspdin, who used lime from the Portland region and burnt and ground it to gain hydraulic properties. Today, cement is a mixture of calcium oxide ($CaO$), silicon dioxide ($SiO_2$), aluminum oxide ($Al_2O_3$), and iron oxide ($Fe_2O_3$). After burning and grinding, Ordinary Portland Cement clinker (OPC) consists of four main clinker phases: Tricalcium Silicate, also *Alite* ($C_3S$), Dicalcium Silicate, also *Belite* ($C_2S$), Tricalcium Aluminate ($C_3A$) and Calcium Aluminate Ferrite ($C_4AF$). [Scholz et al. (2011)]

Cement owes its essential properties to alite, which, as the CaO-richest phase, hardens rapidly with the addition of water (early strength) and achieves very high strengths (late strength). Belite reacts slower than alite and promotes late strength. Tricalcium aluminate shows the fastest initial reaction with water. Depending on its content, adding a sulfate carrier as a solidification regulator is necessary to prevent instant stiffening. Standardized Ordinary Portland Cement is produced solely from these clinker phases, which hydrate under the addition of water. Mono- and Trisulfate (ettringite) and Calcium-Silicate-Hydrate (C-S-H) are the main hydration products. Further cement types contain different natural or artificial additives as constituents, e.g., granulated blast furnace slag, natural and artificial pozzolans, fly ash, burnt shale, limestone, and silica fume. Silica-rich constituents support a secondary pozzolanic reaction to C-S-H phases. Once clinker phases are dissolved in water, ettringite and further hydration products start forming, the pH value increases and ions are continuously solved, which affects interparticle forces and thus the rheology. [Taylor (1997)]

## 3.2 Cementitious pastes

### 3.2.1 Water demand

Cementitious pastes are concentrated, heterogeneous suspensions. The granulometric properties of the raw binder (particle size distribution, shape of the particles) determine the water demand, composed of the water needed for pore space filling and the water for wet-

ting the specific particle surface. Different experimental methods analyze a bulk's water demand, e.g., the Puntke test [Puntke (2002)], or the Marquardt test [Marquardt (2001)]. Both test methods determine the required water amount to wet all particle surfaces within a bulk. On the contrary, the Okamura test defines the required water amount to let a particle network flow. The value is used for the mix design of Self-Compacting Concretes (SCCs) [DIN12350-9]. For cementitious pastes, the water demand varies from 0.25 to 0.35, depending on fineness, specific surface area, particle size distribution, and shape [Hunger (2010); Huß (2012)]. The water-to-cement ratio (w/c ratio) or, in the case of secondary binders, the water-to-binder ratio (w/b ratio) determines the workability and the final concrete strength. With decreasing w/c, the final concrete strength increases - however, the workability decreases. Standard concretes are designed with w/c ratios of 0.4-0.6 (where, of course, aggregates' water demand must also be taken into account). In order to increase the final concrete strength, it is technically possible to mix and process high-strength concretes with w/c-values of 0.2 - 0.3 by using additional superplasticizing agents. Common superplasticizing agents are Melamine sulphonates, Naphthalene sulphonates or Polycarboxylatethers (PCEs). Surface-active or interactive dispersing effects yield fluidization of the paste. Chemicals with surface-active effects reduce the surface tension of the water to be added and increase the efficiency of the fluidization through the water. Dispersants separate the cement particles, prevent them from agglomerating, and release water trapped between agglomerated cement particles. Steric repulsion causes a hindrance of molecular spatial approximation, e.g., cement particles, see [Yoshioka et al. (1997)]. PCEs possess the spatial structure to cause both dispersing effects and steric hindrance and, thus, are the most effective superplasticizers.

## 3.2.2   PCEs as superplasticizing agents

In 1986, the first polycarboxylate ethers (PCE) were developed in Japan, where they enabled the production of high-strength concretes. Due to their structure, PCEs are also called comb polymers: Uncharged side chains that cause steric hindrance are connected with an anionic backbone, consisting of carboxylic acids, see Figure 3.1. Carboxylic acids have functional COOH groups, which are called carboxy groups. The carboxy groups of PCEs are deprotonated in the alkaline cement solution (a proton is released so that the carboxylic acid has an anionic COO- group, Figure 3.1, part (a)), wherefore the backbone becomes negatively charged and adsorbs onto the positively charged cement particles, which causes electrostatic repulsion. The backbone length is variable (part a) [Ng (2013)]. The uncharged side chains of the polymers consist of organic compounds (alcohols, diols, or hydroxycarboxylic acids). The most common PCEs contain polyethylene glycol (PEG) units as diols, which create the steric efficiency of the superplasticizer 3.1, part b). The number of PEG units can vary between 5 to 100 units, 3.1, part n [Ng (2013)]. Thus, PCEs can be polymerized differently according to the a:b:n ratios and tailored to the intended application: If the side chain length increases, a strong steric effect is generated and the flow agent has a retarding effect. If the anionic charge density increases, the superplasticizer adsorbs

quickly, liquefying fast, and strongly. Also, these two effects can be combined.
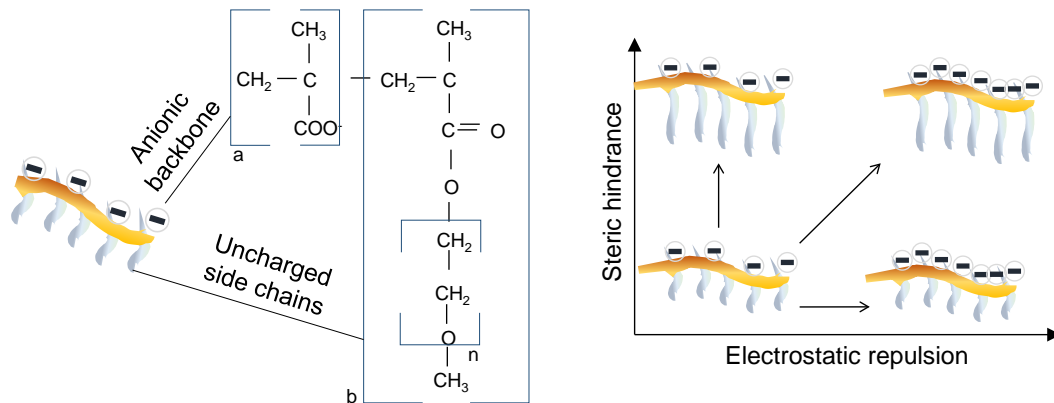


Figure 3.1: Structure of PCE moelcules and the schematic liquefying effect

### 3.2.3  Interparticle forces in cementitious pastes

Interparticle forces in a cementitious paste determine the particle network strength and, thus, rheological properties. For cementitious particles of sizes below a few $\mu$m, Brownian motion can induce diffuse particle movements within the carrier liquid, potentially causing shear-thinning effects, as discussed by [Roussel et al. (2010)]. However, at high particle concentrations, interparticle forces are governed by electrostatic interactions, dispersion forces ( attractive London Van-der-Waals forces), and potentially steric hindrances. Upon dissolution of cement in water, constant ion dissolution and transport lead to the formation of an electrochemical double layer between the cement surface and the carrier liquid [van Cappellen et al. (1993)], schematically illustrated in Figure 3.2. The electrokinetic surface charge of a cement grain in water depends on the pH and ionic strength of the surrounding liquid. The determining ions influencing the surface charge in Portland cement are $Ca^{2+}$, $Ba^{2+}$, $SO_4^{2-}$, $CO_3^{2-}$, $F^-$, $Ag^+$, and $I^-$ [Nägele (1985)]. [Liberto et al. (2019)] established a strong correlation, particularly between calcium content and elastic rheological properties, based on interparticle force calculations.

[Lowke and Gehlen (2015)] demonstrated the significant effect of the $Ca/SO_4$ ratio of the cementitious paste on rheological properties and the zeta potential, which becomes even more important at high solid volume fractions, see [Lowke and Gehlen (2017)]. Moreover, the zeta potential was found to impact the adsorption potential of PCEs on cement particle surfaces, with negative zeta potential values leading to decreased PCE adsorption. The effect of the mineralogical composition on PCE adsorption (and different PCE designs) is beyond the scope of this thesis. Comprehensive research can be found in [Yamada et al. (2001); Plank and Hirsch (2007); Ferrari et al. (2010); Lowke (2013); Mantellato (2017)].

[Flatt and Bowen (2003)] formulated a total force calculation of interparticle forces:
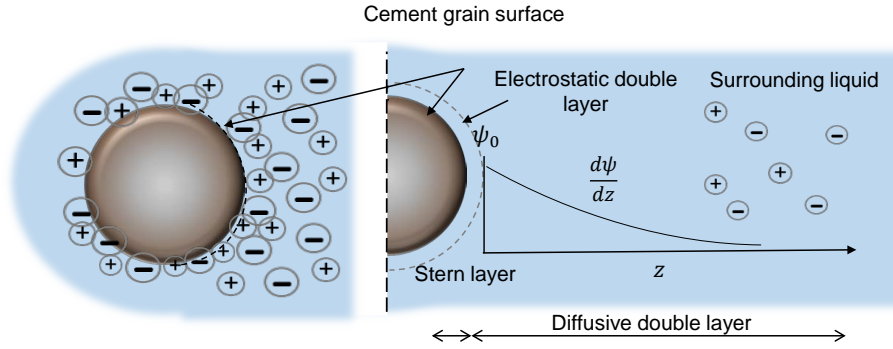
Figure 3.2: Schematic electrostatic double layer concept of a cement grain

$$
\begin{aligned}
G &= \frac{F_{VdW} + F_{ES} + F_{Ste}}{a} \\
&= -\frac{A_{eff(h)}}{12h^2} + 2\pi\epsilon\epsilon_0\kappa\psi^2 \frac{\kappa e^{-\kappa(h-2\lambda)}1 + e^{-\kappa(h-2\lambda)}}{+} \frac{6\pi k_B T}{5s^2}\left[(\frac{2L}{h}^{\frac{5}{3}-1}\right]
\end{aligned}
\tag{3.1}
$$

In Eq.3.1, $F_{VdW}$ are the London van-der-Waals forces, $F_{ES}$ are electrostatic forces and $F_{Ste}$ is the steric hindrance. $a$ displays the interaction radius of two particles. The calculation of dispersion and electrostatic forces follows the fundamentals introduced in Chapter 2. Additionally, an equation for steric forces in the presence of superplasticizers has been included, where $s$ represents the distance between two particles, and $L$ is the steric length extending into the liquid after adsorption (according to various geometric theories, see [Flatt and Bowen (2003)], Eq. (8)).

In densely packed suspensions, the London van-der-Waals forces are the most relevant interparticle forces. However, in presence of PCEs, electrostatic forces change and steric hindrances become important. Comprehensive analyses of their effects on interparticle forces are detailed in works such as in [Yoshioka et al. (1997); Flatt (1999); Lowke (2013)]. Recently, [Nicia et al. (2023)] analyzed the effect of different PCE structures not only on rheological properties, but also the formation of different hydration products.

### 3.2.4   Particle packing and rheology

Cementitious pastes follow the principles of suspension rheology outlined in Chapter 2. Their rheological properties are determined by the percolation threshold $\phi_{perc}$, solid volume fraction $\phi_s$ and maximum solid volume fraction $\Phi_m$. $\phi_{perc}$, which marks the onset of particle interactions, was determined as $\phi_{perc} = 0.26$ by [Bonneau et al. (2000)]. [Flatt (2004a)] provided a broader range of $\phi_{perc}$ between 0.17 and 0.32, accommodating w/c ratios ranging from 1.5 to 0.5. In practical applications, w/c ratios can be significantly lower. A critical solid volume fraction $\phi_{crit}$ is reached once frictional contact forces dominate interparticle forces [Mehdipour and Khayat (2018)]. $\phi_{crit}$ corresponds to the water demand identified through tests such as the Puntke or Marquardt test.

Semi-empirical correlations between particle packing and cement paste rheology were investigated by various researchers. The Krieger-Dougherty model introduced in Chapter 2 applies, in general, for cementitious paste compositions, but also other models have been tested, reviewed by [Santhanam and Kumar (2003)].

[Ferraris and de Larrard (1998)] correlated viscosities of various concretes with a Krieger-Dougherty-adapted formula by [Chang and Powell (1994)]. [Bentz et al. (2012)] reported a weak correlation of particle packing and the Krieger-Dougherty formulation, but correlated different binder compositions and $\phi_s$ of the paste with the effective viscosity.

[Xu et al. (2020)] fitted temperature-related viscosity curves to the packing-density-based Liu-model [Liu (2000)]. [Zhang (2017)] extended the Krieger-Dougherty equation, see Eq. 2.21 for the implementation of hydration effects. While the Krieger-Dougherty model and similar particle packing models offer a simplified approach to relate rheological properties to particle packing, several effects must be considered for the rheological properties of cementitious pastes:

- With increasing specific surface area, stronger interparticle forces occur, which affects $\eta$. [Barnes (1997); Yu et al. (2003); Geisenhanslüke (2009)]

- As particles flocculate due to interparticle forces, rheological properties can change without a change of the macroscopic $\Phi_s$. [Mehdipour and Khayat (2018)]

- With increasing amounts of chemical additives, common structural equations need to be re-defined as they do not include polymer interactions and further chemical manipulations at particle surfaces. [Hot et al. (2014)]

- The hydration degree of cementitious pastes with and without superplasticizers affects the actual $\Phi_s$.

A comprehensive overview of the effect of granulometric properties on rheology is found in [Geisenhanslüke (2009)]. Granulometric optimization can enhance rheological properties, for example by increasing the maximum packing density $\phi_m$. This optimization strategy has been applied in the design of more eco-friendly concretes, see [Fennis-Huijben (2010); Hunger (2010)].

## 3.3  Microstructural models

Microstructural theories for cementitious suspensions calculate rheological properties as the sum of interparticle forces depending on the particle network. Direct particle models and semi-empirical particle models can be distinguished.

### 3.3.1 Direct particle models

The sum of contact points is either estimated from a number of bonds or junctions depending on the number of cement particles, which again are estimated from the particle size distribution, or simulated through particle-based simulation approaches.

Several particle models exist, either as perikinetic (shear rate independent, $\dot{\gamma} = 0$) or orthokinetic (shear rate dependent, $\dot{\gamma} > 0$) models, while the perikinetic calculation can be correlated to a yield stress at rest. The easiest orthokinetic formulation, that integrates the number of bonds in dependence of shear rate, was proposed by [Goodeve (1939)]:

$$-\frac{dJ}{J} = \frac{C_d \dot{\gamma}}{(\dot{\gamma} + \Theta)^{\delta}} \qquad [-] \qquad (3.2)$$

where $J$ is the number of junction between particles and $C_d$, $\Theta$ and $\delta$ are material-dependent constants, where interparticle forces can be integrated. Based on Eq.3.2, Hattori and Izumi (1982) formulated a perikinetic coagulation rate theory as:

$$\eta = B_3 J_t^{2/3} \qquad [Pas] \qquad (3.3)$$

With a friction coefficient $B_3$ in $[Ns]$ and a coagulation rate $J_t$. [Wallevik (2003)] extended Eq. 3.3 regarding the calculation of $J_t$. [Kapur et al. (1997)] defined a microstructural model for flocculated suspensions that directly correlates the number of bonds and interparticle forces with the yield stress:

$$\tau_y = \frac{1}{6} \sum_{k}^{n} \sum_{l=k}^{n} N_{k,l} F_{k,l} \qquad [Pa] \qquad (3.4)$$

In Eq. 3.4, $\tau_y$ is the microstructural yield stress in $[Pa]$, $N_{k,l}$ is the number of particle contacts between two size classes of particles $k, l$ and $F_{k,l}$ the corresponding interparticle forces. All chemical information are stored in the parameter $F_{k,l}$. Models that integrate time-dependency into *bond* or *junction* modeling enable the thixotropy calculation. [Ruckenstein and Mewis (1973)] proposed Eq. 3.5:

$$\begin{aligned} \frac{dN_j}{dt} = &k_1 (2 \sum_{k=1}^{\infty} N_{j+k} - jK_j) \\ &+ k_2 (1/2 \sum_{k=0}^{j-1} N_k N_{j-k-1} - N_j \sum_{k=0}^{\infty} N_k) \end{aligned} \qquad (3.5)$$

Eq. 3.5 describes the breakage and agglomeration of a certain number of bonds $N$ as time derivative and depending on its and breakage and recovery behavior, specified with the

material-dependent parameters $k_1$ and $k_2$. Also [de Kee and Chan Man Fong (1994)] formulated a simplified constitutive equation for the time-dependent bond evolution $n_c$:

$$\frac{dn_c}{dt} = k_c(n_0 - n) + k_1 f_2(\lambda \dot{\gamma}) n \tag{3.6}$$

In Eq.3.6, $n$ is the number of structural bonds, $k_c$ is a creation rate, $k_1$ is a shear-rate dependent creation rate, and $f_2$ is an arbitrary function, which can be correlated, e.g., to interparticle forces or experimentally investigated rheological properties. Further time-dependent structural particle models are presented in the works of [Wallevik (2005)] or [Le-Cao et al. (2020)].

## 3.3.2 Semi-empirical particle models

Semi-empirical microstructural yield stress models correlate the sum of interparticle forces with packing density properties. [Flatt and Bowen (2006)] invented the Yield stress mODEL (YODEL):

$$\tau_0 = m_1 \frac{(\phi - \phi_{perc})^2}{\phi_m * (\phi_m - \phi)} \qquad \text{[Pa]} \tag{3.7}$$

Where $\phi$, $\phi_{perc}$ and $\phi_m$ are the actual, percolation and maximum solid volume fraction and $m_1$ displays a parameter for the interactive particle forces:

$$m_1 = \frac{1,8}{\pi^4} G_{\max} * a^* * u_{k,k} * \left(\frac{f_{\sigma,\Delta}}{R_{v,50}^2}\right) \qquad \text{[Pa]} \tag{3.8}$$

$G_{\max}$ is the sum of particle interactions, $a^*$ and $u_{k,k}$ are shape and curvature information. Information about the particle size distribution (PSD) are stored in the related function $\frac{f_{\sigma,\Delta}}{R_{v,50}^2}$ (more information on all parameters in [Flatt and Bowen (2006, 2007)]). [Mantellato and Flatt (2020)] extended the YODEL model to flow loss analysis in presence of PCEs.

Similarly to Eq.3.7, [Ogawa et al. (1997)] calculated cement paste viscosity:

$$\eta = \eta_v(\phi) + k_2 \eta_s \phi \exp\left\{\frac{U_v(\phi)}{k_B T} - \frac{k_1 d^3 \sigma_p}{\phi k_B T}\right\} \qquad \text{[Pas]} \tag{3.9}$$

In Eq.3.9, $k_1$ and $k_2$ are numerical constants, $k_B T$ are the Boltzmann constant and the absolute temperature, $V_v$ is the activation energy, $V_r$ is the interparticle potential, $r$ and $d$ particle geometric factors, $\eta_s$ the solvent viscosity and $\sigma_p$ is the particle stress with $\sigma_p = \eta_p(\phi, \sigma_p)\dot{\gamma}$.

# 3.4　Phenomenological models

Phenomenological flow models describe macroscopic flow and calculate characteristic rheological properties without the consideration of the suspension's microstructure. Often, experimental flow curves are gained through rheometry, and the corresponding flow curves are fitted to one phenomenological model. Comprehensible overviews for cement paste models can be found in various literature reviews, see e.g., [Tattersall and Banfill (1983); Papo (1988); Barnes (1999); Haist (2009); Roussel et al. (2012)]. Relevant models with regard to this thesis are listed subsequently.

## 3.4.1　Viscoplastic flow models

**Yield stress models**

The Bingham model, Eq.3.10, is the most simple and frequently applied rheological model for cement paste and concrete flow descriptions:

$$\tau(\dot{\gamma}) = \tau_{0,B} + \mu\dot{\gamma} \qquad\qquad \text{[Pa]} \qquad (3.10)$$

with the linear viscosity $\mu$ in [Pas] and the Bingham - yield stress $\tau_{0,B}$ in [Pa].
[Coussot and Ancey (1999)] highlighted the limitation of Eq. 3.10, as it fails to accurately represent material properties across a wide range of shear loads. This limitation is addressed by introducing shear-rate-dependent viscosities, e.g. depicted by the Herschel-Bulkley model:

$$\tau(\dot{\gamma}) = \tau_{0,H-B} + k\dot{\gamma}^n \qquad\qquad \text{[Pa]} \qquad (3.11)$$

with $\tau_{0,H-B}$ as Herschel-Bulkley yield stress in [Pa], $k$ as consistency index in $[(\text{Pas})^n]$ and $n$ as dimensionless exponent for shear-thinning or shear-thickening behavior. The exponent $n$ depicts shear-thinning behavior if $n < 1$ and shear-thickening behavior if $n > 1$. While the Herschel-Bulkley model offers an improved approximation of the flow curve compared to the Bingham model, it may still exhibit significant deviations from the actual flow behavior, particularly at low shear rates [Haist (2009)]. An extension to Eq.3.10 is the modified Bingham model in Eq.3.12:

$$\tau(\dot{\gamma}) = \tau_{0,Bmod} + \mu_1\dot{\gamma} + \mu_2\dot{\gamma}^2 \qquad\qquad \text{[Pa]} \qquad (3.12)$$

Eq.3.12 is represented by a linear and one exponential part. However, [Haist (2009)] mentioned that Eq. 3.12 tends to underestimate the yield stress.

The Casson model introduces the infinity viscosity $\eta_\infty$:

$$\tau(\dot{\gamma}) = \tau_{0,Ca} + \eta_{\infty}\dot{\gamma} + 2(\tau_{0,Ca}\eta_{\infty})^{0.5}\dot{\gamma}^{0.5} \qquad [\text{Pa}] \qquad (3.13)$$

[Papo (1988)] mentioned that Eq.3.13 was less applicable for shear-thinning cementitious pastes in comparison to other models, but showed increased applicability with decreasing w/c ratios. [Toussaint et al. (2009)] combined the Herschel-Bulkley model and the Casson model for the analysis of shear-thickening cement pastes:

$$\tau(\dot{\gamma}) = \tau_{0,T} + 2(\tau_{0,T}\beta)^{0.5}(\dot{\gamma})^{0.5} + \beta\dot{\gamma} + k\dot{\gamma}^n \qquad [\text{Pa}] \qquad (3.14)$$

Eq. 3.14 uses the yield stress $\tau_{0,T}$ and the three adjustable parameters $\beta$, $k$ and $n$, while $k$ and $n$ appear similar in their rheological meaning as used in the Herschel-Bulkley model.

Phenomenological flow curves of Eq.3.10 to Eq.3.14, applied as fitting functions to experimental data, are illustrated in Figure 3.3.



(a) Regressions for shear-thinning pastes

(b) Regressions for shear-thickening pastes
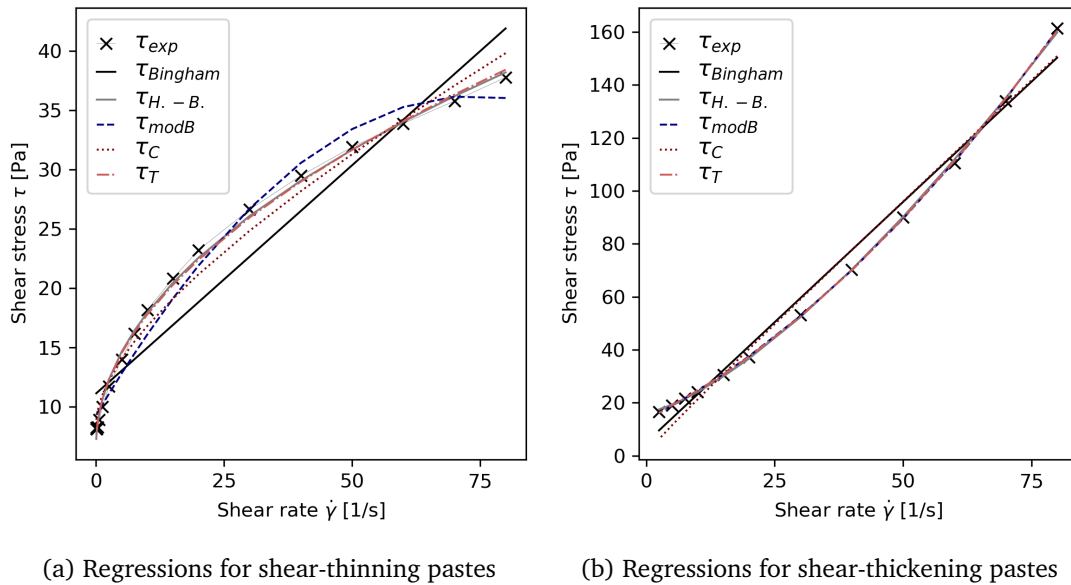
Figure 3.3: Phenomenological regression functions applied to experimental flow curves

Figure 3.3 (a) shows the fitting of the introduced phenomenological models to experimental flow curves of a shear-thinning cement paste. Figure 3.3 (b) displays the fit on a shear-thickening paste. It is obvious that different rheological models approximate the flow behavior better for shear-thinning and shear-thickening behavior.

**Viscosity models**

Viscosity models are less common in concrete technology, because the yield stress value is an important measure e.g. for quality control. However, viscosity formulations introduce

parameters for boundary viscosities, such as the material viscosity close to rest or at infinite shear rate or time, which can be beneficial.

Two easy models are the Sisko model in Eq.3.15 and the Williamson model in Eq.3.16, that are based on the Herschel-Bulkley model but implement either a zero viscosity $\eta_0$, which is the maximum viscosity at $\dot{\gamma} \Rightarrow 0$, or the infinity viscosity $\eta_\infty$, which is the minimum structural viscosity that can be reached at $\dot{\gamma} \Rightarrow \infty$:

$$\eta(\dot{\gamma}) = \eta_\infty + k\dot{\gamma}^{n-1} \qquad [\mathrm{Pas}] \qquad (3.15)$$

$$\eta(\dot{\gamma}) = \frac{\eta_0}{1 + (k\dot{\gamma}^n)} \qquad [\mathrm{Ps}] \qquad (3.16)$$

The Cross model, presented in Eq.3.17, describes $\eta(\dot{\gamma})$ with both a zero viscosity plateau $\eta_0$ at $\dot{\gamma} \Rightarrow 0$, and an infinity viscosity plateau $\eta_\infty$ at $\dot{\gamma} \Rightarrow \infty$:

$$\eta(\dot{\gamma}) = \eta_\infty + \frac{\eta_0 - \eta_\infty}{(1 + c\dot{\gamma})^d} \qquad [\mathrm{Pas}] \qquad (3.17)$$

with $c$ and $d$ as two material-dependent constants. [de Souza Mendes (2009)] presented a calculation for $\eta(\dot{\gamma})$:

$$\eta(\dot{\gamma}) = (1 - (e^{-(\eta_0\dot{\gamma})/\tau_{0,s}})) * ((\tau_{0,s} - \tau_{0,d})/\dot{\gamma}) * e^{-\dot{\gamma}/\dot{\gamma}_c} + \tau_{0,d}/\dot{\gamma} + (k\dot{\gamma}^{n-1}) + \eta_\infty [Pas] \quad (3.18)$$

Eq.3.18 requires several parameters that need to be defined beforehand: $\eta_0$ and $\eta_\infty$ are the zero and infinity viscosity in [Pas], respectively. $\tau_{0,s}$ and $\tau_{0,d}$ display static and dynamic yield stress values in [Pa]. Further, the Herschel-Bulkley model is used. Figure 3.4 displays the viscosity models from Eq.3.11 to Eq.3.17 for (a) a shear-thinning and (b) shear-thickening cement paste.
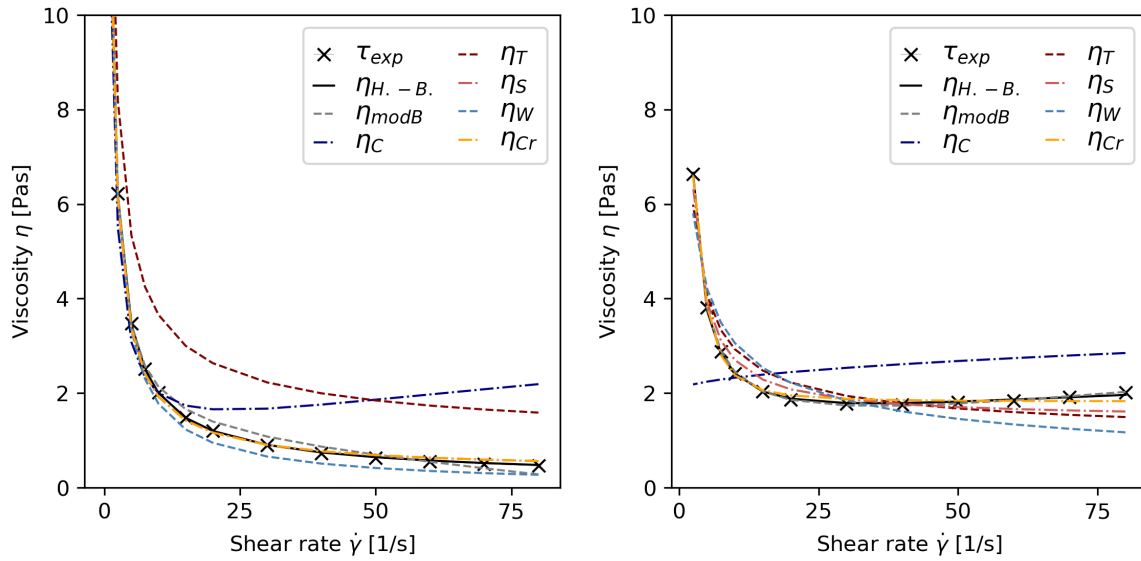
(a) Regressions for shear-thinning pastes

(b) Regressions for shear-thickening pastes

Figure 3.4: Phenomenological regression functions applied to experimental viscosity curves

Again, the applicability of different models varies. Most models depict shear-thinning viscosities, as illustrated in Figure 3.4 (a). Shear-thickening behavior, on the contrary, is not depicted by most of the models. While the Herschel-Bulkley model in Figure 3.4 (b) indicates increasing viscosity $\eta(\dot{\gamma})$, it does not calculate the increasing $\eta$ towards zero. Models that display zero viscosities $\eta_0$, such as the Sisko model or the Cross model, deviate from the experimental data towards higher shear rates.

## 3.5 Thixotropy in cementitious pastes

Thixotropy is the fully reversible time-dependent viscosity change [Goodeve (1939)]. Interparticle forces in the cementitious particle network determine thixotropy. Thus, increasing cement fineness, increased specific surface area, and higher solid volume fractions $\phi_s$ increase thixotropy [Jiao et al. (2021); Biricik and Mardani (2022); Han et al. (2022)]. However, if several parameters are changed simultaneously (e.g., by adding chemical admixtures or workability-enhancing additives such as limestone powder or fly ash), thixotropic properties may vary irregularly due to various interactions. The prediction of the thixotropy, therefore, becomes uncertain. [Ewoldt et al. (2008); Feys et al. (2017)]

Furthermore, cement hydration involves constant alterations in the microstructure and chemical composition. Products form due to hydration reaction and contribute to the development of a structure. On the other hand, once this structure is disrupted, it does not reform. Thus, cementitious building materials exhibit both reversible thixotropy and irreversible structural buildup. A distinction between both effects is difficult. While the effects of reversible thixotropy manifest within seconds, the structural buildup due to hydration becomes significant over a more extended period. [Roussel et al. (2012); Reiter (2019)]

The evaluation of thixotropy and structural buildup is essential for various concrete applications. Initially, thixotropy can support stable concrete mixtures and prevent segregation and sedimentation effects [Lowke (2013)]. However, if not or wrongly considered, thixotropy can decrease concrete workability and its processing, for example the pumpability [Feys et al. (2008); de Schryver and de Schutter (2020)].

In Self-Compacting Concrete (SCC), the concrete flow must be precisely targeted to enable the free-surface, gravity-driven flow into the formwork. Initially, thixotropy supports the viscosity decrease of stable concrete mixtures during pumping, which improves the workability [Assaad et al. (2003); Khayat and Feys (2010); Esmaeilkhanian et al. (2017)]. However, thixotropy can reduce the self-flowing properties of SCC if flow velocities are not sufficient to prevent thixotropic viscosity increase during slow flow, see [Assaad et al. (2003); Biricik and Mardani (2022)].

Thixotropy is beneficial for fabricating vertical constructions into formwork. Structural buildup enables the load transfer within the concrete structure and, thus, can reduce the formwork pressure, see [Billberg (2006); Omran et al. (2012)]

Thixotropy is also crucial in applications like shotcrete and additive manufacturing through extrusion, where fast structural buildup is required after pumping, spreading, or extruding the material at low viscosities. [Jiao et al. (2021); Biricik and Mardani (2022); Ivanova (2023)]

### 3.5.1   Thixotropy analysis

Various methods are available for investigating the thixotropic properties of cementitious pastes and concrete, ranging from experimental techniques to mathematical models. Microstructural and coagulation rate models, as introduced in Section 3.2, calculate interparticle forces and derive the time-dependent strength increase or decrease as thixotropy, see for example [Hattori and Izumi (1982); Wallevik (2009)]. While these models offer precise mathematical formulations, they necessitate many input parameters, and often a distinc chemical and physical analysis. Simplified experimental procedures, along with phenomenological models estimate the structural increase. A short overview is given in the following, [Reiter (2019); Jiao et al. (2021)] provide comprehensive state-of-the-art reports concerning thixotropy in applied cement and concrete research.

In experimental investigations of thixotropy and structural buildup in cementitious pastes and concrete, one common approach is to measure the increase in structural strength over time, often represented by the stress increase $\tau(t)$ [Barnes (1997)]. Rheometric thixotropy tests comprise hysteresis loops, stress growth protocols, penetration tests, or creep tests. Hysteresis loops involve measuring stress responses as shear rates are first applied and then removed, with the enclosed area representing structural recovery. Stress growth protocols, on the other hand, track stress increases at defined times after the material has rested, quantifying thixotropy rates. In these tests, also known as static yield stress tests,

the material is left at rest until the built structure is broken by an applied shear rate, and the material's resistnace is recorded. Oscillatory tests, conversely, examine stress responses during non-destructive applied strains [Mostafa and Yahia (2016)]. Penetration tests involve penetrating the paste with a probe at a constant load, with the penetration depth over time serving as a measure of thixotropy. Creep tests analyze the decay in shear rate necessary for the paste to develop enough structure to withstand a constant applied stress [Kawashima et al. (2013); Qian and Kawashima (2018)].

Experimental measurements are then combined with constitutive thixotropy models, with most studies focusing on linear structural increases. However, some thixotropy models describe nonlinear structural buildup.

Based on constitutive thixotropy modeling as introduced in Chapter 2, [Coussot et al. (2002)] formulated Eq. 3.19for the calculation of a time-dependent structural parameter $\lambda$:

$$\frac{d\lambda}{dt} = \frac{1}{T\lambda^m} - \alpha\lambda\dot{\gamma} \qquad [-] \qquad (3.19)$$

with $\frac{d\lambda}{dt}$ as time-dependent flocculation derivative and $\lambda$ as unit-less structural parameter, $T$ as characteristic flocculation time in [s], $\alpha$ as structural breakdown parameter in [-] and $m$ as scaling factor in [-]. For a simplified engineering approach, [Roussel (2006)] defined three boundary conditions:

- $\lambda_0 = 0$, stating a total deflocculation at t = 0 (directly after mixing)

- m = 1 as linear static yield stress as a function of time

- $\frac{1}{T} \rightarrow 0$: The characteristic structural breakdown and structural buildup are in an equilibrium condition

This simplifies Eq.3.19 to

$$\frac{d\lambda}{dt} = -\alpha\lambda\dot{\gamma} \qquad [-] \qquad (3.20)$$

with an explicit solution of $\frac{d\lambda}{dt}$, the thixotropy-implemented Bingham model yields

$$\tau(\dot{\gamma}) = (1 + \lambda_0 e^{-\alpha\dot{\gamma}t})\tau_0 + \mu\dot{\gamma} \qquad [Pa] \qquad (3.21)$$

At rest with $\dot{\gamma} = 0$, the time dependent shear stress evolution $\tau_{0,s}(t)$ is:

$$\tau_{0,s}(t) = (1+\lambda)\tau_{0,d} = \tau_{0,d} + A_{thix}t \qquad\qquad [Pa] \quad (3.22)$$

With $\tau_{0,s}(t)$ as static yield stress over time $[Pa]$ and $A_{thix}$ as remaining parameter from $\frac{d\lambda}{dt} = \frac{1}{T}$, which displays the linear structural increase in $[Pa/s]$. The experimental investigation of the thixotropy parameter $A_{thix}$ displays a simple approach to measure thixotropy. Generally, a rheometric rotational static yield stress test is applied, displaying the stress growth test at rest, to measure $A_{thix}$, see for example [Lowke (2013); Tan et al. (2015); El Bitouri and Azéma (2022); Ivanova (2023)]. Experimental results of $A_{thix}$ are frequently linked to microstructural properties of cement pastes, see [Lowke (2013); Nicia et al. (2023)]. Boundary effects, such as material destruction during shearing phases, and applicability on mortars, were investigated, e.g., in [Ivanova et al. (2022)].

Several theories exist to model the nonlinear structural buildup. [Perrot et al. (2016)] presented an extension to Eq. 3.21. Eq. 3.23 models an exponential structural increase (correlated to the irreversible, hydration-related structural buildup) after the initial linear structural buildup:

$$\tau_{0,s}(t) = \tau_{0,d} + A_{thix}t(e^{\frac{t}{t_c}} - 1) \qquad\qquad [Pa] \quad (3.23)$$

In Eq. 3.23, $t_c$ presents an arbitrary time value displaying the best fit of experimental data to the proposed nonlinear model. However, also the initial structural buildup can be modeled with nonlinear approaches. [Ma et al. (2018)] developed Eq. 3.24:

$$\tau_{0,s}(t) = \tau_{0,s} + c\lambda(t) + A_{thix} * t \qquad\qquad [Pa] \quad (3.24)$$

In Eq. 3.24, $\tau_{0,s}$ is the static yield stress, $c$ is a structural parameter during the nonlinear flocculation in [Pa] and $\lambda$ is the structural parameter as a function of time. The constitutive equation for $\lambda$ slightly varies from Eq. 3.20:

$$\frac{d\lambda}{dt} = -\frac{1}{\Theta}\lambda - \lambda_{equil} \qquad\qquad [-] \quad (3.25)$$

In Eq. 3.25, $\Theta$ is the relaxation time in [s], similarly to Eq. 3.19, where $T$ is denoted as flocculation time in [s]. $\lambda_{equil}$ displays an equilibrium structural parameter at defined steady state boundary conditions. An explicit solution is calculated as:

$$\lambda(t) = \lambda_{equil} + (\lambda_0 - \lambda_{equil})e^{-\frac{t}{\theta}} \qquad\qquad [-] \quad (3.26)$$

with an explicit boundary condition $\lambda_0$ instead of $\lambda_{equil}$, Eq. 3.24 yields:

$$\tau_{0,s}(t) = \tau_{0,s} + c\left[1 + (\lambda_0 - 1)e^{-\frac{t}{\theta}}\right] + A_{thix}t \qquad \text{[Pa]} \qquad (3.27)$$

The evolution of the storage modulus $G'$ in an oscillatory test is described accordingly:

$$G'(t) = c\left[1 - e^{-\frac{t}{\theta}}\right] + G_{rig}t \qquad \text{[Pa]} \qquad (3.28)$$

with $G'(t)$ as time-dependent storage modulus in [Pa] and a rigidification rate of $G_{rig}$ in [Pa/s], which corresponds to the idea of $A_{thix}$. [Yuan et al. (2017)] showed that in an oscillatory structural buildup test, the evolution of $G'$ is about four orders larger than the stress increase $\tau(t)$ measured by rotational static yield stress tests. They explained this observation with the destructive character of the static yield stress test, wherefore the initially built CSH structure is destroyed during the experiment and colloidal interactions dominate further structural buildup. [Mostafa and Yahia (2016)] applied nonlinear buildup modeling of the storage modulus and compared it to $A_{thix}$ measurements.

Further nonlinear models and their application to cementitious thixotropic behavior can be found, e.g., in [Mujumdar et al. (2002); Le-Cao et al. (2020); Guo et al. (2023)].

## 3.6  Applied rheology: Flow tests as workability estimation

The analysis of rheological properties often requires expensive measurement equipment and complex mathematical procedures. A more straight-forward analysis of flow properties is the performance of flow tests. Flow tests can estimate workability properties on-site. Results of flow tests (both flow length or flow time) can be correlated with rheological parameters such as yield stress and viscosity. The fundamental assumption is that a material stops flowing once the yield stress $\tau_0$ is higher than the impact through gravity or external forces (e.g., pumping, vibration). Commonly applied workability tests are the spread flow, slump or the slump flow test, the V-funnel test, J-ring test, and the L-Box test. As they are applied in this thesis, the *slump flow test* and *L-Box test* are introduced in detail. Both tests are standardized, but slight variations in the geometrical framework and the flow test execution exist. Figure 3.5 illustrates both geometries schematically.

**Slump flow and mini slump flow measurements**

For slump flow measurements, a cone with standardized dimensions with a diameter $d_0$ and height $h_0$ (e.g., Hägermann cone for pastes according to EN 1015-3:2007-05 [DIN1015], or Abrams cone for concrete according to EN 12350-8:2010-12 [DIN12350-8], is first filled
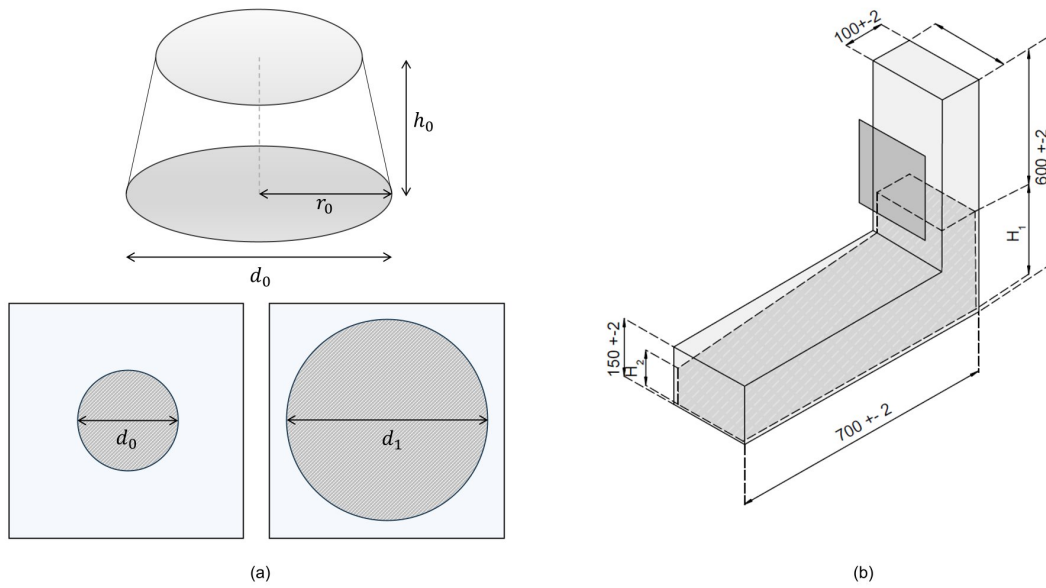
Figure 3.5: Schematic geometries for (a) the slump flow test and (b) the L-Box test

with paste and then pulled so that the paste spreads and reaches a final diameter after the stoppage, see Figure 3.5 (a), $d_1$. [Murata (1984)] correlated the deformation of the slump cone with the mortar's or concrete's rheological properties. Further researchers applied or extended the correlation of slump and yield stress; reviewed, e.g., by [Thrane (2007), pp. 43]. A widely used approach was presented by [Roussel and Coussot (2005)], who derived a correlation between the final diameter in a mini-slump flow test and the yield stress $\tau_0$ depending on the volume of the cone:

$$\tau_0 = \frac{225 \rho g V^2}{128 \pi^2 R^5} \qquad \text{[Pa]} \qquad (3.29)$$

Where $\rho$ is the density in [kg/m$^3$], $g$ the gravity = 9.81 m/s$^2$, $V$ the volume of the mini-slump cone in [m$^3$] and $R$ the measured mini-slump flow radius after stoppage of flow in [m]. The correlation was defined to be valid only for flowable pastes >> 150 mm, where gravitational forces exceed frictional forces. Further correlation equations are reviewed in [Mantellato (2017), pp. 118]. All correlation formulations neglect the inertia of the fluid and the surface tension between fluid and air. Boundary conditions, such as the lifting velocity of the cone and the tension between fluid and plate, are not calculated. Despite several simplifications and neglections, the application of correlation equations between slump flow test and yield stress have become popular in the field of cement and concrete technology. The applicability has been investigated by various researchers, e.g., for reactive pastes in [Tan et al. (2017)] and as qualitative correlation value between different laboratories in a Round-Robin test in [Haist et al. (2020)].

**L-Box and LCPC box test**

The L-Box test is standardized according to EN 12530-10 [DIN1235010], and with its dimensions shown in 3.5 (b), to evaluate the workability of very flowable paste or concrete on site. In an L-Box test, material is filled into the vertical box. After placing, the gate separating the vertical and horizontal box is lifted slowly to prevent effects of inertia. The flow time and final flow length are measured, and, in various cases, also the height of the final flow body in the front and the back. While the L-Box possesses a vertical box where the material is stored before lifting a gate, the LCPC-Box displays a single horizontal channel. [Nguyen et al. (2006)] correlate the final flow length $L$ of concrete to the yield stress $\tau_0$:

$$L = \frac{h_0 \rho g l_0}{2\tau_0} + \frac{l_0^2 \rho g}{4\tau_0} \ln \frac{l_0}{l_0 + 2h_0} \qquad [\text{m}] \qquad (3.30)$$

In Eq.3.30, $L$ is the final flow length in [m], $l_0$ is the width of the L-box in [m], $h_0$ is the height of the flow body after flow stoppage at the beginning of the channel in [m]. While standardized L-Boxes are used for workability tests on-site, smaller L-Boxes have been investigated for the evaluation of cement pastes, e.g., by [Chaparian and Nasouri (2018)]. The L-Box test is also known as dam-break case in several other disciplines that evaluate flow [Almeida and Franco (1994); Aureli et al. (2023)].

## 3.7 Numerical modeling of concrete flow

Numerical modeling of concrete flow has become a valuable tool to support processing and placement predictions of concrete or to study flow properties that cannot be grasped analytically or experimentally. [Tanigawa and Mori (1989)] tested first numerical frameworks for concrete by simulating the slump flow test with a viscoplastic Finite Element approach. Numerical methods became more interesting for flow predictions with the invention of SCC. A short overview of common numerical applications and methods in concrete technology is given below. In general, numerical modeling serves following purposes:

- **Processing predictions** with numerical methods enable the calculation of concrete flow with defined rheological input parameters in a particular geometry, e.g., floors or walls [Wallevik and Wallevik (2011)]. Modeling of concrete pumping helps to understand the correlation between the applied pumping energy and homogeneous rheological parameters or physical phenomena of the material during pumping, e.g., plug flow or particle migration [Spangenberg et al. (2012); Choi et al. (2014); Secrieru (2018); Fataei (2021)].

- **Internal rheology analysis** through numerical simulations helps to investigate shear flow fields, forces, or shear rates in the tested material, e.g., directly at the edge

or between particles. This assists in the understanding of specific flow situations, see e.g., [Wallevik and Wallevik (2017)] for the shear rate evaluation inside concrete trucks, or [Pirharati et al. (2019)] for the study of shear fields in large gap rheometers.

- **Quality control and mix design optimization** Numerical methods can help to adjust the required rheology of a paste or concrete to meet the flowability needs. Without time-consuming experimental loops, theoretical parameter studies with numerical simulations can assess the required rheology, followed by the experimental mix design optimization [de Schryver, Robin (2022); Zhang et al. (2023)].

Numerical modeling techniques using **Discrete particle models** and **Homogeneous fluid flow models** are applied in the field of cement and concrete rheology.

### 3.7.1   Discrete particle models

**Discrete particle models** (DPM) display concrete as a heterogeneous compound of different particles. They calculate flow properties in dependence on particle interactions and calculate forces between these particles based on geometric boundary conditions and applied force models, considering interparticle forces, hydrodynamic and/or frictional forces. Several discrete particle models exist, such as the discrete element method (DEM), dissipative particle dynamics (DPD), smoothed particle hydrodynamics (SPH), and coarse-grained particle methods (GCPM), comprehensivley reviewed, e.g., in [Roussel et al. (2007); de Schryver, Robin (2022)]. A complete literature review is beyond the scope of the thesis, solely DEM and SPH are briefly introduced.

**Discrete element method (DEM)**

DEM was employed by Cundall and Strack in 1971 to solve problems in the field of rock mechanics [Cundall and Strack (1971)]. The aim of DEM is the explanation of granular medium flow through the application of mechanical models on single particles. It calculates the motion of particles (displacement, rotation, interaction forces) by the definition of (I) contact forces and (II) fluid motion through the application of Newton's second law. The particles are modeled as spheres with walls, and contact models at the walls are applied to all particles within a defined volume.

DEM models explain the motion of particles within the concrete and thus aim to investigate phenomena like segregation and bleeding, blockage phenomena, e.g., at narrow formworks or reinforcement bars, see, e.g., [Cui et al. (2018)]. Particle interaction and effects of neighboring particles on one particle motion are critically investigated, e.g., in [Shyshko and Mechtcherine (2013)]. Also, the effect of mixing processes on grains can be investigated, see, e.g., [Schwabe (2013)]. DEM is also used to model the macroscopic flow behavior of concrete, for example for shotcrete processing [Puri and Uomoto (2002)] or SCC flow [Cui et al. (2020)]. Particle migration in pumping processes was investigated with DEM

e.g. by [Tavangar et al. (2023a)]. Thixotropic phenomena were investigated for the cases of L-Box flow or large-gap ViC rheometry by [Tan et al. (2015)]. For parameter studies of macroscopic concrete flow in dependence of the chosen rheological model or numerical boundary conditions, generally the L-Box test or the slump flow test serve as benchmark geometries, as used in [Mechtcherine et al. (2014); Roussel et al. (2016); Li et al. (2021)] and [Mu et al. (2023)].

**Smoothed Particle Hydrodynamics (SPH)**

SPH divides a fluid into single elements. The division into elements is not reliant on real particles, but follows a statistically randomly distributed Monte-Carlo approach. The motion of the single elements subsequently is calculated through the solution of hydrodynamic equations, typically the Navier-Stokes equations, using a Lagrangian approach. SPH is often used to calculate free surface flow, such as debris flow scenarios [Han et al. (2019)]. The effect of thixotropy into a dam-break flow case was implemented by [Vahabi (2021)].

The application of SPH to simulate concrete flow phenomena is an area of ongoing research. [Abo Dhaheer et al. (2016)] investigated the simulation of the J-ring tests for SCC with a closer look on aggregate homogeneity and segregation behavior. [Tran-Duc et al. (2021)] investigated the effects of the coarse aggregates on SCC flow and found the method suitable to correlate coarse aggregate effects with rheological parameters (yield stress and viscosity). SPH is not as proven as DEM or state-of-the-art CFD methods. However, it possesses the benefit to apply many or complex boundary conditions to fluid elements [Shadloo et al. (2016)].

## 3.7.2   Homogeneous fluid modeling

**Homogeneous fluid flow models** assume concrete as a homogeneous one-phase medium. Flow is calculated with the constitutive equations of fluid dynamics and uses the methods of CFD, see Chapter 2. [Wallevik (2003)] published the first comprehensive application of CFD methods on cement paste rheology, applying the method of Finite Differences (FDM) on suspension rheology phenomena. [Thrane (2007)] modeled the form filling of self-compacting concrete (SCC) with CFD-FVM, and combined the understanding of macroscopic, homogeneous flow with the analysis of heterogeneous flow phenomena. CFD modeling of SCC was further tested and developed by further researchers, such as [Jacobsen et al. (2013); Vasilić (2016); Hosseinpoor et al. (2017)]. [Gram (May 2009)] and [Heese (2013)] investigated the application of CFD to the modeling of the previously introduced flow tests slump flow and L-Box. [Fataei (2021)] investigated concrete pumping using CFD regarding particle migration, and [de Schryver et al. (2021)] tested the numerical reliability of CFD applied to concrete pumping.

The comparability of different CFD simulations (using different programs or algorithm packages, and also in comparison to analytical methods and DEM simulations) was tested

by [Roussel et al. (2016)] through benchmarking the slump flow test. [Haustein et al. (2022)] conducted a benchmark test for concrete pumping by testing several boundary conditions. Generally, concrete or cementitious suspensions are modeled using the Bingham or Herschel-Bulkley approach. The implementation of thixotropy into CFD modeling was shortly introduced by [Roussel (2006)]. [de Schryver, Robin (2022)] implemented thixotropy into the pumping simulation of a Bingham fluid.

**Necessity of model regularization**

The application of CFD methods to calculate fluid flow incorporates the challenge of a numerical instability, as the solution of the Navier-Stokes equations at $\dot{\gamma} = 0$ is mathematically not defined. Regularization models introduce a continuous mathematical definition towards $\dot{\gamma} \rightarrow 0$. [Frigaard and Nouar (2005)] and [Saramito and Wachs (2017)] reviewed several regularization methods. Two frequently applied regularization models, also applied in this thesis, are the Papanastasiou regularization by [Papanastasiou (1987)] and the bi-viscous model by [O'Donovan and Tanner (1984)]. Eq. 3.31 displays the Herschel-Bulkley-implemented Papanastasiou regularization:

$$\eta(\dot{\gamma}) = \frac{\tau_0(1 - e^{-m\frac{\dot{\gamma}}{\dot{\gamma}_{crit}}})}{\dot{\gamma}} + k\dot{\gamma}^{n-1} \qquad \text{[Pas]} \qquad (3.31)$$

Eq. 3.31 is an exponential blending function with $m$ as regularization parameter in $[-]$ and the critical shear rate $\dot{\gamma}_{crit}$. Eq. 3.32 presents the bi-viscous model:

$$\eta(\dot{\gamma}) = \min \begin{cases} \eta_0 \\ \dfrac{\tau_0}{\dot{\gamma} + k\dot{\gamma}^{n-1}} \end{cases} \qquad \text{[Pas]} \qquad (3.32)$$

The bi-viscous model defines a plateau value $\eta_0$ as fixed viscosity. The effect of model regularization on computational fluid flow is published in [Thiedeitz et al. (2024)], summarized in Chapter 8.

## 3.7.3   Possibilities and challenges of numerical methods

Concrete is a granular, heterogeneous material. Discrete particle models possess the benefit of particularly describing certain phenomena of particles (such as shape, density, compressibility) and effects between different particles. However, this comes with the drawback of high computational costs. Thus, most particle models are limited in their geometric domain. CFD can display larger computational domains. However, the assumption of a single fluid, as given in CFD models, does not depict the real material. A direct comparison of the

two methods within the RILEM TC 222 (see [Roussel et al. (2016)]) was critically reviewed by [Vasilic et al. (2019)], who resumed that both methods were able to approach the analytical solution for the slump flow test setup. However, both methods have their limitations; and "the choice of the method for the specific application depends on the type of concrete, on the process itself and on the scale of observation" Vasilic et al. (2019), p.60. CFD-DEM methods couple the different mathematical approaches [Tavangar et al. (2023b)]. CFD-DEM becomes useful when not only concrete flow, but especially particle interactions are the point of investigation, which is the case for pervious concrete processing, see e.g., [Nan et al. (2021)]. To minimize computational costs, [Wang et al. (2021)] implemented a speed-up model to a CFD-DEM code to analyze contact forces of particles. However, CFD-DEM incorporates numerical challenges and errors of both approaches, which complicates the numerical set-up and susceptibility to errors.

## 3.8 Summary: The rheology of cementitious pastes

[Coussot and Ancey (1999)] remarked that fluid rheology of dense suspensions is one of the most complicated disciplines in the field of rheology, as not only the material itself, but further effects account to description inaccuracies. Cement pastes, additionally, change their chemical and physical properties constantly. Following Chapter 2 and Chapter 3, rheology affecting factors are summarized:

- **Internal paste factors**: Granulometric properties, chemical admixtures and hydration products affect rheological properties by determining interparticle forces or the rheology of the liquid phase. While direct microstructural models can display these effects, they are neglected in semi-empirical or packing-density related models.

- **External factors**: The analysis of rheological properties depends on the rheometric device, the treatment of the cementitious paste before the measurement or laboratory conditions.

- **Rheological modeling**: Dependent on the macroscopic suspension properties, different rheological models can yield the best results. The application of different models will result in significantly varying rheological parameters. Flow tests provide a fast evaluation of rheological parameters. However, they solely take the Bingham model into account. With increasing deviation from linear viscoplastic flow properties, correlation equations do not comply with the physical properties anymore.

- **Numerical modeling**: While numerical models are a powerful tool to understand or predict concrete flow, the numerical framework incorporates approximations, which affect the final numerical result. Knowledge about both the computational framework and rheological properties is essential.

Summarized, the literature review proves a well-structured "common practice" for viscoplastic material characterization and structural buildup at rest. Reliable numerical DEM

and CFD simulation frameworks for viscoplastic materials are available. Open questions remain for more complex paste behavior. Here, "complex" means the deviation from linear viscoplasticity by nonlinear viscosities and increased viscoelastic and thixotropic material behavior, which changes the steady-state flow to a flow case with transient properties. Several questions arise:

- At which point do cement pastes deviate from linear viscoplastic behavior?

- How can viscoelasticity and thixotropy be measured?

- Which rheological models describe cement paste flow over a large range of shear rate?

- Are flow tests sufficient for the analysis of cementitious paste rheology when deviating from linear viscoplasticity?

- Can CFD support the analysis of transient properties?

# 4. Methodology

## 4.1 Research framework

This thesis aims to comprehensively reveal transient and time-dependent rheological phenomena of cementitious pastes in the intersection of experimental rheology, phenomenological rheology and numerical flow simulations. Following the conclusions in Chapter 3, the research framework is illustrated in Figure 4.1 and Figure 4.2.
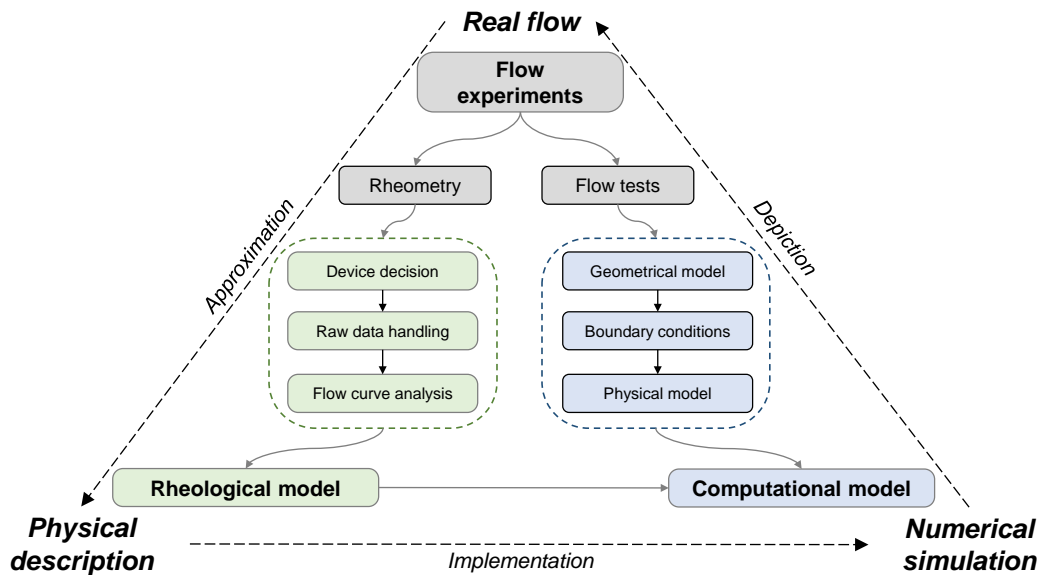
Figure 4.1: Interplay of different rheological fields applied in this thesis

Cementitious paste rheology and flow were experimentally investigated through rheometry and flow tests. While rheometry was the basis for the physical flow description through phenomenological modeling, flow tests were approximated in numerical simulations using Computational Fluid Dynamics (CFD). The CFD model required the implementation of rheological parameters from the rheometric analysis. Finally, the numerical result was compared to the real flow.

The research structure is illustrated in Figure 4.2. Chapter 4 provides an overview of all materials and applied methods. Followed by that, **Part II** and **Part III** provide summaries of published or submitted research. All articles are available open-access. **Part II** summarizes all preliminary investigations related to rheology-affecting features. **Part III** provides the summary of publications that investigate the transient and time-dependent flow character-

istics of cementitious pastes.
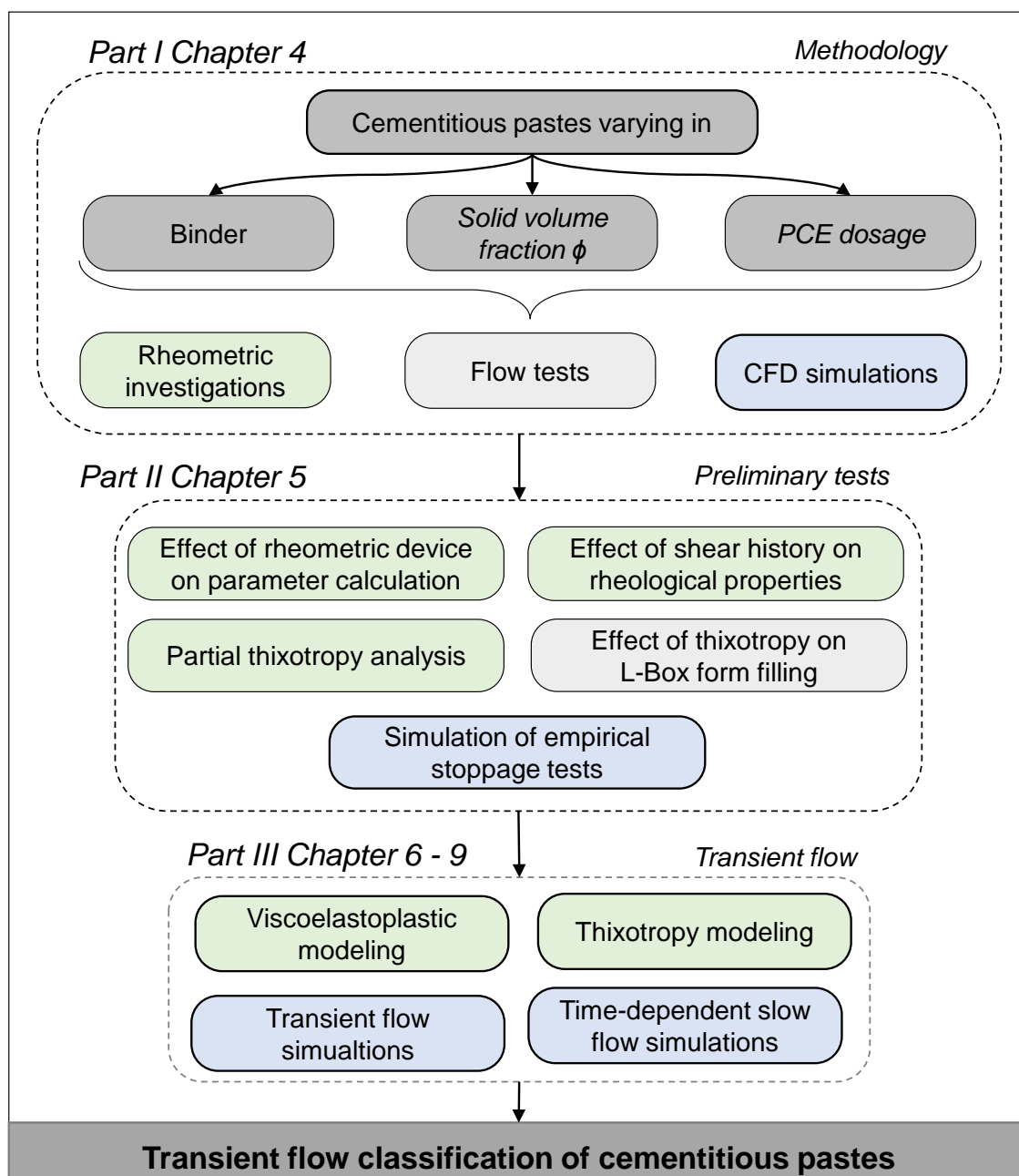


Figure 4.2: Research framework

## 4.2 Materials and methods

### 4.2.1 Physical and chemical properties of raw materials

Three reference binders were investigated: Two Ordinary Portland Cements (OPC) CEM I 42.5 R (following abbreviated as CEM I) and CEM II 42.5 N A-ll (following abbreviated as CEM II); and a Limestone Calcined Clay Cement (following abbreviated as LC3), which was

mixed as a compound of 51.9 % CEM I 42.5 R, 15.6 % limestone powder, 30 % calcined clay and 2.5 % anhydrite. The limestone powder, CEM I and anhydrate were industrially homogenized and mixed as *LC compound* with the calcined clay (CC). The LC3 was an adoption of a new binder system, see `https://lc3.ch/`. LC3 uses calcined clays as pozzolanic additive, see e.g. [Scrivener et al. (2018); Zunino et al. (2021)].

Chemical and physical properties of the binder systems and superplasticizers used in this thesis were analyzed within a research group funded by the German Research Foundation DFG[1]. Data for the CEM I are found in [Lu et al. (2019)]. CEM II was solely characterized within this research work. LC3 details are provided in [Pott et al. (2023)]. The chemical composition of the binder systems, analyzed through ICP-OES method, is collected in Table 4.1.

Table 4.1: Chemical composition of all binder systems

| Binder | CaO [%] | SiO$_2$ [%] | Al$_2$O$_3$ [%] | Fe$_2$o$_3$ [%] | MgO [%] | Na$_2$O [%] | K$_2$O [%] | TiO$_2$ [%] |
|---|---|---|---|---|---|---|---|---|
| CEM I | 62.90 | 19.63 | 5.23 | 2.60 | 1.54 | 0.24 | 0.80 | 3.32 |
| CEM II | 62.21 | 16.90 | 5.00 | 2.26 | 1.43 | 0.80 | 0.87 | 3.15 |
| LC3 | 42.53 | 28.12 | 9.43 | 3.47 | 1.43 | 0.18 | 1.31 | 0.43 |

Different polycarboxylatether-based superplasticizers (PCE, MBCC Group, Mannheim, Germany) were added, depending on the applied binder. For pastes containing CEM I and CEM II, an industrial superplasticizer, commonly used as PCE for ready-mix applications, was utilized (abbreviated as PCE-RM). Comprehensive details regarding the chemical structure and molecular properties can be found in [Lei et al. (2020)]. Main information are presented in Table 4.2. The anionic charge density was determined by [Lei et al. (2020)] using a 0.01 M aqueous NaOH solution at a pH of 12. PCE-RM is characterized by a relatively high anionic charge density and short side chains. For the LC3 pastes, a PCE with a higher retardation effect was used, here abbreviated as PCE-R. Data in brief are found in [Zhang et al. (2021)].

Table 4.2: Information on PCEs

| PCE | Solid content [$wt\%$] | Density [$kg/l$] | Anionic charge density [$\mu m/g$] | Ethylen oxide units [$-$] |
|---|---|---|---|---|
| PCE-RM | 22.6 | 1.06 | 1614 | 20 |
| PCE-R | 20.5 | 1.01 | 1754 | 65 |

Table 4.3 collects physical properties of the binders. The raw density of all binders was investigated using helium pycnometry. The specific surface area was investigated both with the Blaine measurement technique and BET measurements. The particle size distribution

---

[1]see also `https://www.spp2005.de/`

was analyzed through laser diffraction, and is illustrated in Figure 4.3. The diameter at 50% passing ($d_{50}$) is given in Table 4.3.

Table 4.3: Physical properties of all binder systems

| Binder | Specific density $\rho$ [g/cm$^3$] | Blaine SSA [cm$^2$/g] | BET SSA [m$^2$/g] | $d_{50}$ [$\mu$m] | wd$_{Puntke}$ [-] | $\Phi_{wd}$ [-] | $\Phi_{max}$ [-] | $\Phi_{max}$, PCE [-] |
|---|---|---|---|---|---|---|---|---|
| CEM I | 3.11 | 4300 | 1.24 | 13.80 | 0.27 | 0.54 | 0.65 | 0.67 |
| CEM II | 3.06 | 3830 | 1.16 | 13.18 | 0.26 | 0.56 | 0.64 | 0.66 |
| LC3 | 2.89 | 6528 | 2.65 | 9.99 | 0.25 | 0.58 | 0.67 | 0.67 |
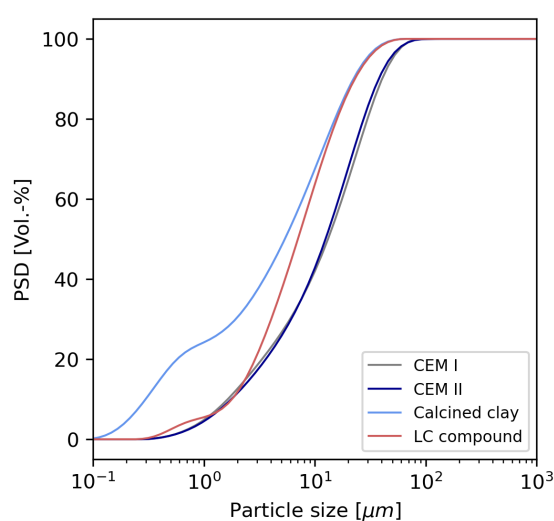


Figure 4.3: Particle size distribution of the raw binders

The water demand of raw binders was analyzed with the Puntke test [Puntke (2002)]. To measure the water demand, a small cup was filled with 100 g of granular material. Water was added through titration and the mixture was manually compacted until the grain surfaces became glossy. Through back-weighting, the water amount within the mixture was calculated and subsequently defined as the water demand $wd_{Puntke}$, and the corresponding packing density was calculated as $\Phi_{wd}$.

The maximum packing density $\Phi_{max}$ was investigated as described in [Lowke (2013), p. 70]. Suspensions with an initial water-to-cement ratio of 0.4 were prepared. 15 minutes after water addition, they were compacted in a pressure filter test with a defined fixed pressure. In several single tests, increasing pressure was applied with maximum pressure values of $\sigma = 2$, 5, 20 and 40 MPa. The compacted samples were dried in a vacuum oven at 105° C and 100 mbar until mass consistency. The air void content was estimated by back-weighting, and packing density $\Phi_{max}(\sigma)$ was calculated. $\Phi_{max}$ without the effect of compaction was then extrapolated from all tests with different maximum pressure values. Packing density measurements were conducted with and without superplasticizer. [Lowke (2013)] highlighted that the experimental $\Phi_{max}$ deviates from the theoretical $\Phi_{max}$ of the

raw binder, as early hydration products are already included in the experimental test. The experiments reveal that PCE leads to a higher $\Phi_{max}$.

## 4.2.2   Mix design of cementitious pastes
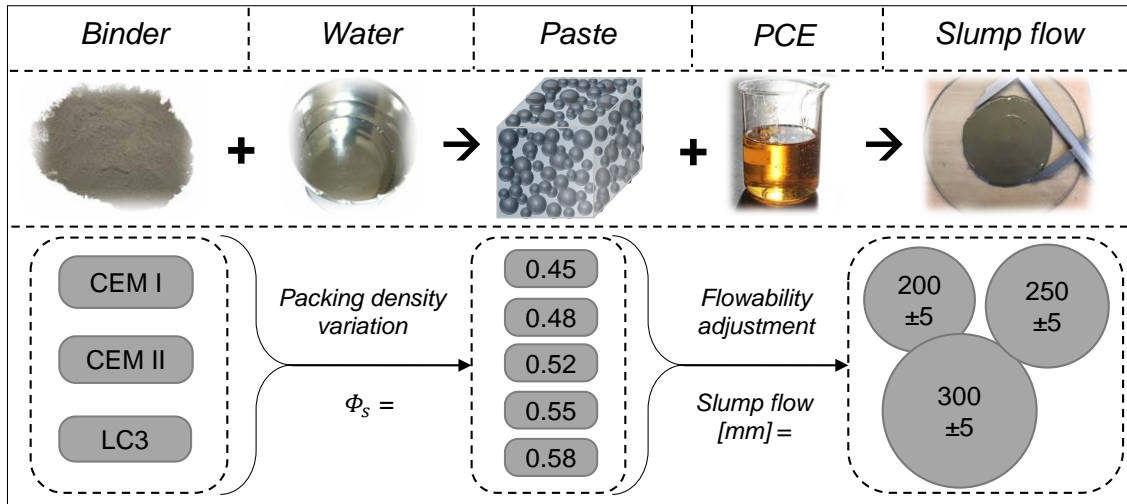


Figure 4.4: Mixture design of cementitious pastes: Variation of binders, solid volume fraction $\Phi_s$ and PCE to adjust the slump flow value towards defined slump diameters

As Figure 4.4 illustrates, cementitious pastes with all binders were prepared with increasing solid volume fraction $\Phi_s$ ranging from $\Phi_s = 0.45$ to $\Phi_s = 0.58$. For a macroscopic comparability of suspension rheology, pastes with the same solid volume fraction $\Phi_s$ were defined, irrespective of $\Phi_{max}$; and, thus, slightly changing relative solid volume fractions $\Phi_{rel} = \Phi_s/\Phi_{max}$. To explore the flowability for different workabilities, PCE was adjusted to three different workability ranges. For concrete, defined workability classes exist. For pastes, these are not available. Thus, given in Figure 4.4, three self-defined workability ranges were targeted: For each binder-$\Phi_s$ combination, slump flow diameters in a slump flow test with a Hägermann cone of SF = 200 ±5, 250 ±5, and 300 ±5 mm were targeted by adjusting the added PCE amount in per cent by weight of cement ($[\%bwoc]$). All mixture compositions are provided in Table 4.4. The last column specifies the required amount of superplasticizer.

For all test series prepared and subsequently analyzed, the slump flow value before the beginning of the experiment (either flow test or rheometry) was defined as crucial quality criterion. If the slump flow diameter deviated from the pre-defined workability class, the test was stopped and had to be started anew. In some cases, the PCE amount had to be adjusted slightly.

Table 4.4: Mixture compositions

| Binder | Test series | $\Phi_s$ [-] | w/c [-] | Binder [kg/m$^3$] | Water [kg/m$^3$] | $\rho_p$ [kg/m$^3$] | PCE [% bwoc] |
|---|---|---|---|---|---|---|---|
| CEM I | CEMI-0.45 | 0.45 | 0.40 | 1399.5 | 550 | 1950 | 0.00 - 0.24 - 0.31 |
| | CEMI-0.48 | 0.48 | 0.35 | 1492.8 | 520 | 2010 | 0.13 - 0.40 - 0.60 |
| | CEMI-0.52 | 0.52 | 0.30 | 1617.2 | 480 | 2100 | 0.66 - 0.85 - 1.29 |
| | CEMI-0.55 | 0.55 | 0.26 | 1710.5 | 450 | 2160 | 1.52 - 1.40 - 2.69 |
| | CEMI-0.58 | 0.58 | 0.23 | 1803.8 | 420 | 2220 | 1.61 - 2.05 - 2.99 |
| CEM II | CEMII-0.45 | 0.45 | 0.40 | 1381.5 | 550 | 1930 | 0.15 - 0.27 - 0.39 |
| | CEMII-0.48 | 0.48 | 0.35 | 1473.6 | 520 | 1990 | 0.17 - 0.44 - 0.57 |
| | CEMII-0.52 | 0.52 | 0.30 | 1596.4 | 480 | 2070 | 0.63 - 0.75 - 0.99 |
| | CEMII-0.55 | 0.55 | 0.26 | 1688.5 | 450 | 2130 | 0.94 - 1.19 - 1.48 |
| | CEMII-0.58 | 0.58 | 0.23 | 1780.6 | 420 | 2200 | 1.44 - 1.77 - 2.77 |
| LC3 | LC3-0.45 | 0.45 | 0.40 | 1295.1 | 550 | 1850 | 0.08 - 0.22 - 0.31 |
| | LC3-0.48 | 0.48 | 0.35 | 1381.4 | 520 | 1900 | 0.26 - 0.39 - 0.54 |
| | LC3-0.52 | 0.52 | 0.30 | 1496.6 | 480 | 1980 | 0.59 - 0.75 - 0.92 |
| | LC3-0.55 | 0.55 | 0.26 | 1582.9 | 450 | 2030 | 0.97 - 1.07 - 1.31 |
| | LC3-0.58 | 0.58 | 0.23 | 1669.2 | 420 | 2090 | 1.51 - 1.74 - 2.01 |

## 4.2.3 Mixing procedure

Cementitious pastes were prepared in mixture compositions as specified in Table 4.4. Deionized water was used for all tests. For each test, a paste of 0.5 l was mixed with a hand drilling machine with a four-bladed screw at a rotational speed of 1700 rpm. The general mixing procedure is shown in Figure 4.5.
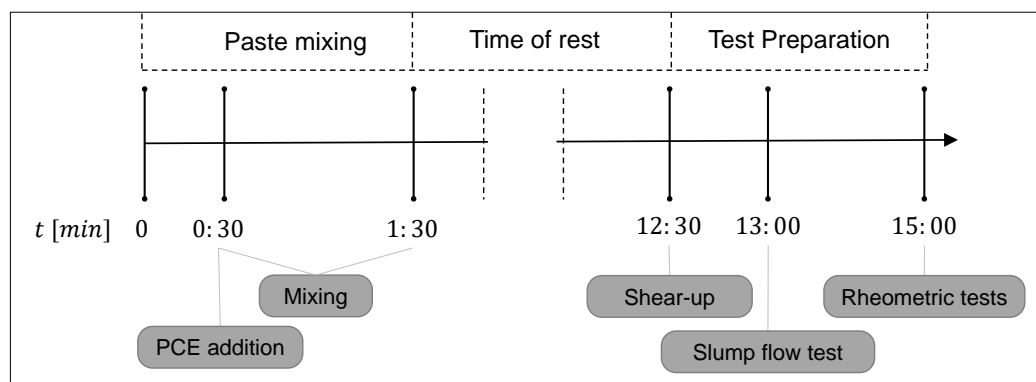


Figure 4.5: Mixing procedure

The binder temperature was controlled at laboratory air temperature of 20° C. The water temperature was adjusted in a kryostate to a temperature that the paste after mixing had a temperature of about 20° C, resulting in water temperatures between 10° C for lower packing densities and 3° C for the highest packing densities. Water and dry binder were mixed for 30 s. PCE was subsequently added and the paste mixed for a total mixing time

of 90 s. The time of PCE addition was chosen to stick to an early addition, but assured repeatability. For LC3 mixtures, this mixing procedure varied. Here, the PCE was added 90 s after water addition. The paste was left at rest until 12:30 min after water addition, and sheared up again for 30 s. The shearing procedure should break initially built hydrates in a controlled, repeatable way to assure homogeneous and repeatable paste flowabilities. Slump flow tests followed the short shearing. If the targeted slump flow diameter was measured, rheometric tests followed instantly, which was defined at a time of 15:00 min after water addition.

### 4.2.4   Rheometric procedures

All rheometric tests were conducted in a controlled laboratory environment with a rheometer by ANTON PAAR (Ostfildern-Scharnhausen, Germany, Series 502). Rotational and oscillatory rheometric tests were performed as introduced in Chapter 2.3, see an overiew of test methods in Figure 4.6. For all tests with parallel plates, a temperature-controlled hood (ANTON PAAR) was installed in the rheometer to prevent evaporation during the experiments. Vane-in-Cup tests were carried out with a cup-cover. Parallel plates had a diameter of 50 mm. The gap height was 1 mm. The plate surface was industrially serrated to prevent wall slip. Serration can affect the actual gap between the plates, which affects the raw data conversion (compare Chapter 2). This fact was neglected for the rheological analysis. Vane-in-Cup tests were conducted with a six-bladed vane.
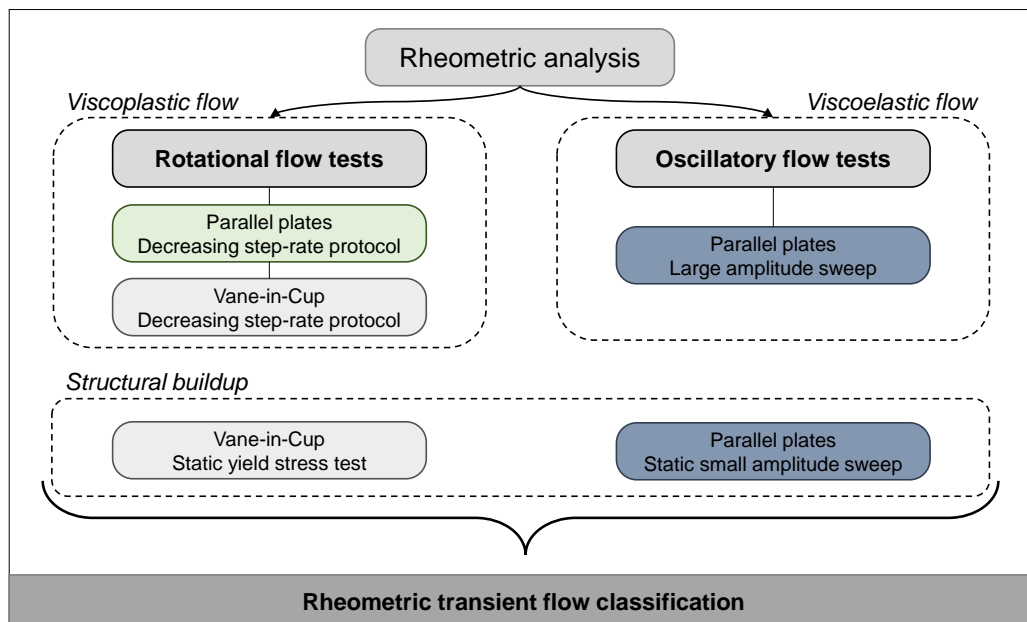


Figure 4.6: Rheological tests

Rotational dynamic flow tests were conducted to calculate viscoplastic properties. Tests were carried out in parallel plates and the Vane-in-Cup system. Oscillatory flow tests served

for the calculation of viscoelastic properties and were carried out with parallel plates. Structural buildup measurements were conducted in the Vane-in-Cup system with a rotational static yield stress setup, and in parallel plates with an oscillatory amplitude sweep setup. All protocols are shortly introduced. Raw data handling followed the theoretical basics introduced in Chapter 2.3. More detailed information about raw data handling and specific applied experimental and analysis methods are found in each corresponding publication.

**Dynamic rotational flow tests**

Dynamic flow of cementitious pastes was analyzed with rotational dynamic step-rate tests. Figure 4.7 (a) shows a parallel-plate test with decreasing $\dot{\gamma}$ in s$^{-1}$ as input parameter and the measured stress values $\tau$. Figure 4.7 (b) depicts the Vane-in-Cup test with defined rotational speed values $n$ in [rpm] with the measured torque value $T$. A constant pre-shear of $\dot{\gamma} = 40$ s$^{-1}$ or $n = 40$ rpm was defined to homogenize the sample. Following, $\dot{\gamma}$ or $n$ decreased stepwise from $\dot{\gamma} = 80$ s$^{-1}$ to $\dot{\gamma} = 0.02$ s$^{-1}$ ($n = 80$ rpm to $n = 0.02$ rpm ). In the parallel-plate tests, the shear stress $\tau$ was directly calculated from the torque $T$. In the Vane-in-Cup test, the torque was plotted.

$\dot{\gamma} - \tau$ flow curves, see Figure 4.8 (a), were calculated from the equilibrium value of each $\dot{\gamma}$-step , displayed in Figure 4.7 (a). $n - T$ curves, see Figure 4.8 (b) were calculated from the Vane-in-Cup measurements.



(a) Rheometric profile with parallel plates        (b) Rheometric profile with Vane-in-Cup
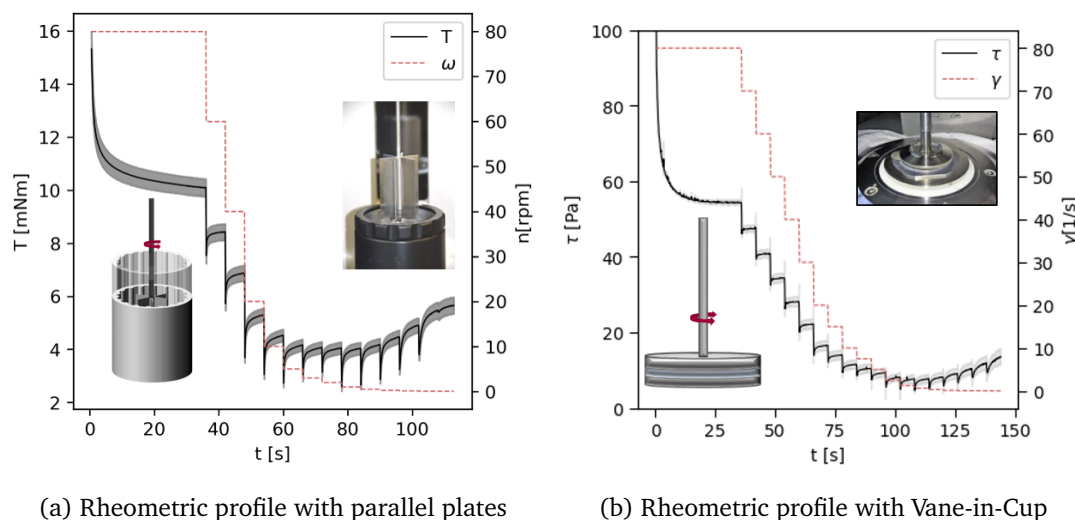
Figure 4.7: Viscoplastic analysis with dynamic stepwise decreasing shear rate profiles

Figure 4.8 displays the flow curves for the test series CEMI-0.52-250. Each rheometric test was conducted three times, and the average was calculated with standard deviations provided in gray shades. Figure 4.8 shows that below a certain shear rate $\dot{\gamma}$ or rotational speed $n$, the corresponding measured shear stress or torque increases. This phenomenon is referred to as structural increase, as the load of $\dot{\gamma}$ or $n$ is not sufficient to break the material's structure. The corresponding $\dot{\gamma}$ or $n$ was calculated as $\dot{\gamma}_{crit}$ or $n_{crit}$.

(a) $\dot{\gamma} - \tau$ flow curve
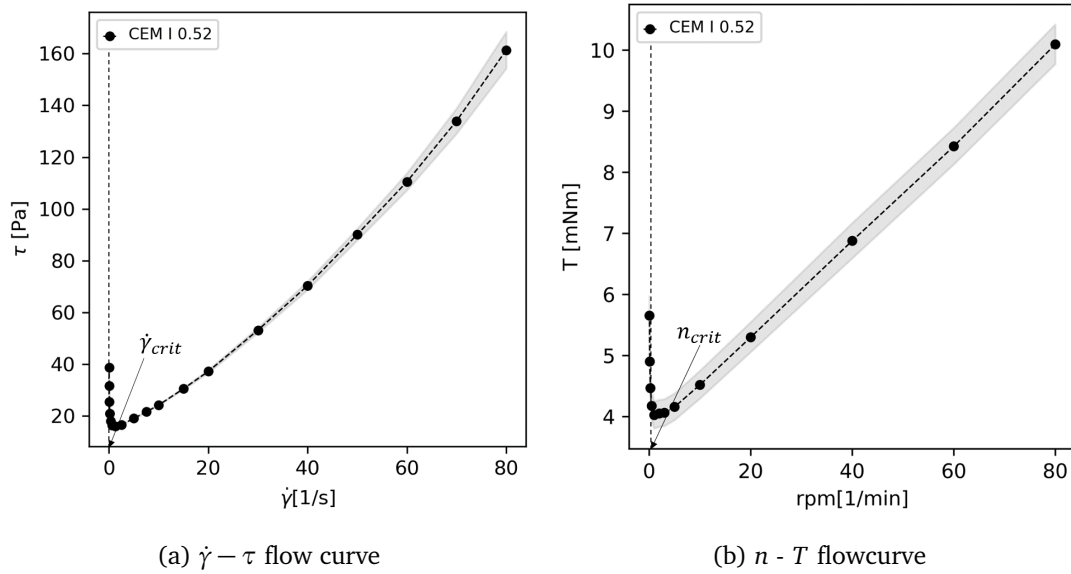
(b) $n$ - $T$ flowcurve

Figure 4.8: Calculated flow curves from rheometric raw data from parallel plates and Vane-in-Cup tests

Flow curves of all test series from the dynamic rheological analysis are available in A.1. All flow curves were analyzed in a phenomenological regression analysis using PYTHON. Regression fits of the models introduced in Chapter 3.4, namely the Bingham model, the Herschel-Bulkley model, the modified Bingham model, the Casson model and the Toussaint model (see Chapter 3.4, Eq. 3.10 to Eq. 3.14)) were applied to the experimental flow data. A minimal code example is made available, see information in B. The regression analysis was solely conducted for the range of shear rates $\dot{\gamma} > \dot{\gamma}_{crit}$. Figure 4.9 displays the results of the regression analysis for (a) the shear-thinning test series CEMI-0.45-250; and (b) the shear-thickening test series CEMI-0.55-250.



(a) Regressions for CEM I 0.45-250

(b) Regressions for CEM I 0.55-250
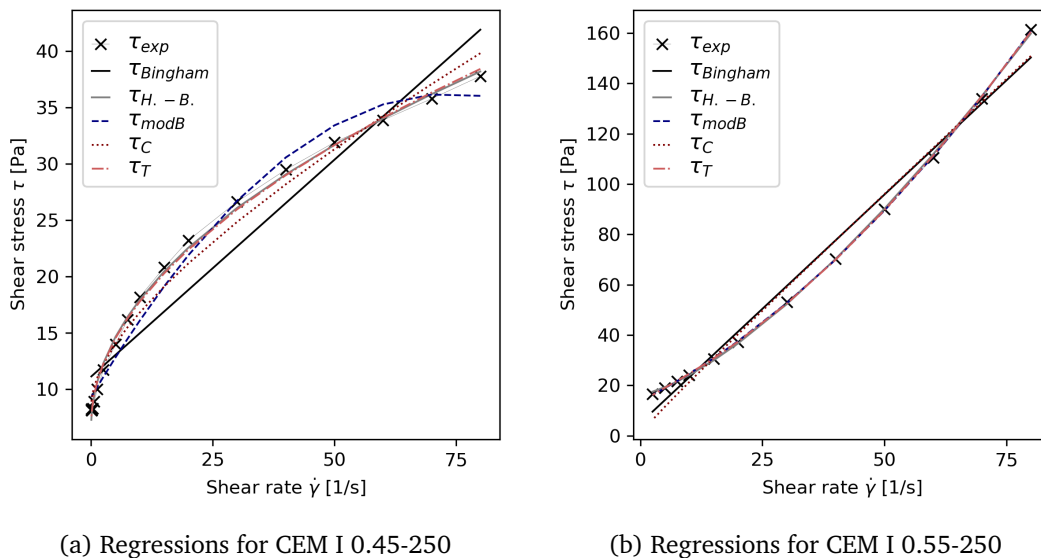
Figure 4.9: Phenomenological regression functions applied to experimental flow curves

The error, subsequently, was calculated as mean squared error (MSE). Figure 4.10 (a) assembles all calculated yield stress values $\tau_0$ of the test series CEMI-250, but depending on $\Phi_s$. The dotted line displays the analytical yield stress value $\tau_{0,slump}$ calculated from the measured slump diameter by applying Eq. 3.29. Figure 4.10 (b) displays the respective calculated error for all test series. All rheological parameters, calculated by fitting the different phenomenological models, are collected in A.1,
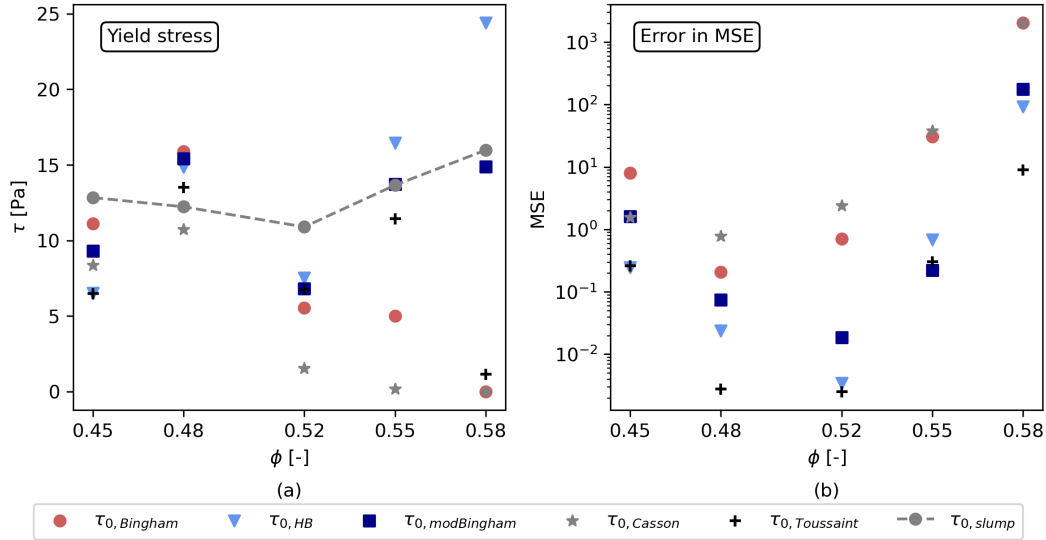


Figure 4.10: (a) Comparison of calculated yield stress values according to different phenomenological models and (b) overall error comparison of regression

### Large Amplitude Oscillatory Sweep tests: LAOS

LAOS tests were conducted to analyze viscoelastic properties. In a strain-controlled oscillatory experiment, $\gamma_0$ ranged from $\gamma_0 = 1 \cdot 10^{-3}\%$ to $\gamma = 1 \cdot 10^2\%$ at a constant frequency of $\omega = 10$ rad/s, and the resulting stress $\tau(t)$ was measured, see 4.11 (a). The rheometer software performs oscillatory cycles using a single input pair of $[\omega \, ; \, \gamma_0]$ until the material reaches a stable state, followed by oversampling of the raw data cycles [Ewoldt and McKinley (2017); Mezger (2016)]. Since cement paste is a constantly evolving material, the regulation of the rheometer software for steady-state was restricted to ten oscillatory cycles, followed by the rheometer-automated oversampling. Both inter-cyclic and intra-cyclic oscillatory techniques were applied to analyze viscoelastic properties. The first harmonics of each oscillatory cycle were directly calculated in the rheometer software, namely the storage modulus $G'$ and the loss modulus $G''$. The $\gamma - G'/G''$ - diagram in 4.11 (b) displays the deformation $\gamma$ on the x-axis and the resulting first order $G'$ and $G''$ on the y-axis, as introduced in Chapter 2. Subsequently, the evolution of the phase shift angle $\delta$, the storage modulus at the end of the LVE range, critical strain rate $\gamma_l$, the crossover point, and corresponding yield strain $\gamma_y$ were calculated using PYTHON protocols. The first harmonics $\gamma - G'/G''$ - diagrams and inter-cyclic parameter analysis of all test series are found in Appendix A.2. A minimal code example is made available, see information in B.

(a) Time-normalized measurement profile

(b) First harmonics in a $\gamma - G'/G''$ - diagram
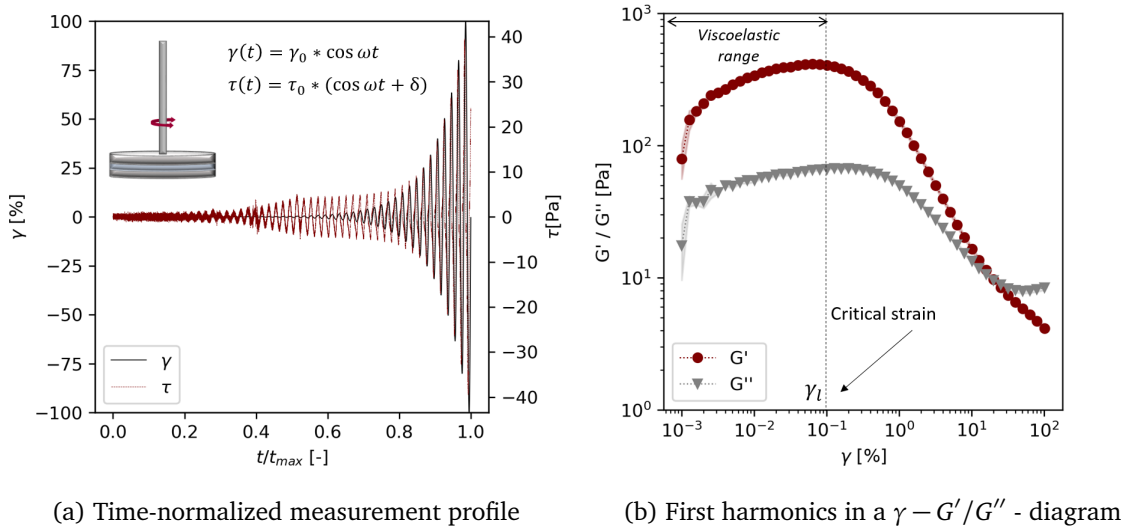
Figure 4.11: Oscillatory rheometric measurement

Intra-cyclic material analysis was conducted with the amplitude data sets of $[\gamma(t), \tau(t)]$. 4.12 (a) shows the time-resolved raw data, which were smoothed to analyze intra-cyclic viscoelastic properties, see 4.12 (b). Intra-cyclic viscoelastic parameters as introduced in Chapter 2 were evaluated with the software MITlaos, `https://web.mit.edu/nnf/research/phenomena/mit_laos.html`, see also [Ewoldt et al. (2007)].



(a) Raw data $[\gamma_0, \tau_0]$

(b) Exemplary smoothed LB curve
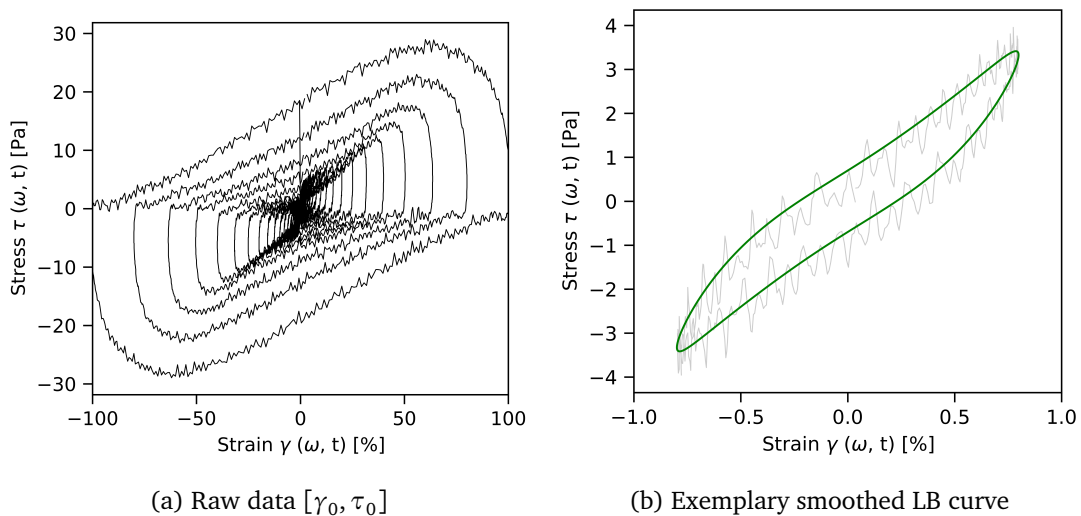
Figure 4.12: Intra-cyclic data evaluation on time-resolved $[\gamma(t), \tau(t)]$

The application of the software MITlaos to calculate Chebyshev polynomials and the further data handling is elaborated in Appendix C.

**Structural buildup measurements: SYS and SAOS**

Structural buildup of cementitious pastes was analyzed with static yield stress tests (SYS) in the Vane-in-Cup device and oscillatory sweep tests with strain amplitudes below the critical

strain (SAOS) in parallel plates. In the SYS test, the paste was left at rest for 30 s, followed by a short shear period of 6 s with $n = 0.115$ min$^{-1}$. The procedure was repeated five times, illustrated in Figure 4.13 (a). The time at rest doubled with every resting period, i.e. 60 s, 120 s, 240 s, and 480 s, leading to a measurement time of 960 s. Following the mathematical fundamentals introduced in Section 3.4, linear and nonlinear structural buildup models were applied to the experimental data, see Figure 4.13 (b).



(a) Raw data $n(t), T(t)$          (b) Regression functions applied to $\tau(t)$
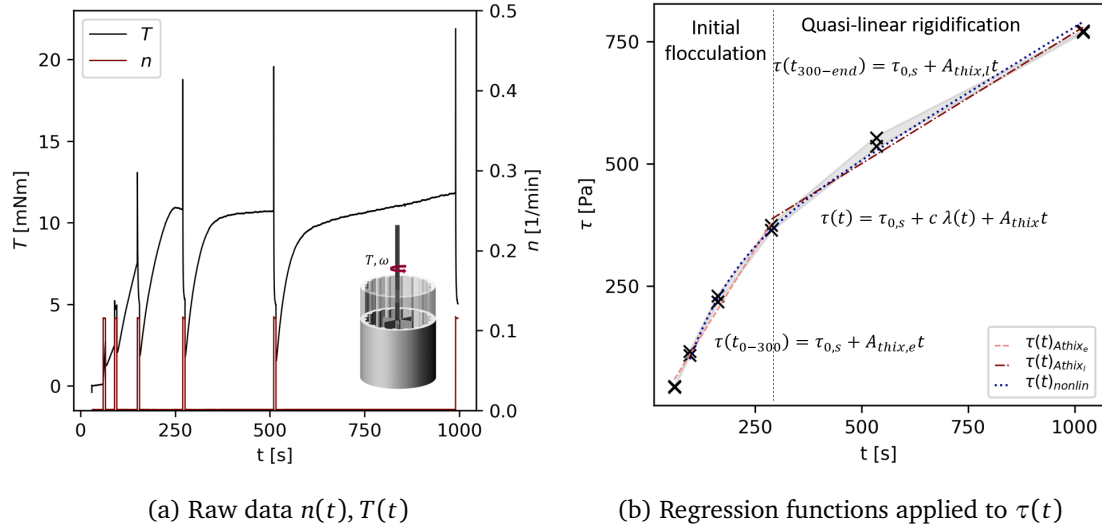
Figure 4.13: Structural buildup analysis with the rotational SYS test



(a) Raw data $\gamma(t), G'(t)/G''(t)$          (b) Calculated data $G'(t), G''(t)$ and $\delta$
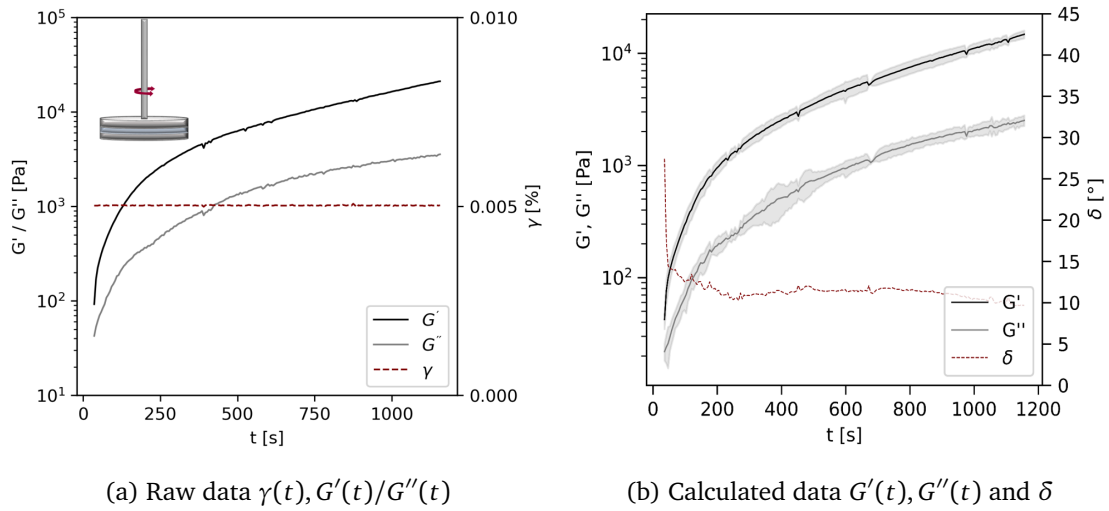
Figure 4.14: Non-destructive SAOS test

Figure 4.14 illustrates the structural buildup analysis with the non-destructive SAOS test at a constant strain $\gamma = 5 \cdot 10^{-3}$ %, and the corresponding measurement of $G'(t)$ and $G''(t)$. The measurement time was about 1000 s. Figure 4.14 (b) illustrates the average and standard deviation of $G'$ and $G''$ from three measurements, together with the evolution of the phase shift angle $\delta(t)$. Model approaches as introduced in Section 3.4, and further developed model techniques to analyze the structural buildup and the flocculation time,

were applied. Consequently, the linear and nonlinear structural buildup at rest with the corresponding parameters $A_{thix}$ ( $A_{thix,early}$, $A_{thixlate}$, $c_{Athix}$) and the nonlinear structural buildup during an oscillatory SAOS test with the parameters $G_{rig}$, $\Theta$, $c$ was analyzed. Raw data and calculated data of structural buildup of both the SYS test and the SAOS test are avalable in A.3 and A.4. Minimal code examples of the applied methods are made available, see information in B.

### 4.2.5 Flow tests

The mini slump flow test and the L-Box test were applied as flow tests to analyze workability, and to calculate rheological parameters from empirical correlation functions as introduced in Section 3.6. The mini slump flow test was conducted with the Hägermann cone as standardized in DIN EN 1015-3:2007-05 [DIN1015]. After placing the sample in the cone (see Figure 4.15 (a)), the cone was lifted. After flow stoppage, which occurred within several seconds, the diameter was measured at two perpendicular locations, and their average was calculated (see Figure 4.15 (b)).
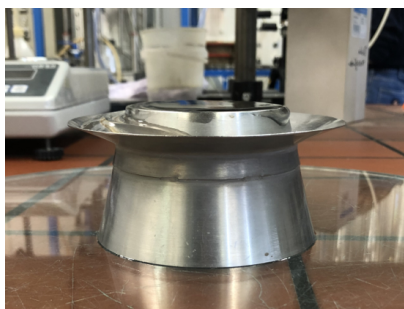


(a) Mini cone before lifting          (b) Measuring the slump flow diameter

Figure 4.15: Mini-Slump flow test

A small L-Box with a modified geometry was designed for a test volume of 0.5 l, illustrated in Figure 4.16: The horizontal section of the L-Box had an inner width of 50 mm and a length of 1200 mm with a clearance height of 50 mm. The vertical section exhibited an inner width of 50 mm, an inner depth of 45 mm with a total height of 540 mm. Both sections were separated with a gate. Plexiglas was used as material to build the L-Box to minimize wall effects while paste flow. The L-Box was filled at closed gate, which was subsequently lifted slowly to minimize inertia effects. The flow procedure was filmed. The final flow length and height at the beginning and end of the flow body were measured. The flow time could, depending on the test series, vary between several seconds and minutes until flow had stopped.

(a) Empty mini L-Box                                (b) Mini L-Box during a flow test
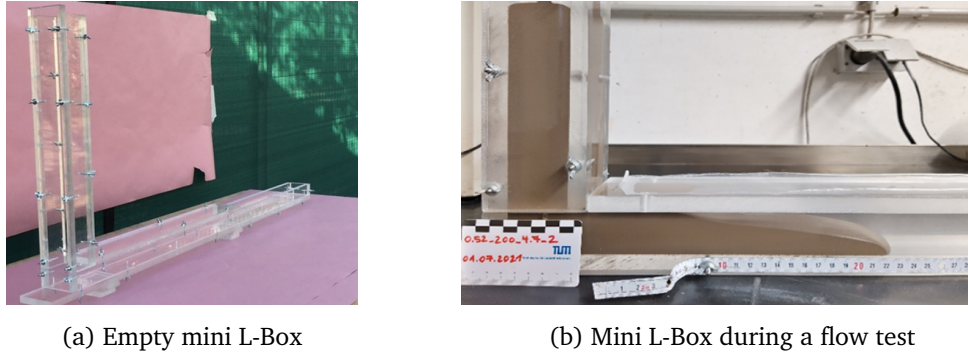
Figure 4.16: L-Box test with a modified L-Box geometry

## 4.2.6   Numerical simulations with OpenFOAM

Numerical simulations were conducted with the software OpenFOAM (Open-source Field Operation And Manipulation, `https://openfoam.org`), which is an open-source software that comes with a package of functions and algorithms to solve the Navier-Stokes equations as introduced in Chapter 2.4. The software uses the programming language C++. In this thesis, the OpenFOAM version 7 with release date from $8^{th}$ July from 2019 was used. OpenFOAM uses the Finite Volume Method (FVM) to solve the transport equations. The Volume-of-Fluid method (VOF) is a numerical technique to compute the free-surface flow of cementitious pastes, which was applied to simulate the mini slump flow test and the mini L-Box test. In VOF calculations, the Navier-Stokes transport equations, introduced in Chapter 2, are extended by a weighting quantity $\alpha$, see Eq. 4.1:

$$\frac{\partial \alpha}{\partial t} + \nabla \cdot (\alpha \mathbf{u}) = 0 \tag{4.1}$$

The momentum equation is extended by the contribution from surface tension effects between the two phases air and paste, displayed by the term $f_\sigma$ in Eq. 4.2 [Brackbill et al. (1992)]:

$$\frac{\partial \rho \mathbf{u}}{\partial t} + \nabla \cdot (\rho \mathbf{u}\mathbf{u}) = -\nabla p + \nabla \cdot \tau + \rho g + f_\sigma \tag{4.2}$$

The fluid density $\rho$ is calculated from the contributions of the two phases $\rho_1$ and $\rho_2$ depending on $\alpha$:

$$\rho = \alpha \rho_1 + (1-\alpha)\rho_2 \tag{4.3}$$

## Numerical setup and modeling strategy

As elaborated in Chapter 2.4, numerical modeling requires pre-processing of the geometry and all boundary conditions, the simulation itself and post-processing of the data. The numerical procedure followed in this thesis is schematically illustrated in Figure 4.17. All steps require different software packages, which are specified in light grey boxes.
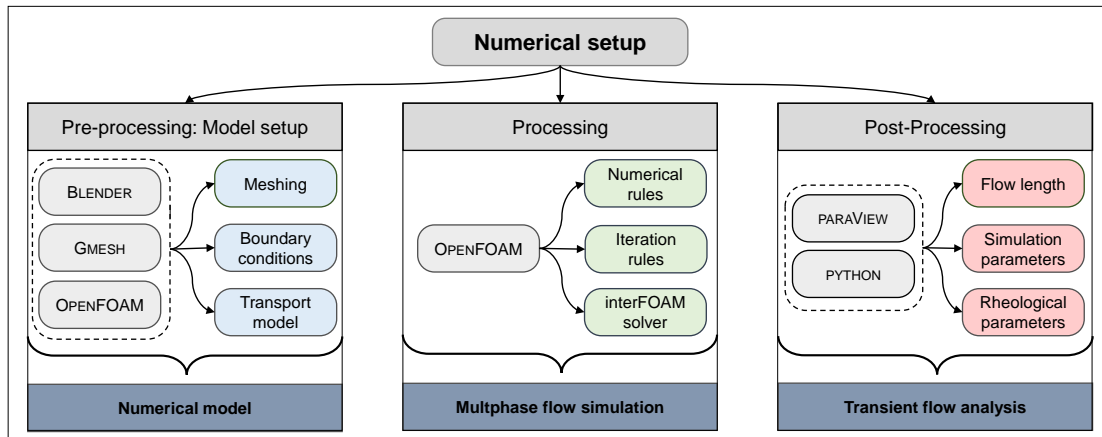


Figure 4.17: Numerical procedure to pre-process, process and post-process simulations in this thesis

## Pre-processing: Implemented geometries, boundary conditions and transport models

The implementation of the L-Box and cone geometry comprised of different approaches. The L-Box was defined in OpenFOAM's *blockmesh* dictionary. The dimensions and defined blocks are illustrated in Figure 4.18.
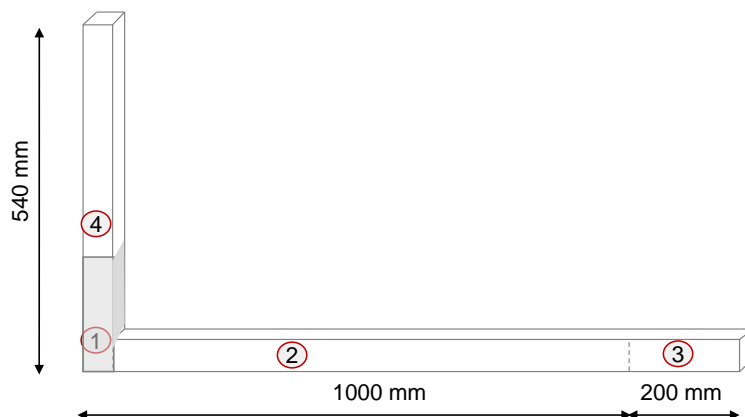


Figure 4.18: Geometrical and box definitions of the L-Box

The first block is the region where the suspension is defined before lifting the gate. The second box is the horizontal section until 1 m length, which is the area where the horizontal section has a top cover. The third box was defined without a top cover. The fourth section was the remaining vertical part of the L-Box.
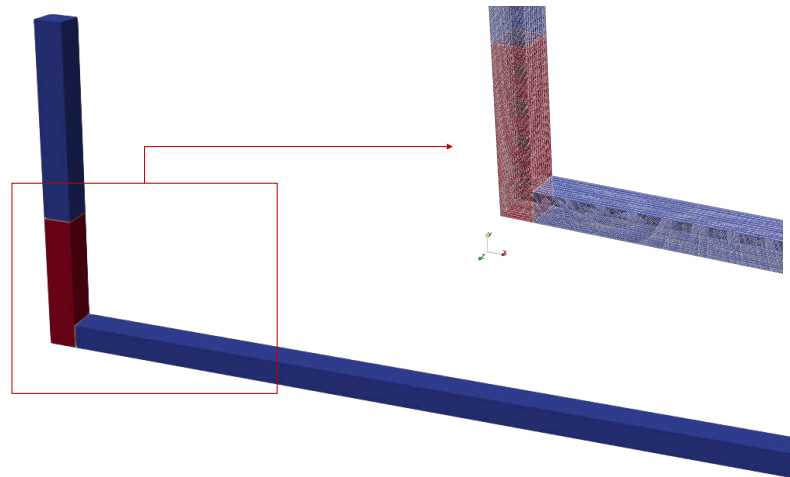
Figure 4.19: Geometrical setup of the L-Box model

Figure 4.19 illustrates a visualization of the L-Box with the post-processing software PAR-
AVIEW (`https://www.paraview.org/`) prior to the flow test. The suspension is shown
in red, the blue parts represent the air. The fine mesh is visible in the magnification.

The cone geometry was defined in the open-source software BLENDER `https://www.`
`blender.org/`. BLENDER generates an .stl file, which can be implemented into the Open-
FOAM structure. The cone from the .stl file was placed in a pre-generated *blockmesh* box,
illustrated in Figure 4.20: Figure 4.20 (a) shows the cone generation in BLENDER. Figure
4.20 (b) shows the visualization with PARAVIEW.
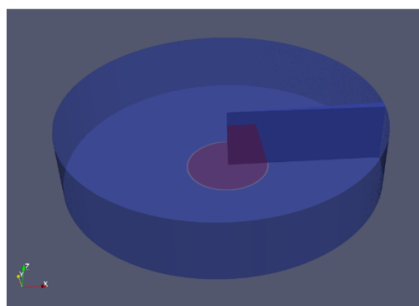


(a) Geometrical model in BLENDER               (b) Model with Slices in PARAVIEW
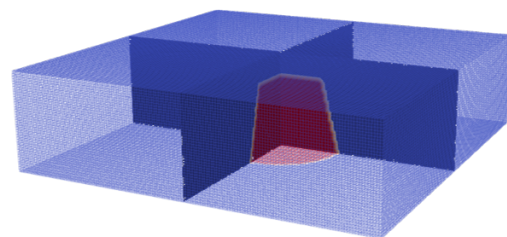
Figure 4.20: Geometrical setup of the cone model

Finally, solely a slice of the cone was set up as whole geometry, to take advantage of the
cone symmetry and reduce computational costs. OpenFOAM provides a *wedge* condition,
which enables the definition of a two-dimensional slice from axi-symmetrical geometries.
The general idea is illustrated in Figure 4.21:
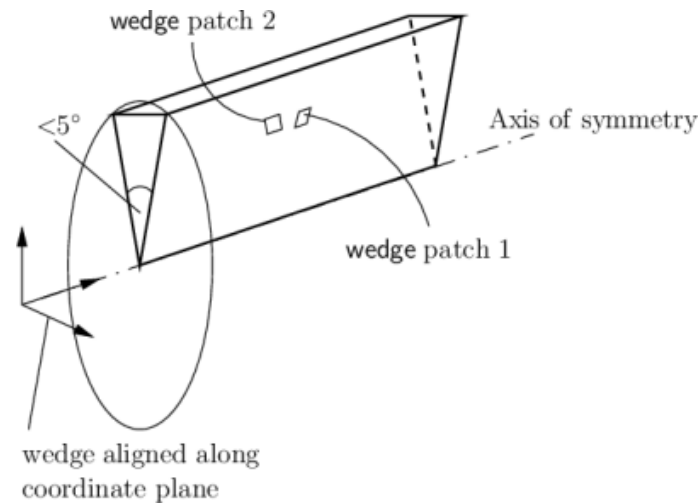
Figure 4.21: Definition of slices with a *wedge* condition in OpenFOAM [OpenFOAM (2017)]

The slice geometry was defined in the open-source mesh generator GMESH `https://gmsh.info/`. GMESH creates a .geo extension file. Figure 4.22 (a) illustrates the slice geometry from GMESH. Figure 4.22 (b) depicts the visualization in PARAVIEW; with a magnification view in Figure 4.22 (c).



(a)   (b)   (c)
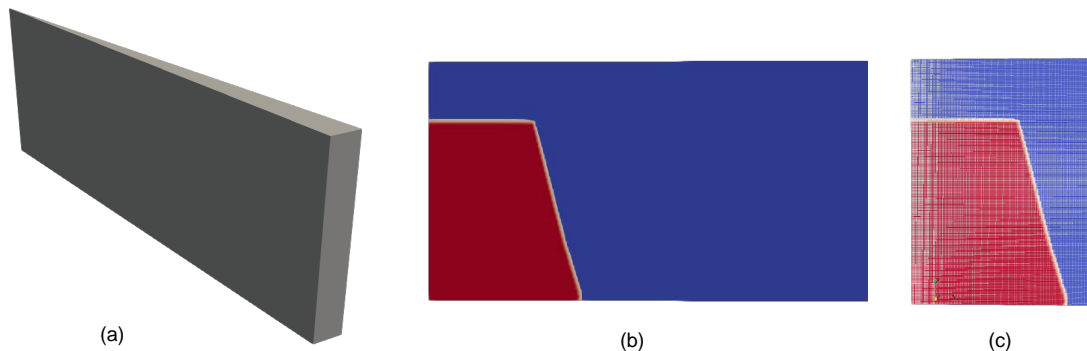
Figure 4.22: Geometrical setup of the slice model

For all geometries, initial and boundary conditions at the faces needed to be declared. As both test methods are general free-surface flow procedures, no external pressure besides gravity was employed. User-dependent artifacts from both test procedures (lifting the gate in an L-Box test and lifting the cone for slump flow measurements) were not considered. In all geometries, a distinction was made between fixed walls and free surfaces (in OpenFOAM, declared as atmosphere). Table 4.5 collects the boundary conditions introduced in Chapter 2.4 for the variables $U$, $p$, $\alpha$ and $S$, which was employed as additional structural buildup derivative, developed for OpenFOAM by [de Schryver, Robin (2022)].

The boundary velocity at fixed walls was defined as Dirichlet condition to be 0, and no additional pressure besides gravity at atmospheric phases was defined. All remaining boundary conditions were defined as Neumann condition, which defines the gradient towards a face.

Table 4.5: Boundary conditions in OpenFOAM

| Boundary face | Field | Type | Conditions | Value |
|---|---|---|---|---|
| Fixed walls | **u** | Dirichlet | noSlip | $\mathbf{u} = 0$ |
| | $p$ | Neumann | *fixedFluxPressure* | $\nabla p = 0$ |
| | $\alpha$ | Neumann | *zeroGradient* | $\nabla \alpha = 0$ |
| | $S$ | Neumann | *zeroGradient* | $\nabla S = 0$ |
| Atmosphere | **u** | Neumann | *pressureInletOutletVelocity* | $\nabla \mathbf{u} = 0$ |
| | $p$ | Dirichlet | totalPressure | $p = 0$ |
| | $\alpha$ | Neumann | *inletOutlet* | $\nabla \alpha = 0$ |
| | $S$ | Neumann | *zeroGradient* | $\nabla S = 0$ |

As Table 4.5 shows, all Neumann conditions were defined to be zero. The implementation of more complicated boundary conditions was beyond the scope of this thesis.

**Processing**

The numerical solution schemes are collected in Table 4.6.

Table 4.6: Numerical solution schemes in OpenFOAM

| Setting | Field | Discretization Scheme |
|---|---|---|
| ddtScheme | default | Euler |
| gradSchemes | default | Gauss linear |
| divSchemes | default | Gauss linear |
| | div(phi, U) | Gauss linear |
| | div(phi, $\alpha$) | Gauss linear |
| | div(phi, S) | Gauss upwind |
| laplacianSchemes | default | Gauss linear |
| interpolationSchemes | default | linear |

While in preliminary research, the effect of numerical schemes on the numerical error was investigated, stable schemes for all simulations finally were chosen. A further analysis was beyond the scope of this thesis.

The OpenFOAM implemented *interFoam* solver was chosen for the solution of the discretized Navier-Stokes equations. The *interFoam* solver utilizes the PIMPLE algorithm to couple the discretized equations for pressure and velocity, which is a combination of the SIMPLE algorithm for steady-state calculation and *PISO* algorithm for transient flow solving, see detailed algorithm explanations in [OpenFOAM (2018)]. The PIMPLE algorithm offers the advantages of capturing transient flow behavior while offering a stable solution for dealing with complex flow conditions and geometries. Convergence control and computational costs are determined by the definition of convergence criteria and the specification

of the iterative loops. The solver settings are collected in Table 4.7. The *smoothed Gauss-Seidel method* was determined as numerical solver. The *smoothed Gauss-Seidel method* is a method where the solution of a quantity is updated iteratively by sweeping through the grid points of a geometric mesh; and updating each point based on the current values of its neighboring points. The "smoothed" version, or Smoothed Gauss-Seidel, introduces a relaxation factor to control the rate at which the solution is updated. A smaller relaxation factor tends to improve stability but may slow down convergence, while a larger relaxation factor can speed up convergence but may lead to instability. The PIMPLE algorithm was chosen with a total number of three inner correctors.

Table 4.7: Solver settings in OpenFOAM

| Setting | $U$ | $p$ | $\alpha$ | $S$ |
|---|---|---|---|---|
| Solver | smoothSolver | PCGr | smoothSolver | smoothSolver |
| Smoother | symGaussSeidel | symGaussSeidel | symGaussSeidel | symGaussSeidel |
| Tolerance | $1e^{-7}$ | $1e^{-7}$ | $1e^{-8}$ | $1e^{-7}$ |
| relative tolerance | 0 | 0.005 | 0.005 | 0.005 |
| Relaxation factor | 1 | 0.95 | 0.95 | 0.95 |

**Post-Processing: Data extraction**

The three-dimensional flow bodies after flow stoppage of the Cone geometry and the L-Box geometry are exemplified in Figure 4.23. Here, only the last time step of the simulated flow time is illustrated.
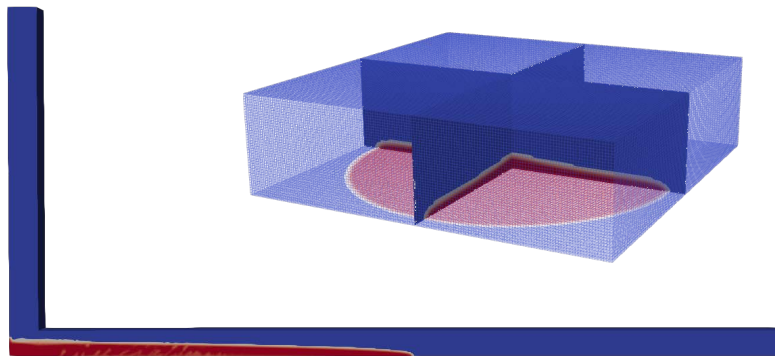


Figure 4.23: Three-dimensional flow length visualization in PARAVIEW

Transient processes and the time-dependent evolution of all parameters specified in Table 4.8 were analyzed by a time-resolved data extraction from OpenFOAM and PARAVIEW, and further analysis in PYTHON. For each simulated time step, text files were generated with all calculated field and scalar values for each cell. The parameters of interest and the final calculation result are collected in Table 4.8.

Table 4.8: Post-Processing parameters

| PARAVIEW analysis | | | PYTHON analysis | | |
|---|---|---|---|---|---|
| Field / Value | Unit | Post-Processing Method | Field operation | Unit | Result |
| $\alpha$ | [-] | 1D Flow extraction | $\alpha \cdot \rho$ | $[\text{kg/m}^3]$ | flow evolution and final flow length |
| $\mathbf{u}$ | [m/s] | 2D Matrix data | $\mathbf{u} \cdot \alpha \cdot \rho$ | $[\text{kg/(m}^2\text{s)}]$ | Flow rate |
| $\dot{\gamma}$ | [1/s] | 2D Matrix data | $\dot{\gamma} \cdot \alpha$ | [1/s] | Shear rate distribution |
| $\nu$ | $[\text{m}^2/s]$ | 2D Matrix data | $\nu \cdot \alpha \cdot \rho$ | [Pas] | Viscosity distribution |
| $S$ | [-] | 2D Matrix data | $S \cdot \rho$ | [-] | Structural parameter distribution |
| $Re$ | [-] | 2D Matrix data | $Re \cdot \alpha$ | [-] | Characteristic flow number |
| $Co$ | [-] | 2D Matrix data | $Co \cdot \alpha$ | [-] | Numerical flow number |
| residuals | $[-]$ | 2D Matrix data | Visualization | [-] | Convergence |

A minimum post-processing set-up was followed for all simulations. First, the finished simulation was imported into the post-processing software PARAVIEW. The three-dimensional flow was visualized, and one-dimensional data in x-direction at $y = 0$ (1D Flow extraction through the PARAVIEW utility *plotoverline*) and two-dimensional data for one geometrical slice in x-y direction (2D Matrix data through the PARAVIEW utility *Slice*) were extracted as .csv files. The data were finally processed in PYTHON. 1D flow data and 2D rheological properties are exemplary visualized in Figure 4.24.



(a) Flow over time in a slump flow test

(b) 2D visualization of $\dot{\gamma}$ in the L-Box
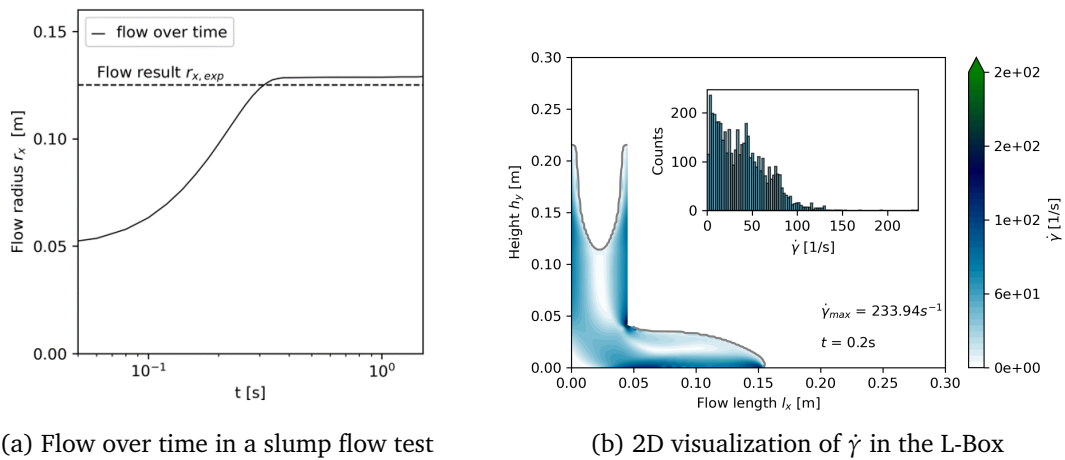
Figure 4.24: Exemplary post-processing visualization of flow data from slump and L-Box simulations

# Part II

# Summary of publications related to preliminary investigations

# 5. What affects the analysis of rheological parameters?

## 5.1 Comparative small and large gap rheometry for non-Newtonian cementitious pastes

*This section summarizes published studies of the author of this thesis:*

[Pre1] **Thiedeitz, M.**; Kränkel, T. (2024) *Comparative Small and Large Gap Rheometry for Cementitious Pastes. Preprints*, 2024020703, doi.org/10.20944/preprints202402.0703.v1

**Author's contribution**: *The first author conceptualized and conducted the rheological modeling, analysis and conclusions. Maik Hobusch and Rundi Zhang provided laboratory support for experimental investigations. Thomas Kränkel reviewed and edited the article.*

### 5.1.1 Motivation and scope

Different rheometric devices yield variations in the measured or calculated rheological parameters, see Chapter 2.3. Large-gap rheometers, such as the Couette or Vane-in-Cup devices, offer the advantage of measuring materials with large particle diameters. However, the shear field is heterogeneous, and a direct calculation of rheological parameters is unattainable. Conversion formulations provide approximations for the calculation of the yield stress $\tau_0$ and viscosity $\mu$ outgoing from rheometric raw data torque $T$ and rotational speed $\omega$. [Nguyen and Boger (1985); Wallevik et al. (2015); Haist et al. (2020)] calculated flow data of cementitious pastes from large gap rheometry and compared them to results obtained from small gap geometries, such as parallel plates. [Haist et al. (2020)] found that the Reiner-Riwlin equation, see Eq. 2.28, calculates viscosities of Newtonian fluids well. However, because the Reiner-Riwlin equation derives $\tau_0$ and $\mu$ based on the linear Newtonian or Bingham model, the Reiner-Riwlin equation introduces errors for cementitious suspensions deviating from Bingham flow behavior. Furthermore, once the flow behavior deviates from linear viscoplastic flow, the choice of rotational velocity values ($\omega$), used as input data for the Reiner-Riwlin equation, significantly affects the results.

Therefore, cementitious pastes with increasingly non-Newtonian flow properties were tested in a rotational Vane-in-Cup (ViC) test. The rheological parameters $\tau_0$ and $\mu$ were calculated

using the Reiner-Riwlin equation, but varying input data for the conversion formulation $[\omega_{min}; \omega_{max}]$. The aim was not only to test the variation of calculated rheological parameters but also to compare the results to absolute parallel plate (PP) measurements, and yield stress values calculated through Eq. 3.29 from a slump flow diameter.

### 5.1.2   Experimental investigations and findings

Pastes from an Ordinary Portland Cement (OPC) CEM I 42.5 R and a Limestone Calcined Clay Cement (LC3) were prepared with three solid contents $\Phi_s = 0.45, \Phi_s = 0.52$ and $\Phi_s = 0.55$. The macroscopic flowability was adjusted to a slump flow value of $250 \pm 5$ mm. An analytical yield stress $\tau_{0,A,R}$ from each slump flow value was calculated by application of Eq. 3.29. Rheometric dynamic PP tests and ViC tests were conducted with a step-rate down profile as introduced in Chapter 4. $\tau - \dot{\gamma}$ - flow curves were directly obtained from PP raw data, and the Bingham model and Herschel-Bulkley model were applied to calculate corresponding yield stress values $\tau_{0,B}$ and $\tau_{0,H-B}$. ViC raw data were first converted from $T$ in [mNm] to $T$ in [Nm], and $n$ in [rpm] to $\omega$ in $\left[\frac{rad}{s}\right]$. Subsequently the Reiner-Riwlin equation (see Eq. 2.28) was applied to calculate $\tau_0$ and $\mu$. Different input ranges of raw data $[\omega_{min}; \omega_{max}]$, both varying in the range size and the section of input data $[\omega_{min}; \omega_{max}]$ (subsequently labeled $\omega$ *steps for RR iteration*), were applied.

The procedure is exemplary illustrated in Figure 5.1 for OPC-0.52 with a section size of four $\omega$ *steps for RR iteration*. With a section size of four, five ranges of $[\omega_{min}; \omega_{max}]$ are obtained from the raw data. Figure 5.1 (a) displays the whole range of $\omega$, Figure 5.1 (b) displays the low velocity values. For each fitted $[T; \omega]$ series, the maximum $\omega, \tau_0$ and $\mu$ are labeled.
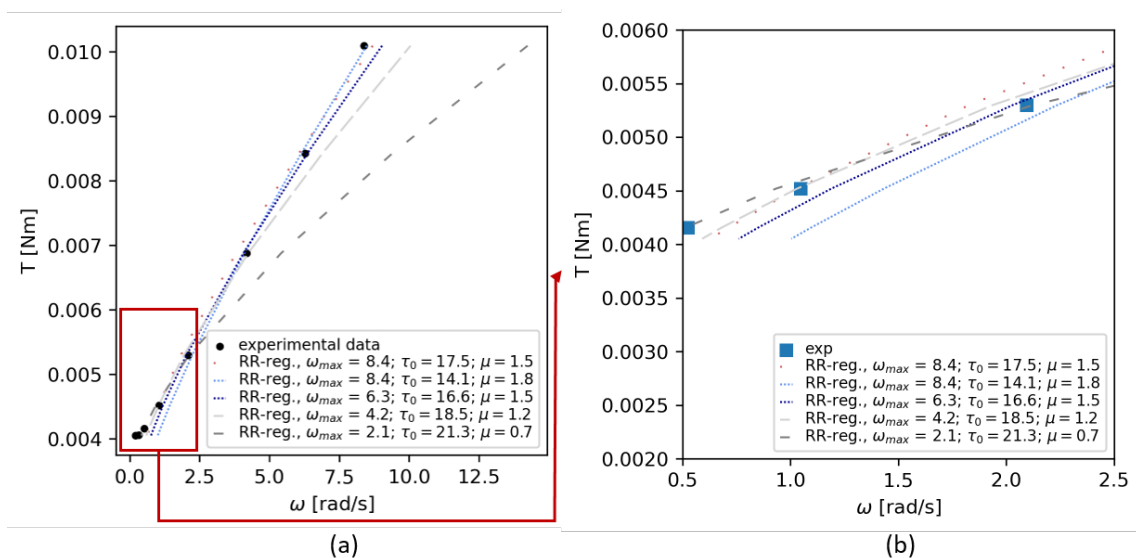


Figure 5.1: Calculation of $T - \omega$ flow curves with different ranges of $\omega$, [Thiedeitz and Kränkel (2024b)]

Fits that satisfy the experimental data at high velocity values, do not fit them at low velocity (see Figure 5.1 (b) ), and vice versa. The illustrated calculation was performed for each of the six test series, for all possible input variations of $\omega$.

Figure 5.2 displays the differently calculated yield stress values. With increasing $\Phi_s$, Bingham yield stress results $\tau_{0,B}$ show increasing deviations. The grey scaled boxes illustrate the variation of $\tau_{0,B,ViC}$ depending on the parameter range $[T; \omega]$ used for the Reiner-Riwlin calculation of $\tau_0$ and $\mu$. Detailed analytical data and error plots can be obtained in the referring publication.
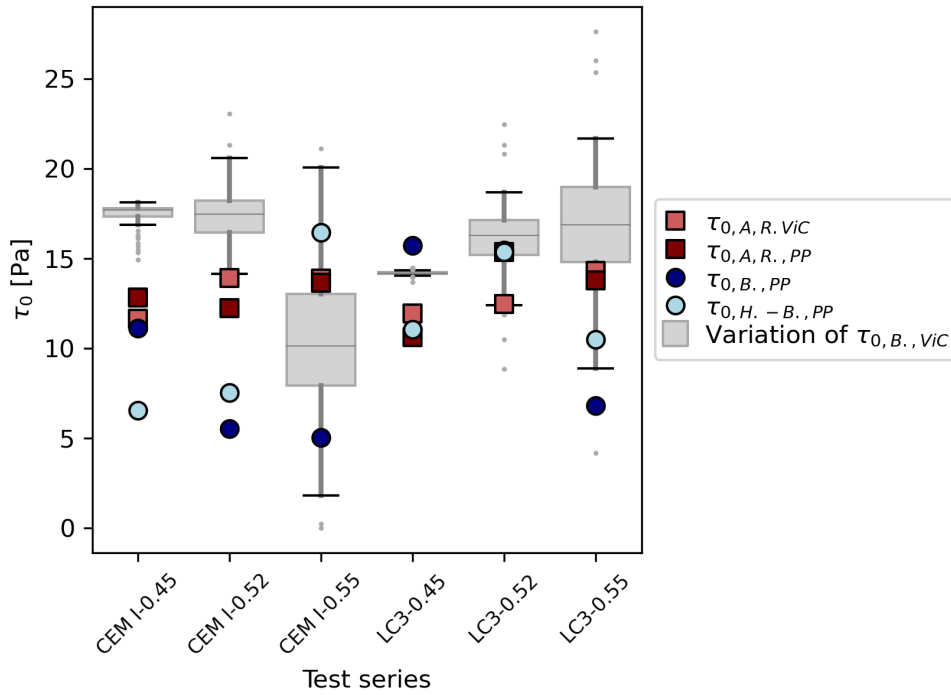


Figure 5.2: Comparison of all $\tau_0$ values gained from ViC data with different Reiner-Riwlin approximations, PP tests with different regression functions and analytical yield stress from slump flow measurements, [Thiedeitz and Kränkel (2024b)]

The results reveal the strong dependency of the calculated yield stress on the chosen rheometric device, regression method and input data for the Reiner-Riwlin equation. With increasing $\Phi_s$, calculated $\tau_0$ values vary up to 100 % (for CEMI-0.55). Variations are larger for the CEMI test series than for the LC3 test series. The ViC system offers numerous advantages for the analysis of rheological parameters. Its large gap allows the measurement of pastes containing particles up to 4 mm, enabling the analysis of materials like mortar. The system's large vane minimizes the impact of paste inhomogeneities, such as segregation effects, making it particularly suitable for measurements over time. However, the rheological analysis of strongly non-Newtonian cementitious pastes evaluated in large gap rheometry should introduce extended raw data conversion formulations, which consider the nonlinear material behavior. Data analysis of $\tau$ and $\mu$ in large gap rheometries is only beneficial if rheological information at one certain velocity range are required.

## 5.2 Effect of Pre-Shear on Agglomeration and Rheological Parameters of Cement Paste

*This section summarizes published studies of the author of this thesis:*

[Pre2] **Thiedeitz, M.**; Dressler, I.; Kränkel, T.; Gehlen, C.; Lowke, D. (2020). *Effect of Pre-Shear on Agglomeration and Rheological Parameters of Cement Paste*. *Materials*, Vol. 13, No.9, p. 2173, doi.org/10.3390/ma13092173 .
Licence: https://creativecommons.org/licenses/by/4.0/

**Author's contribution**: *Mareike Thiedeitz and Inka Mai (born Dressler) shared conceptualization and original writing. The author of this thesis conceptualized and conducted all parts of rheological experimental investigations, rheological modeling, analysis and conclusions. Thomas Kränkel, Dirk Lowke and Christoph Gehlen reviewed and edited the article.*

### 5.2.1 Motivation

Cementitious suspensions flocculate during rest due to attractive interparticle forces, and desagglomerate when shear is induced. The mixing procedure determines the state of flocculation and, thus, affects the rheological properties. The effect of mixing history, initial shear, shearing time and energy of the applied shear on rheological properties of cementitious suspensions was investigated e.g. by [Castillo et al. (2012)]. [Ferron et al. (2013)] investigated the aggregation and breakage kinetics of fresh cement paste depending on different shearing conditions and shear history. [Han and Ferron (2016)] found a significant effect of the mixing method on rheological properties. [Mazanec et al. (2010)] and [Han and Ferron (2015)] investigated the use of high mixing intensities on densely packed suspensions to optimize rheological properties.

Subsequently, the effect of the mixing time on rheological properties of the cementitious pastes in this study was evaluated.

### 5.2.2 Experimental investigations and findings

Pastes from an Ordinary Portland Cement CEM I 42.5 R were prepared with three solid volume fractions $\Phi_s = 0.45, \Phi_s = 0.48$ and $\Phi_s = 0.52$. The macroscopic flowability was adjusted to a slump flow value of $250 \pm 5$ mm. The test series CEMI-0.45 was prepared with and without the addition of PCE. After the mixing procedure, cement paste was left at rest and sheared up again at t = 8 min, 11.5 min or 12.5 min after water addition, respectively. Consequently, the pre-shear before conducting dynamic rotational PP tests was varied from 30 s to 90 s and 300 s. The mini slump flow was measured, followed by the PP test 15 min after water addition. Additionally, the agglomerate mean diameter was

measured in-situ using a Focused Beam Reflectance Measurement Probe (FBRM). With the FBRM technique, a particle or agglomerate diameter is approximated from the scattering time when light is scattered back from a particle that was hit by the light of a rotating laser beam [Heath et al. (2002); Krauss et al. (2018)]. FBRM tests were conducted at the Technical University of Brunswick. The results are available in [Thiedeitz et al. (2020a)]. Here, solely the rheological parameters depending on the pre-shear time are summarized. Rheological parameters yield stress $\tau_{0,B}$ and viscosity $\mu$ were calculated using the Bingham model, to be able to compare linear plastic viscosity values $\mu$. Results are presented in Figure 5.3.
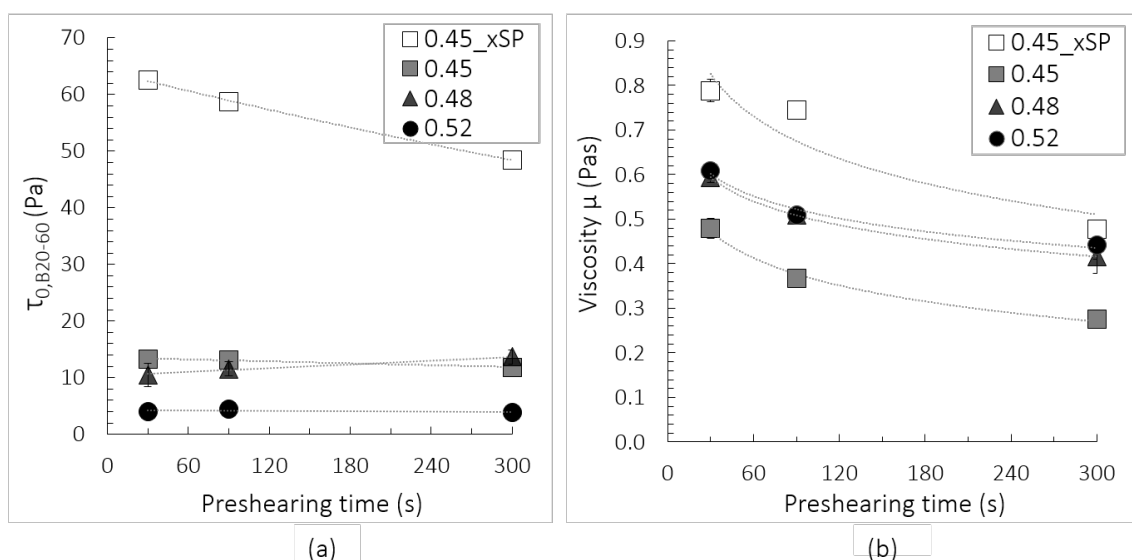


Figure 5.3: Effect of preshearing time on (a) $\tau_{0,B}$ and (b) $\mu$ for all test series, Thiedeitz et al. (2020a)

Figure 5.3 shows the decrease of rheological parameters when the pre-shear time was increased from 30 s to 300 s. The test series without PCE was most affected by the increase of pre-shear: Both the values for $\tau_{0,B}$ and $\mu$ decreased significantly. While the effect or pre-shear on the Bingham yield stress $\tau_{0,B}$ was less for pastes with PCE, the plastic viscosity $\mu$ showed decreased values of about up to 30 %, approaching an infinity viscosity $\mu_{\infty}$ at infinite pre-shear time.

Theoretically, the most de-flocculated state depicts an optimum reference of the particle network to correlate the rheology of cementitious suspensions with their microstructural properties [Roussel (2012); Ma et al. (2018)]. However, an increase of pre-shear time introduces additional mixing energy, and thus, heat, into the cementitious paste, which affects its chemical reactions.

Summarized, the pre-shear time affects the suspenion's rheology. The rheology is not only a function of the granulometry of the raw binder system, but significantly depends on the mixing history. A compromise needs to be defined between deflocculation and additionally applied energy. A direct comparison between rheological experimental test results, once the laboratory preparation is not similar, yields errors.

# 5.3 Thixotropic Structural Build-Up of Cement Pastes at Low Shear Rates

*This section summarizes published studies of the author of this thesis:*

[Pre3] **Thiedeitz, M.**; Kränkel, T.; Bauer, B.; Gehlen, C. (2019). *Thixotropic Structural Build-Up of Cement Pastes at Low Shear Rates.* In: Ivankovic, A. et al. (Ed.): *International Conference on Sustainable Materials : Challenges in Design and Management of Structures : RILEM Publications*, Vol. 4, p. 272–279 E-ISBN: 978-2-35158-218-3

**Author's contribution** *Thomas Kränkel conceptualized the research framework, Bianca Bauer conducted the rheological tests. Result analysis and interpretation, writing and illustration were done by the author of this thesis.*

## 5.3.1 Motivation

Thixotropy investigations for cementitious building materials are, most often, correlated to the measurement of static yield stress increase at material rest, also referred to as thixotropy parameter $A_{thix}$ (see Chapter 3.4). However, thixotropy during flow depends on the applied shear rate $\dot{\gamma}$, as introduced in Chapter 2. The calculation of partial structural buildup becomes crucial to implement thixotropy into the calculation of flow processes rather than buildup at rest. Therefore, the evolution of a partial $A_{thix}$ depending on low shear rates was investigated as initial incentive to understand shear rate dependent thixotropy.

## 5.3.2 Experimental investigations and findings

Investigations on partial $A_{thix}$ were conducted on two cementitious test series using OPC CEM I with w/c ratios of 0.3 and 0.4 (corresponding to solid volume fractions of $\Phi_s = 0.45$ and $\Phi_s = 0.52$). The evolution of static yield stress for the cementitious paste was measured as introduced in Chapter 4. For the calculation of $A_{thix}$, only the linear increase from 120 s to 360 s was taken into account. The "applied shear rate during rest" was increased for eight test series from $\dot{\gamma} = 0s^{-1}$ to $\dot{\gamma} = 0.055s^{-1}$. Thixotropy at rest was defined as 100% $A_{thix}$. Figure 5.4 displays the results of calculated $A_{thix}$ values for different low shear rates $\dot{\gamma}$ at rest.

Figure 5.4 demonstrates that already at slight increase of $\dot{\gamma}$, thixotropy decreases rapidly, approaching an equilibrium value with increasing $\dot{\gamma}$. Due to the hydrating nature of cementitious pastes it can be assumed that the equilibrium value of $A_{thix}$ is connected to a continuous structural build-up due to early nucleation hydration. $A_{thix}$ values for the cementitious paste with higher solid volume fraction are higher, with $A_{thix} = 1.5$ Pa/s at rest for the test series CEMI-0.52 (w/c = 0.3) being nearly four times higher than for CEMI-0.45
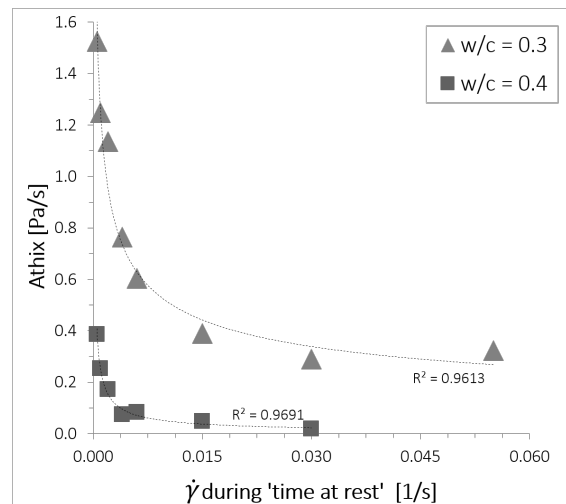
Figure 5.4: $A_{thix}$ in dependence on $\dot{\gamma}$ during rest, [Thiedeitz et al. (2019)]

(w/c = 0.4) with $A_{thix} = 0.4$ Pa/s. However, the general relation between $A_{thix}$ decrease and increasing $\dot{\gamma}$ is similar for the different test series.

The results reveal the strong dependency of $A_{thix}$ on applied shear rates, as partial structural breakdown accommodates the ongoing structural increase. However, it is essential to note that these results, while informative, do not suffice as input for the development of a shear- and time-dependent structural buildup calculation for $\lambda$ similar to Eq. 2.14. To address this limitation, a more in-depth partial structural buildup analysis and a time- and shear-dependent formulation is required.

# 5.4 L-Box Form Filling of Thixotropic Cementitious Paste and Mortar

*This section summarizes published studies of the author of this thesis:*

**Author's contribution** *Mareike Thiedeitz and Thomas Kränkel conceptualized the research framework. L-Box tests and rheological tests were conducted by her and her co-author Nasime Habib, with the support of Janusch Engelhardt and Maik Hobusch. Result analysis and interpretation, writing and illustration were done by the author of this thesis.*

## 5.4.1 Motivation and scope

Flow tests provide a fast, site-applicable test method to analyze rheological parameters. Analytical equations for the slump flow, introduced in Eq. 3.29, and for the L-Box test, introduced in Eq. 3.30, provide a correlation between flow test results and rheological parameters. For materials with Bingham or Herschel-Bulkley flow behavior, the approach of correlating stoppage test results with rheological parameters was validated by various researchers, see Chapter 3.6. However, their applicability becomes questionable when testing materials with increasingly nonlinear flow behavior and thixotropic properties.

As observed in earlier analyses, an increase in the solid volume fraction $\Phi_s$ can result in structural buildup at low shear rates $\dot{\gamma}$. This yields the question of how much these thixotropic effects affect L-Box tests. Unlike slump flow tests, L-Box tests last over an extended time period at decreasing flow velocities. Thus, the effect of thixotropy, calculated through linear structural buildup $A_{thix}$ in a rheometric SYS test, on the L-Box flow was analyzed.

## 5.4.2 Experimental investigations and findings

Tests were performed with cementitious pastes of the test series CEMI-0.45 and CEMI-0.52. PCE was added until mini slump flow values of $200 \pm 5, 225 \pm 5, 250 \pm 5, 275 \pm 5$ and $300 \pm 5$ mm were reached. L-Box tests were conducted on a mini-L-Box with geometric dimensions as introduced in Chapter 4. Rheological PP tests with a dynamic rotational profile and the Bingham regression for the analysis of $\tau_{0,B}$ and $\mu$, and static SYS tests in the ViC geometry for the analysis of $A_{thix}$ were conducted. From the mini-L-Box test, the final flow length, overall flow time and velocity over time of all test series were measured. Wall effects and inertia were neglected for the calculation and application of Eq. 3.30. Following correlations were investigated:

- Effect of slump flow value on the calculated dynamic yield stress $\tau_0$

- Correlation between calculated dynamic yield stress $\tau_0$ and final L-Box flow length

- Correlation between final flow length and thixotropy $A_{thix}$

- Correlation between time of flow, thixotropy and final flow length

Detailed data and illustrations on all results are found in [Thiedeitz et al. (2020b)]. Without displaying all results here, solely the correlation between final flow length and thixotropy $A_{thix}$ is shortly summarized, illustrated in Figure 5.5.
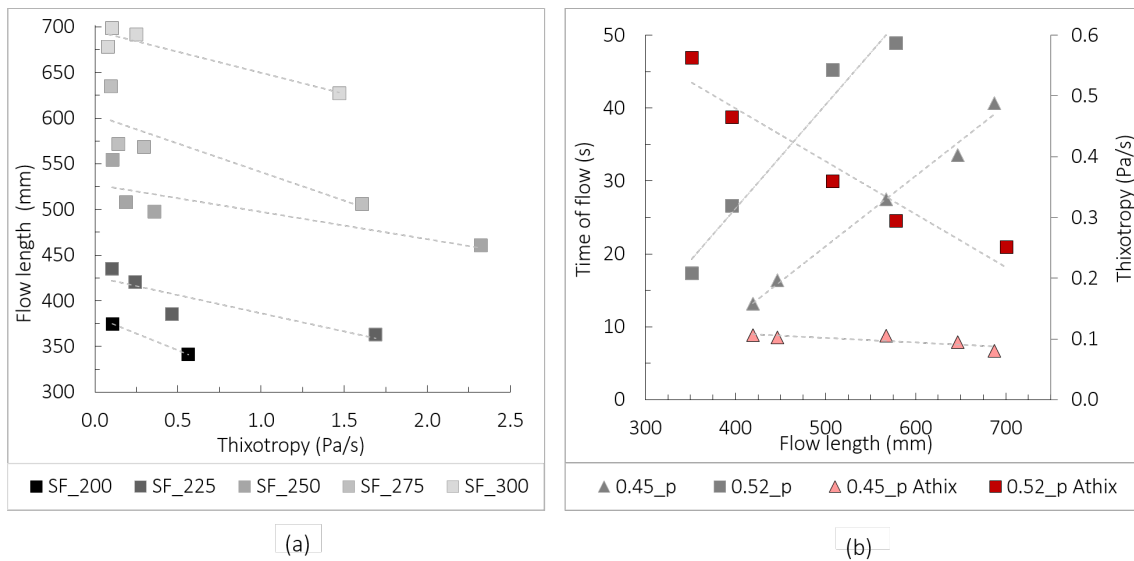


Figure 5.5: Effect of thixotropy values on effective flow length in an L-Box, [Thiedeitz et al. (2020b)]

Figure 5.5 (a) depicts the correlation of L-Box flow length and thixotropy in dependence on the macroscopic flowability data from slump flow. Irrespective of the investigated paste or mortar, data show that with increasing measured thixotropy $A_{thix}$, the flow length value decreases. This is valid for all adjusted slump flow values.

The result clarifies the effect of time-dependency in flow tests once the material exhibits thixotropy: Slump flow tests are short-range tests. Thus, thixotropic effects do not affect the flow. This is different for L-Box tests: Here, the flow process takes longer, and slow velocities enable flow-affecting thixotropic structural buildup (which, again, affects the material viscosity and thus flow velocity).

Figure 5.5 (b) allows a more detailed look on the interdependence of thixotropy, time of flow and final flow length. The test series $\Phi = 0.45_p$ has a low thixotropy of $A_{thix} = 0.1$ Pa/s. With increasing final flow length, time of flow nearly increases linearly, and structural changes do not seem to have an effect on the flow properties. Contrary, the test series $\Phi = 0.52_p$ exhibits ranging thixotropy; with higher thixotropy values ranging from $A_{thix} = 0.22 - 0.60$ Pa/s. Pastes with less flow length exhibit significantly higher thixotropy. The

flow time is higher: This is associated to increasing viscosities due to structural buildup at slow flow, and consequently, decreased velocities.

Summarized, the experimental framework revealed a clear effect of thixotropy on time-dependent flow tests, as the L-Box flow decreases with increasing thixotropy. The research findings, however, lack a clear allocation of time-and shear-rate dependent thixotropy to viscosity increase and velocity decrease, as the flow is a constantly transient process. For a better understanding of these processes, numerical simulation can aid to visualize flow fields and local and transient properties.

## 5.5   Computational modeling of non-Newtonian viscoplastic cementitious pastes

*This section summarizes published studies of the author of this thesis:*

[Pre5]   **Thiedeitz, M.**; Timothy, J.; Kränkel, T. (2022). *Computational modeling and characterization of non-Newtonian visco-plastic cementitious building materials.. 8th European Congress on Computational Methods in Applied Sciences and Engineering, CIMNE,* doi:10.23967/eccomas.2022.06 9
Licence: https://creativecommons.org/licenses/by/4.0/

**Author's contribution** *The author of this thesis conceptualized the research framework. She conducted the rheological tests, with the support of the laboratory stuff members, and numerical simulations. Result analysis, writing and illustration were done by her. Jithender Timothy and Thomas Kränkel reviewed and edited the article.*

### 5.5.1   Motivation and scope

CFD has demonstrated its efficacy for cement and concrete flow tests in empirical stoppage tests [Gram (May 2009); Vasilić (2016); Roussel et al. (2016)] and processing simulations [Wallevik (2009); Secrieru (2018); Fataei (2021); de Schryver, Robin (2022)]. Yet, the impact of increasingly non-Newtonian behavior, as well as the thixotropic contribution, in time-dependent numerical flow simulations needs to be investigated. Since a clear time-resolved structural parameter has not been implemented so far, and the linear thixotropy parameter $A_{thix}$ lacks physical significance for transient flow formulations, first CFD analysis of empirical stoppage tests solely investigated cementitious pastes as viscoplastic material with increasingly non-Newtonian flow properties.

### 5.5.2   Experimental investigations and findings

Cement pastes with CEM I as binder, solid volume fractions $\Phi_s = 0.45, 0.48, 0.52, 0.55$ and 0.58 and a macroscopic flowability of 250 mm ±5 slump flow diameter were investigated. All pastes were rheologically analyzed with dynamic parallel plate rheometry and the Herschel-Bulkley phenomenological regression. For the implementation of the Herschel-Bulkley model into CFD, the bi-viscous regularization model by [O'Donovan and Tanner (1984)] with $\eta_0 = 1000\eta$ was chosen to prevent singularity at $\dot{\gamma} = 0$:

$$\eta = \min \begin{cases} \eta_0 \\ \dfrac{\tau_0}{\dot{\gamma} + k\dot{\gamma}^{n-1}} \end{cases} \tag{5.1}$$

The flow evolution and final flow length values were analyzed using experimental and numerical flow tests. The computational mesh for both test geometries is displayed in Figure 5.6.
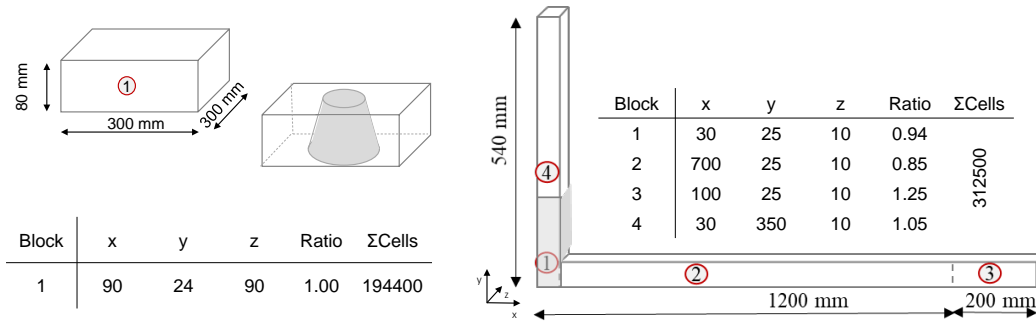


Figure 5.6: Geometric mesh dimensions, [Thiedeitz et al. (5th - 9th Jun 2022)]

While the detailed computational framework and results are found in [Thiedeitz et al. (5th - 9th Jun 2022)], Figure 5.7 displays the comparison of the final flow results of (a) laboratory experiments and (b) the simulated test cases.



(a) Experimental flow test results          (b) Simulated flow test results
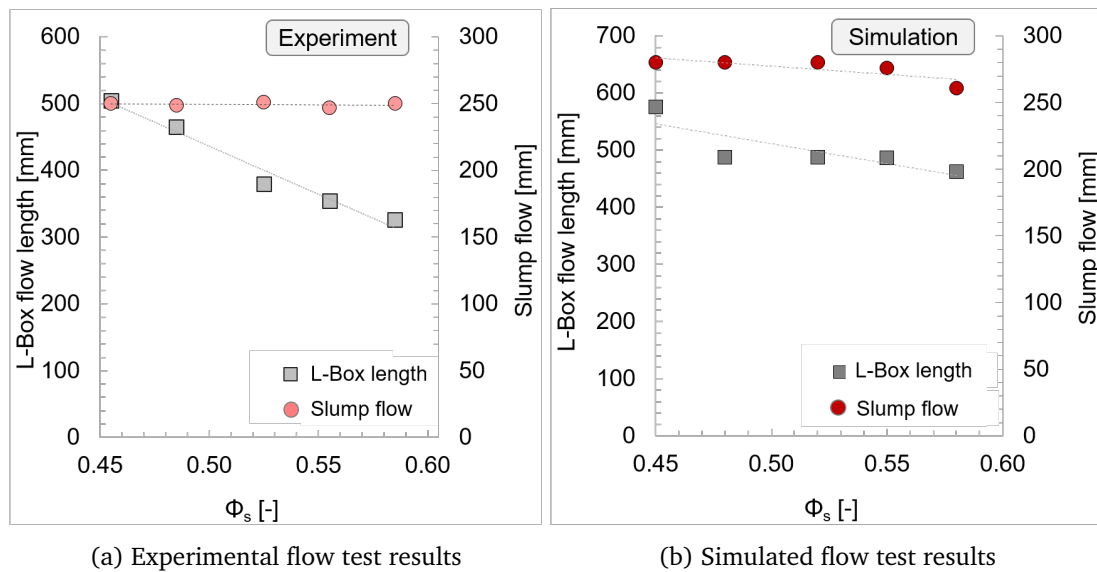
Figure 5.7: Experimental and numerical flow test results, modified from [Thiedeitz et al. (5th - 9th Jun 2022)]

Figure 5.7 (a) demonstrates the divergence in flow behavior between the slump flow and the L-Box flow. While the slump flow diameters remain constant around $d = 250 \pm 5mm$ with increasing $\Phi_s$ (originating from the targeted PCE addition), the L-Box flow length decreases for the same mixtures with increasing $\Phi_s$. However, Figure 5.7 (b) shows that the simulations do not reproduce the experimentally observed flow. A comparison between L-Box experiments and simulations indicates that the numerical L-Box flow length only marginally

decreases with increasing $\Phi_s$. These findings underscore that the Herschel-Bulkley model does not capture thixotropy that affects the experimental L-Box flow. While thixotropy does not affect the slump flow and, subsequently, numerical simulation results do not diverge, the accuracy for L-Box simulations decreases and the flow loss is not computed.

Figure 5.8 visualizes the shear rate distribution at t= 2 *s* for CEMI-0.48-250 and CEMI-0.58-250 in PARAVIEW. The cementitious pastes possess a large range of low $\dot{\gamma}$-values over the flow field, which in real life flow affects the rheological properties. CEMI-0.58-250 possesses lower shear rates at the same time step. The time- and shear rate- dependent material changes, however, are not depicted by the viscoplastic Herschel-Bulkley model.
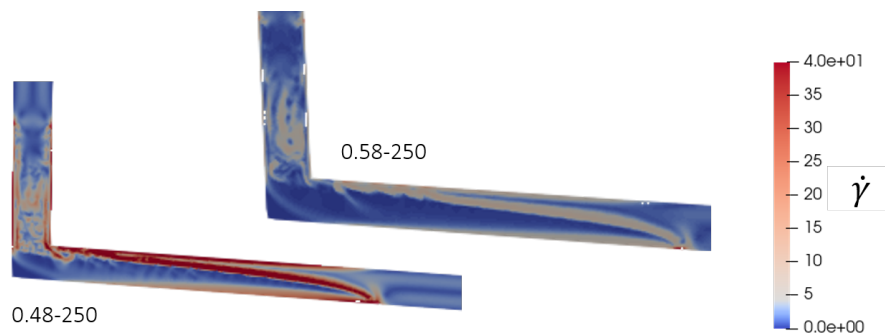


Figure 5.8: Shear rate distribution in L-Box tests with 0.45-250 and 0.58-250 at t=2 *s*, [Thiedeitz et al. (5th - 9th Jun 2022)]

Summarized, the CFD simulations reveal the non-sufficiency of the viscoplastic model to depict time-dependent flow cases. A transient thixotropy parameter, which captures the shear-and time-dependent structural buildup, must be introduced.

Furthermore, the simulations showed that not only the rheological model, but also the mesh design and the regularization method affect the numerical accuracy. Therefore, prior to the implementation of a new rheological model and the analysis of transient flow phenomena, a broad accuracy analysis was required.

# Part III

# Summary of publications related to transient flow modeling and simulation

# 6. Viscoelastoplastic classification of cementitious suspensions: transient and non-linear flow analysis in rotational and oscillatory shear flows

*This chapter summarizes research findings published in this article:*

[Main1] **Thiedeitz, M.**; Kränkel, T.; Gehlen, C. (2022). *Viscoelastoplastic classification of cementitious suspensions: transient and non-linear flow analysis in rotational and oscillatory shear flows*. Rheologica Acta 61, 549-570, doi.org/10.1007/s00397-022-01358-9

## Author's contribution

The author of this thesis conceptualized the research necessity, the modeling approach and the overall structure of the publication. Laboratory experiments were conducted by her, Maximilian Prakesch and Maik Hobusch. Data analysis and interpretation, illustration and writing was done by her. Thomas Kränkel and Christoph Gehlen reviewed and edited the article.

## Copyright Notice

# 6.1   Motivation and scope

Following the preliminary rheological investigations, a comprehensive test program was designed to investigate the viscoplasticity and viscoelasticity of cement pastes as a function of their suspension composition. The focus was put on:

- Construction of a rheological property map to classify the elasto-visco-plastic material behavior of cementitious pastes, and application of it on an experimental setup

- Assessment of simple and well-established analysis methods to calculate rheological parameters, and the analysis of nonlinear elasto-visco-plasticitiy

Cementitious suspensions with a CEM II 42.5 A-LL N and three different solid volume fractions ($\Phi_S = 0.48, \Phi_s = 0.52$ and $\Phi_s = 0.55$ ), and macroscopic flowability values of slump flow = 200 ±5mm, 250 ±5mm and 300 ±5mm were investigated.

**Viscoplastic characterization methods**

For viscoplastic characterization, phenomenological regression analysis was applied to flow curves from rotational dynamic parallel plate rheometry. Different regression functions were applied:

- Analysis of $\tau - \dot{\gamma}$ flow curves: Bingham- and Herschel-Bulkley regression

- Analysis of $\eta - \dot{\gamma}$ viscosity curves: Application of the continuous Cross model and discontinuous modeling, adapted from [Zarei and Aalaie (2020)]

- Agglomeration analysis below the critical shear rate $\dot{\gamma}_{crit}$ through thixotropy formulation by [Roussel (2006)] et al., Eq. 3.22

**Viscoelastic characterization methods**

Viscoelastic analysis in the linear, transient and nonlinear regime was conducted using Large Amplitude Oscillatory Shear (LAOS) rheometry with parallel plates, and different mathematical methods were tested:

- Inter-cyclic linear viscoelastic material analysis in the linear-viscoelastic regime (LVE)

- Intra-cyclic transient and nonlinear viscoelastic analysis of higher harmonics graphically with LB curves and mathematically applying stress decomposition

All mathematical equations, the referring rheological parameters and significance for cement paste rheology are elaborated in [Thiedeitz et al. (2022)]. Main findings are presented in the following.

## 6.2 Main findings

**Viscoplastic modeling**

Flow curves from dynamic parallel plates rheometry were plotted as $\tau - \dot{\gamma}$-curves and $\eta - \dot{\gamma}$-curves, and the regression analysis of the flow curves with the different phenomenological models followed in PYTHON. The focus of investigation was placed on (I) correctness of the regression method as introduced in Chapter 4, (II) robustness of the rheological model and (III) informative value of the rheological parameters gained through the regression method. Figure 6.1 illustrates different selected rheological parameters from the regression analysis depending on the paste composition.
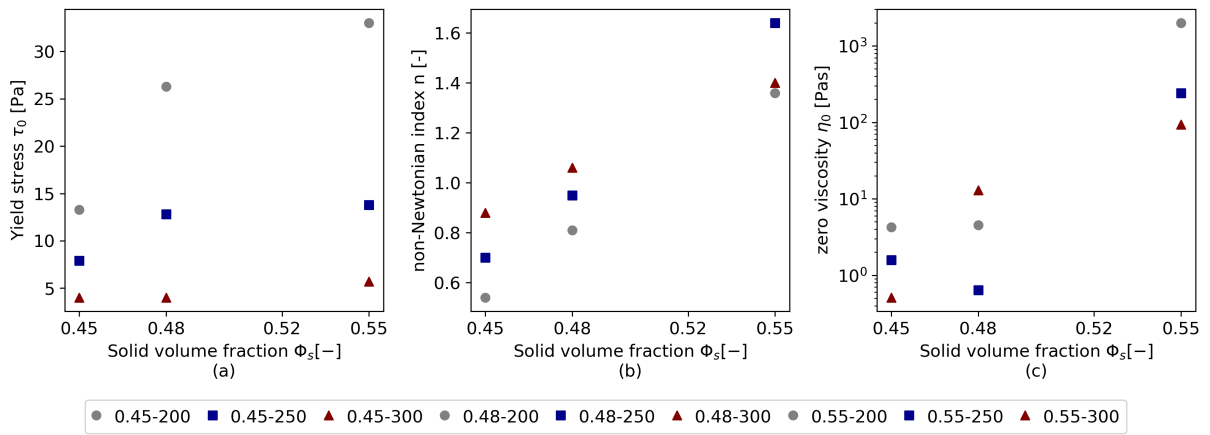


Figure 6.1: Viscoplastic parameters from all test series: (a) Yield stress $\tau_{0,H.-B.}$, (b) non-Newtonian index, (c) zero viscosity $\eta_0$, updated from [Thiedeitz et al. (2022)]

The results show that, as expected, increased slump flow values decrease the yield stress values $\tau_{H.-B.}$, see Figure 6.1 (a). The non-Newtonian index $n$ from the Herschel-Bulkley analysis is illustrated in Figure 6.1 (b). $n$ increases with increasing solid volume fraction $\Phi_s$. While the Herschel-Bulkley analysis could describe increasing nonlinearity for all test series, common viscosity models did not depict the shear-dependent viscosity for pastes with $\phi_s = 0.55$. However, they provided information on the zero viscosity $\eta_0$. Figure 6.1 (c) shows the zero viscosity $\eta_0$ as extrapolation at $\dot{\gamma} = 0$, which ranges between 0.2 Pas for low-viscous pastes at low $\Phi_s$ and around 2000 Pas for the highest $\Phi_s$. Discontinuous viscosity modeling, applied in [Thiedeitz et al. (2022)], depicted a more detailed analysis of $\eta(\Phi_s)$, mostly with a lower regression error. However, continuous mathematical modeling is preferred over discontinuity functions, as they can yield instabilities especially when implementing them into numerical CFD models.

**Viscoelastic modeling: First harmonics**

First harmonics analysis of all test series revealed significant differences in the viscoelastic material response depending on the cement paste composition. While LAOS curves can

be looked up in [Thiedeitz et al. (2022)], Figure 6.2 illustrates the main outcome of the viscoelasticity analysis in the LVE regime.
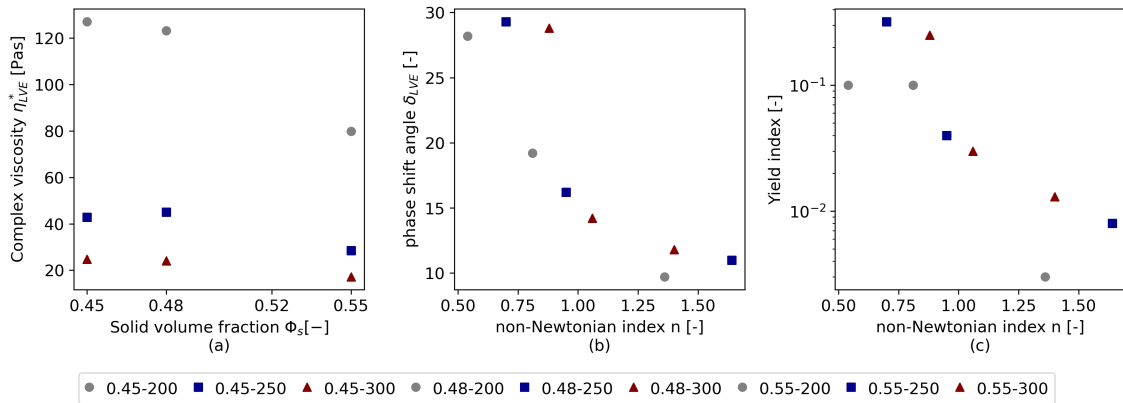


Figure 6.2: Viscoelastic parameter analysis of the first harmonics: (a) complex viscosity $\eta^*$, (b) phase shift angle $\delta$ and (c) the yield index, updated from [Thiedeitz et al. (2022)]

Figure 6.2 (a) illustrates the complex viscosity $\eta^*$ for the linear viscoelastic range, which, in comparison to Figure 6.1 (c), depicts a clear dependence between flowability and $\eta^*_{LVE}$. With increasing superplasticizer amount, $\eta^*_{LVE}$ decreases. Alternatively, the complex shear modulus or the storage modulus could have been chosen for description. Figure 6.2 (b) shows the phase shift angle $\delta$ in the LVE in comparison to the non-Newtonian index $n$ from the viscoplastic analysis. Generally, with increasing $n$ (and, thus, also $\Phi_s$), the phase shift angle $\delta$ decreases indicating a more pronounced elasticity. Figure 6.2 (c) illustrates the yield index, which is the ratio between viscous and elastic range. Again, the correlation to $n$ x is illustrated. A general trend is obvious that with increasing $n$, the yield index decreases, which corresponds to an increased elastic region compared to viscous flow. In this case, not only $\Phi_s$, but also the superplasticizer amount become important: With increased superplasticizer amount, elasticity increases. While the results correspond to previous findings of elasticity of polymer structures, e.g. [Hyun et al. (2011)], combined chemical and microstructural investigations would be required to prove the root of increased elasticity.

**Viscoelastic modeling: Higher harmonics**

The nonlinear viscoelastic material behavior was analyzed graphically through the analysis of LB curves, and mathematically through the evaluation of the strain stiffening ratio $S$, shear thickening ratio $T$, strain stiffening ratio $e_3$ and shear thickening ratio $v_3$. Results for all test series and each LB curve are elaborated in detail in [Thiedeitz et al. (2022)]. Nonlinear viscoelastic analysis methods revealed intra-cyclic differences of the viscoelastic evolution depending on the paste composition.

Exemplary, Figure 6.3 visualizes LB curves for the test series 0.45-250 and 0.55-250. Figure 6.3 (a) shows the whole evolution of the test series 0.55-250. Figure 6.3 (b) reveals the differences of three LB curves in the LVE, transient and highly nonlinear zone. The widening

of the elastic LB curve over time signifies a reduction in the ratio of storage modulus to loss modulus inter-cyclically.



(a) LB curves for CEMII-0.55-250

(b) CEMII-0.45-250 and CEMII-0.55-250
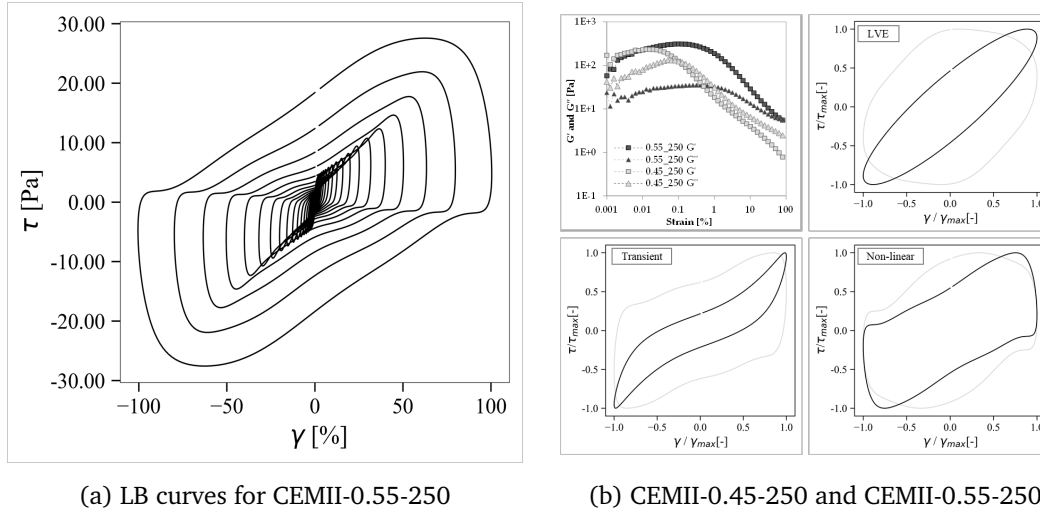
Figure 6.3: nonlinear viscoelastic Lissajous-Bowditch curves at different strain amplitudes $\gamma_0$, [Thiedeitz et al. (2022)]

Mathematically, the evolution of Chebyshev parameters with increasing applied strain amplitude $\gamma_0$ revealed material transitions from elastic to viscous behavior. Within the yielding zone, $S$ and $T$ revealed intracyclic elastic shear stiffening and viscous shear thinning behavior. Strain stiffening behavior increased with $\Phi_s$, but decreased depending on the PCE content. In the nonlinear regime, the material exhibited elastic shear softening ($S$ decreases below 0) and viscous shear thinning ($T$ increases towards 0), leading to increased dominance of viscous effects and improved flowability inter-cyclically.

**Rheological mapping**

Finally, a rheology map for the classification of elasto-visco-plasticity was designed, which grasps descriptive rheological parameters, see Figure 6.4. Figure 6.4 depicts the distinction between elasticity, plasticity and viscosity. The design idea was adopted from the PIPKIN diagram, invented by Pipkin in 1972, see [John et al. (1986)]. From left to right, deformability (through description of shear deformation $\gamma$) and flowability ( through description of the shear rate $\dot{\gamma}$) increase. From the bottom to the top, interparticle forces increase. The inner part of the map shows the variation of cementitious pastes, simplified to the increase of PCE and the increase of solid volume fraction.

The shift from plasticity to viscosity happens through the rheological parameter yield stress $\tau_0$. Below $\tau_0$, flocculation can occur. Beyond, viscous shear flow occurs as a function $f(\dot{\gamma})$. The change between elasticity and viscosity happens at a critical strain rate $\gamma_l$, while flow starts at $\gamma_F$. The yield index stands for the viscoelastic character between soft and brittle failure. Before yielding, the linear-viscoelastic range is described through the storage modulus $G'$ and $\gamma_l$. After yielding, $S(\gamma)$, $T(\gamma)$, $e(\gamma)$ and $v(\gamma)$ describe nonlinearities.
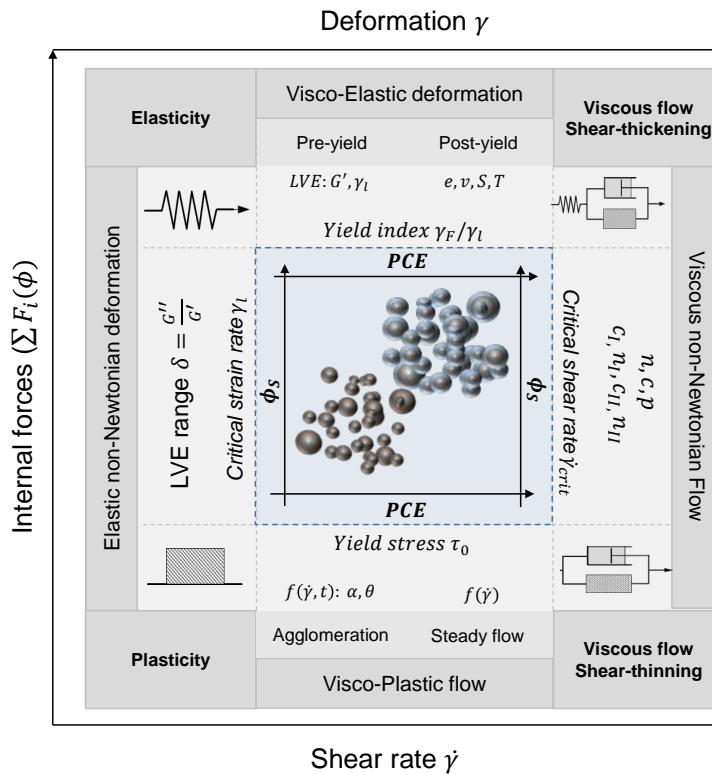
Figure 6.4: Rheological parameter map for viscoelastoplastic classification, modified and updated from [Thiedeitz et al. (2022)]
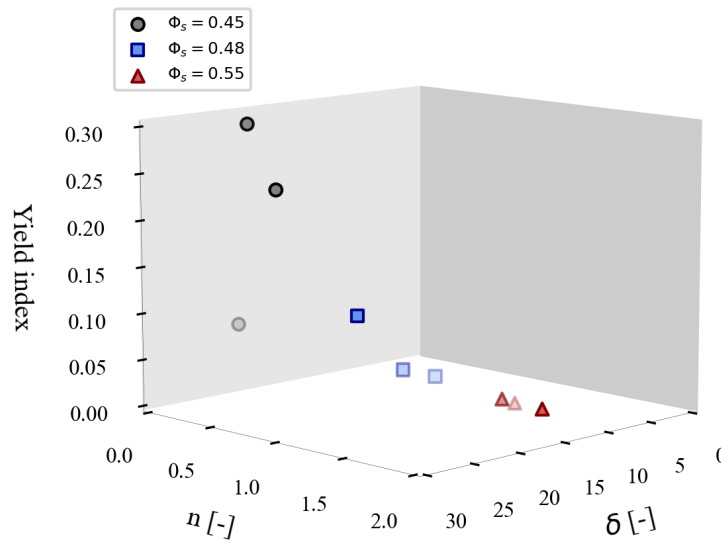


Figure 6.5: Elasto-visco-plastic mapping through non-Newtonian index $n$, phase shift angle $\delta$ and yield index, modified and updated from [Thiedeitz et al. (2022)]

A simple combined mapping of elasto-visco-plastic characterization of all test series is illus-

trated in Figure 6.5. The rheo-box combines the non-Newtonian index $n$, phase shift angle $\delta$ and yield index. With increasing solid volume fraction $\Phi_s$ and superplasticizer content, non-Newtonian behavior changes from viscous and brittle to increasingly soft and elastic while increasing the nonlinear viscosity.

## 6.3 Conclusion and outlook

A methodology was presented to measure viscoplastic and viscoelastic properties of cementitious pastes, and to couple the analysis for a descriptive rheological mapping.

Summarized, the viscoplastic characterization revealed the transition from shear-thinning towards shear-thickening behavior with increasing $\Phi_s$. Viscosity bifurcation below a critical shear rate $\dot{\gamma}_{crit}$ was best depicted through discontinuous modeling. For viscoelastic characterization, the first order oscillatory parameters $G'$, $\gamma_l$, $\delta$ and $\eta^*$ in the LVE range; and the overall evolution of these parameters together with the yield index $\gamma_F/\gamma_l$, characterized viscoelastic properties in the most descriptive way. nonlinear material analysis, however, gave insights into intracyclic strain-softening or strain-stiffing material behavior.

The mathematical methods to characterize nonlinear viscoelasticity require a higher computational effort. However, they gain the benefit of a distinct analysis of microstructural effects, such as the effect of chemical admixtures on viscoelastic properties. Elasto-visco-plastic properties were crucially affected by both $\Phi_s$ and the polymeric content.

Finally, it was found that a phenomenological unifying approach of combined dynamic and oscillatory linear and nonlinear rheological analysis provides elaborated information about the effect of the paste composition on rheological properties. A combination of the presented methods does not lead to comparative (as suggested in previous research) but to complementary material parameters that help to fingerprint the viscoelastic or even elasto-visco-plastic deformation and flow. Prospectively, these methods can be applied effectively test cement-superplasticizer-interactions and optimize the flowability of cementitious pastes.

# 7. Steady and transient phenomenological thixotropy modeling of non-Newtonian cementitious pastes

*This chapter summarizes research findings from an article intended for publication. The article was submitted in 08/2023. Review is pending.*

[Main2] **Thiedeitz, M.**; Kränkel, T.: (2024). *Steady and transient phenomenological thixotropy modeling of non-Newtonian cementitious pastes.* Cement and Concrete Research (submitted 08/2023)

## Author's contribution

The author of this thesis conceptualized the research necessity, the modeling approach and the overall structure of the publication. Modeling ideas were a process where Maximilian Prakesch and Thomas Kränkel supported with ideas. Data analysis and interpretation, illustration and writing was done by her. Thomas Kränkel reviewed and edited the article.

## Copyright Notice

## 7.1 Motivation and scope

Following the elasto-visco-plastic rheological classification, thixotropy modeling and its combination with experimental rheology tests was required for the evaluation of a time- and shear rate dependent parameter $\lambda$. Figure 7.1 displays the viscoplastic and thixotropic range of cementitious pastes: Figure 7.1 (a) shows the dynamic $\tau - \dot{\gamma}$ - flow curves of two different cement pastes, varying in their solid volume fraction $\Phi_S$ but with similar consistencies due to the addition of superplasticizer. The paste with $\Phi_S = 0.45$ has nearly ideal viscoplastic flow behavior. A steady flow model can be chosen to describe nearly the whole range of shear. The paste with $\Phi_S = 0.55$, however, possesses a critical shear rate $\dot{\gamma}_{crit}$: Below $\dot{\gamma}_{crit}$, agglomeration takes place and the stress response increases with decreasing $\dot{\gamma}$.
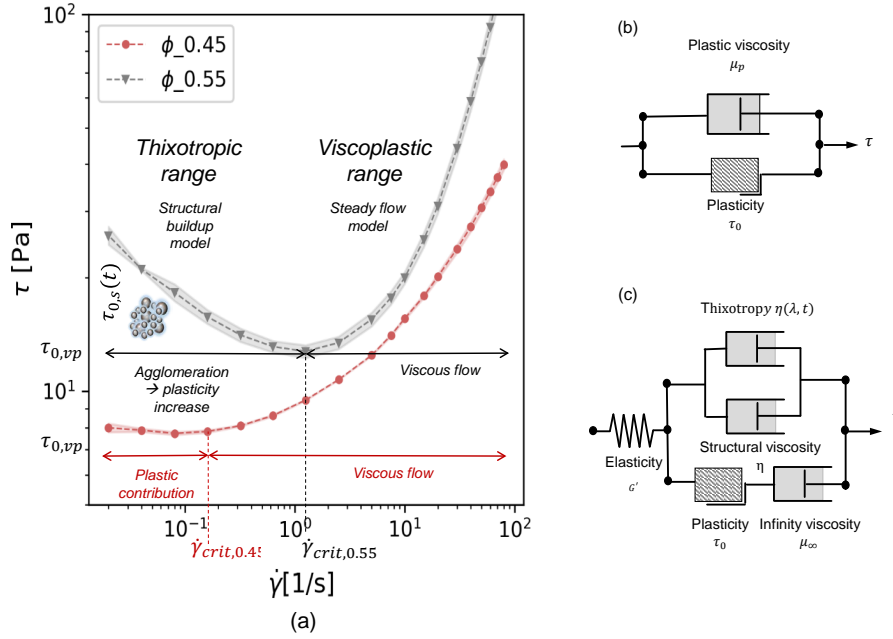
Figure 7.1: Structural buildup in a one-dimensional flow curve below a critical shear rate $\dot{\gamma}$ because of agglomeration processes, [Thiedeitz and Kränkel (2024a)]

The flow curve is, thus, distinguished into a *viscoplastic* range $> \dot{\gamma}_{crit}$ and a thixotropic range $< \dot{\gamma}_{crit}$. The investigation covered two main research aims:

- The mathematical formulation of a time- and shear rate dependent structural parameter $\lambda$ based on existing models, which can be combined with experimental tests

- Assessment of different rheometric procedures on their applicability to analyze thixotropy parameters, and a concluding strategy which procedures serve which benefit

## 7.1.1 Rheological model definition

A simplified kinetic model, based on the formulation from [Cheng and Evans (1965)], was chosen to describe the structural parameter $\lambda$:

$$\frac{d\lambda}{dt} = - k_1 \dot{\gamma} \lambda + k_2 (1 - \lambda) \qquad [-] \qquad (7.1)$$

In Eq. 7.1, $k_1$ is the structural breakdown parameter that depends on the shear rate $\dot{\gamma}$, and $k_2$ is the structural buildup parameter. A similar formulation of $\lambda$ is found in [Le-Cao et al. (2020)]. While the constitutive equation is kept in a generalized form, it equals the thixotropy model from [Coussot et al. (2002)], adapted by [Roussel (2006)]:

$$\frac{d\lambda}{dt} = \frac{1}{T \lambda^m} - \alpha \lambda \dot{\gamma} \qquad [-] \qquad (7.2)$$

Comparing Eq. 7.1 and Eq. 7.2, it becomes clear that $k_1$ equals the deflocculation parameter $\alpha$; and $k_2$ is the reciprocal of the flocculation time $\Theta$, and, thus $k_2 = 1/\Theta$. The main difference is that Eq. 7.1 is strictly normalized to the range $0 \leq \lambda \leq 1$. This makes Eq. 7.1 applicable to use $\lambda$ as scaling factor to other rheological parameters, such as $\tau(t) = \tau \frac{d\lambda}{dt}$ and $\eta(t) = \eta \frac{d\lambda}{dt}$. While a constitutive model illustration for both $k_1$ and $k_2$ can be looked up in the referring publication, the whole constitutive formulation Eq. 7.1 is illustrated in Figure 7.2 with regards to the boundary condition $\lambda_0$, which is the initial structural state.
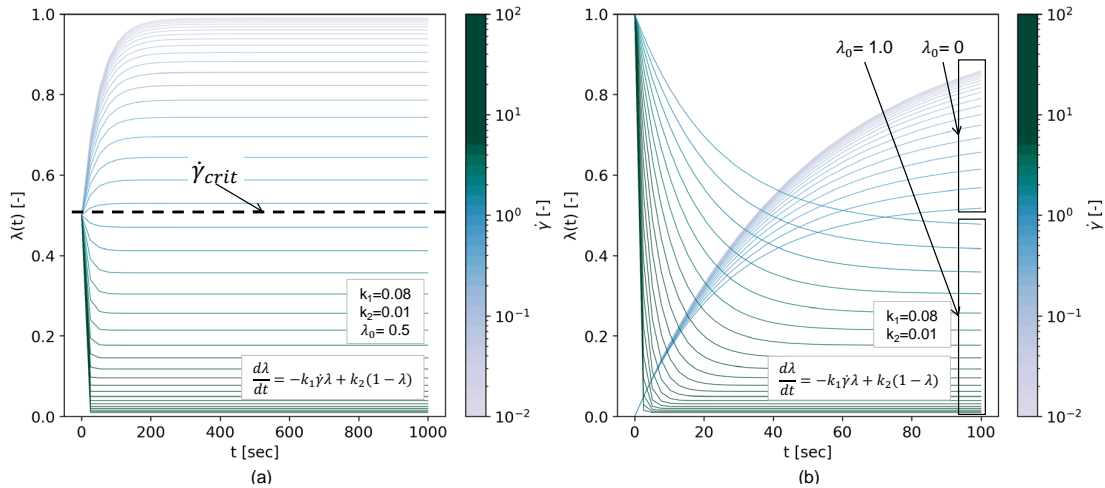


Figure 7.2: Constitutive $\lambda(t)$ modeling with different boundary parameters $\lambda_0$ and structural parameters $k_1$ and $k_2$, [Thiedeitz and Kränkel (2024a)]

Figure 7.2 (a) shows the shear-rate dependent evolution of $\lambda(t)$ for a defined boundary condition of $\lambda_0 = 0.5$. Figure 7.2 (b) illustrates $\lambda(t)$ for each $\lambda_0 = 0$ and $\lambda_0 = 1$. The time scale until 1000 s in (a), and 100 s in (b) was chosen with regards to real life flow- and rest processes. The maximum structural value of $\lambda = 1$, in any case, is reached after a certain time. However, a difference between the presented modeling and real cementitious paste structural buildup must be considered: Due to hydration effects, irreversible structural buildup would, differently than depicted in Figure 7.2 (a), continue. With regards to the scope of this thesis, hydration contributions to structural buildup are not considered. More information on irreversible structural buildup modeling are, e.g., found in [Reiter (2019); Marchesini et al. (2019)].

## 7.2 Experimental procedures and main findings

**Analysis of structural buildup and structural breakdown parameter**

Experimental procedures to investigate structural buildup and breakdown parameters are collected in Figure 7.3, with more detailed information from Figure 7.4 to Figure 7.6.
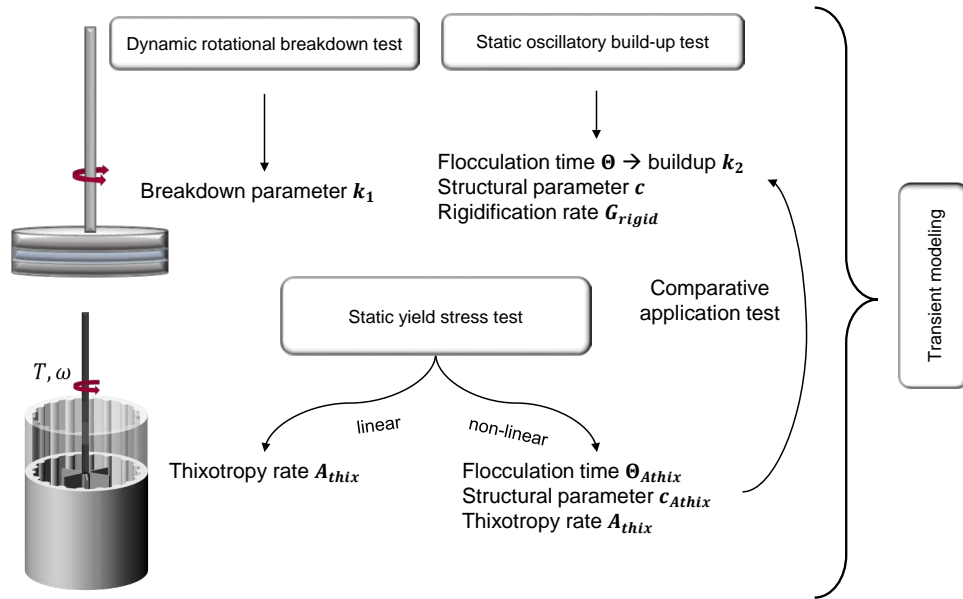
Figure 7.3: Rheometric procedure, [Thiedeitz and Kränkel (2024a)]

A dynamic rotational test at different constant shear rate values $\dot{\gamma}$ was employed to investigate $k_1$, which is illustrated in Figure 7.4. Different shear rates were employed, and the corresponding stress response was fitted to the constitutive breakdown equation $\frac{d\lambda}{dt} = -k_1\dot{\gamma}\lambda$.
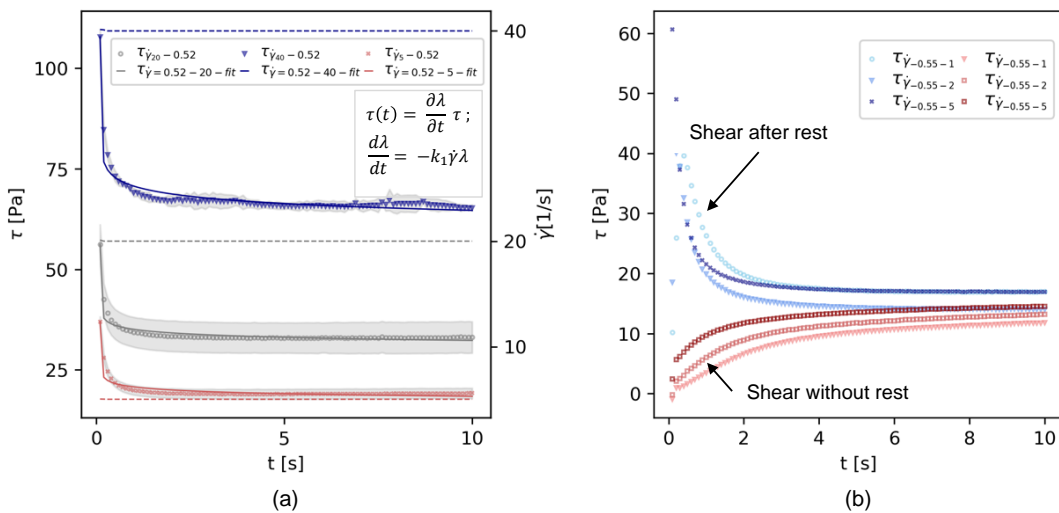


Figure 7.4: Dynamic rotational shear test at constant $\dot{\gamma}$, [Thiedeitz and Kränkel (2024a)]

Figure 7.4 (a) shows the experimental data for $\dot{\gamma} = 40s^{-1}, 20s^{-1}$ and $5s^{-1}$. Figure 7.4 (b) vizualizes the effect of different shear histories. For the shear rates $\dot{\gamma} = 5s^{-1}, 2s^{-1}$ and $1s^{-1}$, tests were carried out after a certain time of rest, wherefore the boundary condition $\lambda_0 = 1$, and without resting time, wherefore $\lambda_0 = 0$. While the quantitative data can be looked up in the belonging publication, it shall be noticed that the initial structural state, together

with shear history, becomes important for the structural breakdown parameter $k_1$.

To analyze $k_2$, two methods were employed. In general, $k_2$ was investigated through identification of the flocculation time $\Theta$, and calculating the reciprocal $k_2 = 1/\Theta$. Figure 7.5 shows the oscillatory SAOS and rotational static SYS test to analyze the structural buildup and flocculation time.
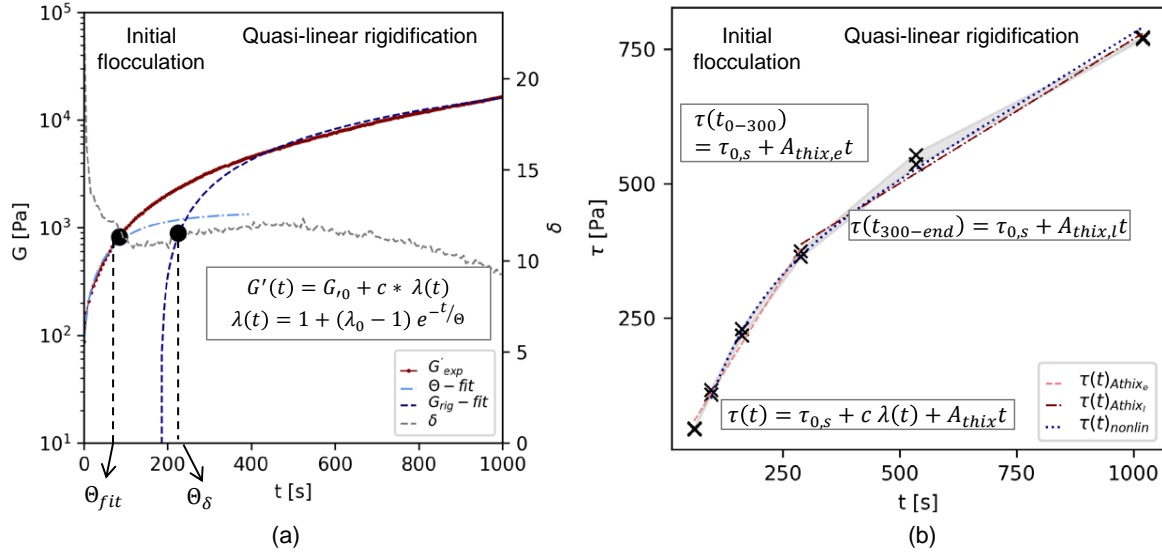


Figure 7.5: (a) Non-destructive oscillatory test and (b) static yield stress test, both to obtain $k_2$ through flocculation time analysis, [Thiedeitz and Kränkel (2024a)]

Figure 7.5 (a) shows the storage modulus $G'$ and phase shift angle response $\delta$ in an oscillatory test. $G'(t)$ was fitted to Eq. 3.28. Additionally to the flocculation time $\Theta_{fit}$, a structural parameter $c$ and the rigidification rate $G_{rig}$ were identified as proposed by [Ma et al. (2018)]. In another approach, the flocculation time was calculated through the analysis of $\delta(t)$. $\Theta_{\delta}$ was reached once the gradient of $\delta(t)$ reached a threshold of 0.1%.

Figure 7.5 (b) illustrates the linear and nonlinear regression analysis for $\tau(t)$ as proposed by [Ma et al. (2018)]. Consequently, a flocculation time $\Theta_{Athix}$ and a structural parameter $c_{Athix}$ could be calculated. Structural buildup was increasingly nonlinear with increasing $\Phi_s$, wherefore the nonlinear regression analysis was more descriptive with a smaller mathematical error. However, the regression parameter $\Theta_{Athix}$ could not be correlated with $\Theta_{fit}$ or $\Theta_{\delta}$. The structural breakdown parameter $k_2$ was consequently calculated from $\Theta_{fit}$.

**Transient flow modeling with time- and shear rate-dependent $\lambda$**

Finally, phenomenological modeling on dynamic flow curves was conducted with a $\lambda$ - implemented Herschel-Bulkley model. It is important to note that Eq. 7.1 incorporates a time-dependent parameter. Thus, to enable phenomenological modeling on experimental data, the measurement time of each shear rate step needed to be implemented.
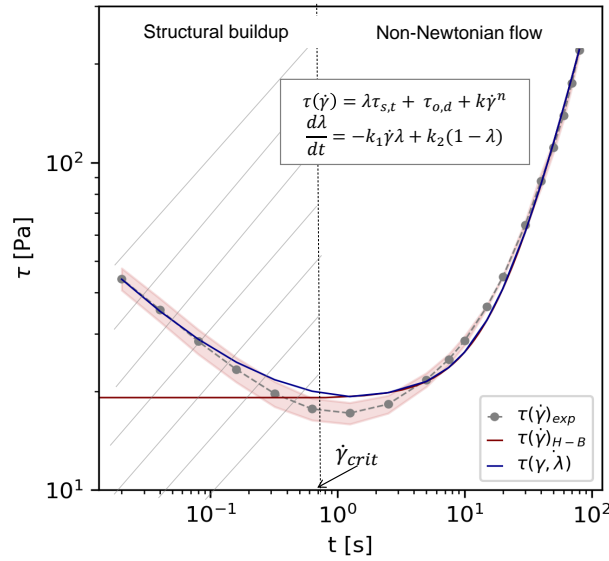
Figure 7.6: Dynamic flow curve, [Thiedeitz and Kränkel (2024a)]

Figure 7.6 shows the difference between a simple Herschel-Bulkley model and a $\lambda$- implemented Herschel-Bulkley model. Below the critical shear rate $\dot{\gamma}_{crit}$, the shear stress increase is accounted for through structural buildup that surpasses structural breakdown. While the final mathematical formulation is still not perfect, it depicts time- and shear-dependent thixotropy that is observed in a parallel-plates experiment.

## 7.3    Conclusion and outlook

A time-dependent $\lambda(t)$-implementation into a dynamic flow model allows the computation of partial structural buildup during the low-shear regime. Knowledge about full structural buildup and structural breakdown parameter ensures a weighting of both physical phenomena close to reality. Rheometric test methods were used to analyze structural buildup and breakdown properties. It was found that the calculated parameters fit well into a transient flow formulation: The buildup parameter $k_2$ can be correlated to the flocculation time $\Theta$ measured during a non-destructive oscillatory test. The understanding of the physical and chemical relation, and, thus, a more elaborated analysis of flocculation time, requires more research. The structural breakdown parameter $k_1$ is highly dependent on boundary parameters and the shearing history.

While the theoretical modeling of Eq. 7.1 is straight-forward and depicts the physical thixotropic properties in a meaningful way, the combination with experimental methods yields challenges: On the one hand, boundary conditions, such as resting time or pre-shear, significantly affect structural properties. Secondly, different experimental and mathematical methods appear promising for the experimental analysis, but yield different results. Global knowledge about structural buildup and breakdown as a function of the mixture com-

position requires a broader experimental data pool and further analytical methods, e.g. calorimetric measurements, analysis of granulometric properties with time and hydration products. However, the proposed model and experimental setup support the understanding of transient thixotropy-including flow. Additionally, the mathematical formulation can be implemented into a phenomenological formulation in a Computational Fluid Dynamics (CFD) setup for the fully resolved time- and shear-dependent flow simulation of thixotropic cementitious building materials.

# 8. The Slump Flow of Cementitious Pastes: Simulation vs. Experiments

*This chapter summarizes research findings published in this article:*

[Main3] **Thiedeitz, M.**; Kränkel, T.; Kartal, D.; Timothy, J.J. (2024). *The Slump Flow of Cementitious Pastes: Simulation vs. Experiments*. *Materials*, 17, 532, doi.org/10.3390/ma17020532

## Author's contribution

The author of this thesis conceptualized the research necessity, the modeling approach and the overall structure of the publication. Laboratory experiments were conducted by her and Maik Hobusch. Numerical simulations were conducted by her and Deniz Kartal. Data analysis and interpretation, illustration and writing was done by her. Thomas Kränkel and Jithender Timothy reviewed the article.

## Copyright Notice

## 8.1   Motivation and scope

*"A computational model relates well to the theory if the computational model describes the mathematical model well and the mathematical model relates to the theory well"*,
[Babuska and Oden (2004)]

First CFD simulations of the slump flow and the L-Box test, see [Thiedeitz et al. (5th - 9th Jun 2022)], revealed challenges in defining an accurate numerical model to compute transient viscous flow. Many CFD simulations of cementitious paste flow available in the literature simplify the rheological material behavior (e.g., Bingham flow, [Roussel et al. (2016)]), focus on steady-state conditions in analytically resolvable geometries [Haustein et al. (2022)], or neglect testing the impact of numerical boundary and regularization methods on the computational accuracy (e.g., [Gram (May 2009); Schaer et al. (2018); Pereira et al. (2022)]). "Ideal numerical benchmark scenarios" compare analytically resolvable test cases with numerical approximations to optimize the numerical framework towards a defined mathematical result. Empirical stoppage tests display the fast on-site estimation of rheological parameters and workability. However, [Frigaard and Nouar (2005)] labeled them "worst-case scenarios" for the numerical analysis, because no analytical solution for the velocity field exists, the local simulation domain changes with every time step and regularization techniques affect the start and stoppage of flow.

Therefore, the article published in [Thiedeitz et al. (2024)] focuses on a reliable computational framework to compute the free-surface flow of cementitious pastes. The effect of spatially-temporally refinement, regularization model and regularization parameters in the slump flow test were investigated. Subsequently, transient properties of cementitious pastes with varying viscosities, described by the Herschel-Bulkley model, were analyzed during slump flow. Modeling of a slice geometry was compared to the fully-resolved three-dimensional cone geometry to save computational costs. The research concept is illustrated in Figure 8.1:
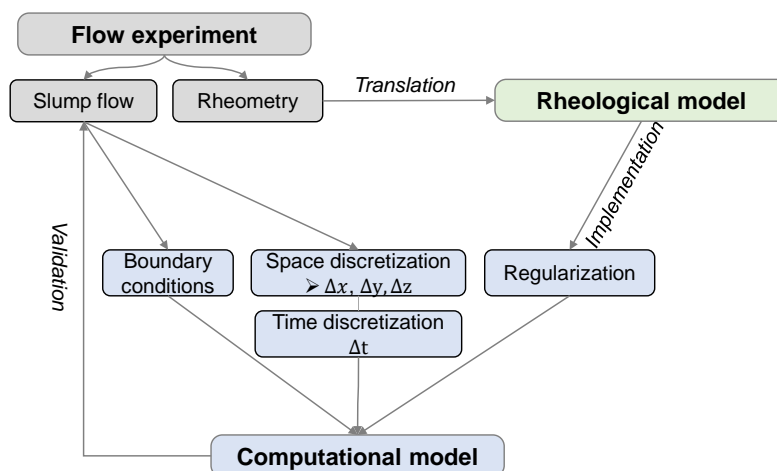


Figure 8.1: Research framework: Flow tests, rheological model and numerical simulation, [Thiedeitz et al. (2024)]

## 8.2   Numerical procedure and findings

Cementitious pastes were prepared with the binder OPC CEM I and solid volume fractions $\phi_s = 0.45, 0.52$ and $0.55$. PCE was added for macroscopic flowability values of $250 \pm 5mm$ as diameter in the slump flow test. Rheometric tests were conducted with the parallel plates geometry in a dynamic rotational step-rate profile. The Herschel-Bulkley model was applied to the flow curves for the analysis of rheological parameters.

The numerical accuracy was tested in a sptial-temporal refinement study. Subsequently, the three-dimensional cone geometry and the slice geometry were compared on their accuracy. Different regularization techniques and parameters were tested on the most accurate numerical model. The numerical accuracy analysis was solely investigated for the test series OPC-0.45. The computational study of viscous flow was performed on all test series.

### 8.2.1   Numerical accuracy

The spatial-temporal refinement analysis comprised of simulations with (1) only fixed time step $\Delta t$, (2) only fixed $\Delta x; \Delta y; \Delta z$ and (3) coupled spatial and temporal refinement. The cone geometry was discretized three times with meshes containing cubical cells (aspect ratio = 1) with dimensions $\Delta x; \Delta y; \Delta z$ = 0.004 m, 0.002 m and 0.001 m, reaching a maximum of 7.2 million cells in the finest mesh refinement. In contrast, for the slice setup, four mesh refinements with a maximum of 63,441 cells in the finest setup were employed. The cell sizes were defined as $\Delta x$ and $\Delta y$= 0.004, 0.002, 0.001 and 0.0005 m at a slice angle of 3 °. Time steps $\Delta t$ were studied between $\Delta t = 4 \times 10^{-3}$ to $\Delta t = 3.125 \times 10^{-5}$ s. The maximum Courant number $Co$ was evaluated for each simulation. The numerical error was calculated as deviation between the numerical final flow radius $r_{x,num}$ and the experimental final flow radius $r_{x,exp}$.
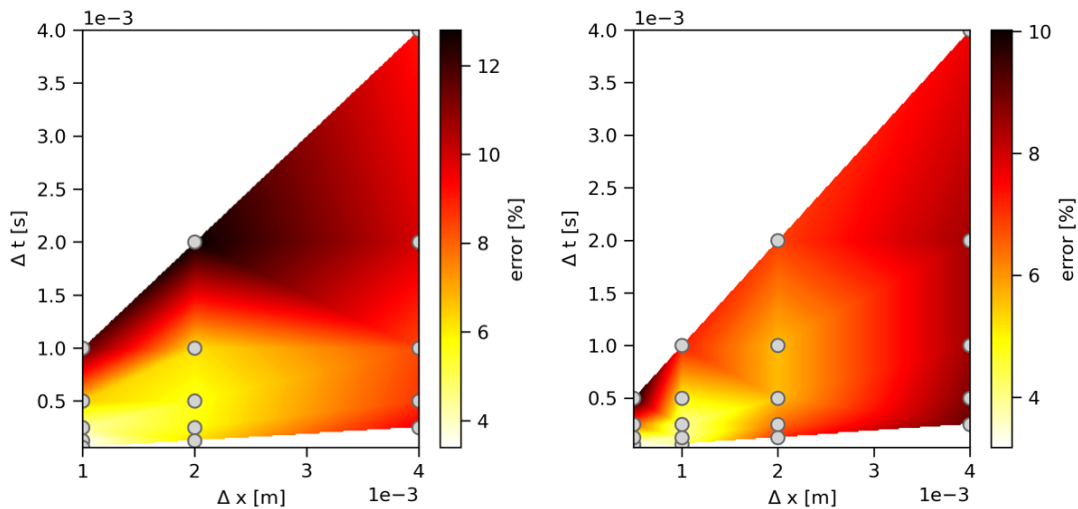


(a) Numerical errors of cone simulations          (b) Numerical errors of slice simulations

Figure 8.2: Error plots for all mesh and time refinements, [Thiedeitz et al. (2024)]

Convergence plots for each test series are available in [Thiedeitz et al. (2024)]. In this summary, Figure 8.2 displays error plots for all simulations depending on the chosen refinement pairs. Figure 8.2 (a) illustrates the error for the three-dimensional cone geometry, Figure 8.2 (b) illustrates the error for the slice geometry. The convergence study revealed a significant combined spatial and temporal discretization effect on the final flow result. Optimized spatial-temporal refinement reduced the error for the cone geometry to $e_x = 8\%$ and for the slice geometry to $e_x = 4\%$. Generally, decreasing Courant numbers contributed to a reduction in the final error.

**Geometrical comparison**

While the slice geometry provided more accurate simulation results due to higher possible mesh refinement, the cone geometry displays the closest approximation to the experimental test case. Figure 8.3 illustrates the comparison of simulation results for the finest cone and slice models, respectively.



(a) Shape comparison

(b) Flow over time comparison
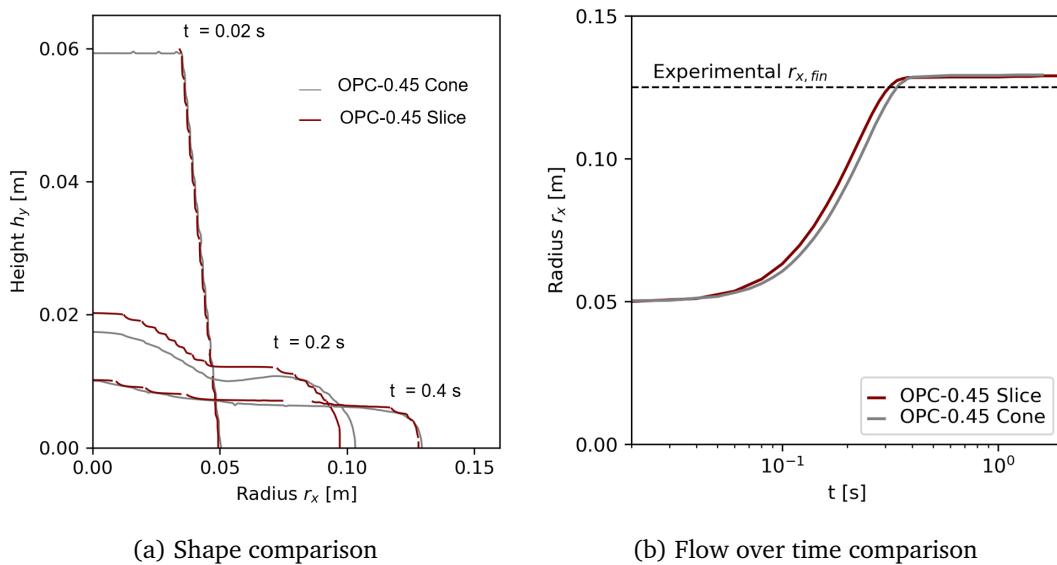
Figure 8.3: Comparison of cone and slice simulations with the highest numerical refinement, [Thiedeitz et al. (2024)]

The comparison reveals shape deviations between the three-dimensional geometry and the slice geometry during the flow. However, because the final flow length showed similar results, the slice geometry was applied for further parameter analysis due to reduced computational costs.

**Regularization study**

The Herschel-Bulkley-implemented Papanastasiou regularization, see Eq. 3.31, and the bi-viscous model, see Eq. 3.32, were tested with varying regularization parameters. For

the Papanastasiou regularization, $m$ was varied at $m = 1, 10, 100$ and 1000. For each $m$ variation, $\dot{\gamma}_{crit}$ was fixed as $\dot{\gamma}_{crit} = 0.001s^{-1}$, and $\dot{\gamma}_{crit} = 0.16s^{-1}$, respectively. While $\dot{\gamma}_{crit} = 0.001s^{-1}$ displays an arbitrary value to define the start of the blending function, $\dot{\gamma}_{crit} = 0.16s^{-1}$ is the mathematically analyzed critical shear rate from the rheological experiment.

For the bi-viscous model, four zero viscosities $\eta_0$ were defined, i.e. $\eta_0 = 1, 10, 100$, and 1000 Pas. Figure 8.4 illustrates the flow over time for all variations:
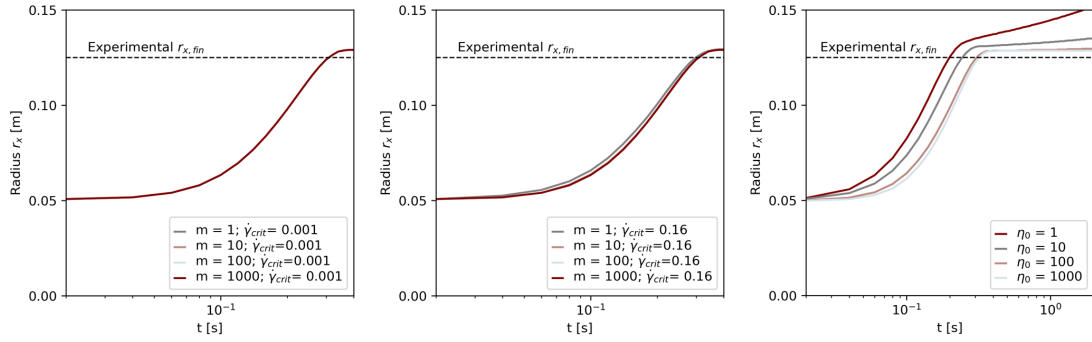


(a) Papanastasiou regularization with $\dot{\gamma} = 0.001$    (b) Papanastasiou regularization with $\dot{\gamma} = 0.16$    (c) Bi-viscous regularization with different $\eta_0$

Figure 8.4: Regularization-dependent flow over time, [Thiedeitz et al. (2024)]

Figure 8.4 (a) and Figure 8.4 (b) show the Papanastasiou model with $\dot{\gamma}_{crit} = 0.001s^{-1}$ and $\dot{\gamma}_{crit} = 0.16s^{-1}$. Once a minimum shear rate of $\dot{\gamma}_{crit} = 0.001s^{-1}$ is chosen, the regularization parameter $m$ does not affect the slump flow radius at all. At $\dot{\gamma}_{crit} = 0.16s^{-1}$, $m$ affects the flow. Increasing $m$ values lead to a slower flow evolution. Figure 8.4 (c) shows that the bi-viscous regularization affects the flow to the highest extended. With decreasing $\eta_0$, the flow velocity (slope of the curve $r_x(t)$) is higher and the final slump flow radius increases. The numerical error $e_x$ decreases with increasing $\eta_0$.

In the numerical slump flow test, regularization plays a crucial role, influencing both the flow result and the transient flow. The Papanastasiou regularization method reduces the numerical compared to experimental results. However, the selection of the parameters $\dot{\gamma}_{crit}$ and $m$ affects the numerical outcome.

## 8.2.2   Viscous flow simulation

Ultimately, the flow of cementitious pastes with increasing $\Phi_s$, namely OPC-0.52 and OPC-0.55, was simulated, utilizing the slice geometry with the most accurate mesh, and the Papanastasiou regularization with $m = 1000$. $\dot{\gamma}_{crit}$ was varied again, with an arbitrary fixed $\dot{\gamma}_{crit} = 0.001s^{-1}$ and the experimental $\dot{\gamma}_{crit}$. Results are displayed in Figure 8.5. Figure 8.5 (a) shows that no variations for different $\dot{\gamma}_{crit}$ appear, because the blending parameter $m$ has been chosen high. Figure 8.5 (b) illustrates the flow of OPC-0.45, OPC-0.52 and OPC-0.55. With increasing $\Phi_s$, and thus, higher viscosities, flow proceeds slower. While the

numerical slump of OPC-0.45 and OPC-0.52 exceeds the experimental result at 0.2 $s$, the simulation for OPC-0.55 continues to increase, and would require more simulation time.
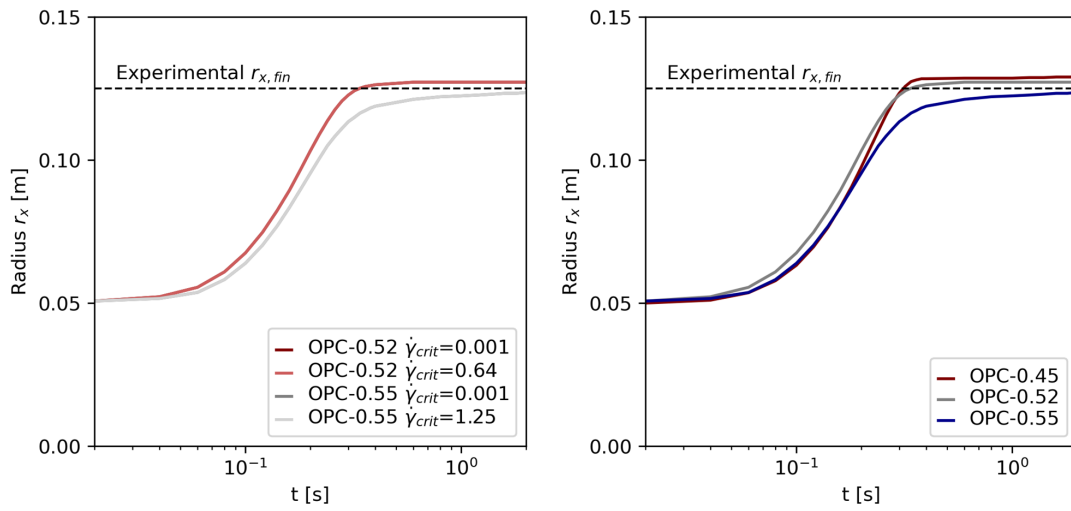


(a) Shape comparison

(b) Flow over time comparison

Figure 8.5: (a) Regularization study for viscous pastes (b) Flow over time for different test series, [Thiedeitz et al. (2024)]
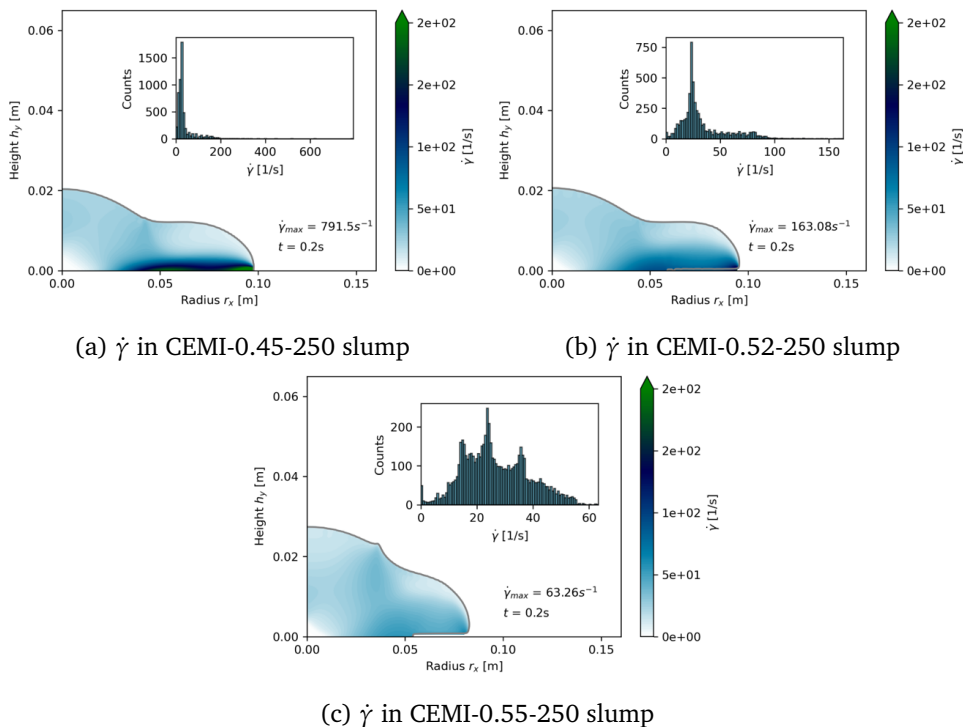


(a) $\dot{\gamma}$ in CEMI-0.45-250 slump

(b) $\dot{\gamma}$ in CEMI-0.52-250 slump

(c) $\dot{\gamma}$ in CEMI-0.55-250 slump

Figure 8.6: Local variation of $\dot{\gamma}$ for two-dimensional shapes, [Thiedeitz et al. (2024)]

Finally, the transient properties of $\dot{\gamma}$, see Figure 8.6, and the cell Reynolds number $Re_c$, see Figure 8.7, were investigated. The shape plots and parameter distribution provide insights

into the transient flow properties of different viscous pastes. A colorbar illustrates the variation of rheological properties over the two-dimensional shape, and a distribution histogram exemplifies the parameter distribution over the cells.



(a) $Re_c$ in CEMI-0.45-250 slump

(b) $Re_c$ in CEMI-0.52-250 slump



(c) $Re_c$ in CEMI-0.55-250 slump
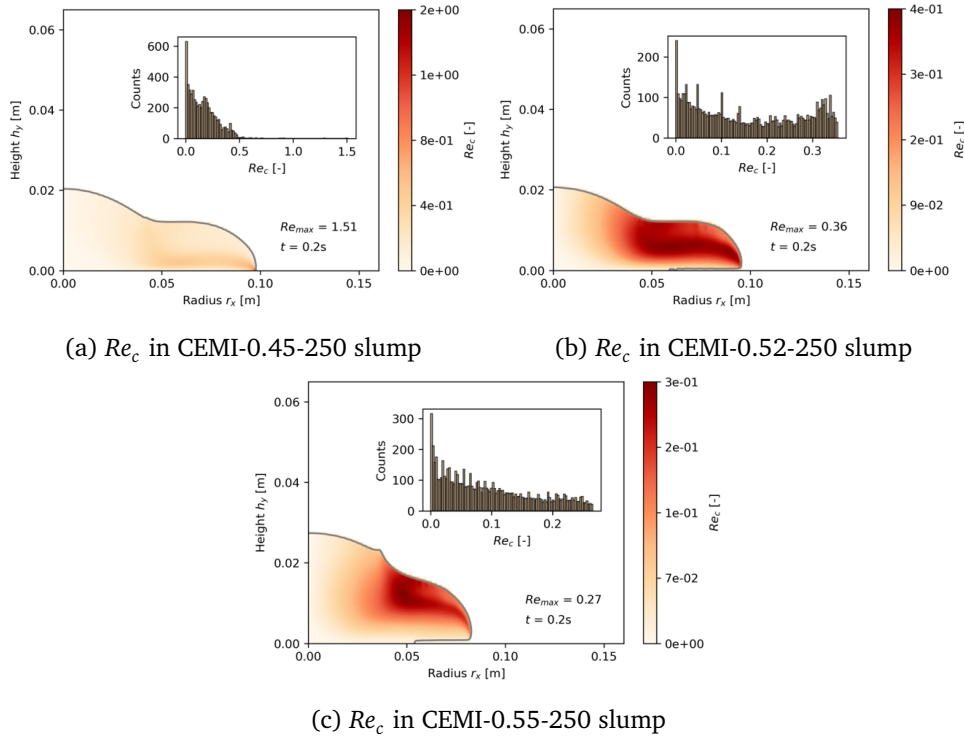
Figure 8.7: Local variation of $Re_c$ for two-dimensional shapes, [Thiedeitz et al. (2024)]

The illustration visualizes the locally different flow patterns: While after 0.2 s, the flow has already stopped around $x_r = 0m, h_y = 0m$, high $\dot{\gamma}$ occur towards the maximum $r_x$ and a thin layer close to the bottom of the slump, with the maximum values specified in Figure 8.6. The test series with lower viscosity quickly approach the final slump flow radius, with the velocity gradient predominantly directed toward the outermost region of the paste. In contrast, the flow occurs more slowly in pastes with a higher solid volume fraction $\phi_s$ and consequently a higher apparent viscosity $\eta$. With increasing $\Phi_s$, both $\dot{\gamma}$ and $Re_c$ decrease strongly.

## 8.3    Conclusions

The study reveals the influence of the numerical model on the simulation result, and, followed by this, transient flow phenomena of different viscous pastes. The findings serve as basis to implement further rheological parameter studies and to investigate slow flow and time-dependent phenomena of cementitious pastes more closely. Further studies could develop distinct characteristic numbers to describe the non-Newtonian flow evolution, e.g. through shape analysis over time, and relate low Reynolds numbers to viscous flow effects.

# 9. Time-dependent flow simulation of thixotropic cementitious pastes

*This chapter summarizes research findings to be published in conference proceedings in 09/2024:*

[Main4] **Thiedeitz, M.**; Timothy, J.J. (2024). *Time-dependent flow simulation of thixotropic cementitious pastes*. 9th European Congress on Computational Methods in Applied Sciences and Engineering (ECCOMAS), June 03 to June 07 2024, Lisboa, Portugal

## Author's contribution

The author of this thesis conceptualized the research necessity, the modeling approach and the overall structure of the publication. Numerical simulations were conducted by her. Rheometric experiments were conducted by her and Maik Hobusch; L-Box tests were conducted by Janusch Engelhardt and Maik Hobusch. All mathematical calculations, simulation analysis, illustrations and writing were done by her. Jithender J. Timothy reviewed and edited the article.

## Copyright Notice

## 9.1   Motivation and scope

Finally, the transient flow of cementitious pastes with special regards to time-dependent properties was investigated.

In [Thiedeitz et al. (2020b)], see summary in Chapter 5, it was demonstrated that thixotropy affects flow results in L-Box tests. With increasing thixotropic structural buildup, measured by static yield stress test rheometry, L-Box flow decreased and exhibited slower velocities. When replicating the L-Box flow in CFD in combination with a viscoplastic model for cementitious pastes without the consideration of thixotropy, the flow decrease was not computed, see [Thiedeitz et al. (5th - 9th Jun 2022)]. The implementation of a thixotropy model into the numerical CFD algorithm required a time- and shear rate-dependent resolvable derivative $\frac{d\lambda}{dt}$, rather than a formulation for structural buildup at rest, as previously investigated through $A_{thix}$. Furthermore, preliminary CFD studies revealed numerical inaccuracies in the chosen numerical models.

Chapter 7, [Thiedeitz and Kränkel (2024a)] presents the analysis of time- and shear rate-dependent structural buildup. Chapter 8, [Thiedeitz et al. (2024)] offers a reliable and accurate CFD model with error-reduced geometric mesh refinement and mathematical regularization. The results were combined to simulate the slump flow and L-Box flow of a thixotropic cementitious paste. Transient flow, the effect of thixotropy on local flow properties and the particular effect of structural buildup and structural breakdown was investigated.

## 9.2   Numerical framework and findings

### 9.2.1   The rheological model

The flow of the test series OPC CEM I with a solid volume fraction of $\Phi_s = 0.55$ was investigated in the slump flow test and the L-Box test. Rotational dynamic step-rate tests and the Herschel-Bulkley regression were conducted to analyze the viscoplastic flow parameters $\tau_{0,H.-B.}$, $k$ and $n$. The structural breakdown parameter $k_1$ was analyzed during steady shear after a period of rest. Structural buildup was analyzed in an oscillatory strain amplitude profile at $\gamma = 5 \cdot 10^{-3}\%$. The increase of the storage modulus $G'(t)$ over a period of 20 min was fitted to Eq. 3.28 as previously applied in Chapter 7. For the subsequent use in OpenFOAM, solely the flocculation time $\Theta$ was utilized.

The numerically implemented rheological model is Eq. 9.1:

$$\eta(\dot{\gamma}) = \frac{(1+\lambda)\tau_0(1-e^{-m\frac{\dot{\gamma}}{\dot{\gamma}_{crit}}})}{\dot{\gamma}} + k\dot{\gamma}^{n-1} \qquad \text{[Pas]} \qquad (9.1)$$

In Eq. 9.1, the shear-rate dependent viscosity $\eta(\dot{\gamma})$ is calculated by the Herschel-Bulkley equation, blended by the Papanastasiou regularization with $m$ as the blending parameter.

Following the findings from Chapter 8, $m = 1000$. $\dot{\gamma}_{crit}$ is the critical shear rate. $\lambda$ is the structural parameter, which is calculated as time- and shear rate- dependent derivative. The code implementation of $\lambda$ into OpenFOAM was developed by [de Schryver, Robin (2022)], who employed the variable $S$ as structural parameter. The implemented thixotropy formulation in OpenFOAM resembles the model proposed by [Roussel (2006)]:

$$\frac{d\lambda}{dt} = \frac{1}{T\lambda} - \alpha\lambda\dot{\gamma} \qquad [-] \quad (9.2)$$

$T$ is equivalent to the flocculation time $\Theta$. The breakdown parameter $\alpha$ corresponds to $k_1$.

Several simulations with varying buildup and breakdown parameters were carried out. For the flocculation time, values of $T = 50, 100, 200$ and $500$ s were tested. For the breakdown parameter, $\alpha = 0.10, 0.15$ and $0.20$.

## 9.2.2 Numerical flow simulation

Simulation results for all simulations are displayed in Figure 9.1. Figure 9.1 (a) shows the flow over time for the slump flow simulations in comparison to the final experimental flow radius $r_{x,fin}$. Figure 9.1 (b) illustrates the flow over time for all L-Box simulations in comparison to the experimental flow length $l_x$.



(a) Numerical slump flow results          (b) Numerical L-Box flow results
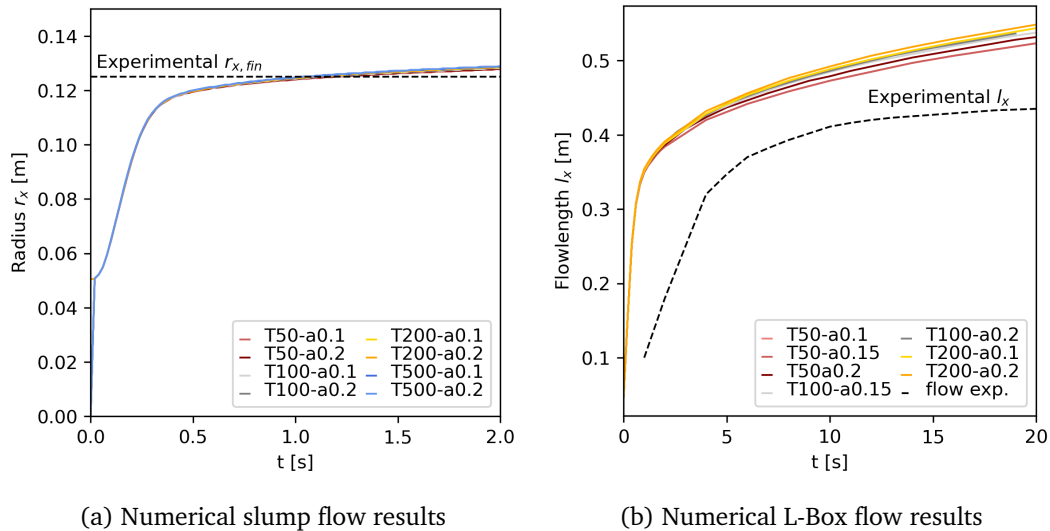
Figure 9.1: Flow over time results for different thixotropy parameters for both geometries

While the slump flow simulation was recorded for 2 s, flow proceeded fast and reached the experimentally measured slump radius after 1 s. The variation of thixotropy parameters did not affect the flow radius. On the contrary, L-Box flow simulations were recorded for 20 s of flow. The simulation time did not suffice to compute the flow stoppage. Furthermore,

thixotropy parameters affected the flow: Longer flocculation times $T$ and higher deflocculation values of $\alpha$ led to faster flow evolution. Conversely, increased thixotropy reduced the flow velocity.

### 9.2.3   The effect of thixotropy on transient and local flow properties

Transient flow properties were analyzed by evaluating the two-dimensional shapes. In Figure 9.2, the shear rate distribution $\dot{\gamma}$ and the structural parameter $S$ are visualized for the simulation cases T50-$\alpha$0.1 over the two-dimensional shapes of the slump (see Figure 9.2 (a) and Figure 9.2 (b)) and the L-Box flow body (see Figure 9.2 (c) and Figure 9.2 (d)). The density distribution of the rheological parameters is stored in the histogram of each graphic, with bin values for the density distribution of 100. The graphics are not normalized to one maximum value to see differences within one flow simulation and point in time mor clearly.



(a) $\dot{\gamma}$ distribution during slump flow

(b) $S$ distribution during slump flow

(c) $\dot{\gamma}$ distribution during L-Box flow

(d) $S$ distribution during L-Box flow
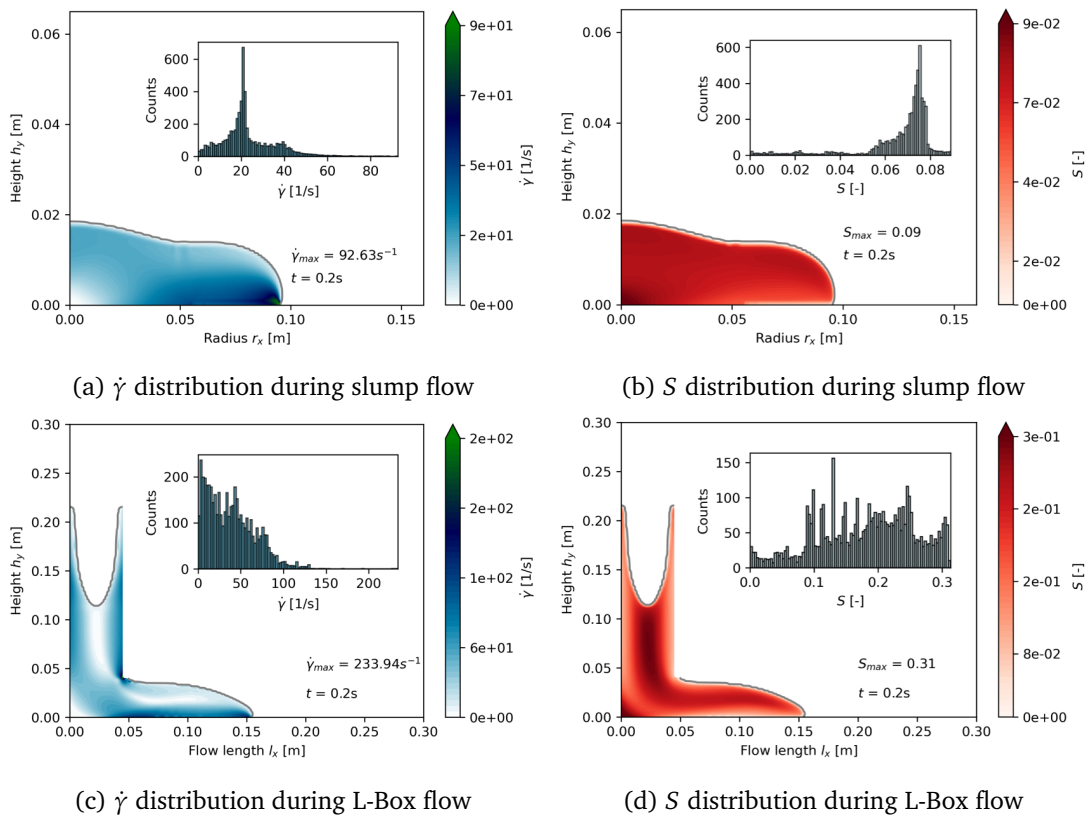
Figure 9.2: Two-dimensional shear rate and structural buildup distribution after 0.2 s of flow

The graphics reveal that shortly after flow start, higher shear rates are apparent in the L-Box, possibly due to a higher pressure field originating from higher gravitational forces and increased acceleration onto the paste. Still, already after 0.2 s of flow, higher structural values $S$ exist in the L-Box, with $S_{max} = 0.31$ compared to a maximum value of $S_{max} = 0.09$ in the slump test. Furthermore, the density distribution illustrates the broad variation of $S$

values over the two-dimensional shape of the L-Box compared to the $S$ distribution in the slump shape.

The time-dependent evolution of the structural parameter $S$ increases the paste viscosity and, along with that, reduces shear rates. Reduced shear rates during flow are exemplary visualized in Figure 9.3. After 1 s, slump flow has nearly stopped. While $\dot{\gamma}_{max} = 13.26 s^{-1}$, both the density distribution and the color distribution in Figure 9.3 (a) illustrate that flow only occurs at the outer radius, but flow has stopped or nearly stopped for the rest of the slump flow body. However, only little structure has built up: Figure 9.3 (b) shows that $S_{max} = 0.2$. Because structural buildup evolves time-dependently, little structural buildup can affect the flow after 1 s. On the contrary, the L-Box is affected by the constantly evolving structural parameter $S$. Figure 9.3 (c) shows low shear rates for the L-Box flow after 10 s of flow. Comparing these data with Figure 9.1 (b), it becomes evident that flow continues for a longer period of time, but at low shear rates. This gives chance to the structural parameter $S$ to evolve, with a maximum value of $S_{max} = 0.7$ in Figure 9.3 (d).



(a) $\dot{\gamma}$ distribution during slump flow

(b) $S$ distribution during slump flow

(c) $\dot{\gamma}$ distribution during L-Box flow

(d) $S$ distribution during L-Box flow
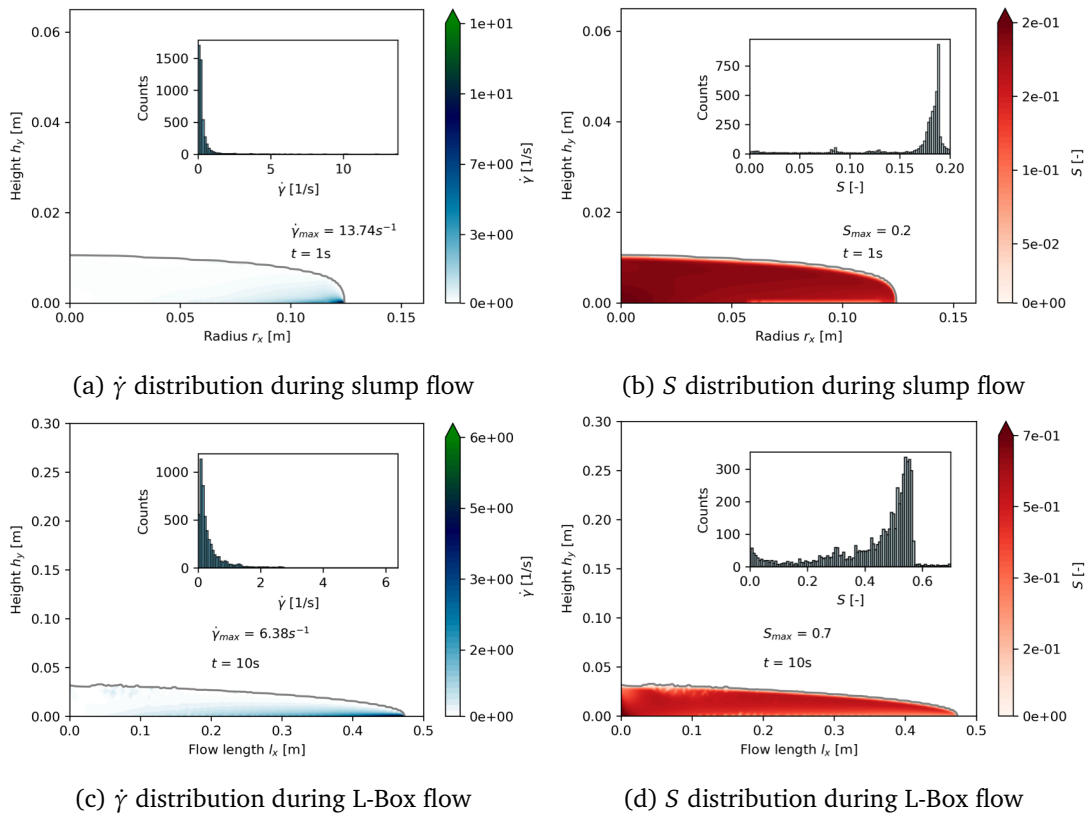
Figure 9.3: Two-dimensional shear rate and structural buildup distribution after 1 s of flow for the slump and 10 s of flow for the L-Box

Figure 9.4 shows the evolution of the structural parameter. Two values for all simulation cases were calculated: Once, only the maximum structural value $s_{max}$ for each calculated time step is illustrated. The virtual value $S_{cum}$ demonstrates the calculated area under the density distribution previously illustrated in the histograms of Figure 9.2.

(a) Numerical slump flow results

(b) Numerical L-Box flow results
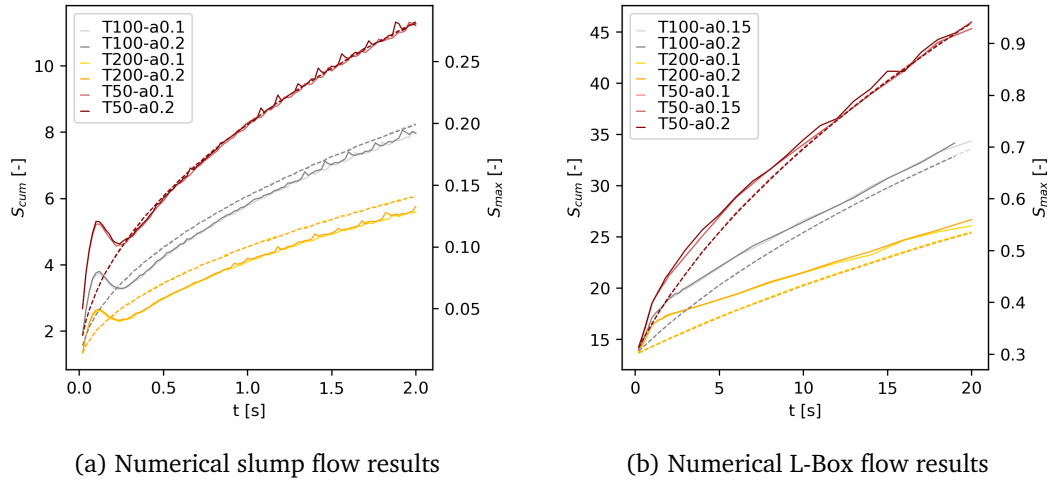
Figure 9.4: Evolution of structural parameter over time

The flocculation time $T$ affects the structural parameter significantly: With decreasing flocculation time, structural buildup proceeds stronger. The deflocculation parameter $\alpha$ shows little influence on both the maximum structural value $S_{max}$ and on $S_{cum}$. However, deflocculation also affects local flow properties significantly, which becomes visible in Figure 9.5. For a chosen time step of t = 4 s, the distribution of the viscosity $\eta$ is visualized for four different L-Box simulations with varying $T$ and $\alpha$.



(a) $\eta$ distribution for T50-a0.1

(b) $\eta$ distribution for T50-a0.2

(c) $\eta$ distribution for T200-a0.1

(d) $\eta$ distribution for T200-a0.1
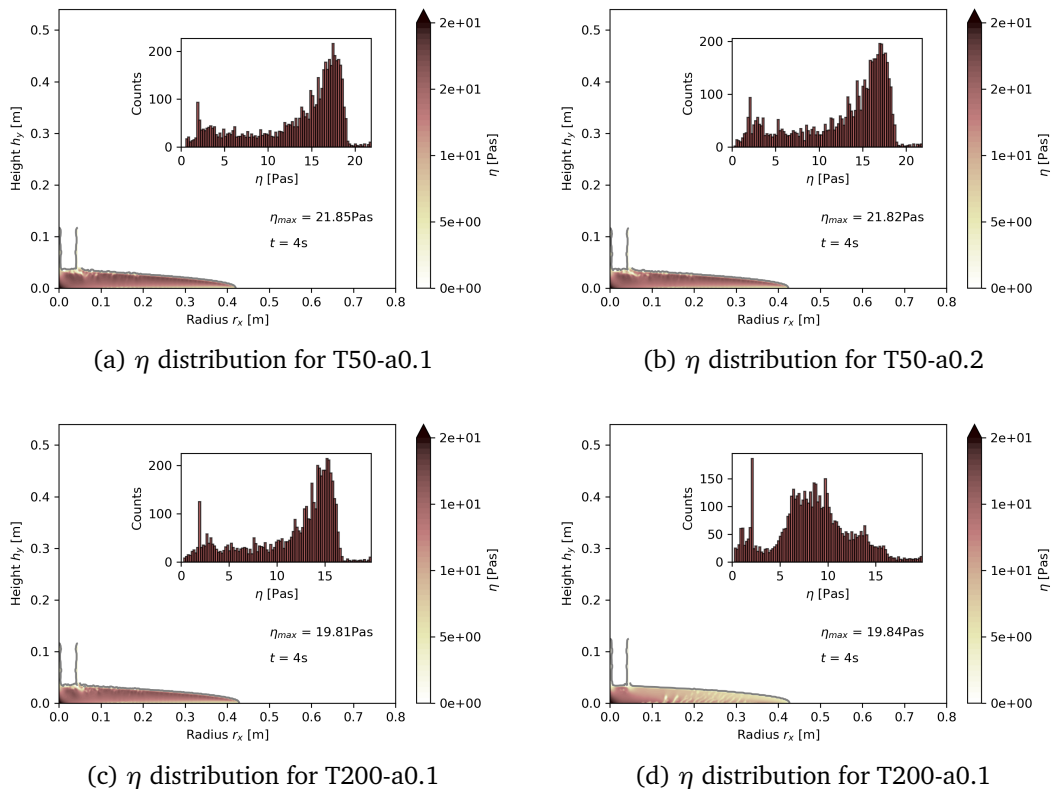
Figure 9.5: Two-dimensional distribution of the viscosity $\eta$ after 4 s of flow for the L-Box

The viscosity depends on the structural evolution. Once the deflocculation parameter $\alpha$ is increased, $\eta$, while exhibiting similar $\eta_{max}$ values, varies over the two-dimensional shape. However, the effect of $\alpha$ on the viscosity also depends on $T$: If the flocculation time $T$ is high, in 9.5 (c) and 9.5 (d) $T = 200$ s and, therefore, structural buildup is weaker compared to lower $T$ values, $\alpha$ affects the viscosity compared to simulations with a flocculation time of $T = 100$ s. The theoretical model for $\frac{d\lambda}{dt}$, presented in Eq. 7.1 in Chapter 7, has already illustrated these dependencies, see Figure 7.2. It beomes clear that with the chosen simulation setup, these dependencies can be replicated and local and transient phenomena of thixotropic paste flow can be calculated and visualized.

## 9.3   Conclusions and outlook

By integrating experimentally determined rheological properties of the cementitious paste into a numerical CFD model, transient and local flow properties were investigated. The slump flow test converged fast towards its ultimate flow diameter. Varying thixotropy parameters did not affect the flow performance of the slump flow test, indicating its classification as a time-independent flow test.

On the contrary, the L-Box flow was affected by thixotropy. As flow duration increased, the structural parameter evolved, influencing rheological parameters and subsequently shear rates during flow. Given that slower flows facilitate additional flocculation, structural buildup exerts a more pronounced effect on the suspension over time. While this relationship is not directly quantifiable, numerical simulation provided the visualization of the thixotropy's influence on local flow phenomena. The two-dimensional visualization of rheological parameter distributions facilitated the comprehension of local and transient flow properties.

However, several research questions remain open. Firstly, research must focus on further experimental analysis of structural buildup and breakdown parameters through rheometry and their subsequent integration into numerical frameworks to model thixotropy accurately and close to reality. Secondly, the impact of mathematical regularization techniques for thixotropy-implemented yield stress equations requires further investigation.

# Part IV

# Wrap-up

# 10. Summary and conclusions

A methodology was presented to understand transient rheology of cementitious pastes. The effect of the paste composition on the viscoelastic, viscoplastic, and thixotropic properties was investigated. Consequently, their flow behavior in flow tests was depicted through numerical simulations. The rheology of cementitious pastes was classified, and solutions were proposed for conducting straightforward, applicable, and adoptable rheometric investigations, rheological phenomenological modeling, and numerical simulations.

## 10.1   Phenomenological flow classification

A general rheology map was introduced to classify the elasto-visco-plastic (EVP) properties of cementitious pastes. Critical yield strains $\gamma_l$ displayed the threshold between elastic deformation and viscous flow behavior. With increasing $\Phi_s$ and superplasticizer amount, $\gamma_l$ increased. The parameters $e$ and $S$ gave insights into the intra-cyclic deformation behavior, which supports the description of superplasticizer effects on nonlinear viscoelastic properties. Meanwhile, the critical yield stresses $\dot{\gamma}_{crit}$ displayed the threshold between plastic contribution and viscous flow for the viscoplastic characterization. While the viscous part beyond $\dot{\gamma}_{crit}$ required different phenomenological models as "best fit", the plastic part below $\dot{\gamma}_{crit}$ was led by flocculation behavior and the elastic contribution. Following a comprehensive study of linear and nonlinear viscoplastic and viscoelastic parameters, the final mapping was reduced to the non-Newtonian index $n$, the phase shift angle $\delta$ and the yield index.

As introduced in Chapter 6, the mapping of the macroscopic EVP properties over all test series is depicted in Figure 10.1 (a). All raw data are stored in Appendix A. Figure 10.1 (a) shows all test series regarding their solid volume fraction $\Phi_s$, irrespective of their binder composition or flowability. The transition from "viscoplastic rigid pastes" to "viscoelastic soft pastes" happens with increasing $\Phi_s$: Because more superplasticizer is needed, no rigid behavior but rather a high viscoelastic regime and transition zone are measured. Figure 10.1 (b) shows the increasing non-Newtonian index $n$ with increasing $\Phi_s$ for all test series.[1] The increase is most pronounced for the CEMI test series; the LC3 series show the lowest $n$ values. Surprisingly, $n$ tends to be higher with higher flowability, which means that superplasticizer addition does not only affect the intra-cyclic strain-stiffening or strain-softening viscoelasticity but also the nonlinear viscoplastic flow.

---

[1]The regression curves in Figure 10.1 (b) and subsequent Figures 10.2 and 10.3 are solely descriptive but do not intend to constitute empirical relationships. Regression parameters are attached in A.5.

(a) EVP mapping with $n$, $\delta$ and Yield index          (b) Non-Newtonian index $n(\Phi_s)$
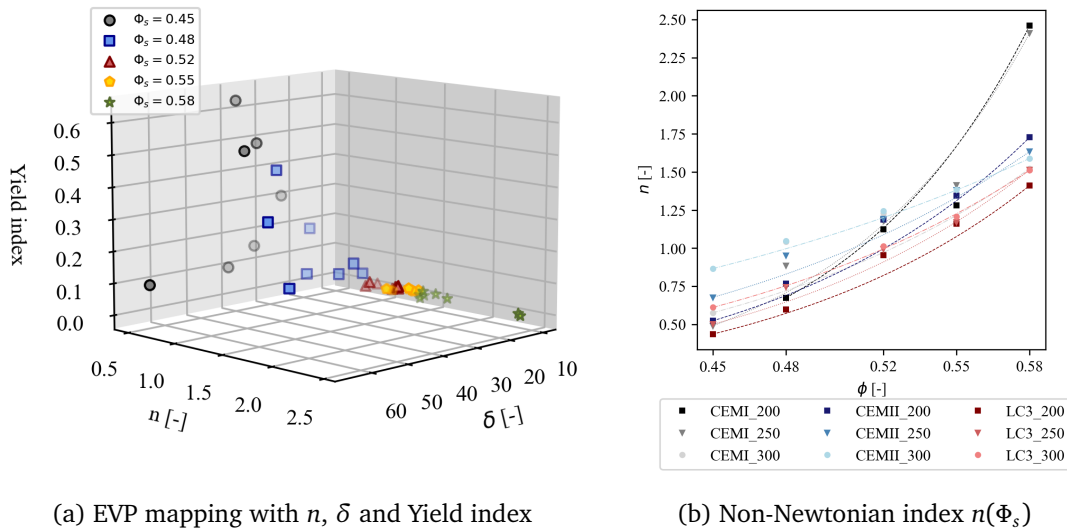
Figure 10.1: Macroscopic viscoelastic and viscoplastic properties of all test series

Thixotropy was analyzed with different measuring and modeling methods. Finally, a time- and shear rate-dependent structural parameter, combining an established constitutive formulation with experimental methods, was posed and analyzed for different pastes. Figure 10.2 displays the two most descriptive thixotropy parameters investigated in Chapter 7 for all test series. Figure 10.2 (a) shows the thixotropy parameter $A_{thix}$ (which is here the early thixotropy $A_{thix,early}$ from Chapter 7). $A_{thix}$ increases with increasing $\Phi_s$, as already investigated for a smaller set in Chapter 7. With increasing flowability, $A_{thix}$ yields smaller values for all test series. With increasing $\Phi_s$, nonlinear modeling of the static yield stress increase $\tau(t)$ displayed the structural buildup better than the linear $A_{thix}$. All calculated values for all test series are attached in Appendix A.3.



(a) $A_{thix}$ depending on $\Phi_s$          (b) $\Theta$ depending on $\Phi_s$
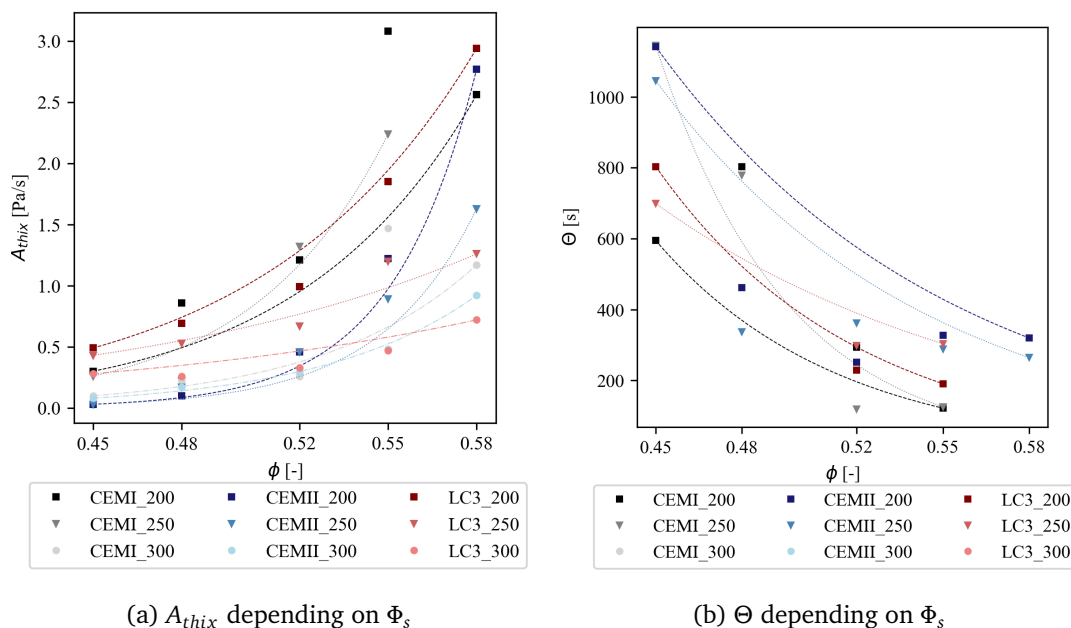
Figure 10.2: Thixotropy and structural buildup analysis for all test series

Figure 10.2 (b) shows the flocculation time $\Theta$, investigated with the non-destructive SAOS test. While the analysis of $\Theta$ still incorporates uncertainties, the general relation between $\Phi_s$ and $\Theta$ becomes obvious: With increasing $\Phi_s$, $\Theta$ decreases, which corresponds to a higher thixotropy. However, while $A_{thix}$ solely displayed the structural buildup at rest, $\Theta$ could be integrated as reciprocal of a structural buildup parameter $k_2$ into a time- and shear rate dependent model for the structural parameter $\lambda$. ll calculated values for all test series are attached in Appendix A.4.

Following the posed research questions at the end of Chapter 3, main findings are briefly outlined subsequently:

**Viscoplastic analysis**

- At which point do cement pastes deviate from linear viscoplastic behavior?
  $\rightarrow$ The solid volume fraction $\Phi_s$ was found to crucially affect the non-Newtonian index and, thus, the deviation from linear viscoplastic paste flow. The flow curve analysis of different binder compositions affects the threshold between shear-thinning, linear, and shear-thickening viscosities. The effect of microstructural properties on the evolution of viscoplastic properties is beyond the scope of this thesis. Varying maximum solid volume fractions $\Phi_{max}$ for the different binders and the subsequent effect on rheology is shortly analyzed in Appendix A.5. Prospective mathematical modeling could investigate the relation between the solid volume fraction and the non-Newtonian index, emphasizing on further microstructural, physical and chemical properties.

**Viscoelastic analysis**

- What affects viscoelasticity?
  $\rightarrow$ With increasing $\Phi_s$, therefore decreasing water-to-binder ratios and increasing superplasticizer amount, the elasticity range increases and the yield index decreases. The strain-stiffening ratio $S$ evolves towards higher peaks at larger strain amplitudes $\gamma_0$, and the shear-thickening ratio $T$ possesses lower peaks at larger $\gamma_0$. The evolution $S(\gamma_0)$ and $T(\gamma_0)$ reveals strong differences depending on PCE and $\Phi_s$. Prospective mathematical modeling could cluster the effectiveness, for example, of superplasticizers.

**Thixotropy**

- What affects thixotropy?
  $\rightarrow$ Thixotropic structural buildup increases with higher solid volume fractions. Superplasticizer reduces $A_{thix}$. The microstructural theories behind, along with the calculation of interparticle forces within a cementitious suspension, has been state of ongoing research. This thesis shall outline that different rheometric investigations and mathematical models yield results with different information. For instance, the

nonlinear structural buildup model for static SYS tests is more descriptive than linear modeling with increasing $\Phi_s$. On the contrary, flocculation analysis became more meaningful with the oscillatory SAOS test.

→ Furthermore, it was elaborated that, while the effect of thixotropy on time- dependent flow is crucial, the structural buildup at rest analysis does not support the analysis of time-dependent flow. Modeling of a time- and shear rate- dependent structural parameter $\lambda$, along with parameters for structural buildup and breakdown, is required.

→ The effect of the structural buildup and breakdown parameters $k_1$ and $k_2$ or the flocculation time $T$ and breakdown parameter $\alpha$ on thixotropy and time-dependent flow was modeled. Challenges arose for the experimental analysis, because boundary conditions, such as an initial structural parameter $\lambda_0$, decisively affected the result. These boundary conditions, however, are ambiguous, and can vary depending on the colloidal network behavior, mixture preparation, resting time or other factors.

**Model choice**

- Which rheological models describe cement paste behavior the best over a large range of shear rate?

  → Various phenomenological models were tested on their suitability for the experimental flow curves. Depending on the rheological behavior, different models yielded the "best" results with the least error, see the flow curve evaluation in Appendix A. However, applying different models for different flow curves means that results are not directly comparable anymore. Therefore, for this thesis, it was chosen that the well-established Herschel-Bulkley model, due to its non-Newtonian index $n$, is applicable for a wide range of cementitious pastes. It deploys the most meaningful information to characterize the flow behavior, while solely three rheological model parameters are applied. The implementation of a structural parameter $\lambda$ could depict flocculation behavior also below the critical shear rate. However, also the Herschel-Bulkley model incorporates drawbacks: It solely displays a consistency index $k$ rather than values for the viscosity $\eta$. In different research frameworks, other models might yield the most suitable fits. The model choice can be very subjective. For instance:

  → The Cross model provides rheological parameters for the viscosity at zero shear rate, $\eta_0$, or infinity shear rates, $\eta_\infty$, which can provide valuable material information, e.g. for the calculation and computation of mixing procedures where viscosities can become rather important than yield stress values.

  → The modified Bingham model divides the viscosity in two contributions, which are likely to be classified as colloidal contribution and viscous dissipation. It further provides a yield stress and an exponential index, which can be calculated as deviation from linear viscoplasticity.

  → Discontinuous viscosity modeling, the viscosity description by de Souza Mendez, Eq. 3.18, or viscosity modeling as presented by Ogawa, Eq. 3.9, can reveal flow discontinuities and nonlinear viscosities more detailed. However, due to an increased

amount of model parameters, the chance to model rheology in the wrong way increases.

Combined models for viscoelasticity, viscoplasticity and thixotropy pledge a holistic rheological classification. It is however pointed out that the experimental analysis, along with single rheological models and a final mapping of relevant parameters, proves to be more descriptive than one single model. It is, therefore, recommended to not draw one holistic model but rather a rheological classification map.

## 10.2   Rheology between modeling and rheometry

Rheological properties were studied both mathematically and experimentally. Briefly summarized, it was found that the geometric device, mixing procedure, rheometric profile, raw data handling and final mathematical regression functions significantly affected the calculated rheological parameters. Some key observations and challenges are outlined:

- The challenge of the state of flocculation: The most-deflocculated or most flocculated microstructural state in cementitious suspensions yields the ideal boundary condition for a repeatable rheometric test and subsequent combination with microstructural properties. However, they are not practically achievable. The choice of mixing procedure therefore depends on the researcher. The effect of all boundary conditions on rheological parameters should be tested beforehand, and subsequently reported.

- The challenge of the unknown flow field: With increasing solid volume fraction, cementitious pastes exhibit increasingly shear-thickening consistencies. Rheometric investigations proved that once cementitious paste deviate from linear viscoplasticity, large-gap rheometry introduces errors. The shear field in the gap is unknown and, therefore, conversion equations from raw data to rheological parameters introduce challenges. Similar challenges arise in small-gap rheometry over the height of the gap.

- Furthermore, once the relation between rheometric input and output (rotational velocity vs. torque) becomes nonlinear, the calculation of rheological parameters depends on the choice of the raw data input range.

## 10.3 Time-dependent paste flow and transient flow computation with CFD

### 10.3.1 Thixotropy effect on time-dependent flow

Thixotropy is the time-dependent change of viscosity. The computation of flow scenarios becomes time-dependent once interparticle forces in cementitious pastes lead to thixotropy, and the applied load to the material (either by an applied pressure field, e.g. in pumping scenarios, gravitational forces in free-surface fall or flows, or mixing energy) is not sufficient to prevent flocculation.

In this thesis, the evolution from time-independent flow scenarios towards time-dependent flow was depicted by the comparison between the slump flow test and the L-Box test. Flow test results of the L-Box test and the relationship between the L-Box flow length and $A_{thix}$ for all test series are illustrated in Figure 10.3.



(a) L-Box results depending on $\Phi_s$        (b) L-Box results depending on $A_{thix}$
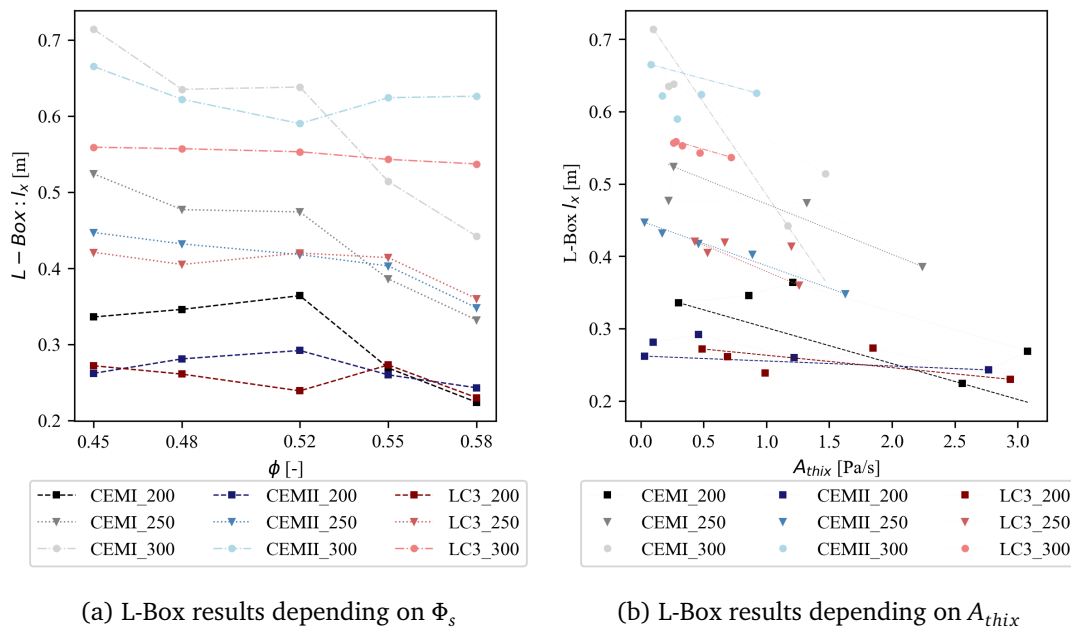
Figure 10.3: Effect of mixture composition and the thixoptropy parameter $A_{thix}$ on the flow length in the L-Box test for all test series

Results for all test series consolidate the findings from previous research summarized in Chapter 5. Flow length results vary depending on the test series. However, all L-Box flow length results decrease with increasing $A_{thix}$. While the relation between thixotropy and flow length was obvious, transient computation required both CFD modeling and a time- and shear rate resolved structural parameter $\lambda$.

## 10.3.2 CFD simulation and analysis of transient features

In the CFD analysis, viscous flow computation, a reliable CFD model for free-surface flow, and thethixotropy-implemented viscous flow were analyzed. Investigations yielded in reliable computational meshes for the slump cone and the L-Box. The effect of the numerical regularization technique was elaborated and reduced to a minimum error. Finally, a time- and shear rate-dependent structural parameter was implemented to analyze the effect of thixotropy on transient flow properties. The findings indicate that parameters such as flocculation time and deflocculation parameter affect the computational flow, aligning well with previously studied thixotropy parameters obtained through rheometry.

Summarized, the accuracy of the computational model is the most significant factor in conducting scientifically reliable analyses of thixotropic free-surface flow. This necessitates comprehensive preliminary work on the numerical model, which can be time-consuming. However, once a reliable CFD model is established, it can significantly enhance the understanding of rheological phenomena, especially with regards to time-dependent properties and the effect of thixotropy on the flow evolution. Several key observations and benefits stemming from this research are briefly outlined:

- The combination of phenomenological modeling and CFD simulation renders model parameters more meaningful, aiding in the selection of the optimal model for a given cementitious material and processing scenario. For instance:

    1. Do I need an implementation of zero viscosity and infinity viscosity? And if so, which parameters are suitable?

    2. How does a yield stress model in comparison to a viscosity model affect the numerical flow?

    3. Are regularization parameters purely numerical or can they be depicted by physical model parameters?

- Advanced post-processing methods aid in the understanding of cement and concrete flow, for example through the visualization of local flow phenomena:

    1. Visualization of the shear rate distribution: Dependent on the geometric conditions and flow evolution, how does the velocity field and thus, the shear rate distribution evolve?

    2. Where does thixotropic structural buildup, consequently, affect or even stop the flow? How do the model parameters need to change to optimize the flow, so how does the mixture need to change?

## 10.4   Outlook and open research questions

Summarized, the thesis introduced a novel framework for categorizing the transient flow behavior of thixotropic cementitious pastes. A bridging between rheometric values, flow tests and CFD simulation was possible through time-independent slump flow tests and time-dependent L-Box tests. The introduced framework is adoptable for the processing scenarios that cannot be replicated in flow tests, but where the evaluation of thixotropy becomes of importance. Subsequently, the modeling and simulation of cement and concrete flow offers a promising avenue for gaining deeper insights into the nonlinear rheology of cement and concrete, visualizing transient properties, and tailoring rheological properties of mixtures to suit specific processing requirements.

Despite (or additionally to) the findings, new research questions emerged in each of the disciplines.

The proposed rheological classification solely offers one approach for measuring and modeling viscoplasticity, viscoelasticity, and thixotropy. However, there is a need to extend this framework towards a comprehensive Transient Thixo-Elasto-Viscoplastic (TTEVP) classification. Such an approach would ensure reliable characterization of composition-dependent rheological properties through robust measurement protocols. A further research framework could explore a wider range of rheological models, establish mathematical and statistical thresholds to determine model adequacy, and apply this framework to various cementitious materials with diverse binder compositions, multi-blended binder systems, and different chemical admixtures. Furthermore, the developing field of automated statistical analysis could assess a variety of rheological models, and develop the field of rheological modeling by introducing novel mathematical approaches.

All applied methods and findings could be coupled with microstructural rheology. The analysis of particle shapes, particle size distributions, the chemical composition of the carrier liquid and hydration products enables the calculation of interparticle forces, and, thus, an estimation for the deformation or flocculation behavior, of cementitious pastes. Independently from this thesis, but along with the research project, the rheological properties from oscillatory tests (yield stress $\tau_y$, yield strain $\gamma_l$ and structural buildup) were coupled with microstructural modeling approaches, see [Ukrainczyk et al. (2020); Thiedeitz et al. (2023)]. Further research is required to develop robust microstructural models to compute the nonlinear rheological properties. Findings could yield in physically-based constitutive models for the $\phi_s$-related non-Newtonian index as illustrated in Figure 10.1, and physically- and chemically driven models for the analysis of flocculation time as illustrated in Figure 10.2. Consequently, targeted TTEVP rheology could be implemented into the mixture design of cement and concrete compositions. Prospectively, a strong focus should be put on the rheology of multi-blended systems and chemical admixtures.

Finally, the application of numerical simulations using Computational Fluid Dynamics yielded in findings, but even more open questions. While a structural parameter could be tested in CFD, and its impact on time-dependent flow aligned with the rheological theory behind,

several mathematical and numerical questions remain open:

- Analysis of the numerical error when highly viscous flow with very low Reynolds numbers occurs
  $\rightarrow$ The effect of low Reynolds numbers $< 1$ on the numerical result, especially the discretization error, has yet to be investigated. Research to analyze the highly viscous flow using the Navier-Stokes equations, focusing on the Navier part of the equations, could enhance the computation of slow flow

- Effect of surface tension in VoF frameworks
  $\rightarrow$ The surface tension between cement paste and air, or concrete and air, has, so far, not been investigated. However, the parameter affects the weighting function of the Navier-Stokes equations in the VoF method. Not only numerical analysis is required, but especially the coupling with experimental investigations on the real surface tension and contact angles of cementitious pastes and air

- The gap between rheometric and numerical thixotropy
  $\rightarrow$ The implementation of structural buildup and breakdown parameters into the numerical transport equations had less effect on the numerical flow than in the experimental tests. Various factors can explain this gap. However, this gap should be investigated, and further thixotropy models should be applied in time-dependent numerical flow simulations.

- The development of further regularization methods
  $\rightarrow$ The regularization method affected the flow result where shear rates tended towards zero. While the effect of regularization in combination with viscoplastic modeling was clearly elaborated, precise regularized thixotropy modeling has yet to be investigated.

- Are viscosity-related models without yield stress a better choice?

# Bibliography

M. S. Abo Dhaheer, S. Kulasegaram, and B. L. Karihaloo. Simulation of self-compacting concrete flow in the j-ring test using smoothed particle hydrodynamics (sph). *Cement and Concrete Research*, 89:27–34, 2016. doi: 10.1016/j.cemconres.2016.07.016. PII: S0008884616304963.

A. B. Almeida and A. B. Franco. Modeling of dam-break flow. In M. H. Chaudhry and L. W. Mays, editors, *Computer Modeling of Free-Surface and Pressurized Flows*, pages 343–373. Springer Netherlands, Dordrecht, 1994. ISBN 978-94-010-4417-2. doi: 10.1007/978-94-011-0964-2{\textunderscore}12.

H. Altenbach. *Kontinuumsmechanik*. Springer Berlin Heidelberg, 2018. ISBN 978-3-662-57503-1. doi: 10.1007/978-3-662-57504-8.

R. Andrew. Global co2 emissions from cement production, 1928-2018. *Earth System Science Data*, 11(4):1675–1710, 2019. doi: 10.5194/essd-11-1675-2019.

G. Artioli and R. Oberti, editors. *The Contribution of Mineralogy to Cultural Heritage*. Mineralogical Society of Great Britain and Ireland, 2019. ISBN 9780903056618. doi: 10.1180/EMU-notes.20.

A. R. Arunothayan, B. Nematollahi, K. H. Khayat, A. Ramesh, and J. G. Sanjayan. Rheological characterization of ultra-high performance concrete for 3d printing. *Cement and Concrete Composites*, 136:104854, 2023. ISSN 09589465. doi: 10.1016/j.cemconcomp.2022.104854.

A. Assaad, K. Khayat, and H. A. Mesbah. Assessment of thixotropy of flowable and self-consolidating concrete. *ACI Materials Journal*, 100(2), 2003. doi: 10.14359/12548. URL https://doi.org/10.14359/12548.

F. Aureli, A. Maranzoni, G. Petaccia, and S. Soares-Frazão. Review of experimental investigations of dam-break flows over fixed bottom. *Water*, 15(6):1229, 2023. doi: 10.3390/w15061229.

N. M. Azmee and N. Shafiq. Ultra-high performance concrete: From fundamental to applications. *Case Studies in Construction Materials*, 9:e00197, 2018. ISSN 22145095. doi: 10.1016/j.cscm.2018.e00197.

I. Babuska and J. Oden. Verification and validation in computational engineering and science: basic concepts. *Computer Methods in Applied Mechanics and Engineering*, 193(36-38):4057–4066, 2004. ISSN 00457825. doi: 10.1016/j.cma.2004.03.002.

H. A. Barnes. Thixotropy—a review. *Journal of Non-Newtonian Fluid Mechanics*, 70(1-2): 1–33, 1997. ISSN 03770257. doi: 10.1016/S0377-0257(97)00004-9.

H. A. Barnes. The yield stress - a review or panta rei - everything flows? *Journal of Non-Newtonian Fluid Mechanics*, 81:133–178, 1999. ISSN 03770257.

H. A. Barnes, J. F. Hutton, and K. Walters. *An introduction to rheology*, volume 3 of *Rheology series*. Elsevier, Amsterdam, 3. impression edition, 1993. ISBN 0-444-87140-3. Hutton, John F. (VerfasserIn) Walters, Kenneth (VerfasserIn).

D. P. Bentz, C. F. Ferraris, M. A. Galler, A. S. Hansen, and J. M. Guynn. Influence of particle size distributions on yield stress and viscosity of cement–fly ash pastes. *Cement and Concrete Research*, 42(2):404–409, 2012. ISSN 00088846. doi: 10.1016/j.cemconres. 2011.11.006.

P. Billberg. *Form pressure generated by self-compacting concrete*, volume 85 of *TRITA-BKN. bulletin*. KTH Architecture and Built Environment, Stockholm, 2006. ISBN 91-7178-464-0.

E. C. Bingham. An investigation of the laws of plastic flow. *Bulletin of the National Institute of Standards and Technology*, 13(2):309, Aug. 1916. doi: 10.6028/bulletin.304. URL https://doi.org/10.6028/bulletin.304.

Ö. Biricik and A. Mardani. Parameters affecting thixotropic behavior of self compacting concrete and 3d printable concrete; a state-of-the-art review. *Construction and Building Materials*, 339:127688, 2022. ISSN 09500618. doi: 10.1016/j.conbuildmat.2022.127688.

O. Bonneau, C. Vernet, M. Moranville, and P.-C. Aitcin. Characterization of the granular packing and percolation threshold of reactive powder concrete. *Cement and Concrete Research*, 30(12):1861–1867, Dec. 2000. doi: 10.1016/s0008-8846(00)00300-8. URL https://doi.org/10.1016/s0008-8846(00)00300-8.

J. Brackbill, D. Kothe, and C. Zemach. A continuum method for modeling surface tension. *Journal of Computational Physics*, 100(2):335–354, 1992. ISSN 00219991. doi: 10. 1016/0021-9991(92)90240-Y. PII: 002199919290240Y.

R. Brown. Xxvii. a brief account of microscopical observations made in the months of june, july and august 1827, on the particles contained in the pollen of plants; and on the general existence of active molecules in organic and inorganic bodies. *The Philosophical Magazine*, 4(21):161–173, 1828. doi: 10.1080/14786442808674769.

A. Castillo, F. Rozas, I. Martínez, and M. Castellote. Understanding cementitious materials in fresh state: A nano-scale study on the effect of the mixing time. *Journal of Alloys and*

*Compounds*, 536:S569–S574, 2012. ISSN 09258388. doi: 10.1016/j.jallcom.2011.12. 106. PII: S0925838811023905.

C. Chang and R. L. Powell. Effect of particle size distributions on the rheology of concentrated bimodal suspensions. *Journal of Rheology*, 38(1):85–98, Jan. 1994. doi: 10.1122/1.550497. URL https://doi.org/10.1122/1.550497.

E. Chaparian and B. Nasouri. L-box- a tool for measuring the "yield stress": A theoretical study. *Physics of Fluids*, 30(8):083101, 2018. ISSN 1070-6631. doi: 10.1063/1.5042410.

D. C. Cheng. Thixotropy. *International journal of cosmetic science*, 9(4):151–191, 1987. ISSN 0142-5463. doi: 10.1111/j.1467-2494.1987.tb00472.x. Journal Article.

D. C.-H. Cheng and F. Evans. Phenomenological characterization of the rheological behaviour of inelastic reversible thixotropic and antithixotropic fluids. *British Journal of Applied Physics*, 16(11):1599–1617, Nov. 1965. doi: 10.1088/0508-3443/16/11/301. URL https://doi.org/10.1088/0508-3443/16/11/301.

R. Chhabra and J. Richardson. *Non-Newtonian Flow and Applied Rheology*. Elsevier, 2008. ISBN 978-0-7506-8532-0. doi: 10.1016/b978-0-7506-8532-0.x0001-7. URL https://doi.org/10.1016/b978-0-7506-8532-0.x0001-7.

M. S. Choi, Y. J. Kim, and J. K. Kim. Prediction of concrete pumping using various rheological models. *International Journal of Concrete Structures and Materials*, 8(4):269–278, 2014. ISSN 1976-0485. doi: 10.1007/s40069-014-0084-1.

P. Coussot and C. Ancey. Rheophysical classification of concentrated suspensions and granular pastes. *Physical Review E*, 59(4):4445–4457, 1999. doi: https://doi.org/10.1103/PhysRevE.59.4445.

P. Coussot, Q. D. Nguyen, H. T. Huynh, and D. Bonn. Viscosity bifurcation in thixotropic, yielding fluids. *Journal of Rheology*, 46(3):573–589, 2002. ISSN 0148-6055. doi: 10.1122/1.1459447.

W. Cui, W.-s. Yan, H.-f. Song, and X.-l. Wu. Blocking analysis of fresh self-compacting concrete based on the dem. *Construction and Building Materials*, 168:412–421, 2018. ISSN 09500618. doi: 10.1016/j.conbuildmat.2018.02.078.

W. Cui, W.-s. Yan, H.-f. Song, and X.-l. Wu. Dem simulation of scc flow in l-box set-up: Influence of coarse aggregate shape on scc flowability. *Cement and Concrete Composites*, 109:103558, 2020. ISSN 09589465. doi: 10.1016/j.cemconcomp.2020.103558.

P. A. Cundall and Q. Strack. A discrete numerical model for granular assemblies. *Geotechnique*, 29:47–65, 1971.

M. Daimon and D. M. Roy. Rheological properties of cement mixes: Ii. zeta potential and preliminary viscosity studies. *Cement and Concrete Research*, 9(1):103–109, 1979. ISSN 00088846. doi: 10.1016/0008-8846(79)90100-5.

D. de Kee and C. F. Chan Man Fong. Rheological properties of structured fluids. *Polymer Engineering and Science*, 34(5):438–445, 1994. ISSN 0032-3888. doi: 10.1002/pen.760340510.

R. de Schryver and G. de Schutter. Insights in thixotropic concrete pumping by a poiseuille flow extension. *Applied Rheology*, 30(1):77–101, 2020. doi: 10.1515/arh-2020-0103.

R. de Schryver, K. El Cheikh, K. Lesage, M. Y. Yardimci, and G. de Schutter. Numerical reliability study based on rheological input for bingham paste pumping using a finite volume approach in openfoam. *Materials (Basel, Switzerland)*, 14(17), 2021. ISSN 1996-1944. doi: 10.3390/ma14175011.

de Schryver, Robin. *Active rheology control of cementitious materials : numerical and experimental pumping investigation*. Dissertation, Ghent University, 2022.

P. R. de Souza Mendes. Modeling the thixotropic behavior of structured fluids. *Journal of Non-Newtonian Fluid Mechanics*, 164(1-3):66–75, 2009. ISSN 03770257. doi: 10.1016/j.jnnfm.2009.08.005. PII: S0377025709001578.

M. Dinkgreve, J. Paredes, M. M. Denn, and D. Bonn. On different ways of measuring "the" yield stress. *Journal of Non-Newtonian Fluid Mechanics*, 238:233–241, 2016. ISSN 03770257. PII: S0377025716302774.

P. Dittmar. 18 lofoten 14 bridge, 2023. URL `https://commons.wikimedia.org/w/index.php?curid=14641803`. CC BY-SA 2.0.

Y. El Bitouri and N. Azéma. On the "thixotropic" behavior of fresh cement pastes. *Eng*, 3 (4):677–692, 2022. doi: 10.3390/eng3040046.

J. Elsen, M. D. Jackson, and E. Ruiz-Agudo. Historic concrete science: Opus caementicium to "natural cements". *Elements*, 18(5):301–307, 2022. ISSN 1811-5209. doi: 10.2138/gselements.18.5.301.

B. Esmaeilkhanian, K. H. Khayat, and O. H. Wallevik. Mix design approach for low-powder self-consolidating concrete: Eco-scc—content optimization and performance. *Materials and Structures*, 50(2):265, 2017. ISSN 1359-5997. doi: 10.1617/s11527-017-0993-y. PII: 993.

P. Estelle, C. Lanos, A. Perrot, and S. Amziane. Processing the vane shear flow data from couette analogy. *Applied Rheology*, 18(3):1–6, 2008.

D. H. Everett. *Grundzüge der Kolloidwissenschaft*. Steinkopff, 1992. ISBN 3798508712.

R. H. Ewoldt. *Nonlinear viscoelastic materials : bioinspired applications and new characterization measures*. Dissertation, Massachusetts Institute of Technology, 2009. URL `http://hdl.handle.net/1721.1/49556`.

R. H. Ewoldt and G. H. McKinley. Mapping thixo-elasto-visco-plastic behavior. *Rheologica Acta*, 56(3):195–210, 2017. ISSN 0035-4511. doi: 10.1007/s00397-017-1001-8. PII: 1001.

R. H. Ewoldt, P. Winter, and G. H. McKinley. MITLaos User Manual, 2007.

R. H. Ewoldt, G. H. McKinley, and A. E. Hosoi. Fingerprinting soft materials. *Journal of Rheology*, 52(6):1427–1458, 2008. ISSN 0148-6055. doi: 10.1122/1.2970095. URL `http://arxiv.org/pdf/0710.5509v1`. Ewoldt, R. H., A. E. Hosoi and G. H. McKinley, "New measures for characterizing nonlinear viscoelasticity in large amplitude oscillatory shear," Journal of Rheology 52(6), 1427-1458 (2008) 10 pages, 3 figures, full-page double-space preprint format.

R. H. Ewoldt, M. T. Johnston, and L. M. Caretta. Experimental challenges of shear rheology: How to avoid bad data. In S. E. Spagnolie, editor, *Complex Fluids in Biological Systems*, Biological and Medical Physics, Biomedical Engineering, pages 207–241. Springer New York, New York, NY, 2015. ISBN 978-1-4939-2064-8. doi: 10.1007/ 978-1-4939-2065-5{\textunderscore}6.

S. Fataei. *Flow-Induced Particle Migration in Concrete under High Shear Rates*. Dissertation, Technische Universität Dresden, 2021.

J. Feda. Elasticity, viscosity and plasticity. In *Creep of Soils and Related Phenomena*, volume 68 of *Developments in Geotechnical Engineering*, pages 136–172. Elsevier, 1992. ISBN 9780444988225. doi: 10.1016/B978-0-444-98822-5.50008-9.

E. Fehling and M. Schmidt. Ultra-high-performance concrete: Research, development and application in europe. In *Proceedings of the International Workshop on Ultra-High Performance Concrete*, volume 228, pages 51–78. American Concrete Institute, 2005. ISBN 9780870316951. doi: 10.14359/16471.

S. A. A. M. Fennis-Huijben. *Design of ecological concrete by particle packing optimization*. Dissertation, Technische Universität Delft, Delft, 2010.

L. Ferrari, J. Kaufmann, F. Winnefeld, and J. Plank. Interaction of cement model systems with superplasticizers investigated by atomic force microscopy, zeta potential, and adsorption measurements. *Journal of Colloid and Interface Science*, 347(1):15–24, 2010. doi: 10.1016/j.jcis.2010.03.005. Journal Article.

C. F. Ferraris and F. de Larrard. Testing and modelling of fresh concrete rheology. Technical report, National Institute of Standards and Technology, 1998. URL `https://doi.org/ 10.6028/nist.ir.6094`.

R. D. Ferron, S. Shah, E. Fuente, and C. Negro. Aggregation and breakage kinetics of fresh cement paste. *Cement and Concrete Research*, 50:1–10, 2013. ISSN 00088846. doi: 10.1016/j.cemconres.2013.03.002.

J. H. Ferziger, M. Perić, and R. L. Street. *Numerische Strömungsmechanik*. Springer Berlin Heidelberg, Berlin, Heidelberg, 2020. ISBN 978-3-662-46543-1. doi: 10.1007/978-3-662-46544-8.

D. Feys, R. Verhoeven, G. de Schutter, A. Co, G. L. Leal, R. H. Colby, and A. J. Giacomin. Influence of thixotropy on pressures required during pumping of concrete. In *AIP Conference Proceedings*, pages 710–712. AIP, 2008. doi: 10.1063/1.2964819.

D. Feys, R. Cepuritis, S. Jacobsen, K. Lesage, E. Secrieru, and A. Yahia. Measuring rheological properties of cement pastes. *RILEM Technical Letters*, 2:129–135, 2017. ISSN 2518-0231. doi: 10.21809/rilemtechlett.2017.43.

B. A. Firth and R. J. Hunter. Flow properties of coagulated colloidal suspensions. *Journal of Colloid and Interface Science*, 57(2):248–256, 1976.

R. J. Flatt. *Interparticle forces and superplasticizers in cement suspensions*. Dissertation, EPFL Lausanne, Lausanne, 1999.

R. J. Flatt. Towards a prediction of superplasticized concrete rheology. *Materials and Structures*, 37(5):289–300, 2004a. ISSN 1359-5997. doi: 10.1007/BF02481674.

R. J. Flatt. Dispersion forces in cement suspensions. *Cement and Concrete Research*, 34 (3):399–408, Mar. 2004b. doi: 10.1016/j.cemconres.2003.08.019. URL https://doi.org/10.1016/j.cemconres.2003.08.019.

R. J. Flatt and P. Bowen. Electrostatic repulsion between particles in cement suspensions. *Cement and Concrete Research*, 33(6):781–791, 2003. ISSN 00088846. doi: 10.1016/S0008-8846(02)01059-1.

R. J. Flatt and P. Bowen. Yodel. *Journal of the American Ceramic Society*, 89(4):1244–1256, 2006. ISSN 0002-7820. doi: 10.1111/j.1551-2916.2005.00888.x.

R. J. Flatt and P. Bowen. Yield stress of multimodal powder suspensions. *Journal of the American Ceramic Society*, 90(4):1038–1044, 2007. ISSN 0002-7820. doi: 10.1111/j.1551-2916.2007.01595.x.

H. Freundlich. *Thixotropy*. Hermann & C, 1935. URL http://catalogue.bnf.fr/ark:/12148/cb321298687.

H. Freundlich. First Report on Viscosity and Plasticity. *The Journal of Physical Chemistry*, 43(8):1106, 1939. ISSN 0092-7325. doi: 10.1021/j150395a020.

I. A. Frigaard and C. Nouar. On the usage of viscosity regularisation methods for viscoplastic fluid flow computation. *Journal of Non-Newtonian Fluid Mechanics*, 127(1):1–26, 2005. ISSN 03770257. doi: 10.1016/j.jnnfm.2005.01.003.

C. Geisenhanslüke. *Einfluss der Granulometrie von Feinstoffen auf die Rheologie von Feinstoffleimen*. Zugl.: Kassel, univ., diss., 2008, Kassel University Press, Kassel, 2009. Geisenhanslüke, Carsten (Verfasser).

D. B. Genovese. Shear rheology of hard-sphere, dispersed, and aggregated suspensions, and filler-matrix composites. *Advances in colloid and interface science*, 171-172:1–16, 2012. doi: 10.1016/j.cis.2011.12.005. Journal Article.

H. Giesekus. *Phänomenologische Rheologie*. Springer, Berlin, 1994. ISBN 9783540575139.

C. F. Goodeve. A general theory of thixotropy and viscosity. *Transactions of the Faraday Society*, 35(0):342–358, 1939. ISSN 0014-7672. doi: 10.1039/TF9393500342.

A. Gram. *Numerical Modelling of Self-Compacting Concrete Flow Gram PhD*. Dissertation, Royal Institute of Technology, May 2009. URL https://www.diva-portal.org/smash/get/diva2:214194/FULLTEXT01.pdf.

Z. Guo, J. Qiu, H. Jiang, Q. Zhu, J. Wang Kwek, L. Ke, and Z. Qu. Experimental and modeling study on the transient flow and time-dependent yield stress of superfine-tailings cemented paste backfill. *Construction and Building Materials*, 367:130363, 2023. ISSN 09500618. doi: 10.1016/j.conbuildmat.2023.130363.

M. Haist. *Zur Rheologie und den physikalischen Wechselwirkungen bei Zementsuspensionen*. Dissertation, Universität Karlsruhe, Karlsruhe, 2009.

M. Haist, J. Link, D. Nicia, S. Leinitz, C. Baumert, T. von Bronk, D. Cotardo, M. Eslami Pirharati, S. Fataei, H. Garrecht, C. Gehlen, I. Hauschildt, I. Ivanova, S. Jesinghausen, C. Klein, H.-W. Krauss, L. Lohaus, D. Lowke, O. Mazanec, S. Pawelczyk, U. Pott, N. W. Radebe, J. J. Riedmiller, H.-J. Schmid, W. Schmidt, E. Secrieru, D. Stephan, M. Thiedeitz, M. Wilhelm, and V. Mechtcherine. Interlaboratory study on rheological properties of cement pastes and reference substances: comparability of measurements performed with different rheometers and measurement geometries. *Materials and Structures*, 53(4), 2020. ISSN 1359-5997. doi: 10.1617/s11527-020-01477-w. PII: 1477.

H. Hamaker. The london—van der waals attraction between spherical particles. *Physica*, 4(10):1058–1072, Oct. 1937. doi: 10.1016/s0031-8914(37)80203-7. URL https://doi.org/10.1016/s0031-8914(37)80203-7.

N. Hamedi, J. Revstedt, E. Tornberg, and F. Innings. A new numerical method for correction of wide gap rheometry data by cfd. In A. Sovari, editor, *Annual transactions of the Nordic Rheology Society*, volume 22, pages 175–178. The Nordic Rheology Society, 2014. 23rd Nordic Rheology Conference ; Conference date: 11-11-2014 Through 15-11-2014.

D. Han and R. D. Ferron. Effect of mixing method on microstructure and rheology of cement paste. *Construction and Building Materials*, 93:278–288, 2015. ISSN 09500618. doi: 10.1016/j.conbuildmat.2015.05.124.

D. Han and R. D. Ferron. Influence of high mixing intensity on rheology, hydration, and microstructure of fresh state cement paste. *Cement and Concrete Research*, 84:95–106, 2016. ISSN 00088846. doi: 10.1016/j.cemconres.2016.03.004.

F. Han, S. Pu, Y. Zhou, H. Zhang, and Z. Zhang. Effect of ultrafine mineral admixtures on the rheological properties of fresh cement paste: A review. *Journal of Building Engineering*, 51:104313, 2022. ISSN 23527102. doi: 10.1016/j.jobe.2022.104313.

Z. Han, B. Su, Y. Li, W. Wang, W. Wang, J. Huang, and G. Chen. Numerical simulation of debris-flow behavior based on the sph method incorporating the herschel-bulkley-papanastasiou rheology model. *Engineering Geology*, 255:26–36, 2019. ISSN 00137952. doi: 10.1016/j.enggeo.2019.04.013.

K. Hattori and K. Izumi. A rheological expression of coagulation rate theory. *Journal of Dispersion Science and Technology*, 3(2):129–145, 1982. ISSN 0193-2691. doi: 10.1080/01932698208943630.

M. A. Haustein, M. Eslami Pirharati, S. Fataei, D. Ivanov, D. Jara Heredia, N. Kijanski, D. Lowke, V. Mechtcherine, D. Rostan, T. Schäfer, C. Schilde, H. Steeb, and R. Schwarze. Benchmark simulations of dense suspensions flow using computational fluid dynamics. *Frontiers in Materials*, 9, 2022. doi: 10.3389/fmats.2022.874144.

A. R. Heath, P. D. Fawell, P. A. Bahri, and J. D. Swift. Estimating average particle size by focused beam reflectance measurement (fbrm). *Particle & Particle Systems Characterization*, 19(2):84, 2002. ISSN 09340866. doi: 10.1002/1521-4117(200205)19:2{\textless}84::AID-PPSC84{\textgreater}3.0.CO;2-1.

C. Heese. *Simulation des rheologischen Verhaltens von zementgebundenen Feinkornsystemen*. Dissertation, Technische Universität Kaiserslautern, Kaiserslautern, 2013. Heese, Christian (Verfasser).

H. Helmholtz. Studien über electrische grenzschichten. *Annalen der Physik und Chemie*, 243(7):337–382, 1879. doi: 10.1002/andp.18792430702. URL https://doi.org/10.1002/andp.18792430702.

M. Hieber, J. C. Robinson, and Y. Shibata. *Mathematical Analysis of the Navier-Stokes Equations*. Springer International Publishing, 2020. doi: 10.1007/978-3-030-36226-3. URL https://doi.org/10.1007/978-3-030-36226-3.

R. Hornig and J. Kielmann. Schwingungsrheometrie vs. hochdruck-kapillarrheometrie. *GAK*, 67:708–719, 2014.

M. Hosseinpoor, K. H. Khayat, and A. Yahia. Numerical simulation of self-consolidating concrete flow as a heterogeneous material in l-box set-up: coupled effect of reinforcing bars and aggregate content on flow characteristics. *Materials and Structures*, 50(2):346, 2017. ISSN 1359-5997. doi: 10.1617/s11527-017-1032-8. PII: 1032.

J. Hot, H. Bessaies-Bey, C. Brumaud, M. Duc, C. Castella, and N. Roussel. Adsorbing polymers and viscosity of cement pastes. *Cement and Concrete Research*, 63:12–19, 2014. ISSN 00088846. doi: 10.1016/j.cemconres.2014.04.005.

M. Hunger. *An integral design concept for ecological self-compacting concrete*. PhD thesis, Eindhoven University of Technology, Apr. 2010.

R. J. Hunter. *Zeta Potential in Colloid Science: Principles and Applications*. Elsevier Science, Burlington, 2013. ISBN 9781483214085.

A. Huß. *Mischungsentwurf und Fließeigenschaften von Selbstverdichtendem Beton (SVB) vom Mehlkorntyp unter Berücksichtigung der granulometrischen Eigenschaften der Gesteinskörnung*, volume 598 of *DAfStb-Heft*. Beuth Verlag GmbH, Berlin, 1. aufl. edition, 2012. ISBN 9783410652007.

D. Hwang and B. Khoshnevis. Concrete wall fabrication by contour crafting. In *Proceedings of the 21st International Symposium on Automation and Robotics in Construction*, Proceedings of the International Symposium on Automation and Robotics in Construction (IAARC). International Association for Automation and Robotics in Construction (IAARC), 2004. doi: 10.22260/ISARC2004/0057.

K. Hyun and M. Wilhelm. Establishing a New Mechanical Nonlinear Coefficient Q from FT-Rheology: First Investigation of Entangled Linear and Comb Polymer Model Systems. *Macromolecules*, 42(1):411–422, 2009. ISSN 0024-9297. doi: 10.1021/ma8017266.

K. Hyun, M. Wilhelm, C. O. Klein, K. S. Cho, J. G. Nam, K. H. Ahn, S. J. Lee, R. H. Ewoldt, and G. H. McKinley. A review of nonlinear oscillatory shear tests: Analysis and application of large amplitude oscillatory shear (laos). *Progress in Polymer Science*, 36(12): 1697–1753, 2011. ISSN 00796700. doi: 10.1016/j.progpolymsci.2011.02.002. PII: S0079670011000281.

I. Ivanova. *Assessing and modelling the structural build-up of concrete in the context of digital fabrication*. Dissertation, Technische Universität Dresden, 2023.

I. Ivanova, E. Ivaniuk, S. Bisetti, V. N. Nerella, and V. Mechtcherine. Comparison between methods for indirect assessment of buildability in fresh 3d printed mortar and concrete. *Cement and Concrete Research*, 156:106764, 2022. ISSN 00088846. doi: 10.1016/j.cemconres.2022.106764.

S. Jacobsen, R. Cepuritis, Y. Peng, M. R. Geiker, and J. Spangenberg. Visualizing and simulating flow conditions in concrete form filling using pigments. *Construction and Building Materials*, 49:328–342, 2013. ISSN 09500618. doi: 10.1016/j.conbuildmat.2013.08.027. PII: S0950061813007575.

P. Jahren and T. Sui. Early concrete history. In P. Jahren and T. Sui, editors, *History of Concrete*, pages 001–056. Co-published with cchemical industry press, 2018. ISBN 978-981-314-573-3. doi: 10.1142/9789813145740{\textunderscore}0001.

H. Jeong, S.-J. Han, S.-H. Choi, Y. J. Lee, S. T. Yi, and K. S. Kim. Rheological property criteria for buildable 3d printing concrete. *Materials (Basel, Switzerland)*, 12(4), 2019. ISSN 1996-1944. doi: 10.3390/ma12040657.

D. Jiao, R. de Schryver, C. Shi, and G. de Schutter. Thixotropic structural build-up of cement-based materials: A state-of-the-art review. *Cement and Concrete Composites*, 122:104152, 2021. ISSN 09589465. doi: 10.1016/j.cemconcomp.2021.104152. PII: S0958946521002201.

Jiri Blazek. *Computational Fluid Dynamics: Principles and Applications*. Elsevier, 2015. ISBN 9780080999951. doi: 10.1016/C2013-0-19038-1.

F. John, J. E. Marsden, L. Sirovich, and A. C. Pipkin. *Lectures on Viscoelasticity Theory*, volume 7. Springer New York, New York, NY, 1986. ISBN 978-0-387-96345-7. doi: 10.1007/978-1-4612-1078-8.

John W. Slater. Overview of cfd verification and validation, Wednesday, 10-Feb-2021 09:38:59 EST. URL https://www.grc.nasa.gov/www/wind/valid/tutorial/overview.html.

H. S. Joyner, editor. *Rheology of Semisolid Foods*. Springer International Publishing, 2019. doi: 10.1007/978-3-030-27134-3. URL https://doi.org/10.1007/978-3-030-27134-3.

P. C. Kapur, P. J. Scales, D. V. Boger, and T. W. Healy. Yield stress of suspensions loaded with size distributed particles. *AIChE Journal*, 43(5):1171–1179, May 1997. doi: 10.1002/aic.690430506. URL https://doi.org/10.1002/aic.690430506.

S. Kawashima, M. Chaouche, D. J. Corr, and S. P. Shah. Rate of thixotropic rebuilding of cement pastes modified with highly purified attapulgite clays. *Cement and Concrete Research*, 53:112–118, 2013. ISSN 00088846. doi: 10.1016/j.cemconres.2013.05.019. PII: S0008884613001336.

K. H. Khayat and D. Feys. *Design, Production and Placement of Self-Consolidating Concrete*. RILEM Bookseries, 1. Springer-Verlag, s.l., 1. aufl. edition, 2010. ISBN 978-90-481-9664-7. URL http://search.ebscohost.com/login.aspx?direct=true&scope=site&db=nlebk&db=nlabk&AN=338202.

K. H. Khayat, W. Meng, K. Vallurupalli, and Le Teng. Rheological properties of ultra-high-performance concrete — an overview. *Cement and Concrete Research*, 124:105828, 2019. ISSN 00088846. doi: 10.1016/j.cemconres.2019.105828.

A. V. Khokhlov. Generalization of a nonlinear maxwell-type viscoelastoplastic model and simulation of creep and recovery curves. *Mechanics of Composite Materials*, 59(3):441–454, 2023. ISSN 0191-5665. doi: 10.1007/s11029-023-10107-9.

H. S. Kim and T. G. Mason. Advances and challenges in the rheology of concentrated emulsions and nanoemulsions. *Advances in Colloid and Interface Science*, 247:397–412, Sept. 2017. doi: 10.1016/j.cis.2017.07.002. URL https://doi.org/10.1016/j.cis.2017.07.002.

H.-W. Krauss, I. Dreßler, and H. Budelmann. Experimentelle bestimmung der zusammenhänge zwischen rheologischen eigenschaften von feststoffreichen suspensionen und deren mikrostruktur. *Chemie Ingenieur Technik*, 90(6):881–887, 2018. doi: 10.1002/cite.201700008.

I. M. Krieger. Shear rate in couette viscometer. *Transactions of the Society of Rheology*, 12(1):5–11, 1968.

I. M. Krieger and T. J. Dougherty. A mechanism for non-newtonian flow in suspensions of rigid spheres. *Transactions of the Society of Rheology*, 3:137–152, 1959.

H.-O. Lamprecht. *Opus caementitium: Bautechnik der Römer*. Beton-Verlag, Düsseldorf, 2., durchges. aufl. edition, 1985. ISBN 376400200X.

G. J. Lauth and J. Kowalczyk. *Einführung in die Physik und Chemie der Grenzflächen und Kolloide*. Springer Berlin Heidelberg, 2016. ISBN 978-3-662-47017-6. doi: 10.1007/978-3-662-47018-3.

K. Le-Cao, N. Phan-Thien, N. Mai-Duy, S. K. Ooi, A. C. Lee, and B. C. Khoo. A microstructure model for viscoelastic–thixotropic fluids. *Physics of Fluids*, 32(12):123106, 2020. ISSN 1070-6631. doi: 10.1063/5.0033199.

L. Lei, C. Chomyn, M. Schmid, and J. Plank. Characterization data of reference industrial polycarboxylate superplasticizers used within priority program dfg spp 2005 "opus fluidum futurum - rheology of reactive, multiscale, multiphase construction materials". *Data in brief*, 31:106026, 2020. doi: 10.1016/j.dib.2020.106026.

Y. Li, J. Hao, C. Jin, Z. Wang, and J. Liu. Simulation of the flowability of fresh concrete by discrete element method. *Frontiers in Materials*, 7, 2021. doi: 10.3389/fmats.2020.603154.

T. Liberto, C. Barentin, J. Colombani, A. Costa, D. Gardini, M. Bellotto, and M. Le Merrer. Simple ions control the elasticity of calcite gels via interparticle forces. *Journal of Colloid and Interface Science*, 553:280–288, 2019. doi: 10.1016/j.jcis.2019.05.083.

D.-M. Liu. Particle packing and rheological property of highly-concentrated ceramic suspensions: determination and viscosity prediction. *Journal of Materials Science*, 35:5503–5507, 2000.

Q. Liu, F. Gómez, J. M. Pérez, and V. Theofilis. Instability and sensitivity analysis of flows using openfoam®. *Chinese Journal of Aeronautics*, 29(2):316–325, 2016. ISSN 10009361. doi: 10.1016/j.cja.2016.02.012.

D. Lowke. *Sedimentationsverhalten und Robustheit Selbstverdichtender Betone*. Dissertation, Technische Universität München, München, 2013.

D. Lowke and C. Gehlen. Effect of pore solution composition on zeta potential and super-plasticizer adsorption. *SP-302: Eleventh International Conference on Superplasticizers and Other Chemical Admixtures in Concrete*, 2015. URL `https://api.semanticscholar.org/CorpusID:99630608`.

D. Lowke and C. Gehlen. The zeta potential of cement and additions in cementitious suspensions with high solid fraction. *Cement and Concrete Research*, 95:195–204, 2017. ISSN 00088846. doi: 10.1016/j.cemconres.2017.02.016.

Z. Lu, M. Haist, D. Ivanov, C. Jakob, D. Jansen, S. Leinitz, J. Link, V. Mechtcherine, J. Neubauer, J. Plank, W. Schmidt, C. Schilde, C. Schröfl, T. Sowoidnich, and D. Stephan. Characterization data of reference cement CEM i 42.5 r used for priority program DFG SPP 2005 "opus fluidum futurum – rheology of reactive, multiscale, multiphase construction materials". *Data in Brief*, 27:104699, dec 2019. doi: 10.1016/j.dib.2019.104699. Available Open Access submittedVersion at https://depositonce.tu-berlin.de/handle/11303/10032.

S. Ma, Y. Qian, and S. Kawashima. Experimental and modeling study on the non-linear structural build-up of fresh cement pastes incorporating viscosity modifying admixtures. *Cement and Concrete Research*, 108:1–9, 2018. ISSN 00088846. doi: 10.1016/j.cemconres.2018.02.022.

C. W. Macosko. *Rheology: Principles, measurements, and applications*. Advances in interfacial engineering series. WILEY-VCH, New York and Weinheim, 1994. ISBN 978-0-471-18575-8. URL `http://swbplus.bsz-bw.de/bsz042044804cov.htm`.

S. Mantellato. *Flow Loss in Superplasticized Cement Pastes*. phdthesis, ETH Zurich, 2017.

S. Mantellato and R. J. Flatt. Shifting factor—a new paradigm for studying the rheology of cementitious suspensions. *Journal of the American Ceramic Society*, 103(6):3562–3574, 2020. ISSN 0002-7820. doi: 10.1111/jace.17040.

F. H. Marchesini, R. M. Oliveira, H. Althoff, and P. R. de Souza Mendes. Irreversible time-dependent rheological behavior of cement slurries: Constitutive model and experiments. *Journal of Rheology*, 63(2):247–262, 2019. ISSN 0148-6055. doi: 10.1122/1.5054879.

I. Marquardt. *Ein Mischungskonzept für selbstverdichtenden Beton auf der Basis der Volumenkenngrößen und Wasseransprüche der Ausgangsstoffe*. Rostock, univ., diss., 2001, Universität Rostock, 2001.

C. I. I. Matthäus. *Performance under pressure: Effect of pumping pressure on additive manufacturing of lightweight aggregate concrete*. Universitätsbibliothek der TU München, München, 2022.

O. Mazanec, D. Lowke, and P. Schießl. Mixing of high performance concrete. *Materials and Structures*, 43(3):357–365, 2010. ISSN 1359-5997.

V. Mechtcherine, A. Gram, K. Krenzer, J.-H. Schwabe, S. Shyshko, and N. Roussel. Simulation of fresh concrete flow using discrete element method (dem). *Materials and Structures*, 47(4):615–630, 2014. ISSN 1359-5997. doi: 10.1617/s11527-013-0084-7.

I. Mehdipour and K. H. Khayat. Understanding the role of particle packing characteristics in rheo-physical properties of cementitious suspensions. *Construction and Building Materials*, 161:340–353, 2018. ISSN 09500618. doi: 10.1016/j.conbuildmat.2017.11.147.

T. Mezger. *Das Rheologie Handbuch*. Hannover: Vincentz, 5., vollständig überarbeitete auflage edition, 2016. ISBN 9783866306332.

J.-M. Morel, F. Takens, B. Teissier, F. Marcellán, and W. van Assche. *Orthogonal Polynomials and Special Functions*, volume 1883. Springer Berlin Heidelberg, Berlin, Heidelberg, 2006. ISBN 978-3-540-31062-4. doi: 10.1007/b128597.

A. M. Mostafa and A. Yahia. New approach to assess build-up of cement-based suspensions. *Cement and Concrete Research*, 85:174–182, 2016. ISSN 00088846. doi: 10.1016/j.cemconres.2016.03.005.

F. Moukalled, L. Mangani, and M. Darwish. *The Finite Volume Method in Computational Fluid Dynamics*. Springer International Publishing, 2016. doi: 10.1007/978-3-319-16874-6. URL https://doi.org/10.1007/978-3-319-16874-6.

J. Mu, Y. Li, J. Hao, Y. Liu, and J. Shen. Research on discrete element simulation of slump test for fresh self-compacting concrete. *Journal of Building Engineering*, 70:106464, 2023. ISSN 23527102. doi: 10.1016/j.jobe.2023.106464.

A. Mujumdar, A. N. Beris, and A. B. Metzner. Transient phenomena in thixotropic systems. *Journal of Non-Newtonian Fluid Mechanics*, 102(2):157–178, 2002. ISSN 03770257. doi: 10.1016/S0377-0257(01)00176-8.

J. Murata. Flow and deformation of fresh concrete. *Materials and Structures*, 17(98):117–129, 1984. ISSN 0025-5432. doi: 10.1007/BF02473663.

E. Nader, S. Skinner, M. Romana, R. Fort, N. Lemonne, N. Guillot, A. Gauthier, S. Antoine-Jonville, C. Renoux, M.-D. Hardy-Dessources, E. Stauffer, P. Joly, Y. Bertrand, and P. Connes. Blood rheology: Key parameters, impact on blood flow, role in sickle cell disease and effects of exercise. *Frontiers in Physiology*, 10, Oct. 2019. doi: 10.3389/fphys.2019.01329. URL https://doi.org/10.3389/fphys.2019.01329.

E. Nägele. The zeta-potential of cement. *Cement and Concrete Research*, 15(3):453–462, 1985. ISSN 00088846. doi: 10.1016/0008-8846(85)90118-8.

X. Nan, Z. Wang, J. Hou, Y. Tong, and B. Li. Clogging mechanism of pervious concrete: From experiments to cfd-dem simulations. *Construction and Building Materials*, 270:121422, 2021. ISSN 09500618. doi: 10.1016/j.conbuildmat.2020.121422.

I. Newton. *Philosophiae Naturalis Principia Mathematica. Auctore Js. Newton*. Jussu Societatis Regiae ac Typis Josephi Streater, 1687. doi: 10.3931/E-RARA-440.

G. B. S. Ng. *Interactions of Polycarboxylate based Superplasticizers with Montmorillonite Clay in Portland Cement and with Calcium Aluminate Cement*. München, technische universität münchen, diss., 2013, Universitätsbibliothek der TU München, München, 2013.

Q. D. Nguyen and D. V. Boger. Direct yield stress measurement with the vane method. *Journal of Rheology*, 29(3):335–347, 1985. ISSN 0148-6055.

T. Nguyen, N. Roussel, and P. Coussot. Correlation between l-box test and rheological parameters of a homogeneous yield stress fluid. *Cement and Concrete Research*, 36(10): 1789–1796, 2006. ISSN 00088846. doi: 10.1016/j.cemconres.2006.05.001.

D. Nicia, C. Jakob, D. Jansen, D. Ivanov, O. Mazanec, J. Dengler, J. Neubauer, and D. Lowke. Thixotropy of superplasticized cement pastes – underlying mechanisms considering the polycarboxylate molecular structure, interparticle interactions and hydration kinetics. *Cement and Concrete Research*, 173:107289, 2023. ISSN 00088846. doi: 10.1016/j. cemconres.2023.107289.

I. T. Norton, F. Spyropoulos, and P. Cox, editors. *Practical Food Rheology*. Wiley-Blackwell, Jan. 2011. doi: 10.1002/9781444391060. URL https://doi.org/10. 1002/9781444391060.

W. L. Oberkampf and T. G. Trucano. Verification and validation in computational fluid dynamics. *Progress in Aerospace Sciences*, 38:209–272, 2002.

E. J. O'Donovan and R. I. Tanner. Numerical study of the bingham squeeze film problem. *Journal of Non-Newtonian Fluid Mechanics*, 15(1):75–83, 1984. ISSN 03770257. doi: 10.1016/0377-0257(84)80029-4.

A. Ogawa, H. Yamada, S. Matsuda, K. Okajima, and M. Doi. Viscosity equation for concentrated suspensions of charged colloidal particles. *Journal of Rheology*, 41(3):769–785, May 1997. doi: 10.1122/1.550875. URL https://doi.org/10.1122/1.550875.

T. G. Oldroyd. On the Formulation of Rheological Equations of State. *Proceedings of the Royal Society of London*, 200(1063):523–541, 1950. URL https://www.jstor.org/ stable/98422.

A. F. Omran, K. H. Khayat, and Y. M. Elaguab. Effect of scc mixture composition on thixotropy and formwork pressure. *Journal of Materials in Civil Engineering*, 24(7):876–888, 2012. ISSN 0899-1561. doi: 10.1061/(ASCE)MT.1943-5533.0000463.

OpenFOAM. OpenFOAM: API Guide v2112 - The open source CFD toolbox. https: //www.openfoam.com/documentation/guides/latest/api/classFoam_1_ 1wedgeFvPatchField.html, 2017. [Online; accessed 02-December-2023].

OpenFOAM. OpenFOAMWiki. `https://openfoamwiki.net/index.php/OpenFOAM_guide/The_PIMPLE_algorithm_in_OpenFOAM`, 2018. [Online; accessed 02-December-2023].

T. C. Papanastasiou. Flows of materials with yield. *Journal of Rheology*, 31(5):385–404, 1987. ISSN 0148-6055. doi: 10.1122/1.549926.

A. Papo. Rheological models for cement pastes. *Materials and Structures*, 21(1):41–46, 1988. ISSN 0025-5432. doi: 10.1007/BF02472527.

J. B. Pereira, Y. T. Sáo, and G. de Freitas Maciel. Numerical and experimental application of the automated slump test for yield stress evaluation of mineralogical and polymeric materials. *Rheologica Acta*, 61(2):163–182, 2022. ISSN 0035-4511. doi: 10.1007/s00397-021-01321-0.

A. Perrot, D. Rangeard, and A. Pierre. Structural built-up of cement-based materials used for 3d-printing extrusion techniques. *Materials and Structures*, 49(4):1213–1220, 2016. ISSN 1359-5997. doi: 10.1617/s11527-015-0571-0.

T. Peterfi, editor. *Methodik der wissenschaftlichen Biologie. Erster Band: Allgemeine Morphologie.Zweiter Band: Allgemeine Physiologie.* Julius Springer, 1928.

N. Phan-Thien and N. Mai-Duy. *Understanding Viscoelasticity*. Springer International Publishing, 2017. doi: 10.1007/978-3-319-62000-8. URL `https://doi.org/10.1007/978-3-319-62000-8`.

A. P. Philipse. *Brownian Motion*. Springer International Publishing, 2018. ISBN 978-3-319-98052-2. doi: https://doi.org/10.1007/978-3-319-98053-9. URL `https://www.ebook.de/de/product/33508063/albert_p_philipse_brownian_motion.html`.

M. E. Pirharati, D. Ivanov, H.-W. Krauss, C. Schilde, and D. Lowke. Numerical simulation of the flow behavior of newtonian fluids in a wide gap rheometer by CFD. In *RILEM Bookseries*, pages 588–595. Springer International Publishing, Aug. 2019. doi: 10.1007/978-3-030-22566-7_68. URL `https://doi.org/10.1007/978-3-030-22566-7_68`.

J. Plank and C. Hirsch. Impact of zeta potential of early cement hydration phases on superplasticizer adsorption. *Cement and Concrete Research*, 37(4):537–542, 2007. ISSN 00088846. doi: 10.1016/j.cemconres.2007.01.007.

U. Pott and D. Stephan. Penetration test as a fast method to determine yield stress and structural build-up for 3d printing of cementitious materials. *Cement and Concrete Composites*, 121:104066, 2021. ISSN 09589465. doi: 10.1016/j.cemconcomp.2021.104066.

U. Pott, C. Crasselt, N. Fobbe, M. Haist, M. Heinemann, S. Hellmann, D. Ivanov, C. Jakob, D. Jansen, L. Lei, R. Li, J. Link, D. Lowke, V. Mechtcherine, J. Neubauer, D. Nicia, J. Plank,

S. Reißig, T. Schäfer, C. Schilde, W. Schmidt, C. Schröfl, T. Sowoidnich, B. Strybny, N. Ukrainczyk, J. Wolf, P. Xiao, and D. Stephan. Characterization data of reference materials used for phase ii of the priority program dfg spp 2005 "opus fluidum futurum - rheology of reactive, multiscale, multiphase construction materials". *Data in brief*, 47: 108902, 2023. doi: 10.1016/j.dib.2023.108902.

W. Puntke. Wasseranspruch von feinen kornhaufwerken. forschen, messen, optimieren. *Beton*, 52(5):242–248, 2002.

U. C. Puri and T. Uomoto. Characterization of distinct element modeling parameters for fresh concrete and its application in shotcrete simulations. *Journal of Materials in Civil Engineering*, 14(2):137–144, 2002. ISSN 0899-1561. doi: 10.1061/(ASCE) 0899-1561(2002)14:2(137).

Y. Qian and S. Kawashima. Distinguishing dynamic and static yield stress of fresh cement mortars through thixotropy. *Cement and Concrete Composites*, 86:288–296, 2018. ISSN 09589465. doi: 10.1016/j.cemconcomp.2017.11.019.

K. Ram, M. Serdar, D. Londono-Zuluaga, and K. Scrivener. Does carbon footprint reduction impair mechanical properties and service life of concrete? *Materials and structures*, 56 (1):6, 2023. ISSN 1359-5997. doi: 10.1617/s11527-022-02090-9.

A. U. Rehman and J.-H. Kim. 3d concrete printing: A systematic review of rheology, mix designs, mechanical, microstructural, and durability characteristics. *Materials (Basel, Switzerland)*, 14(14), 2021. ISSN 1996-1944. doi: 10.3390/ma14143800.

M. Reiner and H. Eyring. Deformation and flow. an elementary introduction to theoretical rheology. *Physics Today*, 3(4):35–36, 1950. ISSN 0031-9228. doi: 10.1063/1.3066868.

L. Reiter. *Structural Build-up for Digital Fabrication with Concrete - Materials, Methods and Processes*. PhD thesis, ETH Zurich, 2019.

N. Roussel. A thixotropy model for fresh fluid concretes. *Cement and Concrete Research*, 36 (10):1797–1806, 2006. ISSN 00088846. doi: 10.1016/j.cemconres.2006.05.025.

N. Roussel. *Understanding the rheology of concrete*. Woodhead Publishing, Cambridge Philadelphia, PA, 2012. ISBN 9780857095282.

N. Roussel. Rheological requirements for printable concretes. *Cement and Concrete Research*, 112:76–85, 2018. ISSN 00088846. doi: 10.1016/j.cemconres.2018.04.005.

N. Roussel and P. Coussot. "fifty-cent rheometer" for yield stress measurements: From slump to spreading flow. *Journal of Rheology*, 49(3):705–718, 2005. ISSN 0148-6055. doi: 10.1122/1.1879041.

N. Roussel, M. R. Geiker, F. Dufour, L. N. Thrane, and P. Szabo. Computational modeling of concrete flow: General overview. *Cement and Concrete Research*, 37(9):1298–1307, 2007. ISSN 00088846. doi: 10.1016/j.cemconres.2007.06.007.

N. Roussel, A. Lemaître, R. J. Flatt, and P. Coussot. Steady state flow of cement suspensions. *Cement and Concrete Research*, 40(1):77–84, 2010. ISSN 00088846. doi: 10.1016/j. cemconres.2009.08.026.

N. Roussel, G. Ovarlez, S. Garrault, and C. Brumaud. The origins of thixotropy of fresh cement pastes. *Cement and Concrete Research*, 42(1):148–157, 2012. ISSN 00088846. doi: 10.1016/j.cemconres.2011.09.004.

N. Roussel, A. Gram, M. Cremonesi, L. Ferrara, K. Krenzer, V. Mechtcherine, S. Shyshko, J. Skocec, J. Spangenberg, O. Svec, L. N. Thrane, and K. Vasilic. Numerical simulations of concrete flow. *Cement and Concrete Research*, 79:265–271, 2016. ISSN 00088846. doi: 10.1016/j.cemconres.2015.09.022.

E. Ruckenstein and J. Mewis. Kinetics of structural changes in thixotropic fluids. *Journal of Colloid and Interface Science*, 44(3):532–541, 1973. doi: 10.1016/0021-9797(73) 90332-9.

M. Rütten. *Verallgemeinerte newtonsche Fluide*. Springer Berlin Heidelberg, Berlin, Heidelberg, 2019. ISBN 978-3-662-56225-3. doi: 10.1007/978-3-662-56226-0.

M. Santhanam and S. Kumar. Particle packing theories and their appliction in concrete mixture proportioning: A review. *The Indian Concrete Journal*, pages 1324–1331, 2003.

P. Saramito and A. Wachs. Progress in numerical simulation of yield stress fluid flows. *Rheologica Acta*, 56(3):211–230, 2017. ISSN 0035-4511. doi: 10.1007/s00397-016-0985-9.

N. Schaer, J. Vazquez, M. Dufresne, G. Isenmann, and J. Wertel. On the Determination of the Yield Surface within the Flow of Yield Stress Fluids using Computational Fluid Dynamics. *Journal of Applied Fluid Mechanics*, 11(4):971–982, 2018. doi: 10.18869/ acadpub.jafm.73.247.27981.

M. Schmidt, E. Fehling, and S. Fröhlich, editors. *Nachhaltiges Bauen mit ultra-hochfestem Beton: Ergebnisse des Schwerpunktprogrammes 1182 = Sustainable Building with Ultra-High Performance Concrete : Results of the German Priority Programme 1182*, volume 22 of *Schriftenreihe Baustoffe und Massivbau*. Kassel Univ. Press, Kassel, 2014. ISBN 978-3-86219-480-3.

W. Scholz, W. Hiese, R. Möhring, and H. Bruckner, editors. *Baustoffkenntnis*. Werner, 17., neu bearb. u. erw. aufl. edition, 2011. ISBN 9783804152489.

J.-H. Schwabe. Planetenmischer mit dynamisch getriebenen mischarmen. *10. Kolloquium Getriebetechnik : Technische Universität Ilmenau, 11. - 13.*, 2013. URL `http: //nbn-resolving.de/urn:nbn:de:gbv:ilm1-2013100033-161-9`.

K. Scrivener, F. Martirena, S. Bishnoi, and S. Maity. Calcined clay limestone cements (lc3). *Cement and Concrete Research*, 114:49–56, 2018. ISSN 00088846. doi: 10.1016/j. cemconres.2017.08.017.

E. Secrieru. *Pumping behaviour of modern concretes*, volume Heft 2018/2 of *Schriftenreihe des Institutes für Baustoffe*. Saechsische Landesbibliothek- Staats- und Universitaetsbibliothek Dresden and Technische Universität Dresden, Dresden, 2018. doi: 234912.

M. S. Shadloo, G. Oger, and D. Le Touzé. Smoothed particle hydrodynamics method for fluid flows, towards industrial applications: Motivations, current state, and challenges. *Computers & Fluids*, 136:11–34, 2016. ISSN 00457930. doi: 10.1016/j.compfluid.2016.05.029.

C. Shi, Z. Wu, J. Xiao, D. Wang, Z. Huang, and Z. Fang. A review on ultra high performance concrete: Part i. raw materials and mixture design. *Construction and Building Materials*, 101:741–751, 2015. ISSN 09500618. doi: 10.1016/j.conbuildmat.2015.10.088.

S. Shyshko and V. Mechtcherine. Developing a discrete element model for simulating fresh concrete: Experimental investigation and modelling of interactions between discrete aggregate particles with fine mortar between them. *Construction and Building Materials*, 47:601–615, 2013. ISSN 09500618. doi: 10.1016/j.conbuildmat.2013.05.071. PII: S0950061813004698.

J. Spangenberg, N. Roussel, J. H. Hattel, H. Stang, J. Skocek, and M. R. Geiker. Flow induced particle migration in fresh concrete. *Cement and Concrete Research*, 42(4):633–641, 2012. ISSN 00088846. doi: 10.1016/j.cemconres.2012.01.007.

A. C. Sparavigna. Some notes on ancient concrete. *International Journal of Sciences*, 0(02):1–6, 2014. ISSN 2410-4477. doi: 10.18483/ijSci.412.

J. F. Stoltz, S. Gaillard, and M. Lucius. A study of the visco-elastic properties of blood in transient flow. *Journal of Biomechanics*, 13(4):341–346, 1980. ISSN 00219290. doi: 10.1016/0021-9290(80)90013-5. PII: 0021929080900135.

Y. Tan, G. Cao, H. Zhang, J. Wang, R. Deng, X. Xiao, and B. Wu. Study on the thixotropy of the fresh concrete using dem. *Procedia Engineering*, 102:1944–1950, 2015. ISSN 18777058. doi: 10.1016/j.proeng.2015.06.138.

Z. Tan, S. A. Bernal, and J. L. Provis. Reproducible mini-slump test procedure for measuring the yield stress of cementitious pastes. *Materials and Structures*, 50(6), Oct. 2017. doi: 10.1617/s11527-017-1103-x. URL https://doi.org/10.1617/s11527-017-1103-x.

Y. Tanigawa and H. Mori. Analytical study on deformation of fresh concrete. *Journal of Engineering Mechanics*, 115(3):493–508, 1989. ISSN 0733-9399. doi: 10.1061/(ASCE)0733-9399(1989)115:3(493).

G. H. Tattersall and P. F. G. Banfill. *The Rheology of fresh concrete*. Pitman, Boston, 1983. ISBN 0-273-08558-1.

T. Tavangar, M. Hosseinpoor, J. S. Marshall, A. Yahia, and K. H. Khayat. Discrete-element modeling of shear-induced particle migration during concrete pipe flow: Effect of size distribution and concentration of aggregate on formation of lubrication layer. *Cement and Concrete Research*, 166:107113, 2023a. ISSN 00088846. doi: 10.1016/j.cemconres. 2023.107113.

T. Tavangar, M. Hosseinpoor, J. S. Marshall, A. Yahia, and K. H. Khayat. Four-way cfd-dem coupling to simulate concrete pipe flow: Mechanism of formation of lubrication layer. *SSRN*, 2023b. doi: 10.2139/ssrn.4351120. URL https://papers.ssrn.com/sol3/papers.cfm?abstract_id=4351120.

H. Taylor. *Cement chemistry*. Thomas Telford Publishing, 2nd edition edition, 1997. doi: 10. 1680/cc.25929. URL https://www.icevirtuallibrary.com/doi/abs/10.1680/cc.25929.

B. H. Thacker, S. W. Doebling, F. M. Hemez, M. C. Anderson, J. E. Pepin, and E. A. Rodriguez. Concepts of model verification and validation, 2004.

M. Thiedeitz and T. Kränkel. Steady and transient phenomenological thixotropy modeling of non-newtonian cementitious pastes, submitted. *Cement and Concrete Research*, xx(x): xxx–xxx, 2024a.

M. Thiedeitz and T. Kränkel. Comparative small and large gap rheometry for cementitious pastes. *Preprints*, 2024b. doi: 10.20944/preprints202402.0703.v1.

M. Thiedeitz, T. Kränkel, and C. Gehlen. Thixotropic structural build-up of cement pastes at low shear rates. In A. M. Ivankovic, M. K. Maric, A. Strauss, and T. Kisicek, editors, *International Conference on Sustainable Materials*, volume 5, pages 272–279. RILEM Publications, 2019. ISBN 978-1-5108-9297-2.

M. Thiedeitz, I. Dressler, T. Kränkel, C. Gehlen, and D. Lowke. Effect of Pre-Shear on Agglomeration and Rheological Parameters of Cement Paste. *Materials (Basel, Switzerland)*, 13(9), 2020a. ISSN 1996-1944. doi: 10.3390/ma13092173. Journal Article.

M. Thiedeitz, T. Kränkel, and C. Gehlen. Thixotropy-dependent form filling ability of cement paste. In V. Mechtcherine, K. Khayat, and E. Secrieru, editors, *Rheology and Processing of Construction Materials*, volume 23 of *RILEM Bookseries*, pages 273–280. Springer International Publishing, Cham, 2020b. ISBN 978-3-030-22565-0. doi: 10. 1007/978-3-030-22566-7_32.

M. Thiedeitz, T. Kränkel, and C. Gehlen. Viscoelastoplastic classification of cementitious suspensions: transient and non-linear flow analysis in rotational and oscillatory shear flows. *Rheologica Acta*, 61(8-9):549–570, 2022. ISSN 0035-4511. doi: 10.1007/s00397-022-01358-9.

M. Thiedeitz, C. Crasselt, P. Xiao, N. Ukrainczyk, W. Schmidt, and T. Kränkel. Multidisciplinary approach for the prediction of cement paste rheological properties: physical

analysis, experimental rheology and microstructural modelling. *ce/papers*, 6(6):715–724, 2023. ISSN 2509-7075. doi: 10.1002/cepa.2812.

M. Thiedeitz, T. Kränkel, D. Kartal, and J. J. Timothy. The slump flow of cementitious pastes: Simulation vs. experiments. *Materials (Basel, Switzerland)*, 17(2), 2024. ISSN 1996-1944. doi: 10.3390/ma17020532. URL `https://www.mdpi.com/1996–1944/17/2/532`.

M. Thiedeitz, J. Timothy, and T. Kränkel, editors. *8th European Congress on Computational Methods in Applied Sciences and Engineering // Computational modelling and characterization of non-Newtonian visco-plastic cementitious building materials*, 5th - 9th Jun 2022. CIMNE. doi: 10.23967/eccomas.2022.069.

L. N. Thrane. *Form Filling with Self-Compacting Concrete*. Dissertation, Technical University of Denmark, Lyngby, 2007.

F. Toussaint, C. Roy, and P.-H. Jézéquel. Reducing shear thickening of cement-based suspensions. *Rheologica Acta*, 48(8):883–895, 2009. ISSN 0035-4511. doi: 10.1007/s00397-009-0362-z.

T. Tran-Duc, T. Ho, and N. Thamwattana. A smoothed particle hydrodynamics study on effect of coarse aggregate on self-compacting concrete flows. *International Journal of Mechanical Sciences*, 190:106046, 2021. ISSN 00207403. doi: 10.1016/j.ijmecsci.2020.106046.

N. Ukrainczyk, M. Thiedeitz, T. Kränkel, E. Koenders, and C. Gehlen. Modeling SAOS Yield Stress of Cement Suspensions: Microstructure-Based Computational Approach. *Materials (Basel, Switzerland)*, 13(12), 2020. ISSN 1996-1944. doi: 10.3390/ma13122769. Journal Article.

M. Vahabi. The effect of thixotropy on dam-break flow: a numerical study by smoothed particle hydrodynamics. *Journal of the Brazilian Society of Mechanical Sciences and Engineering*, 43(11), 2021. ISSN 1678-5878. doi: 10.1007/s40430-021-03241-9.

P. van Cappellen, L. Charlet, W. Stumm, and P. Wersin. A surface complexation model of the carbonate mineral-aqueous solution interface. *Geochimica et Cosmochimica Acta*, 57 (15):3505–3518, 1993. ISSN 0016-7037. doi: 10.1016/0016-7037(93)90135-j.

K. Vasilić. *A numerical model for self-compacting concrete flow through reinforced sections*. Dissertation, Technische Universität Dresden and Bundesanstalt für Materialforschung und -prüfung, 2016.

K. Vasilic, A. Gram, and J. E. Wallevik. Numerical simulation of fresh concrete flow: insight and challenges. *RILEM Technical Letters*, 4:57–66, 2019. ISSN 2518-0231. doi: 10.21809/rilemtechlett.2019.92. URL `https://creativecommons.org/licenses/by/4.0/`.

J. E. Wallevik. *Rheology of particle suspensions*. Dissertation, The Norwegian University of Science and Technology, 2003.

J. E. Wallevik. Thixotropic investigation on cement paste: Experimental and numerical approach. *Journal of Non-Newtonian Fluid Mechanics*, 132(1-3):86–99, 2005. ISSN 03770257. doi: 10.1016/j.jnnfm.2005.10.007. PII: S0377025705002314.

J. E. Wallevik. Rheological properties of cement paste. *Cement and Concrete Research*, 39 (1):14–29, 2009. ISSN 00088846. doi: 10.1016/j.cemconres.2008.10.001.

J. E. Wallevik and O. H. Wallevik. Analysis of shear rate inside a concrete truck mixer. *Cement and Concrete Research*, 95:9–17, 2017. ISSN 00088846. doi: 10.1016/j.cemconres.2017. 02.007. PII: S0008884616310961.

O. H. Wallevik and J. E. Wallevik. Rheology as a tool in concrete science. *Cement and Concrete Research*, 41(12):1279–1288, 2011. ISSN 00088846. doi: 10.1016/j.cemconres. 2011.01.009.

O. H. Wallevik, D. Feys, J. E. Wallevik, and K. H. Khayat. Avoiding inaccurate interpretations of rheological measurements for cement-based materials. *Cement and Concrete Research*, 78:100–109, 2015. ISSN 00088846. doi: 10.1016/j.cemconres.2015.05.003.

D. Wang, C. Shi, Z. Wu, J. Xiao, Z. Huang, and Z. Fang. A review on ultra high performance concrete: Part ii. hydration, microstructure and properties. *Construction and Building Materials*, 96:368–377, 2015. ISSN 09500618. doi: 10.1016/j.conbuildmat.2015.08. 095.

X. Wang, W. Li, J. Ren, Q. Luo, Y. Fang, and F. Xing. Computational fluid dynamics—discrete element method simulation of the contact forces between microcapsules using a speed-up method with reduced young's modulus. *Powder Technology*, 392:23–37, 2021. ISSN 00325910. doi: 10.1016/j.powtec.2021.06.043.

J. F. Wendt. *Computational Fluid Dynamics*. Springer Berlin Heidelberg, Berlin, Heidelberg, 1992. ISBN 978-3-662-11352-3. doi: 10.1007/978-3-662-11350-9.

Wikimedia Commons. Image with CC BY-SA 3.0 License, 2023. URL `https://commons.wikimedia.org/w/index.php?curid=761864`. CC BY-SA 3.0.

M. Wilhelm, D. Maring, and H.-W. Spiess. Fourier-transform rheology. *Rheologica Acta*, 37 (4):399–405, 1998. ISSN 0035-4511.

Z. Xu, Y. Miao, H. Wu, X. Yuan, and C. Liu. Estimation of viscosity and yield stress of cement grouts at true ground temperatures based on the flow spread test. *Materials*, 13(13):2939, June 2020. doi: 10.3390/ma13132939. URL `https://doi.org/10.3390/ma13132939`.

K. Yamada, S. Ogawa, and S. Hanehara. Controlling of the adsorption and dispersing force of polycarboxylate-type superplasticizer by sulfate ion concentration in aqueous phase. *Cement and Concrete Research*, 31(3):375–383, 2001. ISSN 00088846. doi: 10.1016/S0008-8846(00)00503-2.

K. Yoshioka, E. Sakai, M. Daimon, and A. Kitahara. Role of steric hindrance in the performance of superplasticizers for concrete. *Journal of the American Ceramic Society*, 80(10): 2667–2671, 1997. ISSN 0002-7820. doi: 10.1111/j.1151-2916.1997.tb03169.x.

A. B. Yu, C. L. Feng, R. P. Zou, and R. Y. Yang. On the relationship between porosity and interparticle forces. *Powder Technology*, 130(1-3):70–76, 2003. ISSN 00325910. doi: 10.1016/S0032-5910(02)00228-0. PII: S0032591002002280.

Q. Yuan, X. Lu, K. H. Khayat, D. Feys, and C. Shi. Small amplitude oscillatory shear technique to evaluate structural build-up of cement paste. *Materials and Structures*, 50(112): 1–12, 2017. ISSN 1359-5997. doi: 10.1617/s11527-016-0978-2.

M. Zarei and J. Aalaie. Application of shear thickening fluids in material development. *Journal of Materials Research and Technology*, 9(5):10411–10433, 2020. ISSN 22387854. doi: 10.1016/j.jmrt.2020.07.049.

L. Zhang, R. Li, L. Lei, and J. Plank. Characterization data of reference industrial polycarboxylate superplasticizer vp 2020/15.2 used for priority program dfg spp 2005 "opus fluidum futurum - rheology of reactive, multiscale, multiphase construction materials". *Data in brief*, 39:107657, 2021. doi: 10.1016/j.dib.2021.107657.

Y. Zhang. *Study on Microstructure and Rheological Properties of Cement-Chemical Admixtures-Water Dispersion System at Early Stage*. Dissertation, Tsinghua University, Peking, 2017. URL 10.1007/978-981-10-4570-7.

Z. Zhang, H. Wang, and N. Gao. Simulation and parameter prediction model of rheological properties of fiber reinforced concrete. *Case Studies in Construction Materials*, 18:e01963, 2023. ISSN 22145095. doi: 10.1016/j.cscm.2023.e01963.

F. Zunino, F. Martirena, and K. Scrivener. Limestone calcined clay cements (lc3). *ACI Materials Journal*, 118(3), 2021. ISSN 0889325X. doi: 10.14359/51730422.

# Standards

[DIN1] DIN1015.   DIN EN 1015-3:2007-05, Prüfverfahren für Mörtel für Mauerwerk_- Teil_3: Bestimmung der Konsistenz von Frischmörtel (mit Ausbreittisch); EN_1015-3:1999+A1:2004+A2:2006, 2007.

[DIN2] DIN12350-8.   DIN EN 12350-8:2019-09, Prüfung von Frischbeton_- Teil_8: Selbstverdichtender Beton_- Setzfließversuch, Deutsche Fassung EN_12350-8:2019, 2019. URL https://doi.org/10.31030/3045733.

[DIN3] DIN12350-9.   DIN EN 12350-9:2010-12, Prüfung von Frischbeton_- Teil_9: Selbstverdichtender Beton_- Auslauftrichterversuch; Deutsche Fassung EN_12350-9:2010, 2010.

[DIN4] DIN1235010.   DIN EN 12350-10:2010-12, Prüfung von Frischbeton_- Teil_10: Selbstverdichtender Beton_- L-Kasten-Versuch; Deutsche Fassung EN_12350-10:2010, 2010.

[DIN5] DIN1324. DIN 1342-1:2003-11, Viskosität - Teil 1: Rheologische Begriffe, 2003. URL https://doi.org/10.31030/9502317.

[DIN6] DIN53019.   DIN 53019-1:2008-09, Viskosimetrie_- Messung von Viskositäten und Fließkurven mit Rotationsviskosimetern_- Teil_1: Grundlagen und Messgeometrie, 2008. URL https://doi.org/10.31030/1439277.

# Appendix

# A. Rheological results

The data set of all illustrated raw data is accessible at doi:10.14459/2024mp1741807.

# A.1 Viscoplastic flow curve analysis
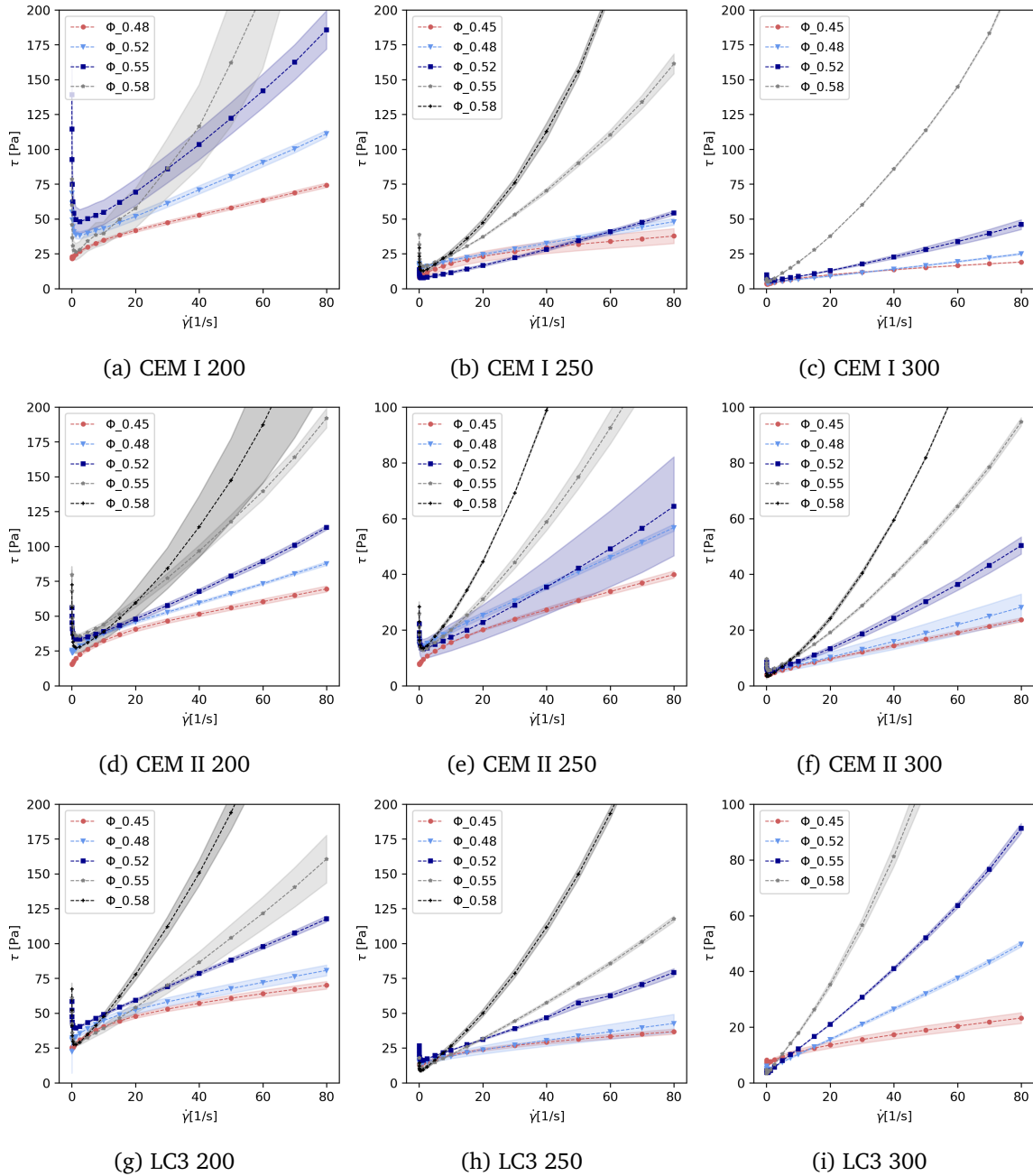


Figure A.1: Dynamic $\tau - \dot{\gamma}$ flow curves of all test series with the rotational parallel-plates test

Fig. A.1 illustrates the shear flow curves for the binders CEM I, CEM II and LC3 in a $\tau - \dot{\gamma}$ - diagram, with slump flow values of $200 \pm 5$, $250 \pm 5$ and $300 \pm 5$ mm, respectively. All flow curves are presented in a linear axes scale. The figures present the average flow curve with standard variations in shaded colors.

Table A.1: Phenomenological regression analysis for the test series CEMI-200

| Model | Par. | Unit | Solid volume fractions | | | | |
|---|---|---|---|---|---|---|---|
| | | | 0.45 | 0.48 | 0.52 | 0.55 | 0.58 |
| Bingham | $\tau_0$ | $[Pa]$ | x | 25.7 | 33.7 | 35.9 | 0.0 |
| | $\mu$ | $[Pas]$ | x | 0.6 | 1.0 | 1.8 | 4.1 |
| Herschel-Bulkley | $\tau_0$ | $[Pa]$ | x | 21.4 | 36.3 | 45.8 | 39.5 |
| | $k$ | $[Pas^n]$ | x | 2.68 | 0.55 | 0.51 | 0.01 |
| | $n$ | $[-]$ | x | 0.68 | 1.12 | 1.28 | 2.46 |
| mod. Bingham | $\tau_0$ | $[Pa]$ | x | 24.0 | 35.2 | 42.1 | 29.9 |
| | $\mu_1$ | $[Pas]$ | x | 0.89 | 0.82 | 1.23 | 0.00 |
| | $\mu_2$ | $[Pas]$ | x | 0.004 | 0.002 | 0.007 | 0.057 |
| Casson | $\tau_0$ | $[Pa]$ | x | 19.6 | 19.6 | 15.6 | 0.001 |
| | $\eta_\infty$ | $[Pas]$ | x | 0.21 | 0.44 | 1.08 | 4.12 |
| Toussaint | $\tau_0$ | $[Pa]$ | x | 19.6 | 34.5 | 43.4 | 10.8 |
| | $\beta$ | $[Pas]$ | x | 0.21 | 0.01 | 0.01 | 1.06 |
| | $k$ | $[Pas^n]$ | x | 0.00 | 0.33 | 0.36 | 0.00 |
| | $n$ | $[-]$ | x | 0.40 | 1.21 | 1.34 | 3.90 |

Table A.2: Phenomenological regression analysis for the test series CEMI-250

| Model | Par. | Unit | Solid volume fractions | | | | |
|---|---|---|---|---|---|---|---|
| | | | 0.45 | 0.48 | 0.52 | 0.55 | 0.58 |
| Bingham | $\tau_0$ | $[Pa]$ | 11.1 | 15.9 | 5.5 | 5.0 | 0.0 |
| | $\mu$ | $[Pas]$ | 0.38 | 0.41 | 0.59 | 1.82 | 4.18 |
| Herschel-Bulkley | $\tau_0$ | $[Pa]$ | 6.5 | 14.9 | 7.5 | 16.5 | 24.4 |
| | $k$ | $[Pas^n]$ | 3.69 | 0.69 | 0.26 | 0.29 | 0.01 |
| | $n$ | $[-]$ | 0.49 | 0.89 | 1.18 | 1.41 | 2.41 |
| mod. Bingham | $\tau_0$ | $[Pa]$ | 9.3 | 15.4 | 6.8 | 13.7 | 14.9 |
| | $\mu_1$ | $[Pas]$ | 0.73 | 0.46 | 0.47 | 0.98 | 0 |
| | $\mu_2$ | $[Pas]$ | 0 | 0 | 0 | 0.01 | 0.06 |
| Casson | $\tau_0$ | $[Pa]$ | 8.4 | 10.7 | 1.5 | 0.2 | 0 |
| | $\eta_\infty$ | $[Pas]$ | 0.15 | 0.16 | 0.45 | 1.76 | 4.16 |
| Toussaint | $\tau_0$ | $[Pa]$ | 6.5 | 13.5 | 6.8 | 11.4 | 1.1 |
| | $\beta$ | $[Pas]$ | 0.01 | 0.04 | 0.01 | 0.14 | 1.75 |
| | $k$ | $[Pas^n]$ | 3.24 | 0.1 | 0.17 | 0.09 | 0 |
| | $n$ | $[-]$ | 0.48 | 1.18 | 1.26 | 1.64 | 3.90 |
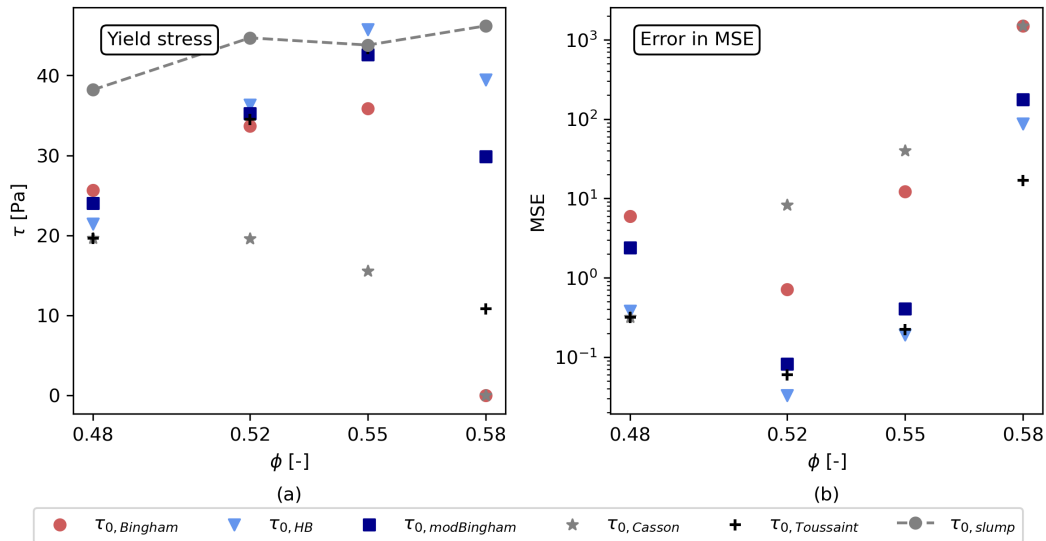
(a) $\tau_0$ values and mean squared error for different regressions of CEMI-200 test series
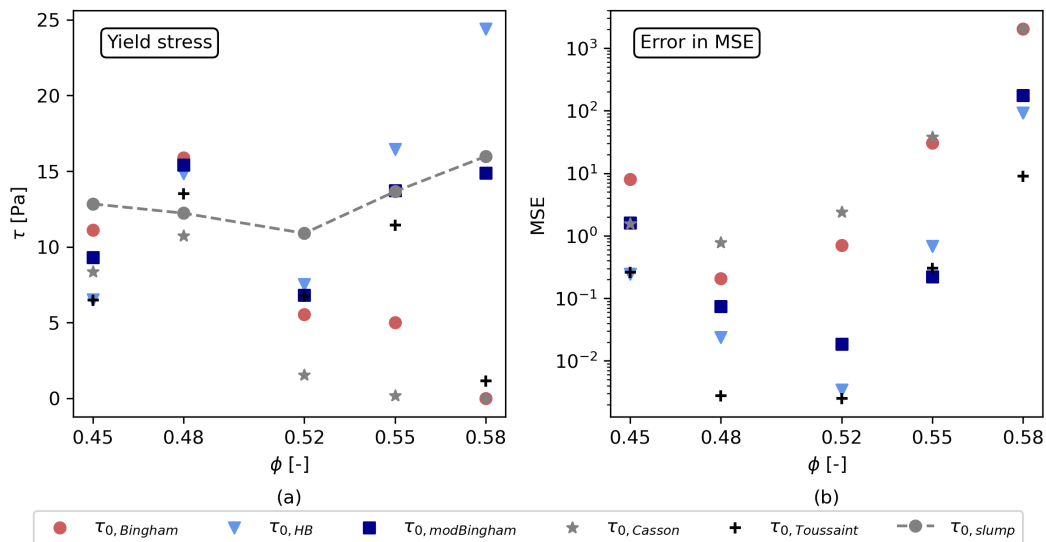


(b) $\tau_0$ values and mean squared error for different regressions of CEMI-250 test series
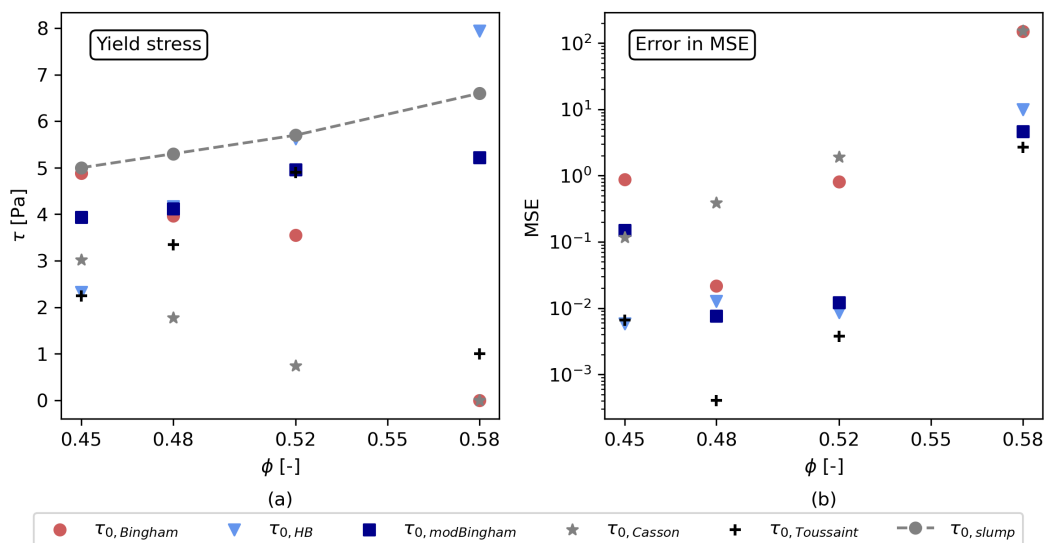


(c) $\tau_0$ values and mean squared error for different regressions of CEMI-300 test series

Figure A.2: Phenomenological regression analysis of CEMI test series

Table A.3: Phenomenological regression analysis for the test series CEMI-300

| Model | Par. | Unit | Solid volume fractions | | | | |
|---|---|---|---|---|---|---|---|
| | | | 0.45 | 0.48 | 0.52 | 0.55 | 0.58 |
| Bingham | $\tau_0$ | $[Pa]$ | 4.9 | 4.0 | 3.5 | x | 0.0 |
| | $\mu$ | $[Pas]$ | 0.2 | 0.3 | 0.5 | x | 2.5 |
| Herschel-Bulkley | $\tau_0$ | $[Pa]$ | 2.3 | 4.2 | 5.6 | x | 8.0 |
| | $k$ | $[Pas^n]$ | 1.35 | 0.22 | 0.18 | x | 0.28 |
| | $n$ | $[-]$ | 0.58 | 1.04 | 1.23 | x | 1.52 |
| mod. Bingham | $\tau_0$ | $[Pa]$ | 3.9 | 4.1 | 5.0 | x | 5.2 |
| | $\mu_1$ | $[Pas]$ | 0.31 | 0.24 | 0.37 | x | 1.14 |
| | $\mu_2$ | $[Pas]$ | -0.002 | 0.000 | 0.002 | x | 0.021 |
| Casson | $\tau_0$ | $[Pa]$ | 3.0 | 1.8 | 0.7 | x | 0.001 |
| | $\eta_\infty$ | $[Pas]$ | 0.09 | 0.16 | 0.42 | x | 2.53 |
| Toussaint | $\tau_0$ | $[Pa]$ | 2.3 | 3.3 | 4.9 | x | 1.0 |
| | $\beta$ | $[Pas]$ | 0.01 | 0.04 | 0.01 | x | 1.19 |
| | $k$ | $[Pas^n]$ | 1.10 | 0.03 | 0.11 | x | 0.002 |
| | $n$ | $[-]$ | 0.57 | 1.35 | 1.31 | x | 2.45 |

(a) $\tau_0$ values and mean squared error for different regressions of CEMII-200 test series



(b) $\tau_0$ values and mean squared error for different regressions of CEMII-250 test series



(c) $\tau_0$ values and mean squared error for different regressions of CEMII-300 test series

Figure A.3: Phenomenological regression analysis of CEMII test series

Table A.4: Phenomenological regression analysis for the test series CEMII-200

| Model | Par. | Unit | Solid volume fractions | | | | |
|---|---|---|---|---|---|---|---|
| | | | 0.45 | 0.48 | 0.52 | 0.55 | 0.58 |
| Bing-ham | $\tau_0$ | [Pa] | 21.8 | 27.5 | 28.06 | 21.9 | 1.7 |
| | $\mu$ | [Pas] | 0.7 | 0.8 | 1.03 | 2.0 | 3.3 |
| Herschel-Bulkley | $\tau_0$ | [Pa] | 13.5 | 23.9 | 32.2 | 34.8 | 31.2 |
| | $k$ | [Pas^n] | 5.56 | 2.15 | 0.44 | 0.43 | 0.14 |
| | $n$ | [−] | 0.52 | 0.77 | 1.19 | 1.34 | 1.73 |
| mod. Bingham | $\tau_0$ | [Pa] | 19.0 | 26.1 | 30.7 | 31.1 | 27.3 |
| | $\mu_1$ | [Pas] | 1.18 | 0.98 | 0.81 | 1.25 | 0.84 |
| | $\mu_2$ | [Pas] | -0.006 | -0.003 | 0.003 | 0.010 | 0.032 |
| Cas-son | $\tau_0$ | [Pa] | 16.0 | 19.8 | 14.4 | 6.0 | 0.001 |
| | $\eta_\infty$ | [Pas] | 0.24 | 0.29 | 0.55 | 1.51 | 3.33 |
| Toussaint | $\tau_0$ | [Pa] | 13.2 | 19.8 | 30.0 | 29.5 | 13.1 |
| | $\beta$ | [Pas] | 0.04 | 0.29 | 0.01 | 0.06 | 0.73 |
| | $k$ | [Pas^n] | 4.29 | 0.00 | 0.25 | 0.19 | 0.002 |
| | $n$ | [−] | 0.50 | 0.50 | 1.29 | 1.49 | 2.55 |

Table A.5: Phenomenological regression analysis for the test series CEMII-250

| Model | Par. | Unit | Solid volume fractions | | | | |
|---|---|---|---|---|---|---|---|
| | | | 0.45 | 0.48 | 0.52 | 0.55 | 0.58 |
| Bing-ham | $\tau_0$ | [Pa] | 10.1 | 14.3 | 10.7 | 4.1 | 0.0 |
| | $\mu$ | [Pas] | 0.4 | 0.5 | 0.6 | 1.5 | 3.0 |
| Herschel-Bulkley | $\tau_0$ | [Pa] | 7.5 | 13.8 | 13.0 | 13.1 | 16.1 |
| | $k$ | [Pas^n] | 1.65 | 0.66 | 0.28 | 0.28 | 0.20 |
| | $n$ | [−] | 0.68 | 0.95 | 1.19 | 1.38 | 1.63 |
| mod. Bingham | $\tau_0$ | [Pa] | 9.0 | 14.1 | 12.2 | 10.8 | 12.0 |
| | $\mu_1$ | [Pas] | 0.57 | 0.56 | 0.50 | 0.86 | 1.05 |
| | $\mu_2$ | [Pas] | -0.002 | -0.000 | 0.002 | 0.008 | 0.027 |
| Cas-son | $\tau_0$ | [Pa] | 6.9 | 8.4 | 4.5 | 0.2 | 0.001 |
| | $\eta_\infty$ | [Pas] | 0.17 | 0.25 | 0.41 | 1.46 | 3.00 |
| Toussaint | $\tau_0$ | [Pa] | 6.8 | 8.4 | 11.9 | 9.7 | 6.1 |
| | $\beta$ | [Pas] | 0.17 | 0.25 | 0.01 | 0.08 | 0.54 |
| | $k$ | [Pas^n] | 0.07 | 0.000 | 0.16 | 0.11 | 0.03 |
| | $n$ | [−] | 0.45 | 0.40 | 1.30 | 1.55 | 2.02 |

Table A.6: Phenomenological regression analysis for the test series CEMII-300

| Model | Par. | Unit | Solid volume fractions | | | | |
|---|---|---|---|---|---|---|---|
| | | | 0.45 | 0.48 | 0.52 | 0.55 | 0.58 |
| Herschel-Bingham | $\tau_0$ | $[Pa]$ | 4.3 | 4.5 | 3.2 | 0.2 | 0.0 |
| | $\mu$ | $[Pas]$ | 0.2 | 0.3 | 0.6 | 1.1 | 1.9 |
| Herschel-Bulkley | $\tau_0$ | $[Pa]$ | 3.7 | 4.8 | 5.3 | 5.9 | 4.5 |
| | $k$ | $[Pas^n]$ | 0.44 | 0.24 | 0.19 | 0.20 | 0.16 |
| | $n$ | $[-]$ | 0.87 | 1.05 | 1.24 | 1.38 | 1.59 |
| mod. Bingham | $\tau_0$ | $[Pa]$ | 4.0 | 4.7 | 4.7 | 4.5 | 3.2 |
| | $\mu_1$ | $[Pas]$ | 0.29 | 0.27 | 0.40 | 0.62 | 0.69 |
| | $\mu_2$ | $[Pas]$ | -0.001 | 0.000 | 0.002 | 0.006 | 0.018 |
| Casson | $\tau_0$ | $[Pa]$ | 2.4 | 2.0 | 0.6 | 0.001 | 0.001 |
| | $\eta_\infty$ | $[Pas]$ | 0.13 | 0.18 | 0.48 | 1.09 | 1.84 |
| Toussaint | $\tau_0$ | $[Pa]$ | 2.4 | 4.0 | 4.6 | 4.0 | 2.1 |
| | $\beta$ | $[Pas]$ | 0.13 | 0.03 | 0.02 | 0.08 | 0.25 |
| | $k$ | $[Pas^n]$ | 0.00 | 0.06 | 0.11 | 0.09 | 0.04 |
| | $n$ | $[-]$ | 0.40 | 1.28 | 1.35 | 1.55 | 1.86 |
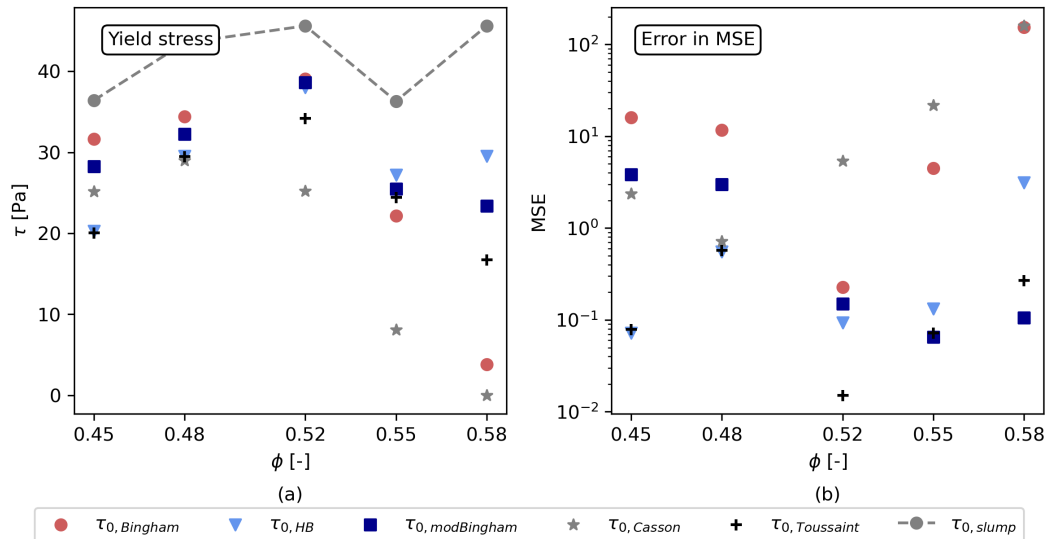
(a) $\tau_0$ values and mean squared error for different regressions of LC3-200 test series
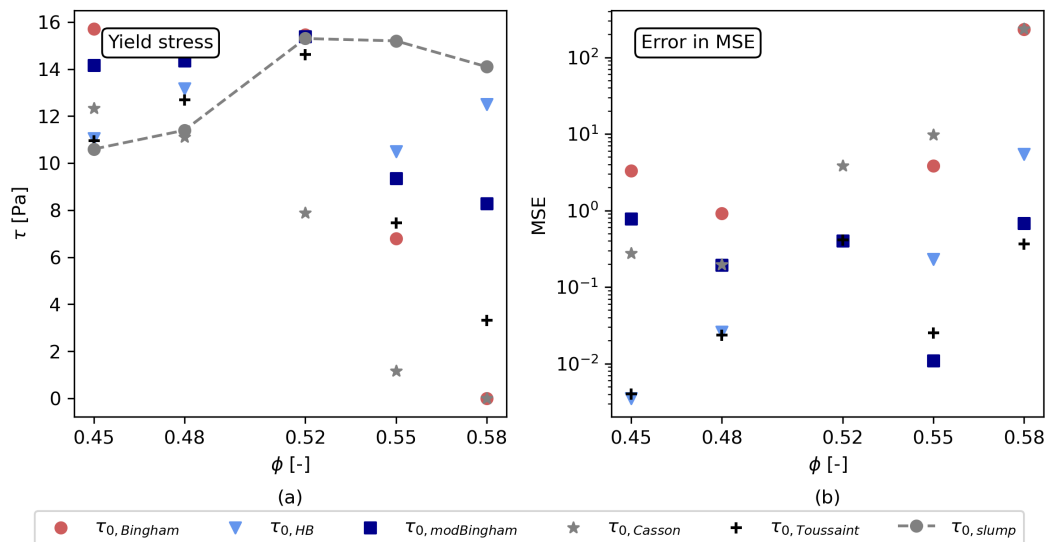


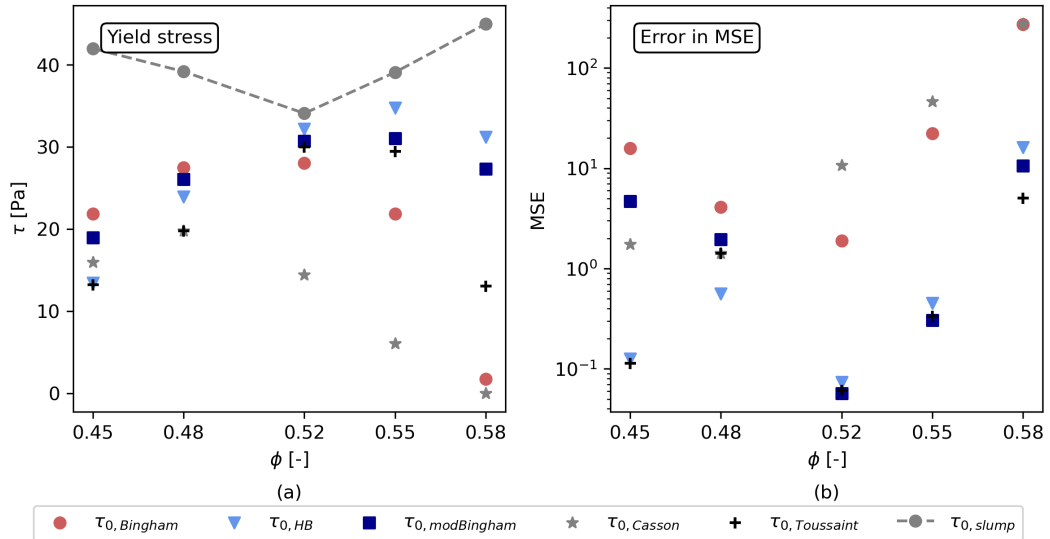(b) $\tau_0$ values and mean squared error for different regressions of LC3-250 test series
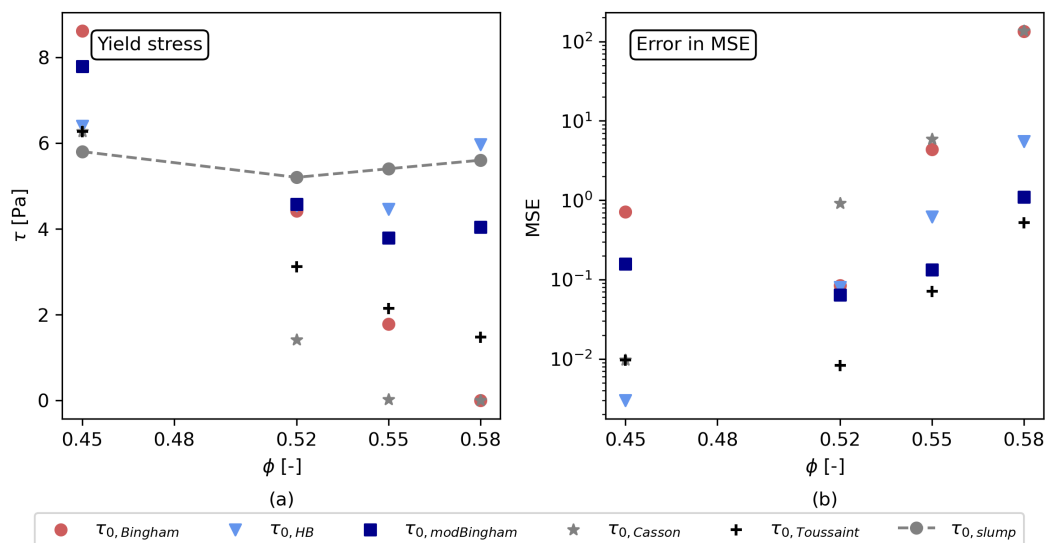


(c) $\tau_0$ values and mean squared error for different regressions of LC3-300 test series
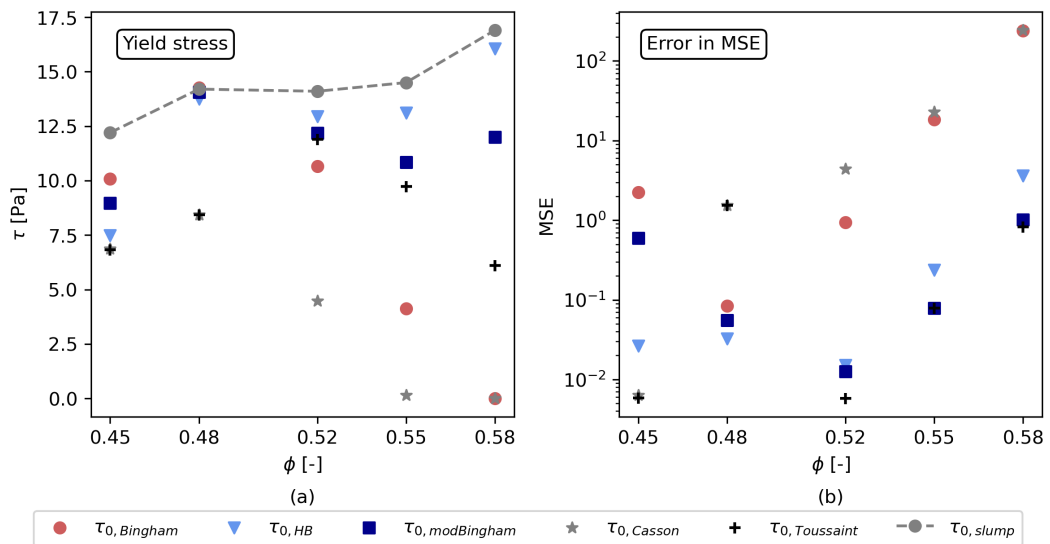
Figure A.4: Phenomenological regression analysis of LC3 test series

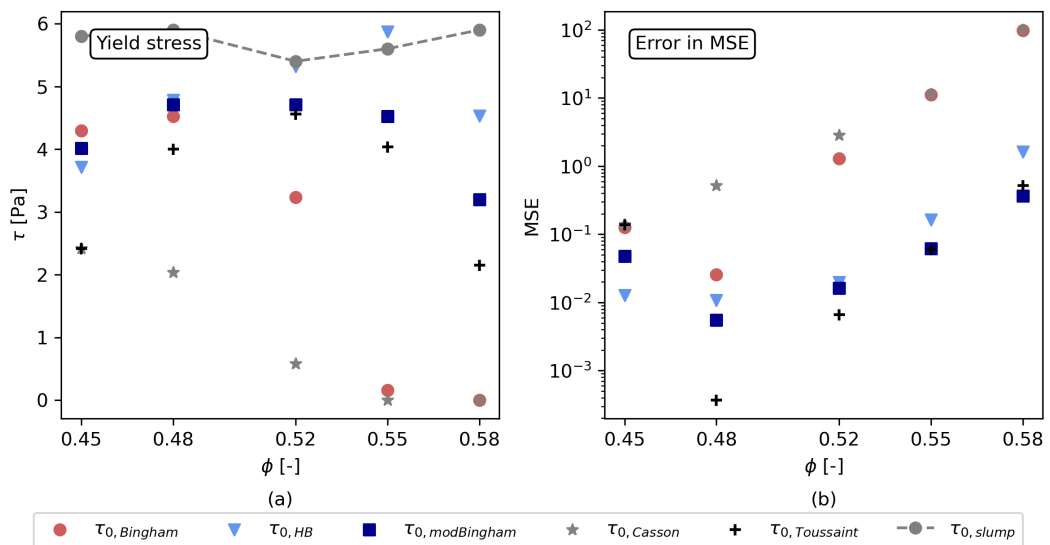Table A.7: Phenomenological regression analysis for the test series LC3-200

| Model | Par. | Unit | Solid volume fractions | | | | |
|---|---|---|---|---|---|---|---|
| | | | 0.45 | 0.48 | 0.52 | 0.55 | 0.58 |
| Herschel-Bingham | $\tau_0$ | $[Pa]$ | 31.6 | 34.4 | 39.0 | 22.1 | 3.8 |
| | $\mu$ | $[Pas]$ | 0.5 | 0.6 | 1.0 | 1.7 | 4.1 |
| Herschel-Bulkley | $\tau_0$ | $[Pa]$ | 20.3 | 29.6 | 38.0 | 27.2 | 29.5 |
| | $k$ | $[Pas^n]$ | 7.36 | 3.72 | 1.21 | 0.82 | 0.67 |
| | $n$ | $[-]$ | 0.44 | 0.60 | 0.95 | 1.16 | 1.41 |
| mod. Bingham | $\tau_0$ | $[Pa]$ | 28.2 | 32.3 | 38.6 | 25.5 | 23.4 |
| | $\mu_1$ | $[Pas]$ | 1.02 | 1.04 | 1.03 | 1.36 | 2.21 |
| | $\mu_2$ | $[Pas]$ | -0.007 | -0.006 | -0.001 | 0.004 | 0.024 |
| Casson | $\tau_0$ | $[Pa]$ | 25.1 | 29.0 | 25.2 | 8.1 | 0.001 |
| | $\eta_\infty$ | $[Pas]$ | 0.15 | 0.16 | 0.40 | 1.14 | 4.15 |
| Toussaint | $\tau_0$ | $[Pa]$ | 20.0 | 29.4 | 34.2 | 24.4 | 16.7 |
| | $\beta$ | $[Pas]$ | 0.01 | 0.01 | 0.08 | 0.04 | 0.55 |
| | $k$ | $[Pas^n]$ | 6.68 | 2.74 | 0.22 | 0.46 | 0.13 |
| | $n$ | $[-]$ | 0.42 | 0.62 | 1.23 | 1.26 | 1.71 |

Table A.8: Phenomenological regression analysis for the test series LC3-250

| Model | Par. | Unit | Solid volume fractions | | | | |
|---|---|---|---|---|---|---|---|
| | | | 0.45 | 0.48 | 0.52 | 0.55 | 0.58 |
| Herschel-Bingham | $\tau_0$ | $[Pa]$ | 15.7 | 15.3 | 15.5 | 6.8 | 0.0 |
| | $\mu$ | $[Pas]$ | 0.3 | 0.4 | 0.8 | 1.3 | 3.3 |
| Herschel-Bulkley | $\tau_0$ | $[Pa]$ | 11.1 | 13.2 | 15.4 | 10.5 | 12.5 |
| | $k$ | $[Pas^n]$ | 2.86 | 1.11 | 0.82 | 0.63 | 0.37 |
| | $n$ | $[-]$ | 0.50 | 0.75 | 0.99 | 1.17 | 1.52 |
| mod. Bingham | $\tau_0$ | $[Pa]$ | 14.2 | 14.3 | 15.4 | 9.4 | 8.3 |
| | $\mu_1$ | $[Pas]$ | 0.51 | 0.48 | 0.80 | 1.05 | 1.52 |
| | $\mu_2$ | $[Pas]$ | -0.003 | -0.002 | -0.000 | 0.004 | 0.026 |
| Casson | $\tau_0$ | $[Pa]$ | 12.3 | 11.1 | 7.9 | 1.2 | 0.001 |
| | $\eta_\infty$ | $[Pas]$ | 0.09 | 0.12 | 0.44 | 1.14 | 3.32 |
| Toussaint | $\tau_0$ | $[Pa]$ | 11.0 | 12.7 | 14.6 | 7.5 | 3.3 |
| | $\beta$ | $[Pas]$ | 0.01 | 0.02 | 0.01 | 0.17 | 0.95 |
| | $k$ | $[Pas^n]$ | 2.29 | 0.42 | 0.57 | 0.17 | 0.03 |
| | $n$ | $[-]$ | 0.49 | 0.86 | 1.05 | 1.39 | 2.00 |

Table A.9: Phenomenological regression analysis for the test series LC3-300

| Model | Par. | Unit | Solid volume fractions | | | | |
|---|---|---|---|---|---|---|---|
| | | | 0.45 | 0.48 | 0.52 | 0.55 | 0.58 |
| Herschel-Bingham | $\tau_0$ | $[Pa]$ | 8.6 | x | 4.4 | 1.8 | 0.0 |
| | $\mu$ | $[Pas]$ | 0.2 | x | 0.6 | 1.1 | 2.5 |
| Herschel-Bulkley | $\tau_0$ | $[Pa]$ | 6.4 | x | 4.5 | 4.5 | 6.0 |
| | $k$ | $[Pas^n]$ | 1.15 | x | 0.53 | 0.43 | 0.29 |
| | $n$ | $[-]$ | 0.61 | x | 1.01 | 1.21 | 1.51 |
| mod. Bingham | $\tau_0$ | $[Pa]$ | 7.8 | x | 4.6 | 3.8 | 4.0 |
| | $\mu_1$ | $[Pas]$ | 0.30 | x | 0.54 | 0.77 | 1.10 |
| | $\mu_2$ | $[Pas]$ | -0.001 | x | 0.000 | 0.004 | 0.021 |
| Casson | $\tau_0$ | $[Pa]$ | 6.3 | x | 1.4 | 0.2 | 0.001 |
| | $\eta_\infty$ | $[Pas]$ | 0.07 | x | 0.41 | 1.05 | 2.46 |
| Toussaint | $\tau_0$ | $[Pa]$ | 6.3 | x | 3.1 | 2.1 | 1.5 |
| | $\beta$ | $[Pas]$ | 0.07 | x | 0.16 | 0.35 | 0.83 |
| | $k$ | $[Pas^n]$ | 0.00 | x | 0.05 | 0.02 | 0.01 |
| | $n$ | $[-]$ | 0.80 | x | 1.40 | 1.75 | 2.12 |

## A.2 Viscoelastic flow curve analysis
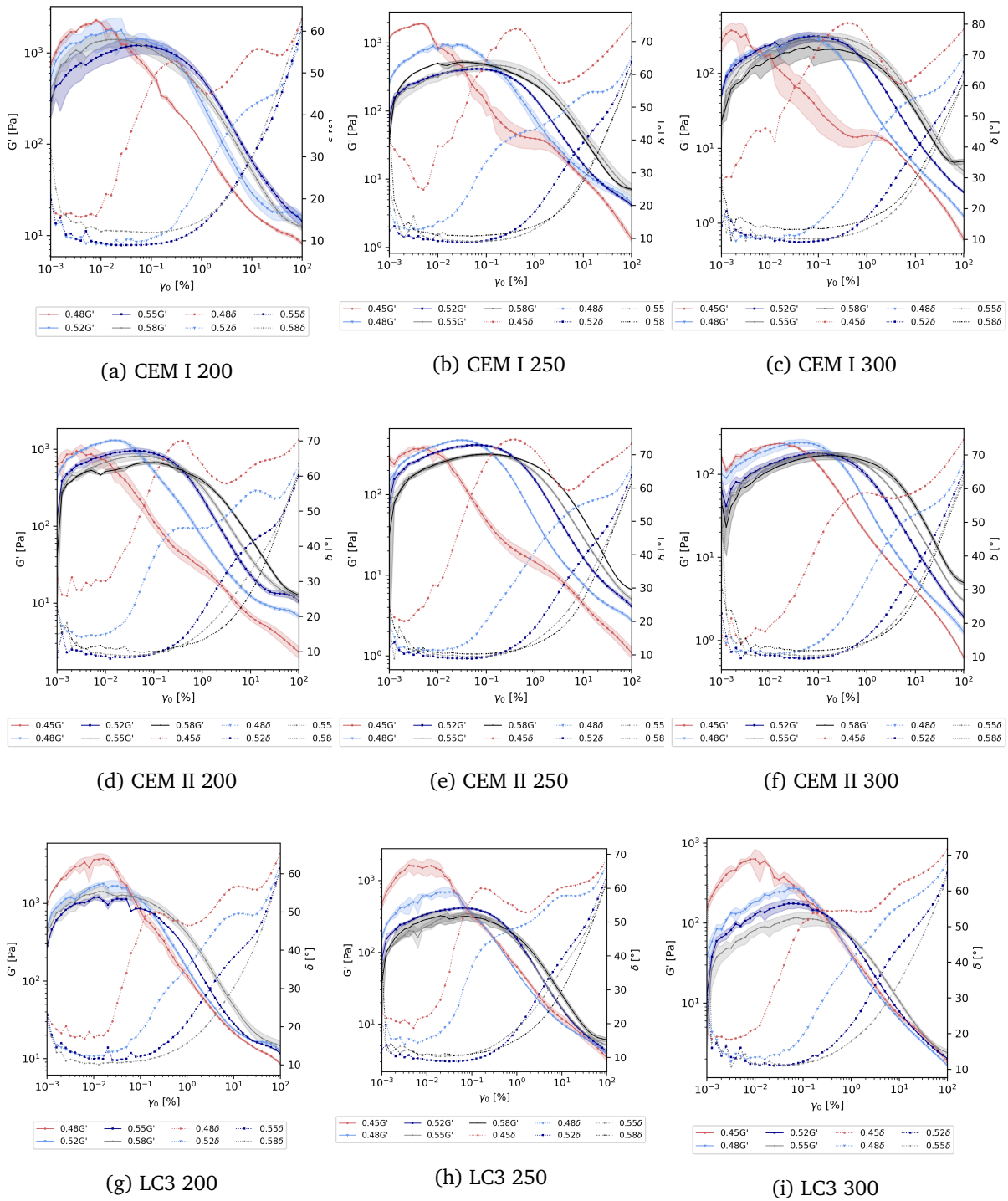


Figure A.5: First harmonics of the storage modulus $G'$ and the phase shift angle $\delta$ for all test series

Table A.10: First harmonic viscoelastic parameters for CEM I test series

| Model | Par. | Unit | Solid volume fractions | | | | |
|---|---|---|---|---|---|---|---|
| | | | 0.45 | 0.48 | 0.52 | 0.55 | 0.58 |
| CEM I 200 | $G'$ | $[Pa]$ | x | 1,809.3 | 1,321.7 | 991.1 | 1,154.2 |
| | $G''$ | $[Pa]$ | x | 688.9 | 240.7 | 172.2 | 245.0 |
| | $\gamma_l$ | $[\%]$ | x | 0.02 | 0.04 | 0.25 | 0.08 |
| | $\gamma_F$ | $[\%]$ | x | 0.08 | 20.30 | 25.30 | 31.80 |
| | $\tau_y$ | $[Pa]$ | x | 0.31 | 0.54 | 2.54 | 0.94 |
| CEM I 250 | $G'$ | $[Pa]$ | 1,137.7 | 718.5 | 339.3 | 397.6 | 440.3 |
| | $G''$ | $[Pa]$ | 717.8 | 391.8 | 66.4 | 76.4 | 86.4 |
| | $\gamma_l$ | $[\%]$ | 0.01 | 0.06 | 0.25 | 0.50 | 0.16 |
| | $\gamma_F$ | $[\%]$ | 0.10 | 1.59 | 14.90 | 26.30 | 31.80 |
| | $\tau_y$ | $[Pa]$ | 0.11 | 0.52 | 0.87 | 2.04 | 0.71 |
| CEM I 300 | $G'$ | $[Pa]$ | 326.4 | 237.3 | 255.6 | 258.8 | 201.3 |
| | $G''$ | $[Pa]$ | 279.1 | 80.2 | 52.1 | 55.8 | 48.0 |
| | $\gamma_l$ | $[\%]$ | 0.00 | 0.16 | 0.32 | 0.64 | 0.10 |
| | $\gamma_F$ | $[\%]$ | 0.03 | 1.50 | 11.2 | 28.3 | 31.0 |
| | $\tau_y$ | $[Pa]$ | 0.01 | 0.40 | 0.83 | 1.68 | 0.21 |

Table A.11: First harmonic viscoelastic parameters for CEM II test series

| Model | Par. | Unit | Solid volume fractions | | | | |
|---|---|---|---|---|---|---|---|
| | | | 0.45 | 0.48 | 0.52 | 0.55 | 0.58 |
| CEM II-200 | $G'$ | $[Pa]$ | 863.7 | 1,004.9 | 795.4 | 693.8 | 553.5 |
| | $G''$ | $[Pa]$ | 476.2 | 433.8 | 146.0 | 125.4 | 112.4 |
| | $\gamma_l$ | $[\%]$ | 0.01 | 0.04 | 0.16 | 0.20 | 0.32 |
| | $\gamma_F$ | $[\%]$ | 0.03 | 0.64 | 20.3 | 28.3 | 30.3 |
| | $\tau_y$ | $[Pa]$ | 0.05 | 0.44 | 1.29 | 1.42 | 1.80 |
| CEM II-250 | $G'$ | $[Pa]$ | 320.2 | 368.6 | 339.3 | 253.2 | 262.4 |
| | $G''$ | $[Pa]$ | 189.4 | 135.3 | 66.4 | 53.1 | 56.3 |
| | $\gamma_l$ | $[\%]$ | 0.01 | 0.10 | 0.25 | 0.50 | 0.63 |
| | $\gamma_F$ | $[\%]$ | 0.02 | 1.50 | 20.1 | 30.0 | 33.1 |
| | $\tau_y$ | $[Pa]$ | 0.04 | 0.40 | 0.87 | 1.30 | 1.70 |
| CEM II-300 | $G'$ | $[Pa]$ | 187.9 | 189.0 | 146.9 | 147.0 | 142.3 |
| | $G''$ | $[Pa]$ | 129.0 | 56.2 | 31.4 | 33.5 | 36.5 |
| | $\gamma_l$ | $[\%]$ | 0.05 | 0.16 | 0.40 | 0.63 | 1.01 |
| | $\gamma_F$ | $[\%]$ | 0.10 | 2.53 | 10.1 | 25.0 | 30.0 |
| | $\tau_y$ | $[Pa]$ | 0.1 | 0.3 | 0.6 | 1.0 | 1.5 |

Table A.12: First harmonic viscoelastic parameters for LC3 test series

| Model | Par. | Unit | Solid volume fractions | | | | |
|---|---|---|---|---|---|---|---|
| | | | 0.45 | 0.48 | 0.52 | 0.55 | 0.58 |
| LC3-200 | $G'$ | $[Pa]$ | x | 2,534.2 | 1,666.6 | 1,086.0 | 1,277.1 |
| | $G''$ | $[Pa]$ | x | 1,244.6 | 396.7 | 216.6 | 238.6 |
| | $\gamma_l$ | $[\%]$ | x | 0.03 | 0.03 | 0.03 | 0.04 |
| | $\gamma_F$ | $[\%]$ | x | 0.08 | 3.1 | 30.1 | 31.5 |
| | $\tau_y$ | $[Pa]$ | x | 0.90 | 0.43 | 0.28 | 0.52 |
| LC3-250 | $G'$ | $[Pa]$ | 1,146.1 | 461.9 | 339.3 | 281.3 | 265.6 |
| | $G''$ | $[Pa]$ | 695.2 | 265.7 | 66.4 | 64.4 | 56.8 |
| | $\gamma_l$ | $[\%]$ | 0.03 | 0.06 | 0.25 | 0.25 | 0.25 |
| | $\gamma_F$ | $[\%]$ | 0.04 | 0.25 | 18.0 | 25.3 | 33.5 |
| | $\tau_y$ | $[Pa]$ | 0.34 | 0.34 | 0.87 | 0.73 | 0.69 |
| LC3-300 | $G'$ | $[Pa]$ | 593.5 | 193.1 | 144.9 | 95.5 | |
| | $G''$ | $[Pa]$ | 283.3 | 87.7 | 35.6 | 24.4 | x |
| | $\gamma_l$ | $[\%]$ | 0.02 | 0.16 | 0.20 | 0.40 | x |
| | $\gamma_F$ | $[\%]$ | 0.05 | 1.59 | 10.1 | 25.2 | x |
| | $\tau_y$ | $[Pa]$ | 0.10 | 0.34 | 0.30 | 0.39 | x |

## A.3   Thixotropy analysis: Static yield stress test
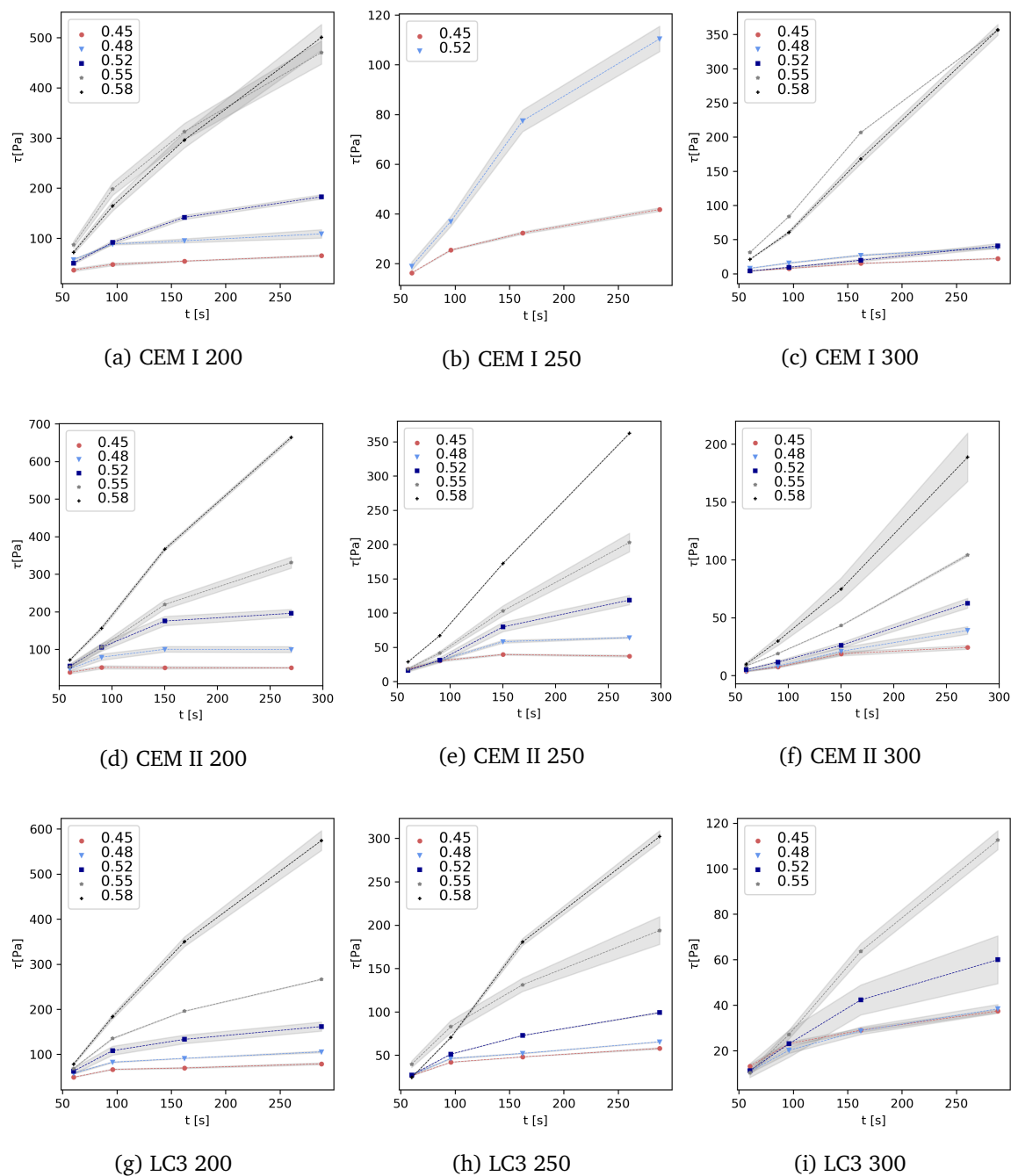


Figure A.6: Structural buildup measurements of all test series with the static yield stress test

Figure A.6 illustrates all structural buildup measurements with the static SYS test in the Vane-in-Cup geometry for the time scale until t = 300 s. The x-axis and y-axis are illustrated in linear scale. For the different test series, the range of the y-axis varies. With increasing solid volume fraction, the slope of $\tau(t)$ increased significantly.

Table A.13: Thixotropy parameters for CEM I test series

| Series | Par. | Unit | Solid volume fractions | | | | |
|---|---|---|---|---|---|---|---|
| | | | 0.45 | 0.48 | 0.52 | 0.55 | 0.58 |
| CEM I-200 | $A_{thix}$ | $[Pa/s]$ | 0.30 | 0.86 | 1.21 | 3.08 | 2.56 |
| | $c$ | $[Pa]$ | 227.4 | 578.9 | 386.7 | 580.0 | 476.5 |
| | $\Theta$ | $[s]$ | 18.8 | 20.0 | 27.4 | 29.5 | 25.7 |
| CEM I-250 | $A_{thix}$ | $[Pa/s]$ | 0.26 | 0.22 | 1.32 | 2.24 | x |
| | $c$ | $[Pa]$ | 130.6 | 412.8 | 109.5 | 624.6 | x |
| | $\Theta$ | $[s]$ | 21.5 | 117.5 | 52.7 | 146.1 | x |
| CEM I-300 | $A_{thix}$ | $[Pa/s]$ | 0.1 | 0.22 | 0.26 | 1.47 | 1.17 |
| | $c$ | $[Pa]$ | 19.9 | 58.2 | x | x | x |
| | $\Theta$ | $[s]$ | 32.8 | 28.6 | x | x | x |

Table A.14: Thixotropy parameters for CEM II test series

| Series | Par. | Unit | Solid volume fractions | | | | |
|---|---|---|---|---|---|---|---|
| | | | 0.45 | 0.48 | 0.52 | 0.55 | 0.58 |
| CEM II-200 | $A_{thix}$ | $[Pa/s]$ | 0.03 | 0.10 | 0.46 | 1.22 | 2.77 |
| | $c$ | $[Pa]$ | 0.0 | 586.8 | 589.7 | 728.4 | 1187 |
| | $\Theta$ | $[s]$ | 4.7 | 22.0 | 44.1 | 79.4 | 116.7 |
| CEM II-250 | $A_{thix}$ | $[Pa/s]$ | 0.03 | 0.17 | 0.46 | 0.89 | 1.63 |
| | $c$ | $[Pa]$ | 0.0 | 549.5 | 321.3 | 428.4 | 736.8 |
| | $\Theta$ | $[s]$ | 2.75 | 30.8 | 68.4 | 102.5 | 122.2 |
| CEM II-300 | $A_{thix}$ | $[Pa/s]$ | 0.08 | 0.17 | 0.29 | 0.48 | 0.92 |
| | $c$ | $[Pa]$ | 137.5 | 89.6 | 129.6 | 204.9 | 329.6 |
| | $\Theta$ | $[s]$ | 38.7 | 81.6 | 108.6 | 122.1 | 136.9 |

Table A.15: Thixotropy parameters for LC3 test series

| Series | Par. | Unit | Solid volume fractions | | | | |
|---|---|---|---|---|---|---|---|
| | | | 0.45 | 0.48 | 0.52 | 0.55 | 0.58 |
| LC3-200 | $A_{thix}$ | $[Pa/s]$ | 0.49 | 0.69 | 0.99 | 1.85 | 2.94 |
| | $c$ | $[Pa]$ | 559.9 | 571.8 | 587.1 | 582.1 | 512.5 |
| | $\Theta$ | $[s]$ | 17.0 | 18.8 | 23.1 | 25.9 | 28.8 |
| LC3-250 | $A_{thix}$ | $[Pa/s]$ | 0.43 | 0.53 | 0.67 | 1.20 | 1.26 |
| | $c$ | $[Pa]$ | 366.0 | 536.3 | 274.7 | 379.8 | 185.6 |
| | $\Theta$ | $[s]$ | 18.8 | 17.4 | 23.3 | 24.7 | 34.7 |
| LC3-300 | $A_{thix}$ | $[Pa/s]$ | 0.28 | 0.26 | 0.33 | 0.47 | 0.72 |
| | $c$ | $[Pa]$ | 176.0 | 104.2 | 82.2 | 97.0 | x |
| | $\Theta$ | $[s]$ | 20.2 | 24.0 | 30.0 | 33.0 | x |

## A.4   Structural buildup and flocculation time: SAOS tests
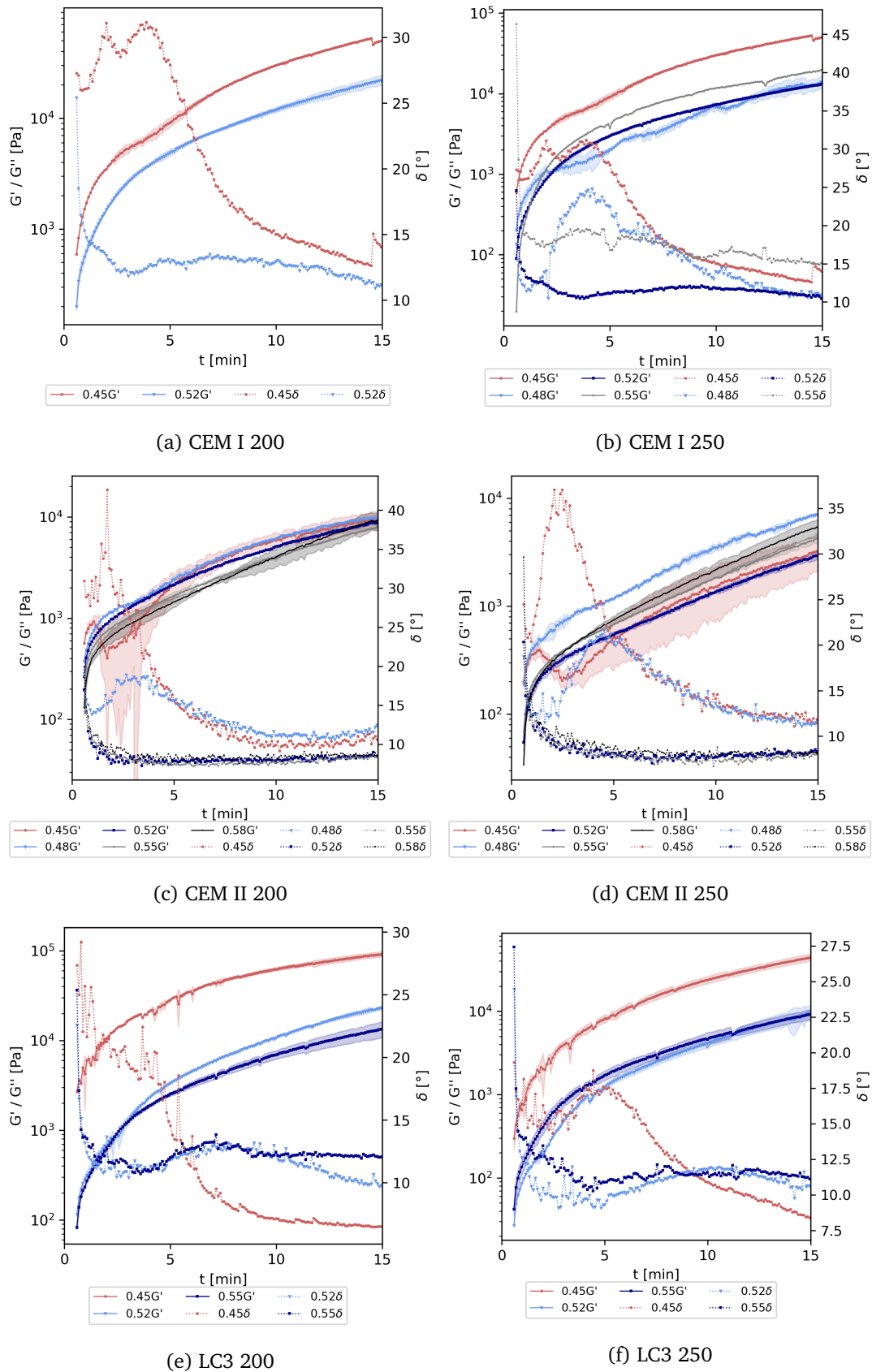


Figure A.7: Structural buildup measurements of all test series with the SAOS test

Table A.16: Structural buildup parameters for CEM I test series

| Series | Par. | Unit | Solid volume fractions | | | | |
|--------|------|------|------|------|------|------|------|
| | | | 0.45 | 0.48 | 0.52 | 0.55 | 0.58 |
| CEM I 200 | $G_{rig}$ | [$Pa/s$] | 84.4 | x | 43.0 | x | x |
| | $c_{SAOS}$ | [$Pa$] | 7,878 | x | 2,284 | x | x |
| | $\Theta_{perc}$ | [$s$] | 176.4 | x | 120.1 | x | x |
| | $\Theta_\delta$ | [$s$] | 594.4 | x | 294.4 | x | x |
| CEM I 250 | $G_{rig}$ | [$Pa/s$] | 83.9 | 42.6 | 52.0 | 64.0 | x |
| | $c_{SAOS}$ | [$Pa$] | 75,573 | 2,302 | 1,601 | 1,121 | x |
| | $\Theta_{perc}$ | [$s$] | 1145 | 779 | 120 | 126 | x |
| | $\Theta_\delta$ | [$s$] | 783 | 782 | 312 | 333 | x |

Table A.17: Structural buildup parameters for CEM II test series

| Series | Par. | Unit | Solid volume fractions | | | | |
|--------|------|------|------|------|------|------|------|
| | | | 0.45 | 0.48 | 0.52 | 0.55 | 0.58 |
| CEM II 200 | $G_{rig}$ | [$Pa/s$] | 12.4 | 11.4 | 12.5 | 16.9 | 26.3 |
| | $c_{SAOS}$ | [$Pa$] | 16,081 | 6,402 | 2,535 | 2,578 | 2,251 |
| | $\Theta_{perc}$ | [$s$] | 1141 | 462 | 252 | 328 | 320 |
| | $\Theta_\delta$ | [$s$] | 795 | 779 | 307 | 325 | 314 |
| CEM II 250 | $G_{rig}$ | [$Pa/s$] | 5.6 | 13.0 | 6.6 | 10.9 | 14.8 |
| | $c_{SAOS}$ | [$Pa$] | 4180 | 1812 | 964 | 972 | 954 |
| | $\Theta_{perc}$ | [$s$] | 1045 | 338 | 362 | 289 | 265 |
| | $\Theta_\delta$ | [$s$] | 975 | 330 | 375 | 448 | 375 |

Table A.18: Structural buildup parameters for LC3 test series

| Series | Par. | Unit | Solid volume fractions | | | | |
|--------|------|------|------|------|------|------|------|
| | | | 0.45 | 0.48 | 0.52 | 0.55 | 0.58 |
| LC3 200 | $G_{rig}$ | [$Pa/s$] | 98.7 | x | 74.0 | 27.0 | x |
| | $c_{SAOS}$ | [$Pa$] | x | x | 1163 | 969 | x |
| | $\Theta_{perc}$ | [$s$] | 803 | x | 131 | 122 | x |
| | $\Theta_\delta$ | [$s$] | 775 | x | 229 | 191 | x |
| LC3 250 | $G_{rig}$ | [$Pa/s$] | 54.2 | x | 26.9 | 24.5 | x |
| | $c_{SAOS}$ | [$Pa$] | x | x | 338 | 621 | x |
| | $\Theta_{perc}$ | [$s$] | 519 | x | 128 | 120 | x |
| | $\Theta_\delta$ | [$s$] | 699 | x | 299 | 304 | x |

The structural buildup analysis with the oscillatory SAOS test showed that the LC3 test series possessed a higher structural buildup parameter $G_{rig}$ than the other binder compositions. This corresponds to its physical properties: The increased specific surface area, see Table 4.3, leads to increased interparticle forces and, thus, higher flocculation than for the CEMI and CEMII test series.

## A.5   Microstructural effects on the non-Newtonian index

All test series were described by their actual paste solid volume fraction $\Phi_s$. However, physical and chemical analysis, reported in Chapter 4, proved that the different binders vary in their particle size distribution and, thus, their maximum packing density $\Phi_{max}$ and their water demand with the corresponding packing density $\Phi_{wd}$. To analyze the effect of the granulometric properties on the rheological properties, the relative solid volume fraction $\Phi_{rel}$ was calculated as $\Phi_{rel} = \Phi_s \,/\, \Phi_{max}$.

Furthermore, the ratio between the packing density at the water demand $\Phi_{wd}$ and $\Phi_{rel}$ was calculated. Theory states that when the water amount equals the water demand, the network strength yields its maximum due to interparticle forces, but also chemical additives such as superplasticizer become most efficient.

In Figure A.8 (a), $n(\Phi_s)$ is illustrated for all test series. On the contrary, Figure A.8 (b) $n(\Phi_{wd}/\Phi_{rel})$.
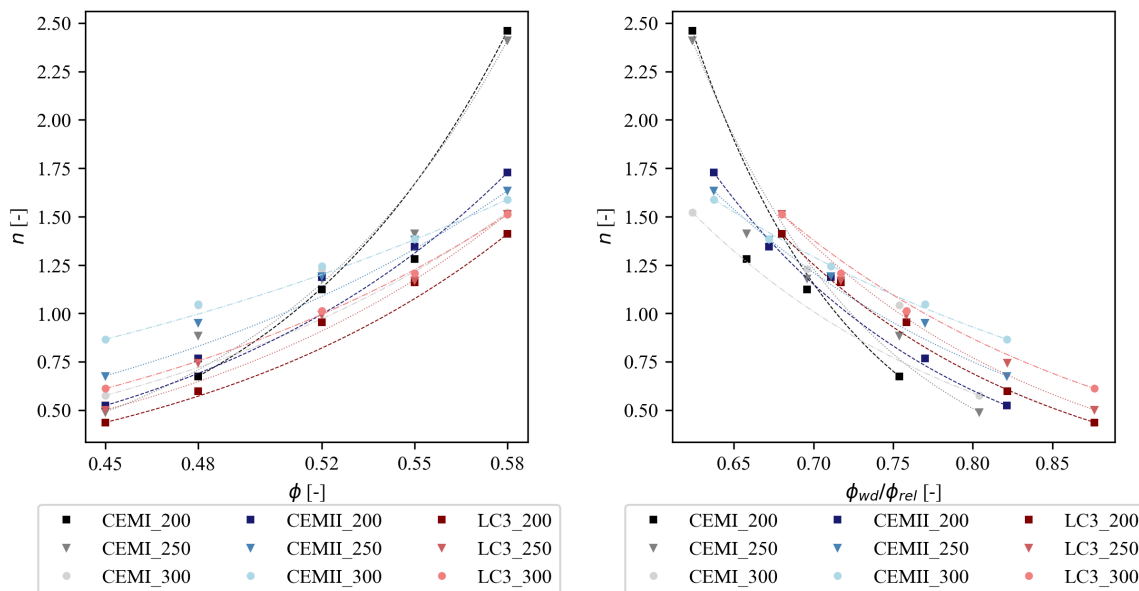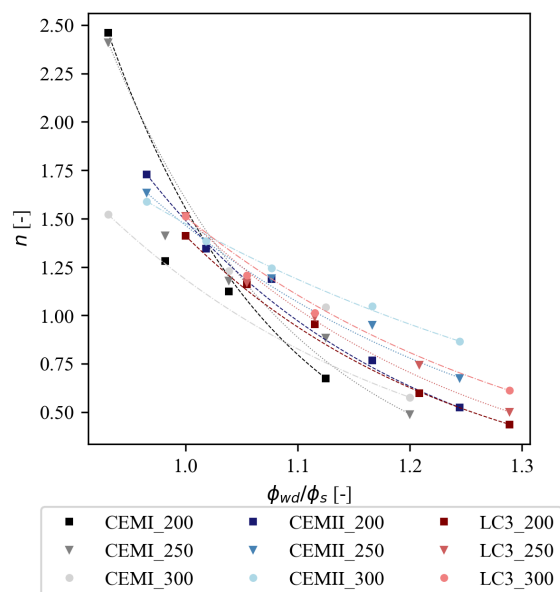


(a) $n(\Phi_s)$ for all test series            (b) $n(\Phi_{wd}/\Phi_{rel})$ for all test series

Figure A.8: Effect of microstructural packing density properties on the non-Newtoinian index $n$

While it appears in Figure A.8 (a) that LC3 compositions possess the lowest non-Newtonian indices, Figure A.8 (b) reveals that the normalization to the microstructural threshold values $\Phi_{wd}$ and $\Phi_{max}$ changes the relationship. While CEMI test series still yield the highest $n$ values with $n > 2$, the evolution of $n(\Phi_s)$ is different as values on the x-axis are shifted. Because the ratio $\Phi_{wd}/\Phi_{rel}$ did not appear descriptive, a third illustration shows $n(\Phi_{wd}/\Phi_s)$. In Figure A.9, the x-axis $n(\Phi_{wd}/\Phi_s)$ describes the ratio between the actual solid volume fraction and the optimum solid volume fraction for (I) high interparticle forces and (II) effective superplasticizer use. At $n(\Phi_{wd}/\Phi_s) > 1$, the evolution of $n(\Phi_s)$ is a measure for the robustness of paste consistency depending on PCE and water. At $n(\Phi_{wd}/\Phi_s) < 1$, nonlinear

flow increases exponentially.



(a) $n(\Phi_{wd}/\Phi_s)$ for all test series

Figure A.9: Effect of microstructural packing density properties on the non-Newtoinian index $n$

It was chosen not to model the findings to an empirical correlation equation, because it could falsify the relationship between cement paste viscosities and physical and chemical interactions. However, prospective research could combine the results with further microstructural investigations. Findings could lead to chemical and microstructural-based modeling of nonlinear flow of cementitious pastes.

## A.6 Regression parameters for plots in the summary

Table A.19: Regression parameters for $n(\phi_s)$ relation

| Regression | | Test series | | | | | | | | |
|---|---|---|---|---|---|---|---|---|---|---|
| | | CEMI-200 | CEMI-250 | CEMI-300 | CEMII-200 | CEMII-250 | CEMII-300 | LC3-200 | LC3-250 | LC3-300 |
| Log. | Slope | 12.9 | 12.2 | 7.5 | 9.2 | 6.8 | 4.7 | 9.0 | 8.5 | 7.0 |
| | Intercept | -6.6 | -6.2 | -3.9 | -4.8 | -3.4 | -2.2 | -4.9 | -4.5 | -3.6 |
| | $R^2$ | 0.91 | 0.95 | 0.64 | 0.95 | 0.95 | 0.99 | 0.96 | 0.97 | 0.99 |

Table A.20: Regression parameters for $\Theta(\Phi_s)$ relation

| Regression | | Test series | | | | | | | | |
|---|---|---|---|---|---|---|---|---|---|---|
| | | CEMI-200 | CEMI-250 | CEMI-300 | CEMII-200 | CEMII-250 | CEMII-300 | LC3-200 | LC3-250 | LC3-300 |
| Log. | Slope | -15.8 | -22.1 | x | -9.8 | -10.6 | x | -14.4 | -8.3 | x |
| | Intercept | 13.5 | 17.0 | x | 11.4 | 11.7 | x | 13.2 | 10.3 | x |
| | $R^2$ | 0.28 | 0.94 | x | 0.50 | 0.53 | x | 0.98 | 0.92 | x |

Table A.21: Regression parameters for $A_{thix}(n)$ relation

| Regression | | Test series | | | | | | | | |
|---|---|---|---|---|---|---|---|---|---|---|
| | | CEMI-200 | CEMI-250 | CEMI-300 | CEMII-200 | CEMII-250 | CEMII-300 | LC3-200 | LC3-250 | LC3-300 |
| Log. | Slope | 16.5 | 21.5 | 18.9 | 34.8 | 30.7 | 18.8 | 13.8 | 8.3 | 7.3 |
| | Intercept | -8.6 | -11.0 | -10.8 | -19.2 | -17.4 | -10.9 | -6.9 | -4.6 | -4.5 |
| | $R^2$ | 0.54 | 0.97 | 0.58 | 0.99 | 0.94 | 0.99 | 0.98 | 0.90 | 0.74 |

Table A.22: Regression parameters for $l_x(A_{thix})$ relation

| Regression | | Test series | | | | | | | | |
|---|---|---|---|---|---|---|---|---|---|---|
| | | CEMI-200 | CEMI-250 | CEMI-300 | CEMII-200 | CEMII-250 | CEMII-300 | LC3-200 | LC3-250 | LC3-300 |
| Lin. | Slope | -0.05 | -0.07 | -0.25 | -0.01 | -0.06 | -0.05 | -0.02 | -0.07 | -0.05 |
| | Intercept | 0.30 | 0.54 | 0.74 | 0.26 | 0.45 | 0.67 | 0.28 | 0.45 | 0.57 |
| | $R^2$ | 0.16 | 0.69 | 0.46 | 0.25 | 0.98 | 0.21 | 0.19 | 0.18 | 0.83 |

# B. Minimal code examples

Minimal code examples with experimental raw data are stored in a public repository on GITHUB, `https://github.com`. The repository does not show all codes and functions applied, but provides an overview on several regression functions for the rheological analysis methods introduced in Chapter 3. The repository is available online at

`https://github.com/Mareike-99/rheocem2024_public.git`

The folder can be cloned and directly run locally - the codes solely refer to data that are stored in the same folder. The code is open to use and share, licenced under the MIT Licence (see `https://opensource.org/license/mit/`.

The readme.file is copied here to provide an overview.

————————————————-

This repository is to show minimal examples on how rheological data of cementitious pastes, originating from rheometric tests, were analyzed.

Following analysis methods are available:

———————————————— "VP-regressions.py"

The file fits experimental flow curves, consisting of the raw data shear rate and shear stress, to phenomenological models:

- Bingham model

- Herschel-Bulkley model

- modified Bingham model

- Casson model

- Toussaint model

- Cross model

- Sisko model

- Williamson model

Flow curve data are stored in the files "PPdyn_0.45-250.xlsx"
"PPdyn_0.55-250.xlsx"

————————————————-

LAOS-intercyclic.py

The code analyzes raw data of a large amplitude oscillatory sweep test with 51 strain amplitudes. Both first harmonic rheological data and oscillatory wave data are stored. The code plots the data as strain-sorage modulus / loss modulus plot. The linear viscoelastic range, critical strain, crossover point and yield index are calculated. The code reads the data:

"LAOS_0.55_250_1.csv"
"LAOS_0.55_250_2.csv"
"LAOS_0.55_250_3.csv"

————————————————-

"Vane_RenerRiwlin.py"

The code analyzes rheometric raw data from large gap Vane-in-Cup rheometry. Several functions were implemented:

- Reiner-Riwlin equation for the whole gap

- Reiner-Riwlin equation with a partially sheared gap

- Second-Krieger solution (not applied in this code, but implemented)

- function to loop through the raw data with varying input ranges and input range steps

By running this code, the variation of calculated yield stress and viscosity values is plotted, together with the MSE.

The code reads the data:

"Vane_0.45-250.xlsx"
"Vane_0.55-250.xlsx"

————————————————-

"SYS-Athix-nonlin.py"

This file is to calculate structural buildup in different ways from a static yield stress test. The procedure in the code is:

- Read the raw data

- Average the raw data

- Read the shear-ups and maximum torque after rest, and store them in arrays

- From the increasing torque values, calculate structural buildup as:

    1. $A_{\text{thix,early}}$
    2. $A_{\text{thix,late}}$
    3. Nonlinear thixotropy increase

- Plot the data and store parameters in a dataframe

The code reads the data:

"Vane_0.45-250.xlsx"
"Vane_0.55-250.xlsx"

———————————————-

"SYS-Athix-nonlin.py"

This code is to analyze structural buildup. The increase of storage modulus is fitted to a phenomenological function that analyzes the structural increase in two parts: First, with an exponential function to calculate a flocculation parameter theta. Second, the linear static increase after flocculation is analyzed as rigidification parameter.

The procedure in the code is:

- read the raw data

- fit the flocculation function with different input arrays

- fit the rigidification function with different input arrays

- find the best fit

The code reads the data:

"SAOS_0.55_250.csv"

# C. MITLaos for nonlinear viscoelastic characterization

The MITLaos software is provided R.H. Ewoldt, A.E. Hosoi, G.H. McKinley, see

`https://web.mit.edu/nnf/research/phenomena/mit_laos.html`

The software calculates rheological data from a Large Amplitude Oscillatory Shear protocol. Reference information for the user manual are stored in Ewoldt et al. (2007). The software provides a MATLAB code that starts a GUI to read data from an oscillatory experiment.

The procedure in this thesis to calculate non-linear viscoelastic parameters was

1. Run a self-employed MATLAB code that converts the experimental data from an oscillatory experiment, provided as .csv file, into MATLAB arrays. Data of each amplitude were stored in a single array

2. Start the MITLaos GUI

3. Read and analyze each MATLAB file for each single amplitude

4. store all calculated viscoelastic parameters $e$, $v$, $S$, $T$, two-dimensional and three-dimensional visualizations of LB curves in text files

5. post-process the analyzed data (e.g., in EXCEL, PYTHON or MATLAB)

**Output visualization from MITLaos GUI**

Figure C.1 depicts the visual output in the user interface of the MITLaos software. The time-dependent raw data input strain $\gamma(t)$ and output stress $\tau(t)$ are illustrated in the upper left. Time-resolved LB curves illustrate filtered $\gamma - \tau$ and $\dot{\gamma} - \tau$ curves. The filter function is part of the MITLaos software. Within the software, Fourier-Transformation as introduced in Eq. 2.35 and Chebyshev decomposition as introduced in Eq. 2.36 calculate viscoelastic parameters. They are stored in single text files for each amplitude sweep. The intensity of the higher harmonics and Chebyshev coefficients are illustrated in the user interface.
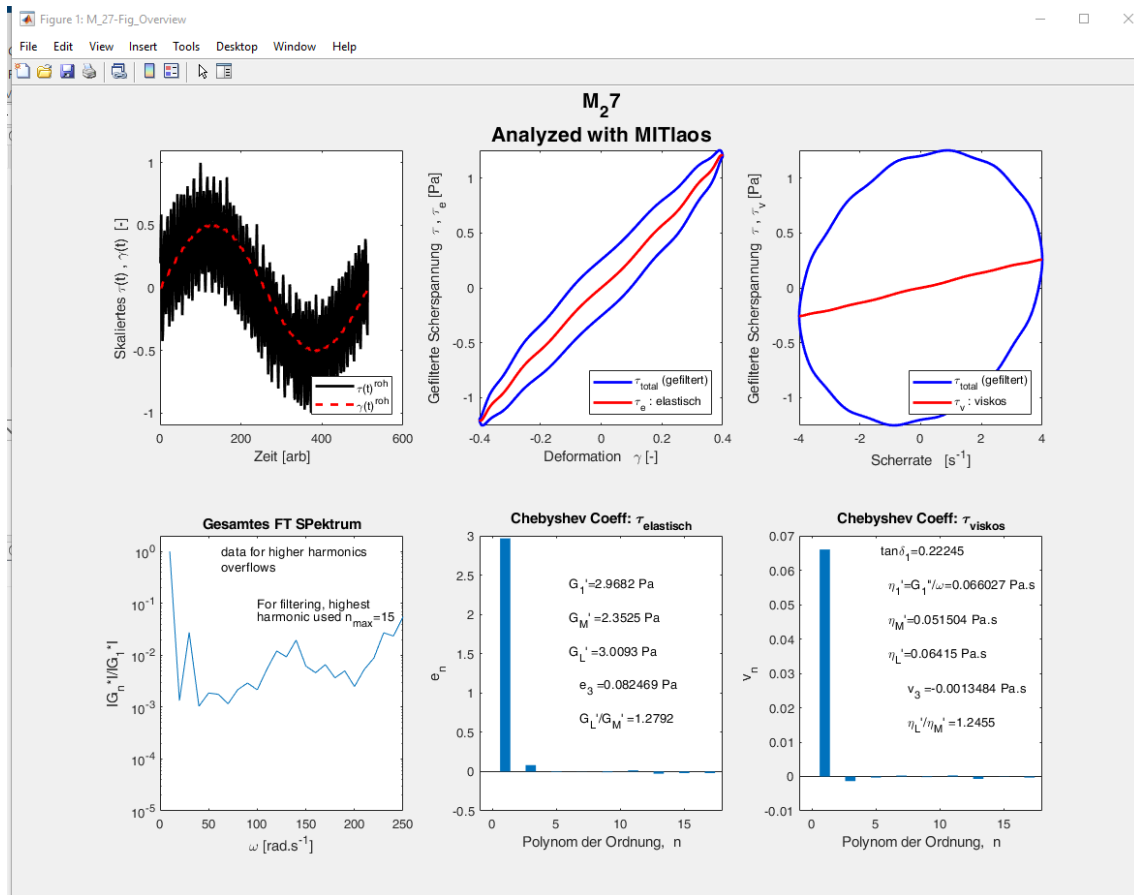
Figure C.1: Output data from MITLaos

**Visualization of viscoelastic parameters**

After all amplitudes o one test series were analayzed with the MITLaos software, LB curves were plotted directly in a MATLAB protocol, illustrated in Figure C.2. The first harmonics of the full LAOS experiment are illustrated in the upper left graphic of Figure C.2. In three plots, LB curves of the linear viscoelastic regime, transient regime and non-linear regime were visualized. This enabled the graphical interpreation of intra-cyclic strain thickening or strain thinning material behavior.

The viscoelastic parameters of all test series, stored in text files as output from the MITLaos software, were finllay read ad visualized in a PYTHON code. Figure C.3 exemplary illustrates two different visualizations. Figure C.3 (a) illustrates different LB curves for one test series. The illustration shows the different material behavior within the linear viscoelastic, transient and non-linear regime. Figure C.3 (b) displays the evolution of the strain-stiffening ratio $S$ for different test series.
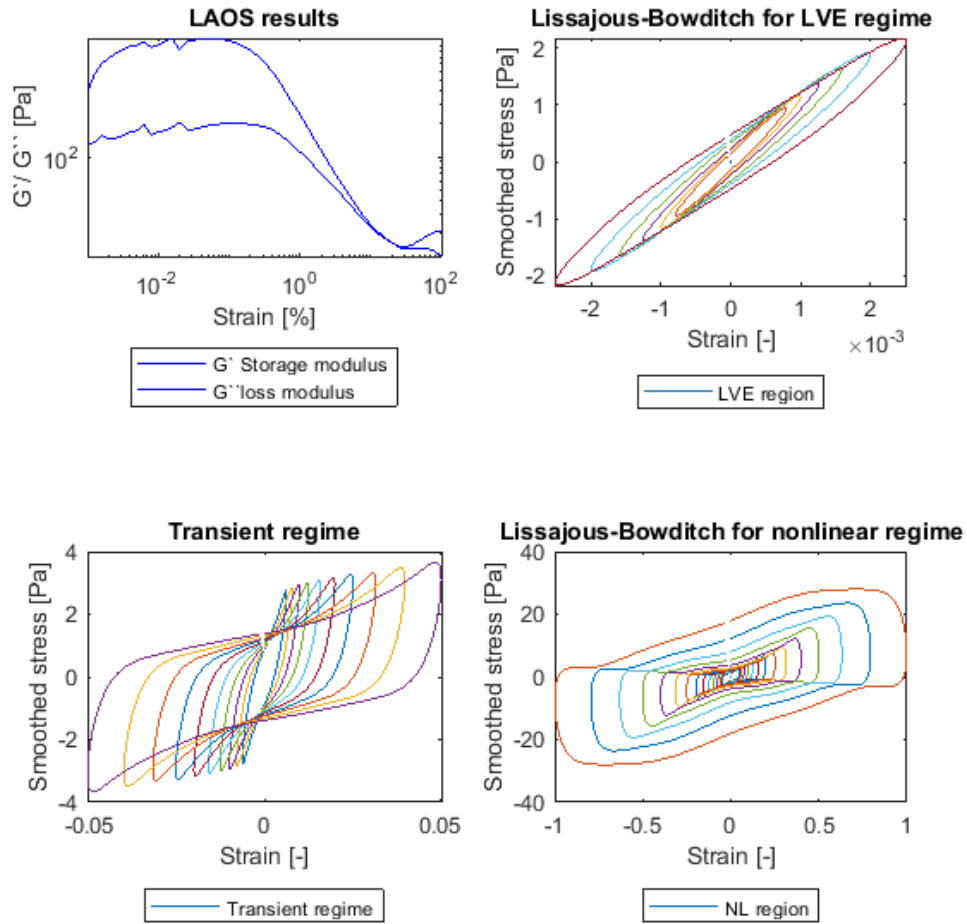
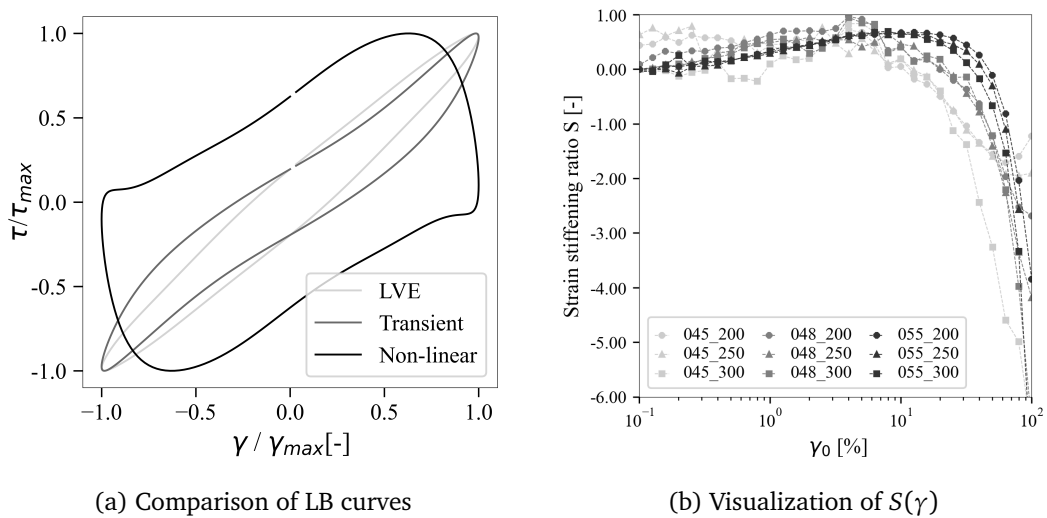Figure C.2: Visualizetion of all LB curves from output data generated with MITLaos



(a) Comparison of LB curves

(b) Visualization of $S(\gamma)$

Figure C.3: Analysis of non-linear viscoelastic parameters

# D. Complete List of Publications

## Publications related to this thesis

### Journal articles

[J1] **Thiedeitz, M.**; Kränkel, T.; Kartal, D.; Timothy, J.J. (2024). *The Slump Flow of Cementitious Pastes: Simulation vs. Experiments. Materials*, 17, 532, doi.org/10.3390/ma17020532

[J2] **Thiedeitz, M.**; Kränkel, T.: (2024). *Steady and transient phenomenological thixotropy modeling of non-Newtonian cementitious pastes. Cement and Concrete Research* (submitted)

[J3] **Thiedeitz, M.**; Kränkel, T.; Gehlen, C. (2022). *Viscoelastoplastic classification of cementitious suspensions: transient and non-linear flow analysis in rotational and oscillatory shear flows. Rheologica Acta* 61, 549-570, doi.org/10.1007/s00397-022-01358-9

[J4] **Thiedeitz, M.**; Dressler, I.; Kränkel, T.; Gehlen, C.; Lowke, D. (2020). *Effect of Pre-Shear on Agglomeration and Rheological Parameters of Cement Paste. Materials*, Vol. 13, No.9, p. 2173, doi.org/10.3390/ma13092173

[J5] **Thiedeitz, M.**; Habib, N.; Kränkel, T.; Gehlen, C. (2020).*L-Box Form Filling of Thixotropic Cementitious Paste and Mortar. In: Materials*, Vol. 13, No. 7, p. 1760, doi.org/10.3390/ma13071760

[J6] Haist, M. et al., [...]; **Thiedeitz, M.**, et al. (2020). *Interlaboratory study on rheological properties of cement pastes and reference substances: comparability of measurements performed with different rheometers and measurement geometries.. Materials and Structures,*Vol. 53, No. 4, doi.org/10.1617/s11527-020-01477-w

[J7] Ukrainczyk, N.; **Thiedeitz, M.**;,Kränkel, T.; Koenders, E.; Gehlen, C. (2020). *Modeling SAOS Yield Stress of Cement Suspensions: Microstructure-Based Computational Approach. In: Materials*, Vol. 13, No. 12, p. 2769, doi.org/10.3390/ma13122 769

### Conference articles

[C1] **Thiedeitz, M.**; Crasselt, C.; Xiao, P.; Ukrainczyk, N.; Schmidt, W.; Kränkel, T.: (2023). *Multidisciplinary approach for the prediction of cement paste rheological properties: physical analysis, experimental rheology and microstructural modeling. Proceedings of*

*21. International Baustofftagung, 13 to 15 September 2023 - Weimar, Deutschland* /doi.org/10.1002/cepa.2812

[C2] **Thiedeitz, M.**; Timothy, J.; Kränkel, T. (2022). *Computational modeling and characterization of non-Newtonian visco-plastic cementitious building materials.. 8th European Congress on Computational Methods in Applied Sciences and Engineering, CIMNE*, doi:10.23967/eccomas.2022.06 9

[C3] **Thiedeitz, M.**; Kränkel, T.; Gehlen, C. (2019). *Thixotropic Structural Build-Up of Cement Pastes at Low Shear Rates.*. In: Ivankovic, A. et al. (Ed.): *International Conference on Sustainable Materials : Challenges in Design and Management of Structures : RILEM Publications*, Vol. 4, p. 272–279 E-ISBN: 978-2-35158-218-3

[C4] **Thiedeitz, M.**; Kränkel, T.; Gehlen, C. (2019). *Thixotropy-Dependent Form Filling Ability of Cement Paste.*. In: Mechtcherine, V.; Khayat, K.; Secrieru, E. (Ed.): *Rheology and Processing of Construction Materials; Springer International Publishing, RILEM Bookseries*, p. 273–280, doi.org/10.1007/978-3-030-22566 -7

## Non-peer-reviewed articles

[M1] **Thiedeitz, M.**; Kränkel, T. (2024) *Comparative Small and Large Gap Rheometry for Cementitious Pastes.*. *Preprints*, 2024020703 doi.org/10.20944/preprints202402.0703.v1

## Further publications

[M1] **Thiedeitz, M.**; Tarrab Maslaton, N.; Kränkel, T. (2024). *Workability of low-clinker mortars with recycled fine aggregates and different polymers as superplasticizer. Conference proceedings for ICCM: 12th ACI/RILEM International Conference on cementitious materials and alternative binders for sustainable concrete, 23 to 26 June 2024 - Toulouse, France*, (accepted)

[M2] **Thiedeitz, M.**; Engelhardt, J.; Kränkel, T. (2024). *Effect of Water/Binder Ratio on Fresh and Hardened Properties of Mortars with Rice Husk Ashes as Additive. Conference proceedings for 6th Symposium on Ultra-High Performance Concrete and High Performance Building Materials for Sustainable Construction, 06 to 08 March 2024 - Kassel, Germany*, (accepted)

[M3] Tappertz, L.; Klein, N.; **Thiedeitz, M.**; Kränkel, T.: (2023). *Vergleichende Ökobilanzierung offenporiger Beton- und Asphaltdeckschichten im Straßenbau. Proceedings of 21. International Baustofftagung, 13 to 15 September 2023 - Weimar, Deutschland* https://doi.org/10.1002/cepa.2969

[M4] **Thiedeitz, M.**, Ostermaier, B.; Kränkel, T. (2022). *Rice husk ash as an additive in mortar – Contribution to microstructural, strength and durability performance Resources, Conservation and Recycling,* Vol. 184, p. 106389, `https://doi.org/10.1016/j.resconrec.2022.106389`

[M5] Schmidt, W. et al, [...] ; **Thiedeitz, M.**, et al. (2021). *Sustainable circular value chains: From rural waste to feasible urban construction materials solutions.. Developments in the Built Environment 6,* p. 100047, `https://doi:10.1016/j.dibe.2021.100047`

[M6] Schmidt, W., et. al, [...] ; **Thiedeitz, M.**, et al. (2021). *Challenges, Opportunities and Potential Solution Strategies for Environmentally and Socially Responsible Urban Development of Megacities in Africa*. Pereira, Eduardo B.; Barros, Joaquim A. O.; Figueiredo, Fabio P. (Ed.): In: *Proceedings of the 3rd RILEM Spring Convention and Conference, Springer International Publishing, RILEM Bookseries*, p. 119–132, `https://doi.org/10.1007/978-3-030-76547-7_11`

[M7] **Thiedeitz, M.**, Schmidt, W.; Härder, M.; Kränkel, T (2020). *Performance of Rice Husk Ash as Supplementary Cementitious Material after Production in the Field and in the Lab*. *Materials*, Vol. 13, No. 19, p. 4319, `https://doi.org/10.3390/ma13194319`